Measurement of the Cross Section for the Process $e^+e^- \rightarrow W^+W^- \rightarrow q\bar{q}q\bar{q}$ and Determination of the W Mass with the L3 Detector

Ho Jong Lee
Humboldt University Berlin
2000

Measurement of the Cross Section for the Process $e^+e^- \to W^+W^- \to q\bar{q}q\bar{q}$ and Determination of the W Mass with the L3 Detector

DISSERTATION

zur Erlangung des akademischen Grades
doctor rerum naturalium
(dr. rer. nat.)
im Fach Physik

eingereicht an der
Mathematisch-Naturwissenschaftlichen Fakultät I
Humboldt-Universität zu Berlin

von
Herr Dipl.-Phys. Ho Jong Lee
geboren am 05.05.1968 in Ahn-Dong, S.Korea

Präsident der Humboldt-Universität zu Berlin:
Prof. Dr. Jürgen Mlynek

Dekan der Mathematisch-Naturwissenschaftlichen Fakultät I:
Prof. Dr. Bernhard Ronacher

Gutachter:

1. Prof. Dr. Thomas Hebbeker
2. Prof. Dr. Paul Söding
3. Prof. Dr. Martin Pohl

eingereicht am: 15. Dezember 2000
Tag der mündlichen Prüfung: 22. März 2001

To

Jung-Hoi and Hoik

Abstract

This thesis describes a measurement of the cross section for the process $e^+e^- \rightarrow W^+W^- \rightarrow q\bar{q}q\bar{q}$ and the determination of the W mass with the L3 detector at LEP.

In a data sample corresponding to a total luminosity of 232 pb^{-1} collected at center-of-mass energy between 183 GeV and 189 GeV, 1957 four-fermion events with pairs of hadronic jets are selected. Based on these events, the cross sections for the doubly resonant process $e^+e^- \rightarrow W^+W^- \rightarrow q\bar{q}q\bar{q}$ have been measured to be 7.94 ± 0.45 (stat) ± 0.21 (syst) pb and 7.53 ± 0.25 (stat) ± 0.17 (syst) pb at 183 GeV and 189 GeV respectively. Using the selected events of the other final states of the process $e^+e^- \rightarrow W^+W^-$ and combining all the final states, the total cross sections and the hadronic branching fraction of the W decays are measured:

$$\begin{aligned} \sigma_{\mathrm{WW}}^{183\ \mathrm{GeV}} &= 16.10 \pm 0.66\ (\mathrm{stat}) \pm 0.26\ (\mathrm{syst})\ \mathrm{pb}, \\ \sigma_{\mathrm{WW}}^{189\ \mathrm{GeV}} &= 16.36 \pm 0.37\ (\mathrm{stat}) \pm 0.22\ (\mathrm{syst})\ \mathrm{pb}, \\ Br(\mathrm{W} \rightarrow q\bar{q}) &= 68.36 \pm 0.69\ (\mathrm{stat}) \pm 0.33\ (\mathrm{syst})\ \%, \end{aligned}$$

where the lepton universality is assumed. These results are consistent with Standard Model expectations. The measured hadronic branching fraction allows a determination of the CKM matrix element

$$|V_{cs}| = 1.035 \pm 0.032\ (\mathrm{stat}) \pm 0.016\ (\mathrm{syst}).$$

The mass of the W boson is determined by the direct reconstruction of the W decays in $W^+W^- \rightarrow q\bar{q}q\bar{q}$ and $W^+W^- \rightarrow q\bar{q}l\nu$ events. The combined result from all final states is

$$M_{\mathrm{W}} = 80.325 \pm 0.081\ (\mathrm{stat}) \pm 0.060\ (\mathrm{syst})\ \mathrm{GeV}.$$

A division of the data into positively and negatively charged W bosons yields

$$M_{\mathrm{W^+}} \; - \; M_{\mathrm{W^-}} = +0.28 \pm 0.42 \text{ GeV},$$

where only $q\bar{q}e\nu$, $q\bar{q}\mu\nu$ and $q\bar{q}q\bar{q}$ events have been used. This result is consistent with CPT invariance.

In 1999, W-pair events were produced between 192 GeV and 202 GeV center-of-mass energy. These data correspond to an integrated luminosity of 234 pb^{-1}. The hadronic cross sections are measured, and the preliminary results are reported. Combining all final states in W-pair production and all the selected events between 183 GeV and 202 GeV center-of-mass energy, the mass of the W boson is measured. The preliminary result obtained is

$$M_{\mathrm{W}} \; = \; 80.312 \; \pm \; 0.060 \text{ (stat)} \; \pm \; 0.058 \text{ (syst) GeV}.$$

.

Keywords:

W boson, cross section, branching ratio, mass

Zusammenfassung

Diese Arbeit beschreibt die Messung der Wirkungsquerschnitte für die Reaktion $\mathrm{e^+e^-} \rightarrow \mathrm{W^+W^-} \rightarrow q\bar{q}q\bar{q}$ und die Bestimmung der W-Masse mit dem L3-Detektor am LEP.

In einem Datensample gesammelt bei den Schwerpunktsenergien zwischen 183 GeV und 189 GeV, das einer Gesamtluminosität von 232 pb^{-1}entspricht, sind 1957 Vier-Fermion-Ereignisse mit hadronischen Jetpaaren selektiert worden. Auf diese Ereignisse basierend wurden die Wirkungsquerschnitte für die Reaktion $\mathrm{e^+e^-} \rightarrow \mathrm{W^+W^-} \rightarrow q\bar{q}q\bar{q}$ gemessen, jeweils 7.94 ± 0.45 (stat) $\pm$ 0.21 (syst) pb und 7.53 ± 0.25 (stat) $\pm$ 0.17 (syst) pb entsprechend 183 GeV und 189 GeV. Unter der Benutzung der selektierten Ereignisse der anderen Endzustände der Reaktion $\mathrm{e^+e^-} \rightarrow \mathrm{W^+W^-}$ und der Kombination aller Endzustände wurden die Gesamtwirkungsquerschnitte und hadronische Verzweigungsverhältnisse (Br) des W-Zerfalls gemessen:

$$\begin{aligned}\sigma_{\mathrm{WW}}^{183\ \mathrm{GeV}} &= 16.10 \pm 0.66\ (\mathrm{stat}) \pm 0.26\ (\mathrm{syst})\ \mathrm{pb},\\ \sigma_{\mathrm{WW}}^{189\ \mathrm{GeV}} &= 16.36 \pm 0.37\ (\mathrm{stat}) \pm 0.22\ (\mathrm{syst})\ \mathrm{pb},\\ Br(\mathrm{W} \rightarrow q\bar{q}) &= 68.36 \pm 0.69\ (\mathrm{stat}) \pm 0.33\ (\mathrm{syst})\ \%,\end{aligned}$$

wobei die Lepton-Universalität angenommen ist. Die Ergebnisse sind konsistent mit der Standardmodelerwartung. Das gemessene hadronisches Verzweigungsverhältnis erlaubt eine Bestimmung des CKM-Matrixelement

$$|V_{cs}| = 1.035 \pm 0.032\ (\mathrm{stat}) \pm 0.016\ (\mathrm{syst}).$$

Die Masse des W-Bosons ist bei der direkten Rekonstruktion des W-Zerfalls in $\mathrm{W^+W^-} \rightarrow q\bar{q}q\bar{q}$- und $\mathrm{W^+W^-} \rightarrow q\bar{q}l\nu$-Ereignisse bestimmt worden. Das kombinierte Ergebnis von allen Endzuständen ist

$$M_{\mathrm{W}} \;=\; 80.325 \;\pm\; 0.081\ (\mathrm{stat}) \;\pm\; 0.060\ (\mathrm{syst})\ \mathrm{GeV}.$$

Eine Teilung der Daten in positiv und negativ geladene W-Bosonen ergibt

$$M_{\mathrm{W^+}} \;-\; M_{\mathrm{W^-}} = +0.28 \pm 0.42\ \mathrm{GeV},$$

wobei nur $q\bar{q}e\nu$, $q\bar{q}\mu\nu$- und $q\bar{q}q\bar{q}$-Ereignisse benutzt wurden. Dieses Ergebnis ist konsistent mit der CPT-Erhaltung.

In 1999, W-Paarereignisse wurden zwischen 192 GeV- und 202 GeV- Schwerpunktsenergien produziert. Diese Daten entsprechen einer integrierte Luminosität von 234 pb^{-1}. Die hadronische Wirkungsquerschnitte wurden gemessen, und die vorläufigen Ergebnisse sind berichtet. Alle Endzustände der W-Paar-Produktion und alle selektierten Ereignisse zwischen den Schwerpunktsenergien von 183 GeV and 202 GeV wurden kombiniert, und die Masse des W-Bosons ist gemessen. Das vorläufigen Ergebnis ist

$$M_{\mathrm{W}} \;=\; 80.312 \;\pm\; 0.060\ (\mathrm{stat}) \;\pm\; 0.058\ (\mathrm{syst})\ \mathrm{GeV}.$$

.

Sclagwörter:
W-Boson, Wirkungsquerschnitt, Verzweigungsverhältnis, Masse

Inhaltsverzeichnis

Kapitel 1

Introduction

One of man's enduring quests has been to understand why nature is the way it is. What is matter made of and what holds it together ? About 25 centuries ago the Ionian Greeks argued that the apparent complexity and variety of nature could be understood in terms of a few simple underlying laws. There is no obvious reason why nature should be so complicated.

Particle physics is the science of the fundamental nature of matter and its research represents man's effort to answer this question. The question why the nature is the way it is can be answered in terms of elementary particles and their interactions. It seems that all known matter is built from a small number of different particles, held together by a few fundamental forces. The theoretical framework for this phenomenon is the Standard Model [1, 2]. According to this theory all matter is made up of quarks and leptons, whose interactions with one another are mediated by the exchange of gauge particles (Table 1.1). The interactions of the elementary particles with one another can be confined to four broad categories: electromagnetic, weak, strong and gravitational (Figure 1.1).

The electron is classified as a lepton, and its electromagnetic interactions with atomic nuclei are mediated by a photon. Electromagnetism has an unlimited range. It can be felt directly as agencies that push or pull. Electromagnetic interactions are responsible for all the familiar chemical and physical properties of ordinary solids, liquids and gases. Weak interactions are of such short range (less than 10^{-13} centimeter) and are so weak that they can not be perceived

Lepton	Charge(e)	Mass	Quark	Charge(e)	Mass
e^-	-1	1/2 MeV	u	2/3	$\sim$ 5 MeV
ν_e	0	$<$ 1.5 eV	d	$-1/3$	$\sim$ 8 MeV
μ^-	-1	105 MeV	c	2/3	$\sim$ 1.5 GeV
ν_μ	0	$<$ 0.17 MeV	s	$-1/3$	$\sim$ 170 MeV
τ^-	-1	1.78 GeV	t	2/3	$\sim$ 174 GeV
ν_τ	0	$<$ 18.2 MeV	b	$-1/3$	$\sim$ 4.4 GeV

Gauge Boson	Spin	Mass (GeV)	Range of Force
Photon (γ)	1	0	∞
$W^\pm$	1	80.41	$\sim 10^{-18}$ m
Z	1	91.187	$\sim 10^{-18}$ m
Gluon (g)	1	0	$\sim 10^{-15}$ m
Graviton (G)	2	0	∞

Tabelle 1.1: *Fundamental particles in the Standard Model. Three generations of elementary particles are known to exist today. Included are six quarks (up, down, strange, charm, bottom, top), six leptons (electron, muon, tau, and a neutrino associated with each of the three), and four types of force-carrying particles, the bosons (photon, gluons, Z,W).*

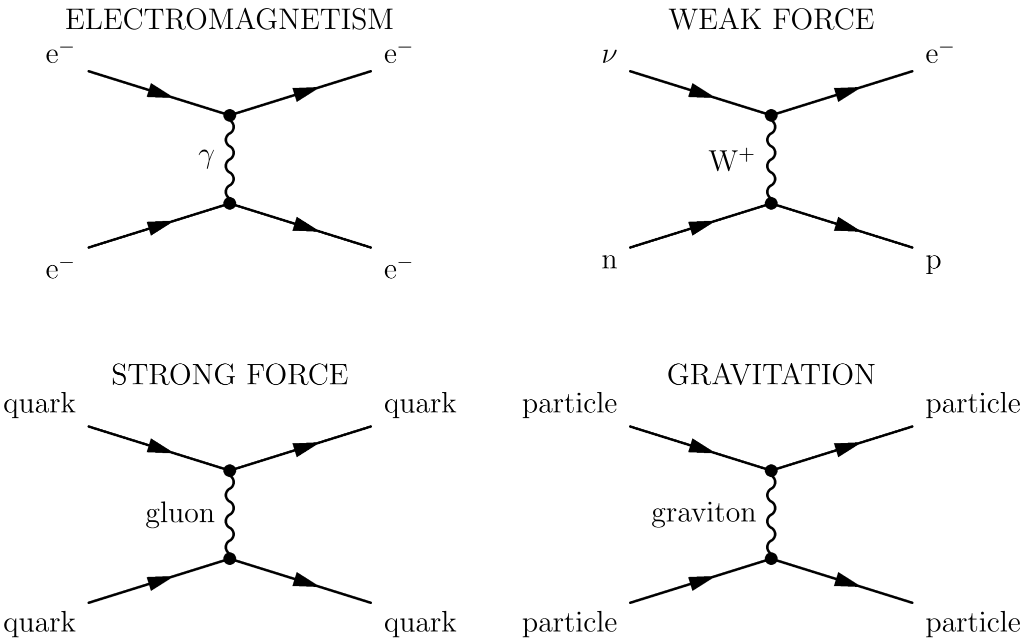

Abbildung 1.1: *Interactions between particles can be visualized through feynman diagrams in which two vertexes are connected. The force between the two particles is transmitted by the exchange of a third particle, which is said to be virtual because it cannot be directly observed. It exists for too short a time. Of these exchanged quanta only the graviton has yet to be observed, although there is confidence that it also exits.*

directly. They are responsible for processes as the beta decay of a radioactive atomic nucleus. They provide also the first step in the chain of thermonuclear reactions in the sun, a step in which two protons fuse to form a deuterium nucleus, a positron and a neutrino. The weak vector bosons ($W^{\pm}$,Z) are the mediators of these interactions [1]. The proton, the neutron and many other particles are classified as hadrons, and are made up of three fractionally charged quarks. Quarks are held together by a strong interaction, and that interaction is mediated by the exchange of eight gauge particles called gluons. The quarks and gluons in turn have a new kind of charge named color, on which the strong force acts. Each of the quarks can carry one of three kinds of color charge: red, green or blue.

---

[1] In the first step of the chain mentioned above, the W boson doesn't interact directly with the proton and neutron but rather with the constituents of these particles, the charged quarks.

Hadrons do not exhibit a color charge; the sum of the component quarks' colors must be white, or color neutral. The strong forces are limited in range to about 10^{-13} centimeters. The most familiar of the interactions is gravitation. Gravity keeps our feet on the ground and the planets in their orbits. By positing an analogy with the other three interactions one could assume that another gauge particle, the graviton, mediates the gravitational interaction, but such a particle has not yet been detected. In all it is now believed there are at least six quarks with six corresponding antiquarks, each in three varieties of color, six leptons and six corresponding antiparticles, one photon, three weak vector bosons, eight gluons and perhaps a graviton.

The masses of the elementary particles

As depicted in Table 1.1, only the upper limits on the neutrino masses have been determined. This is because the neutrinos are difficult to observe experimentally. The Standard Model fixes the neutrino mass to zero as there is no right-handed neutrino in the model (see Chapter 2). In measuring the neutrino masses one can test the Standard Model. More discussion to the neutrino masses can be found in Chapter 2. In contrast to the leptons, free quarks have never been observed. This explains why the masses of quarks are not very precise. Nevertheless, the quark model is believed to be correct because of its success in predicting the outcome of high-energy collisions of an electron and a positron, the anti-particle of the electron. The leptons and quarks are called fermions due to their spin of 1/2. The mass of gauge bosons has also been probed. Some of them have zero masses and some of them are roughly 100 times heavier than the proton mass of 1 GeV. This is a simple consequence of the uncertainty principle in quantum mechanics, which states that uncertainties in our knowledge of the momentum and the position of a particle are inversely proportional to each other. Accordingly, the range of a force is inversely proportional to the mass of the particle that transmits it. If the exchanged particle has a large mass, more energy must be borrowed in order to support its existence, and the debt must be repaid more swiftly lest the discrepancy be discovered. The distance the particle can travel before it must be reabsorbed is thereby reduced and thus the corresponding force has a short range. Therefore electromagnetism and gravity, which are infinite in range, arise from the exchange of massless gauge bosons, where the weak force has an exceedingly small sphere of influence due to the large masses of the exchange gauge bosons. Nevertheless, the question remains as to the role of the gluons. They have zero mass and a finite range, but this is not precise. Indeed, the strong interactions between quarks follow an inverse-square law and have infinite range. The example of electromagnetism explains why strong interactions have finite range. Electromagnetic forces between two neutral atoms are hardly experienced until the electrons of one neutral atom start to overlap the region of the electrons of the other neutral atom. In the same manner, a nucleon-nucleon-system can only experience strong interaction at short distances when the quarks in one nucleon can sense the quark in the other, since the nucleons are color neutral.

Four different interactions

Maxwell showed us that obviously different phenomena can be unified in one theoretical description. In the 18th century there was no apparent relation between the static electricity, the magnetic force and the light emitted by a candle. Today they are unified under the name electromagnetism. Indeed the four different forces (electromagnetic, weak, strong and gravitational) could also be different manifestations of some underling unique force. Actually, the idea which lies at the heart of the standard model is that electromagnetism and the weak force both stem from a single and more fundamental theory, the electroweak theory. The theory was developed independently by Sheldon Glashow, Steven Weinberg and Abdus Salam. The electroweak theory makes precise predictions about the properties of the mediated gauge bosons W and Z, also called intermediate vector bosons. The discovery of W and Z bosons at CERN in 1983 was a triumph in theoretical and experimental physics increasing the credibility of the Standard Model. The electroweak unification means that the photon and the intermediate vector bosons belong to the same family of four particles. But at low energies the photon and the W and Z particles are unlike siblings, since the first is massless and the other three are among the heaviest particles that exist. According to the electroweak theory, unification is manifest only at high energies above the mass of the intermediate vector bosons. At such energies, the mass of the gauge bosons that mediate the two interactions, electromagnetism and weak, are effectively small and the interactions are equivalent. It is the breaking of the symmetry of nature, that gives large masses to the W and the Z while leaving the photon massless. The principal actor in the breaking of symmetry is the Higgs boson introduced by Peter Higgs. The Higgs boson is also responsible for the fact that quarks and leptons within the same family have masses at all. The question remains whether there is a way to unify the strong interaction with the weak interaction into a single *grand unified theory.* There are already many attempts for a further unification. The most popular grand unified theories incorporate a new symmetry of nature called *supersymmetry* [3, 4, 5, 6].

Why does the model have three generations ?

The Standard Model is a very powerful theory that successfully describes all the known particle physics phenomena. It provides a very elegant theoretical framework and has passed very precise tests which are at the 0.01% level. In spite of this, the Standard Model leaves one hungry for further explanation because of its incompleteness. One of the open question is the question asked above. In addition, the model accounts neither for the pattern of quark and lepton masses nor for the pattern of charges. There is a mixing of quark generations, but no mixing of lepton generations (see Chapter 2 for more detail). The Standard Model also fails to predict constants like the coupling constants representing the strengths of the interactions. Most problematic is the Higgs boson. Higgs boson has not been verified by experiment and the model does not predict what it's mass must be. These difficulties are a **challenge** but do not devalue the standard model. It will remain a component of a more comprehensive theory.

Physicists have had great success explaining the world. After the discovery of the W and Z boson, a question arose whether the properties of these bosons match with the predictions of the SM. To answer this question, a large electron-positron collider (LEP) has been built at CERN, which operated from 1989 - 2000. It operated for several years at center-of-mass energies of about 91 GeV, near the Z pole. The basic measurements performed at the Z peak have provided us with an extremely accurate knowledge of the parameters of the Z boson: its mass, partial widths, and total width. In 1996, LEP started with a first run above the $e^+e^- \rightarrow W^+W^-$ threshold later followed by runs at higher center-of-mass energies (now called LEP2). The W bosons produced at LEP2 give us a unique opportunity to study these gauge bosons in a clean environment.

Science is an experimental subject. Even the most appealing and well-tested theories must sometimes be rejected. New experimental observations often reveal inconsistencies or serious errors in existing theories. In this thesis the cross-section measurements of the W-pair production in e^+e^- annihilations in the hadronic decay channel are performed and the W mass is determined. The W mass is one of the key parameters of the electroweak theory. An improved accuracy makes the tests of the SM more stringent. Other experimental tests of the SM can be done with the measurements of the production cross-section in dependence of the center-of-mass energy, since the triple gauge-boson couplings play a role in the tree-level cross-section.

The outline of this thesis reads as follows: In Chapter 2 the Standard Model of particle physics is briefly introduced with special emphasis on W pair-production. Chapter 3 is devoted to the explanation of the Large Electron Positron Ring and the L3 experiment, with which the data used in this thesis have been recorded. A presentation of the simulation of the data is given in Chapter 4. The selection of hadronic WW events from a large amount of data is described in detail in Chapter 5, dealing with the extraction of physics information from the hadronic WW events selected. The cross section of hadronic WW pair-production is measured and the results are interpreted providing the study of the systematic errors. The next part of this thesis deals with the measurement of the W mass. Chapter 6 explains the method used to and summarizes the results. The thesis ends with a summary and interpretation of the results in Chapter 7, giving a preliminary results of the new data from the LEP2 experiments and prospects for experiments in the future. An appendix is added to the body of the thesis being of importance for special parts of this work.

Kapitel 2

Theoretical Basis

In this chapter some properties of the Standard Model and the insights that it provides will be reviewed. Special emphasis is placed on the necessity of the massive W boson in the electroweak model. The following sections are based upon References [7, 8, 9, 10, 11].

2.1 Standard Model

Quantum field theory was developed in the early 1930's through unification of special relativity and quantum mechanics[1]. And there has been steady and extraordinary progress in particle physics, both in profound theoretical insights and remarkable experimental discoveries. A theoretical framework of these developments is the Standard Model, which represents a field theory with local gauge symmetry. This is a special class of a quantum field theory in which an invariance principle that implies the existence of interactions mediated by gauge

---

[1] To understand how relativity leads to the field concept, suppose some impetus is given to a particle. This does not produce any instantaneous change in the forces acting on a neighboring particle because according to relativity no signal can travel faster than the finite speed of light. In order to maintain the conservation of energy and momentum at every instant, we say that the pushed particle produces a field, which carries energy and momentum through surrounding space and eventually hands some of it over to the neighboring particle. When quantum mechanics is applied to the field,we find that the energy and momentum must come in discrete quanta, which we identify with the elementary particles. Thus in the quantum field theory, the elementary particle interactions are interpreted in terms of exchanges of particles themselves.

bosons exists. The fundamental quantity of this theory is the Lagrangian, which is the difference between the kinetic energy and the potential energy.

In the following sections the construction of the Standard Electroweak Lagrangian is described.

2.1.1 Invariance Principles

Symmetries and apparent symmetries in the laws of nature have played a role in the construction of physical theories, and they acquired special significance with the advent of quantum mechanics. In a mathematical language the symmetries are equivalent to operations which leave the form of the field equations unchanged.

There are two kinds of symmetries. A global symmetry, which states that some law of physics remains invariant when the same transformation is applied everywhere in space and time. But it would be nice to find symmetries which correspond to things we can actually do, like changing fields only in a finite region, which is more general. We ought be able to fix our phase conventions here without regard for how they are chosen on the moon. This symmetry is called a local symmetry and stands for the invariance of the law of physics even when a different transformation takes place at each point in space and time. The present theory of electroweak interaction is a theory of local symmetry.

Noether's theorem maintains that for every symmetry of the Lagrangian there exists a corresponding conserved current. The simplest example is the derivation of quantum electrodynamics (QED) from the local phase invariance. The Lagrangian for a free non-interacting particle of spin $\frac{1}{2}$ and mass m like electrons is

$$\mathcal{L} \;=\; i\overline{\psi}\gamma^{\mu}\partial_{\mu}\psi - m\overline{\psi}\phi. \tag{2.1}$$

Requiring the Lagrangian to be invariant under local changes of the phase of ψ,

$$\psi(x) \;\to\; e^{i\alpha(x)}\psi(x), \tag{2.2}$$

we are obliged to introduce a new term, because the derivative of ψ picks up an extra term $ie^{i\alpha(x)}\psi\partial_\mu\alpha$ under local phase transformations:

$$\partial_\mu\psi(x) \;\rightarrow\; e^{i\alpha(x)}\partial_\mu\psi(x) + ie^{i\alpha(x)}\psi\partial_\mu\alpha. \tag{2.3}$$

Introducing a covariant derivative D_μ with a new vector field A_μ, the unwanted term disappears and the new Lagrangian becomes invariant under local gauge transformations, where

$$\partial_\mu \;\rightarrow\; D_\mu \;=\; \partial_\mu - ieA_\mu \tag{2.4}$$

with the transformation of

$$A_\mu \;\rightarrow\; A_\mu \;+\; \frac{1}{e}\partial_\mu\alpha. \tag{2.5}$$

The charge of the electron is taken to be $-e$. The invariant Lagrangian is

$$\mathcal{L} \;=\; \overline{\psi}(i\gamma^\mu\partial_\mu \;-\; m)\psi \;+\; e\overline{\psi}\gamma^\mu\psi A_\mu, \tag{2.6}$$

where a new vector field A_μ, called the gauge field, couples to ψ through the last term in Eq. 2.6. The full Lagrangian must also include a free term for the gauge field, which could look like

$$\mathcal{L} \;=\; -\frac{1}{4}F_{\mu\nu}F^{\mu\nu} \;+\; \frac{1}{2}m^2 A_\mu A^\mu. \tag{2.7}$$

The problem lies in the fact that whereas $F_{\mu\nu}F^{\mu\nu}$ with $F_{\mu\nu} \;=\; \partial_\mu A_\nu \;-\; \partial_\nu A_\mu$ is invariant, the additional term $\frac{1}{2}m^2 A_\mu A^\mu$ is not gauge invariant. To ensure the gauge invariance the gauge field must be massless. Now we have constructed a Lagrangian of QED for one fermion:

$$\mathcal{L} \;=\; \underbrace{\overline{\psi}(i\gamma^\mu\partial_\mu \;-\; m)\psi}_{\text{Kinematic term and mass of } \psi} \;+\; \underbrace{e\overline{\psi}\gamma^\mu\psi A_\mu}_{\text{Interaction}} \;-\; \underbrace{\frac{1}{4}F_{\mu\nu}F^{\mu\nu}}_{\text{Kinematic term of the photon field}}\;. \tag{2.8}$$

This Lagrangian describes a spin $\frac{1}{2}$ charged fermion, a spin 1 neutral gauge boson and the interaction of the fields between them. The interaction term in Eq. 2.8 may be written $-j^\mu_{em}A_\mu$, where

$$j^\mu_{em} \;=\; -e\overline{\psi}\gamma^\mu\psi \tag{2.9}$$

represents the electromagnetic current. Of significance here is that the existence of the vector field A_μ is a consequence of a local symmetry. One may ask whether this cannot be dealt with the assumption of global symmetry. If we apply the global phase transformation of the Eq. 2.1, we see that this Lagrangian is invariant under the global phase transformation. Therefore, given only global symmetry there would be no electromagnetic forces between charged particles, no photons and no light.

This one dimensional phase transformation corresponds to a group of unitary 1 x 1 matrices:

$$\psi \ \rightarrow \ U\psi, \text{ where } U^{\dagger}U = 1 \text{ with } U \ = \ e^{i\alpha(x)}. \tag{2.10}$$

The group of all such matrices is U(1) and the symmetry involved is called U(1) gauge invariance. This strategy can be extended to the group SU(2) and color SU(3).

2.1.2 Yang-Mills Theory

The idea elaborated in the previous section can be generalised and more complex phase transformations are possible. This step was taken by Yang and Mills, who extended the idea to an Isospin space. The local $SU(2)$ transformation takes the form

$$\psi \ \rightarrow \ exp(i\frac{g}{2}\boldsymbol{\tau}\cdot\boldsymbol{\alpha}(x))\psi(x), \tag{2.11}$$

where $\boldsymbol{\tau}$ stands for the non-commuting Pauli matrices τ_1, τ_2, τ_3 and g for a coupling constant. Once again the derivative in the weak isospin lagrangian has to be replaced by a covariant derivative to be invariant under the local gauge transformation:

$$\partial_\mu \ \rightarrow \ D_\mu \ = \ \partial_\mu + i\frac{g}{2}\boldsymbol{\tau}\cdot\mathbf{W}_\mu. \tag{2.12}$$

The gauge fields $\mathbf{W}_\mu$ (it takes three of them this time, $W_\mu^1, W_\mu^2, W_\mu^3$, one gauge field for each of the three Pauli generators) are required by the local gauge invariance. The vector nature of the fields leads to an additional vector product term in the field transformation

$$\mathbf{W}_\mu \ \rightarrow \ \mathbf{W}_\mu \ - \ \frac{1}{g}\partial_\mu\boldsymbol{\alpha} \ - \ \boldsymbol{\alpha}\times\mathbf{W}_\mu. \tag{2.13}$$

These three new vector fields $\mathbf{W}_\mu$ require their own free Lagrangian, where once again the gauge fields must be massless. The free Lagrangian of the spin-1 gauge bosons (the kinematic energy terms) is

$$\mathcal{L} = -\frac{1}{4} W_{\mu\nu} W^{\mu\nu}, \tag{2.14}$$

where $W_{\mu\nu}$ is modified due to the non-Abelian character of the group to the form

$$\mathbf{W}_{\mu\nu} = \partial_\mu \mathbf{W}_\nu - \partial_\nu \mathbf{W}_\mu - g \mathbf{W}_\mu \times \mathbf{W}_\nu . \tag{2.15}$$

The term $g\mathbf{W}_\mu \times \mathbf{W}_\nu$ in Eq. 2.14 , which arises from the non-commuting properties, gives additional terms, which are products of both three and four W^μ fields. They give rise to vertices connecting three and four field lines (Figure 2.1). The existence of such vertices is an important consequence of the theory. They arise because of the non-Abelian nature of the theory. Arriving at the complete Yang-Mills Lagrangian, it is invariant under local $SU(2)$ gauge transformations and describes the interactions of three massless vector gauge fields with the matter fields of Dirac. This idea plays a fundamental role in the weak isospin-hypercharge ($\mathrm{U(1)_Y} \times \mathrm{SU(2)_L}$) symmetry in the weak interactions, see below.

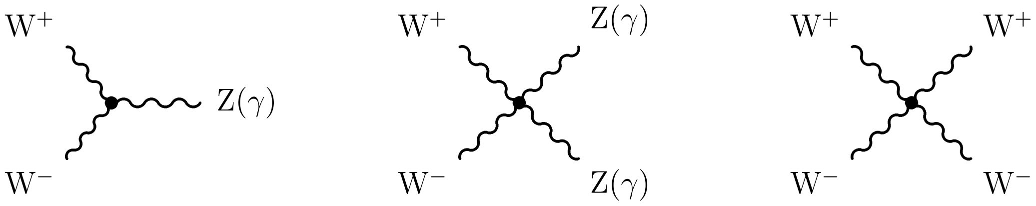

Abbildung 2.1: *Examples of vertices involving three or four fields; they arise from the self-interacting terms of the boson fields.*

2.1.3 Gauge Theory of the Electroweak Interactions

To create a complete theory of nature, one starts from the principle of gauge invariance and looks for a group which can describe the experimental observations.

The group representation of the Standard Model is given by

$$G_{\mathrm{SM}} = \mathrm{U(1)_Y} \times \mathrm{SU(2)_L} \times \mathrm{SU(3)_C}. \tag{2.16}$$

The symmetry group $\mathrm{SU(3)_C}$ describes the strong interactions, Quantum Chromodynamics (QCD), where the subscript C stands for colour,the name for the interaction charge. The $\mathrm{U(1)_Y} \times \mathrm{SU(2)_L}$ part with four vector fields, three of which are associated with the $\mathrm{SU(2)_L}$ group called $W^i, i = 1 \ldots 3$ and one B associated with the $\mathrm{U(1)_Y}$ describes the weak and electromagnetic interactions.

The main goal in the construction of the unified electroweak interaction is to incorporate the massive gauge bosons $(\mathrm{W}^{\pm}, \mathrm{Z})$, while leaving the photon massless. So what does the data on weak and electromagnetic processes suggest in that we end up with the group $\mathrm{U(1)_Y} \times \mathrm{SU(2)_L}$? And how can this group account for the massive gauge bosons ?

The empirical facts[12] governing the formulation of the Electroweak Standard Model show the following family structure of the fermions:

$$\begin{pmatrix} \nu_{\mathrm{e}} \\ \mathrm{e}^- \end{pmatrix}_{\mathrm{L}} \quad \begin{pmatrix} \nu_{\mu} \\ \mu^- \end{pmatrix}_{\mathrm{L}} \quad \begin{pmatrix} \nu_{\tau} \\ \tau^- \end{pmatrix}_{\mathrm{L}} \quad \begin{array}{ccc} \nu_{\mathrm{eR}} & \nu_{\mu\mathrm{R}} & \nu_{\tau\mathrm{R}} \\ \mathrm{e}_{\mathrm{R}}^- & \mu_{\mathrm{R}}^- & \tau_{\mathrm{R}}^- \end{array}$$

$$\begin{pmatrix} \mathrm{u} \\ \mathrm{d}' \end{pmatrix}_{\mathrm{L}} \quad \begin{pmatrix} \mathrm{c} \\ \mathrm{s}' \end{pmatrix}_{\mathrm{L}} \quad \begin{pmatrix} \mathrm{t} \\ \mathrm{b}' \end{pmatrix}_{\mathrm{L}} \quad \begin{array}{ccc} \mathrm{u_R} & \mathrm{c_R} & \mathrm{t_R} \\ \mathrm{d_R} & \mathrm{s_R} & \mathrm{b_R} \end{array}$$

The fermions appear as families with left-handed doublets and right-handed singlets. For the neutrinos, an idealization of massless neutrinos is assumed, since no experimental evidence[2] for right-handed ν's or left-handed $\bar{\nu}$'s exists. Thus, we do not need a ν_{R} field to describe the weak interactions of the neutrino. In the following the construction of the electroweak theory is applied to a single generation of leptons. In this form, it is neither complete. However, it illustrates the model, and the generalizations are simple to make.

The fermions can be characterised by the weak isospin $\mathrm{SU(2)_L}$ and weak hypercharge $\mathrm{U(1)_Y}$ transformations, where the subscript L signifies that the SU(2)

---

[2] Recent experimental results based on solar, atmospheric and reactor neutrino experiments [13, 14] indicate the possible existence of neutrino oscillations which would require that neutrinos have non-vanishing mass. Confirmation of these results and their consistent interpretation is needed.

interaction is left-handed and only the left-handed component of particles participate in the interaction. The definition of a left-handed doublet is

$$\mathrm{L} \;\equiv\; \begin{pmatrix} \nu \\ \mathrm{e} \end{pmatrix}_{\mathrm{L}} \;=\; \begin{pmatrix} \frac{1}{2}(1-\gamma_5)\nu \\ \frac{1}{2}(1-\gamma_5)\mathrm{e} \end{pmatrix}, \tag{2.17}$$

and a right-handed singlet is

$$\mathrm{R} \;\equiv\; \mathrm{e_R} \;=\; \frac{1}{2}(1+\gamma_5)\mathrm{e}. \tag{2.18}$$

The subscript Y refers to the weak hypercharge, which is defined such that

$$Q \;=\; I_3 \;+\; \frac{Y}{2}. \tag{2.19}$$

The I_3 of the neutrino is $+\frac{1}{2}$ and the I_3 of the left-handed electron is $-\frac{1}{2}$. The I_3 of a right-handed singlet is 0, since the isospin $I = 0$. Thus $Y_{\mathrm{L}} = -1$ and $Y_{\mathrm{R}} = -2$. In the previous section, the invariance with respect to the weak isospin SU(2) was discussed. A Lagrangian which is invariant with respect to rotations in weak hypercharge space is also required. In this case the Lagrangian may be written as

$$\mathcal{L} \;=\; \mathcal{L}_{gauge} \;+\; \mathcal{L}_{leptons}, \tag{2.20}$$

where

$$\mathcal{L}_{gauge} \;=\; -\frac{1}{4}W_{\mu\nu}W^{\mu\nu} \;-\; \frac{1}{4}B_{\mu\nu}B^{\mu\nu} \tag{2.21}$$

with $\mathbf{W}_{\mu\nu} \;=\; \partial_\mu \mathbf{W}_\nu \;-\; \partial_\nu \mathbf{W}_\mu \;-\; g\mathbf{W}_\mu \times \mathbf{W}_\nu$ and $B_{\mu\nu} \;=\; \partial_\mu B_\nu \;-\; \partial_\nu B_\mu$. The matter term for massless leptons and their interactions is

$$\mathcal{L}_{leptons} \;=\; \overline{\mathbf{R}}i\gamma^\mu \underbrace{(\partial_\mu \;+\; ig_1\frac{Y}{2}B_\mu)}_{D^1_\mu}\mathbf{R} \;+\; \overline{\mathbf{L}}i\gamma^\mu \underbrace{(\partial_\mu \;+\; ig_1\frac{Y}{2}B_\mu \;+\; i\frac{g_2}{2}\boldsymbol{\tau}\cdot\mathbf{W}_\mu)}_{D^2_\mu}\mathbf{L}, \tag{2.22}$$

where D^1_μ and D^2_μ are the covariant derivatives of the $SU(2)_{\mathrm{L}}$ iso-scalars and iso-spinors. The g_1 denotes the Abelian $U(1)$ gauge coupling and g_2 the non-Abelian $SU(2)$ coupling.

A mass term for the electron is not $\mathrm{U(1)_Y} \times \mathrm{SU(2)_L}$ invariant. Furthermore, this symmetry also requires four massless electroweak gauge bosons. But the observed non-zero values for the charged leptons, $\mathrm{W}^\pm$ and Z^0 masses violate the assumed $\mathrm{U(1)_Y} \times \mathrm{SU(2)_L}$ symmetry. To give masses to the gauge bosons and constituent fermions, the electroweak symmetry must be spontaneously broken, as discussed below. The mechanism behind this symmetry breaking is the Higgs mechanism.

2.1.4 Spontaneous Symmetry Breaking

Suppose, a real scalar field ϕ described by the Lagrangian

$$\mathcal{L} = \frac{1}{2}(\partial_\mu \phi)^2 - (\frac{1}{2}\mu^2\phi^2 + \frac{1}{4}\lambda\phi^4), \tag{2.23}$$

is introduced with $\lambda > 0$ and $\mu^2 < 0$. Compare this with the Klein-Gordon Lagrangian

$$\mathcal{L} = \frac{1}{2}(\partial_\mu \phi)(\partial^\mu \phi) - \frac{1}{2}m^2\phi^2, \tag{2.24}$$

which gives the Klein-Gordon equation[3] and describes a particle of spin 0 and mass m. The second term of Eq. 2.23 looks like a mass, but with the wrong sign. How can this Lagrangian be interpreted ? If the second term is a mass term, then m is imaginary, which is nonsense. The answer to this question lies in understanding Feynman calculus, which is a perturbation procedure. Perturbation calculations start from the ground state (the vacuum), and treat the fields as fluctuations about that state. To determine where the ground state is, we look for the minimum of the potential $\mathcal{V}$. The potential is

$$\mathcal{V}(\phi) = \frac{1}{2}\mu^2\phi^2 + \frac{1}{4}\lambda\phi^4 \tag{2.26}$$

and therefore the minimum occurs at

$$\phi = \pm v \qquad \text{with} \quad v = \sqrt{-\mu^2/\lambda}. \tag{2.27}$$

Now we can write

$$\phi(x) = v + \eta(x), \tag{2.28}$$

where η represents the quantum fluctuations about the minimum. In this case the Feynman calculus will be formulated in terms of deviations from $\phi = +v$,

---

[3] The Klein-Gordon equation is

$$\partial_\mu \partial^\mu \phi + m^2\phi = 0. \tag{2.25}$$

but this does not imply any loss of generality since $\phi = -v$ can always be reached by reflection symmetry. After rewriting the Lagrangian, we obtain

$$\mathcal{L} = \frac{1}{2}(\partial_\mu \eta)^2 - \lambda v^2 \eta^2 - \lambda v \eta^3 - \frac{1}{4}\lambda \eta^4 + const. \tag{2.29}$$

The second quantity is now a mass term with the correct sign, and identifying the first two terms with Eq. 2.6 gives

$$m_\eta = \sqrt{2\lambda v^2} = \sqrt{-2\mu^2}. \tag{2.30}$$

The higher-order terms in η represent the interaction of the η field with itself.

It must be remembered that the Lagrangians (Eq. 2.23) and (Eq. 2.29) are completely equivalent. They represent exactly the same physical system. Only the notation has been changed. But a transformation like (Eq. 2.28) cannot change the physics. So what happened ? It should be emphasized that in particle physics, perturbation theory requires that calculation of the fluctuations be done around the minimum energy. The perturbation series does not converge if expansion occurs around the unstable point $\phi = 0$. In perturbation theory, the Lagrangian (Eq. 2.29) gives the correct picture of physics; the Lagrangian (Eq. 2.23) does not. Therefore, the scalar particle does have a mass.

Regarding the question of why this is called the spontaneous symmetry breaking, one must consider the original Lagrangian (Eq. 2.23). This is even in ϕ: It is invariant as $\phi \to -\phi$. But the reformulated Lagrangian (Eq. 2.29) is not even in η; the symmetry has been broken. We call this spontaneous symmetry-breaking because no external agency is responsible.

We now return to the Higgs mechanism formulated in the SM. To formulate the Higgs mechanism in such a way that the $W^\pm$ and Z^0 become massive and the photon remains massless a weak isospin doublet of complex scalar fields (Higgs doublet)

$$\phi = \begin{pmatrix} \phi^+ \\ \phi^0 \end{pmatrix} \quad \text{where} \quad \begin{array}{c} \phi^+ \equiv (\phi_1 + i\phi_2)/\sqrt{2}, \\ \phi^0 \equiv (\phi_3 + i\phi_4)/\sqrt{2}, \end{array} \tag{2.31}$$

with ϕ_i real is introduced. To get the positive electric charge for ϕ^+ and zero charge for ϕ^0 the weak hypercharge Y must be set to 1.

To generate gauge boson masses, we use the Higgs potential of the form

$$\mathcal{V}(\phi) \;=\; \mu^2\phi^\dagger\phi \;+\; \lambda(\phi^\dagger\phi)^2, \tag{2.32}$$

with $\mu^2 < 0$ and $\lambda > 0$. This potential is at its minimum when

$$\phi^\dagger\phi \;\equiv\; \frac{1}{2}(\phi_1^2 \;+\; \phi_2^2 \;+\; \phi_3^2 \;+\; \phi_4^2) \;=\; -\frac{\mu^2}{2\lambda}. \tag{2.33}$$

Then we choose the minimum that has the vacuum expectation values

$$\phi_1 \;=\; \phi_2 \;=\; \phi_4 \;=\; 0, \quad \phi_3^2 \;=\; -\frac{\mu^2}{\lambda} \;\equiv\; v^2. \tag{2.34}$$

The choice of this particular vacuum

$$\phi_0 \;\equiv\; \sqrt{\frac{1}{2}}\begin{pmatrix} 0 \\ v \end{pmatrix} \tag{2.35}$$

with $I = \frac{1}{2}$, $I_3 = -\frac{1}{2}$ and $Y = 1$ breaks both SU(2) and $\mathrm{U}(1)_Y$ symmetries. But $\mathrm{U}(1)_{em}$ symmetry with $Q = I_3 + Y/2$ remains unbroken, since ϕ_0 is neutral. Thus the vacuum is invariant under $\mathrm{U}(1)_{em}$ transformations, and the photon remains massless.

We now expand $\phi(x)$ around this particular vacuum. The result is that, due to gauge invariance, we can rewrite $\phi(x)$ in the form of

$$\phi(x) \;=\; \sqrt{\frac{1}{2}}\begin{pmatrix} 0 \\ v + h(x) \end{pmatrix}. \tag{2.36}$$

In this model, of the four scalar fields, the only one that remains is the Higgs field $h(x)$, which is a gauge-invariant fluctuation separate from the vacuum state. So the symmetry-breaking sector gives rise to only one new particle, the Higgs scalar. The mass of this field is given by

$$M_h^2 \;=\; 2\mu^2 \;=\; 2\lambda v^2. \tag{2.37}$$

The $SU(2) \times U(1)$ gauge invariant Higgs Lagrangian for the scalar fields

$$\mathcal{L}_{scalar} \;=\; |(i\partial_\mu \;-\; g_1\frac{Y}{2}B_\mu \;-\; g_2\frac{\boldsymbol{\tau}}{2}\cdot\mathbf{W}_\mu)\phi|^2 \;-\; V(\phi), \tag{2.38}$$

should be added to the Lagrangian (Eq. 2.20). But before doing this we substitute the vacuum expectation value ϕ_0 for $\phi(x)$ in this Lagrangian to identify the gauge boson masses. The relevant term looks as follows:

$$
\begin{aligned}
&|(-\, ig_2\frac{\boldsymbol{\tau}}{2}\cdot \mathbf{W}_\mu \;-\; ig_1\frac{1}{2}B_\mu)\phi|^2 \\
&= \frac{1}{8}\left|\begin{pmatrix} g_2W^3_\mu \;+\; g_1B_\mu & g_2(W^1_\mu - iW^2_\mu) \\ g_2(W^1_\mu \;+\; iW^2_\mu) & -\, g_2W^3_\mu + g_1B_\mu \end{pmatrix}\begin{pmatrix} 0 \\ v \end{pmatrix}\right|^2 \\
&= \frac{1}{8}v^2g_2^2\left[(W^1_\mu)^2 \;+\; (W^2_\mu)^2\right] \;+\; \frac{1}{8}v^2(g_1B_\mu \;-\; g_2W^3_\mu)(g_1B^\mu \;-\; g_2W^{3\mu}) \qquad (2.39)\\
&= (\frac{1}{2}vg_2)^2W^+_\mu W^{-\mu} \;+\; \frac{1}{8}v^2(W^3_\mu, B_\mu)\begin{pmatrix} g_2^2 & -\, g_1g_2 \\ -g_1g_2 & g_1^2 \end{pmatrix}\begin{pmatrix} W^{3\mu} \\ B^\mu \end{pmatrix},
\end{aligned}
$$

where $W^\pm \;\equiv\; (W^1 \;\mp\; iW^2)/\sqrt{2}$.

The first of these gives a mass to the charged $W^\pm$ bosons

$$
M_W \;=\; \frac{1}{2}vg_2. \qquad (2.40)
$$

The physical content becomes transparent, if the remaining term is transformed to the physical fields

$$
\begin{aligned}
A_\mu &= W^3_\mu \sin\theta_W + B_\mu \cos\theta_W \\
Z_\mu &= W^3_\mu \cos\theta_W - B_\mu \sin\theta_W. \qquad (2.41)
\end{aligned}
$$

These physical fields diagonalize the mass term so that the remaining term can be identified with

$$
\frac{1}{2}M_Z^2Z_\mu^2 \;+\; \frac{1}{2}M_A^2A_\mu^2. \qquad (2.42)
$$

This gives one massless and one massive combination with

$$
\begin{aligned}
A_\mu &= \frac{g_1W^3_\mu \;+\; g_2B_\mu}{\sqrt{g_1^2 \;+\; g_2^2}} \quad \text{with } M_A \;=\; 0, \\
& \qquad\qquad\qquad\qquad\qquad\qquad\qquad (2.43)\\
Z_\mu &= \frac{g_2W^3_\mu \;-\; g_1B_\mu}{\sqrt{g_1^2 \;+\; g_2^2}} \quad \text{with } M_Z \;=\; \frac{1}{2}\sqrt{g_1^2 \;+\; g_2^2}.
\end{aligned}
$$

The mixing angle θ_W is therefore related to the couplings g_1 and g_2 by

$$
\cos\theta_W \;=\; \frac{g_2}{\sqrt{g_1^2 \;+\; g_2^2}} \;=\; \frac{M_W}{M_Z}, \qquad \sin\theta_W \;=\; \frac{g_1}{\sqrt{g_1^2 \;+\; g_2^2}}. \qquad (2.44)
$$

This is interesting as a model constructed in this way with a Higgs doublet predicts the relation

$$\rho \equiv \frac{M_W^2}{M_Z^2 \cos^2 \theta_W} = 1 \tag{2.45}$$

for the W and Z masses. It is evident that the photon is a combination of W_μ^3 and B_μ. This means that the photon couples to a combination of the weak isospin and the hypercharge. This fact required a very careful choice of the values of the hypercharges for the different fields. The photon has a coupling of strength

$$\mathrm{e} = \frac{g_1 g_2}{\sqrt{g_1^2 + g_2^2}}, \tag{2.46}$$

which is a combination of the $SU(2)$ coupling g_2 and the $U(1)$ coupling g_1. One must note that the model was constructed in a way that the photon must be massless. Thus, $M_A = 0$ is not a prediction, but rather a consistency check.

2.1.5 Fermion Masses

The Higgs field is also responsible for the generation of fermion masses. They are produced via Yukawa couplings of left and right-handed fermion fields to the Higgs field. The physical quark mass eigenstates are not the same as the quark weak eigenstates. The W mixes quarks among the three generations. This mixing is described by the Cabibbo-Kobayashi-Maskawa (CKM) matrix and by convention, the mixing is placed on the down-type quarks. The quarks (d,s,b) mix to give the weak eigenstates $(\mathrm{d}', \mathrm{s}', \mathrm{b}')$:

$$\phi = \begin{pmatrix} d' \\ s' \\ b' \end{pmatrix} = \begin{pmatrix} V_{ud} & V_{us} & V_{ub} \\ V_{cd} & V_{cs} & V_{cb} \\ V_{td} & V_{ts} & V_{tb} \end{pmatrix} \begin{pmatrix} d \\ s \\ b \end{pmatrix} \tag{2.47}$$

The Standard Model cannot predict the values of the fermion masses, the coupling constants of the CKM matrix, or even the number of generations of particles. All these quantities have to be experimentally determined. The predictions of the Standard Model, with the experimental values as input, can then be tested against further experimental measurements.

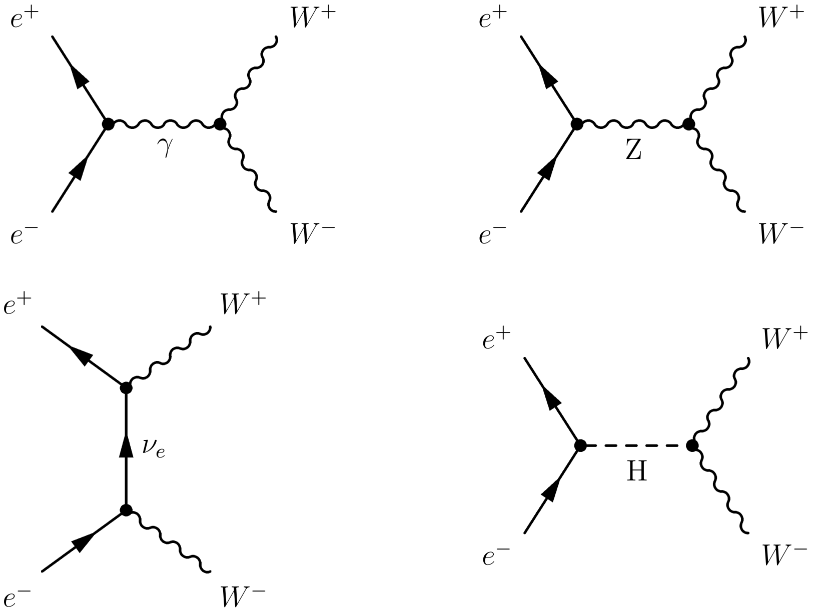

Abbildung 2.2: *Feynman diagrams of* $e^+e^- \to W^+W^-$.

2.2 W Pair Production in e^+e^- Annihilation

Within the SM, W couplings and mass are precisely predicted from the known parameters of the weak-interaction theory. Since very little of this picture has been tested experimentally, one may expect to find surprising results if it is probed in detail. In e^+e^- interactions, the pair production of charged bosons, $e^+e^- \to W^+W^-$, can proceed by four processes, as shown in Figure 2.2. The fourth reaction $e^+e^- \to H \to W^+W^-$ has a negligible cross section at LEP 2 because the coupling between Higgs and the light electrons is very small[4]. In what remains, each of the diagramms individually is divergent, violating unitarity. It is one of the fascinating properties of the SM, that in adding the γ and Z exchanges coherently to the t-channel ν exchange, the sum of the diagrams contains the correct cancellations to preserve unitarity. Thus the study of the cross section $\sigma(e^+e^- \to W^+W^-)$ as a function of center-of-mass energy (Figure 2.3) will provide, for the first time, a detailed test of the three gauge boson vertex. In other words, a small deviation of these couplings from their gauge theory values violates the subtle cancellation among the three contributions and

---

[4] A Higgs-exchange diagram is suppressed by a factor m_e/M_W.

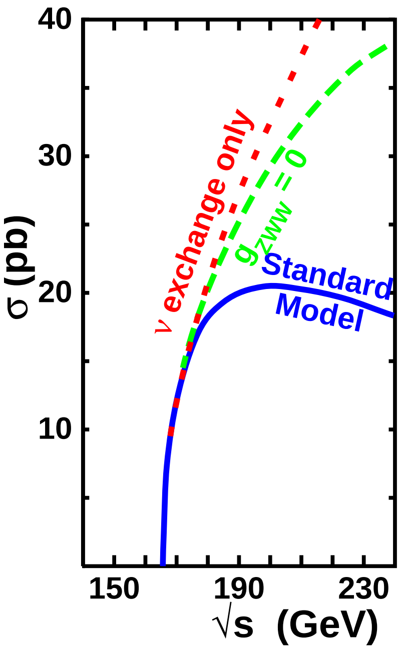

Abbildung 2.3: *The W-pair cross section, σ_{WW}, as a function of the center-of-mass energy, $\sqrt{s}$. The solid curve shows the Standard Model expectation. The dashed curve shows the expectation if there is no ZWW coupling. The dotted curve shows the expectation if only t-channel ν_{e} exchange in W-pair production is considered.*

can hence lead to observable effects. The set of these three diagrams is called CC03[5] [15]. Interesting is the fourth diagram, if the Higgs sector is interacting strongly. This enhances the cross section of the $\mathrm{e}^+\mathrm{e}^-$ annihilation into W pairs.

It might be useful to know that within the framework of the Standard Model, also four quadruple gauge boson vertices $\gamma\gamma\mathrm{W}^+\mathrm{W}^-$, $\gamma\mathrm{ZW}^+\mathrm{W}^-$, $\mathrm{ZZW}^+\mathrm{W}^-$ and $\mathrm{W}^+\mathrm{W}^-\mathrm{W}^+\mathrm{W}^-$ exist. They lead to $\mathrm{W}^+\mathrm{W}^-\gamma$ and $\mathrm{W}^+\mathrm{W}^-\mathrm{Z}$ final states in $\mathrm{e}^+\mathrm{e}-$ interactions. At LEP2, $\mathrm{W}^+\mathrm{W}^-\mathrm{Z}$ production is below the kinematic threshold.

---

[5] CC is an abbreviation for charged current and it implies the production of fermion pairs, where the sum of the charges in each pair is non-zero. These are the contributing processes to the $\mathrm{W}^+\mathrm{W}^-$ events. 03 stands for the number three. The CC03 diagrams are the three diagrams shown in Figure 2.2 excluding a fourth diagram with Higgs.

Well above the W pair threshold, $W^+W^-\gamma$ production becomes visible, similar to QED radiative corrections to W^+W^- production. Interesting here is that there are no $\gamma\gamma\gamma$, $\gamma\gamma Z$, γZZ and ZZZ triple gauge vertices within the SM. The interactions $\gamma\gamma\gamma$, $\gamma\gamma Z$ and γZZ do not appear because the photon couples only to electric charge. The ZZZ coupling is forbidden because of the conservation of weak isospin $((I=1, I_3=0) \nrightarrow (I=1, I_3=0)+(I=1, I_3=0))$.

2.2.1 W^+W^- Cross Section

The cross section for $e^+e^- \to W^+W^-$ can be given schematically as

$$\sigma_{\mathrm{WW}} \; = \; \sigma_0^{\mathrm{WW}} \, (1 \; + \; \delta_{\mathrm{EW}} \; + \; \delta_{\mathrm{QCD}}). \tag{2.48}$$

The various terms correspond to

(i) σ_0^{WW}: the Born contribution from the three CC03 diagrams for $e^+e^- \to W^+W^-$.

(ii) δ_{EW}: higher-order electroweak radiative corrections, including loop corrections, real photon emission, etc.

(ii) δ_{QCD}: higher-order QCD corrections to W^+W^- final states containing $q\bar{q}$ pairs. Such QCD corrections can lead to additional jets in the final states, e.g. $W^+W^- \to q\bar{q}q\bar{q}g$ from one hard gluon emission.

The terms (i) and (ii) will be considered in some detail in section 2.2.2.

The W^+W^- Off-shell Cross Section

The first step in the extraction of the information from the W-pair production is the calculation of on-shell cross section. On this stage, the width of the W boson is neglected ($\Gamma_{\mathrm{W}} = 0$) and a stable W boson is assumed. Thus, the total cross section begins to rise exactly at $\sqrt{s} = 2M_{\mathrm{W}}$. To describe the W pair production properly, a finite width of the W boson must be considered. The leading-order cross section for off-shell W pair production is given as in Ref.[16] through

$$\sigma(s) \; = \; \int_0^s ds_1 \int_0^{(\sqrt{s}-\sqrt{s_1})^2} ds_2 \rho(s_1)\rho(s_2)\sigma_0(s, s_1, s_2), \tag{2.49}$$

where

$$\rho(s) \;=\; \frac{1}{\pi}\frac{\Gamma_{\rm W}}{M_{\rm W}}\frac{s}{(s\;-\;M_{\rm W}^2)^2\;+\;s^2\Gamma_{\rm W}^2/M_{\rm W}^2} \tag{2.50}$$

is the relativistic Breit-Wigner spectral function associated to the $\mathrm{W}^{\pm}$ propagators. The $\sigma_0(s, s_1, s_2)$ is the cross section of the W pair with invariant masses s_1 and s_2 at the leading order. It can be written in terms of the ν, γ and Z exchange contributions (CC03) and their interferences:

$$\sigma_0(s, s_1, s_2) \;=\; \frac{g^4}{256\pi s^2 s_1 s_2}[a_{\gamma\gamma}\;+\;a_{\rm ZZ}\;+\;a_{\gamma \rm Z}\;+\;a_{\nu\nu}\;+\;a_{\nu \rm Z}\;+\;a_{\nu\gamma}], \tag{2.51}$$

where $g^4 = e^4/\sin^4\theta_{\rm W}$. Explicit expressions for the various contributions can be found in Ref.[16]. If s_1 and s_2 are set equal to $M_{\rm W}^2$, then $\sigma_0(s, M_{\rm W}^2, M_{\rm W}^2)$ becomes the on-shell $\mathrm{W}^+\mathrm{W}^-$ cross section $\sigma^{on}(s)$.

In the virtual W propagator in Eq. 2.50 an s-dependent W width (*running−width*),

$$\Gamma_{\rm W}(s) \;=\; \frac{s}{M_{\rm W}^2}\Gamma_{\rm W}, \tag{2.52}$$

like at LEP1 for the Z boson is used, where $\Gamma_{\rm W}\;\equiv\;\Gamma_{\rm W}(M_{\rm W}^2)$.

2.2.2 Radiative Corrections

In order to interpret the precise measurements, the theoretical predictions need to take into account higher-order radiative corrections including loop diagrams.

Loop diagrams are the representations of the corrections that have closed loops. To analyse a certain physical process, one draws all the diagrams, including the diagrams with more than one loop that has the appropriate external lines and adds it all up. The sum total of all Feynman diagrams with the given external lines then represents the actual physical process. Of course this means that there is an infinite probability of interactions, since there are infinitely many Feynman diagrams for any particular reaction. Fortunately, each vertex within a diagram has a factor α, which is by far smaller than 1. The factor α is a measure of the probability for absorption or emission of a certain mediator. Due to the factor's small numerical value, diagrams with increasingly greater number of vertices contribute less and less to the final results. In total, the loop effects are in general, quite small and typically of order 0.1% in size.

The complete set of $\mathbf{O}(\alpha)$ next-to-leading order corrections to $\mathrm{W^+W^-}$ production has been calculated by several groups [**?**, 17]. Here only the two largest effects will be mentioned, the coulomb corrections and initial state radiation (ISR). A conservative overall uncertainty on the cross section is estimated to be ±2% [18].

Coulomb corrections

Coulomb interaction between the two W bosons occur before they decay. This effect is largest near threshold where the W bosons are produced nearly at rest and separate slowly. The Coulomb correction at lowest order is included in the off-shell $\mathrm{W^+W^-}$ cross section through

$$\sigma(s) \; = \; \int_0^s ds_1 \int_0^{(\sqrt{s}-\sqrt{s_1})^2} ds_2 \rho(s_1)\rho(s_2)\sigma_0(s,s_1,s_2)[1 \; + \; \delta_C(s,s_1,s_2)], \quad (2.53)$$

where the term $\delta_C(s,s_1,s_2)$ represents the Coulomb correction. The effect of this QED radiative corrections is shown in Figure 2.4.

Initial state radiation

Initial state radiation (ISR) is the largest electroweak correction to the $\mathrm{W^+W^-}$ cross section. It comes from the emission of photons from the incoming $\mathrm{e^+}$ and $\mathrm{e^-}$ and reduce the effectively available center-of-mass energy. Thus the cross section is reduced, too (see Figure 2.4). The ISR corrected cross section in the flux function [19] approach is given by:

$$\sigma^{ISR}(s) \; = \; \int_{s_{min}}^{s} \frac{ds'}{s} F(x,s)\sigma(s'), \quad (2.54)$$

where s' is the reduced center-of-mass energy squared, $x = 1 - s'/s$ and the radiator function $F(x,s)$ is :

$$F(x,s) \; = \; tx^{t-1}(1 \; + \; S) \; + \; H(s',s), \quad (2.55)$$

with

$$t \; = \; \frac{2\alpha}{\pi}[ln(\frac{s}{m_{\mathrm{e}}^2}) \; - \; 1]. \quad (2.56)$$

The S term comes from soft and virtual photon emission and the $H(s',s)$ term comes from hard photon emission [20].

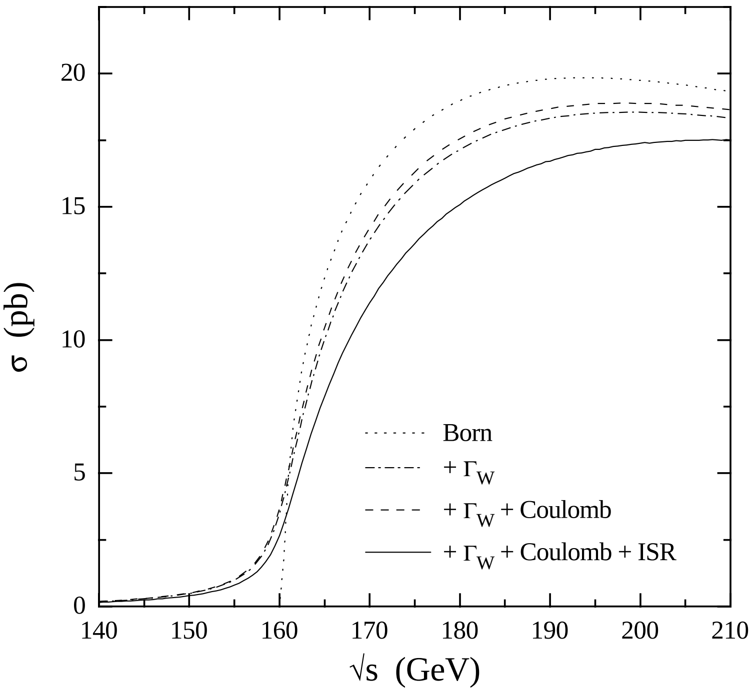

Abbildung 2.4: *The cross section for* $e^+e^- \to W^+W^-$ *in various approximations; (i) Born (on-shell) cross section, (ii) Born (off-shell) cross section with* $\Gamma_W = 2.08$ *GeV, (iii) with first order Coulomb corrections, and (iv) with initial state radiation.*

2.2.3 W Decay

W bosons decay to all states allowed by the SM. Thus they have a finite width. Moreover, the branching ratios enter the cross sections for definite fermions in the final state.

In lowest order the partial width for the decay of a W boson into two fermions (massless fermions are assumed) is given by

$$\Gamma^{Born}_{W \to f_i \bar{f}_j{}'} = N_c^f \frac{\alpha}{12 \sin\theta_W} M_W |V_{ij}|^2, \tag{2.57}$$

where i,j denote the generation index and f, f' stand for u, d' or ν, l. l stands for lepton. The colour factor is N_c^f, which is 1 for leptons and 3 for quarks. For leptonic decays the mixing matrix is the unit matrix. For decays into quarks there is a non-trivial mixing matrix. Neglecting the non-diagonal elements, which have very small values, the dominant mixing matrix elements for quarks at LEP2 are only from the two hadronic decays W → ud' and W → cs'. The decay W → tb' is kinematically not allowed. Counting each hadronic decay with a colour factor of 3 and adding the possibilities in leptonic decays, an approximation for the total width can be obtained:

$$\Gamma_{\mathrm{W}}^{Born} \approx (2 \times 3 + 3)\frac{\alpha}{12\sin\theta_{\mathrm{W}}}M_{\mathrm{W}} \approx \frac{3\alpha}{4\sin\theta_{\mathrm{W}}}M_{\mathrm{W}}. \tag{2.58}$$

Including radiative corrections and QCD corrections, a total width is given as sum of all partial decay widths:

$$\Gamma_{\mathrm{W}} = \Gamma_{\mathrm{e}\nu} + \Gamma_{\mu\nu} + \Gamma_{\tau\nu} + \Gamma_{\mathrm{W}\to had} = \frac{3G_F M_{\mathrm{W}}^3}{2\sqrt{2}\pi}(1 + \frac{2}{3}\Delta_{QCD}^{(had)}), \tag{2.59}$$

where $\Delta_{QCD}^{(had)}$ stands for QCD corrections. Writing the width in terms of the Fermi constant G_F and M_{W}, the corrections can be easily accounted. The fermion mass effects are small for the W decay, as the quark masses are small compared with M_{W}. QCD corrections for hadronic W decays also correct the total W-pair production cross section due to its dependence on Γ_{W} arising from the W boson propagator. For cross section of specific four-fermion final states in W pair production, the change in W decay branching fractions must also be taken into account. The branching ratios (BR) are the various ratios $\Gamma_{\mathrm{W}}^{a\bar{b}}/\Gamma_{\mathrm{W}}^{tot}$. The branching ratios expected in the SM are [18]

$$\begin{aligned} BR(\mathrm{W} \to \mathrm{e}\nu) &= 0.1083 \\ BR(\mathrm{W} \to \mu\nu) &= 0.1083 \\ BR(\mathrm{W} \to \tau\nu) &= 0.1082 \\ BR(\mathrm{W} \to had.) &= 0.6751 \end{aligned} \tag{2.60}$$

The branching ratios in the W$^+$W$^-$ decay channels can be given in three possible combinations of W decay modes:

$$\begin{aligned} \text{fully leptonic} \quad \mathrm{WW} &\to l\nu l\nu \approx 10.6\% \\ \text{semileptonic} \quad \mathrm{WW} &\to q\bar{q}l\nu \approx 43.8\% \\ \text{fully hadronic} \quad \mathrm{WW} &\to q\bar{q}q\bar{q} \approx 45.6\% \end{aligned} \tag{2.61}$$

CC	$\bar{d}u$	$\bar{s}c$	$e^+\nu_e$	$\mu^+\nu_\mu$	$\tau^+\nu_\tau$
$d\bar{u}$	43	11	20	10	10
$e\bar{\nu}_e$	20	20	56	18	18
$\mu^-\bar{\nu}_\mu$	10	10	18	19	9

Tabelle 2.1: *Number of Feynman diagrams for W pair produced four-fermion final states*

2.2.4 Four Fermion Production

The analysis of the W pair production requires the selection of four fermion final states. However beside CC03, there are contributions from other diagrams with the same initial and final states, but different intermediate states [21]. Table 2.1 shows the number of diagrams contributing for final states that can be reached by W pair intermediate states. The additional diagrams modify the results for total and differential cross sections as calculated on the basis of the CC03 diagrams. The effects are usually small except if electrons or electron-neutrinos are produced. In that case t-channel diagrams with the electron line going from the initial to the final state contribute, leading to additional diagrams (see Figure 2.5).

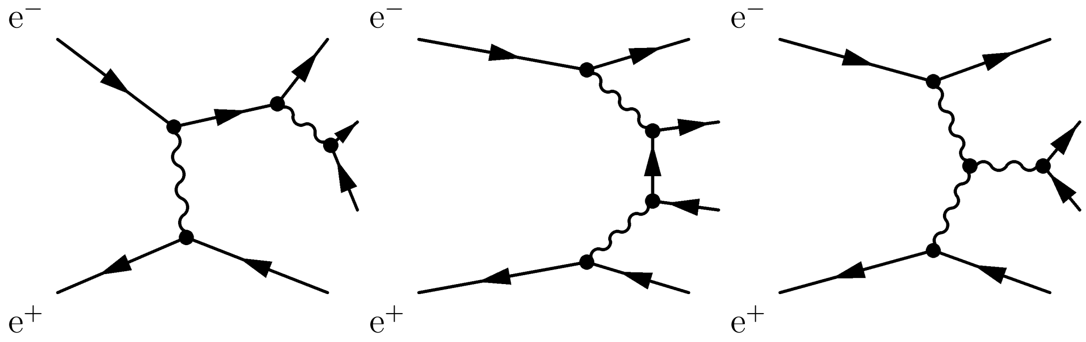

Abbildung 2.5: *Examples of additional diagrams for final states with electrons and electron-neutrinos.*

If the produced final state consists of particle-antiparticle pairs, the final state can also be obtained through intermediate Z pair production, leading to extra Feynman diagrams.

2.2.5 Motivation for the M_W Measurement

The gauge bosons W and Z couple directly to all particles which have weak interactions. Even those particles which are too heavy to be pair-produced at the Z will affect the properties of these resonances through their virtual effects in loop diagrams. The loop effects are typically of order 0.1% in size. To see these effects, the parameters of the SM have to be determined to an accuracy of 0.1% or better. The three parameters in the SM are directly sensitive to the properties of the Z: the finestructure constant α, the Fermi constant G_μ from the muon decay and the Z mass. G_μ and α are the best known electroweak constants of nature. LEP has measured M_Z to a similar accuracy as G_μ, which is more than we hoped for, with its value [22]:

$$M_Z = 91.1882 \pm 0.0022 \text{ GeV}, \tag{2.62}$$

where the values of G_μ and α are [22]:

$$G_\mu = (1.16639 \pm 0.00001) \times 10^{-5} \text{ GeV}^{-2} \tag{2.63}$$

$$\alpha = (7.297352533 \pm 0.000000027) \times 10^{-3} \tag{2.64}$$

Now the current measurements are sufficiently precise that they are sensitive to the loop effects like in Figure 2.6. The mass for the W and Z are related in the SM by the formula

$$M_W^2 = \frac{\pi\alpha}{\sqrt{2}G_\mu(1 - M_W^2/M_Z^2)} \frac{1}{1 - \Delta r}, \tag{2.65}$$

where $\Delta r = 0$ at tree level and where Δr is m_t and m_H dependent when loop diagrams due to virtual boson and fermion exchanges as in Figure 2.6 are

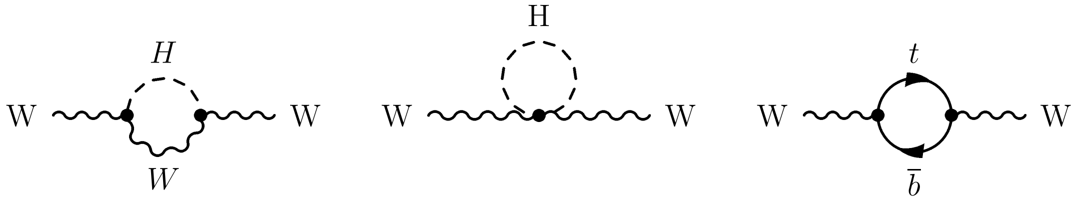

Abbildung 2.6: *Loop quantum corrections to M_W in the Standard Model*

included. The predicted mass of the W boson from precision electroweak data (LEP1, SLD, νN)[23] is

$$M_{\mathrm{W}} = 80.386 \pm 0.025\ GeV. \tag{2.66}$$

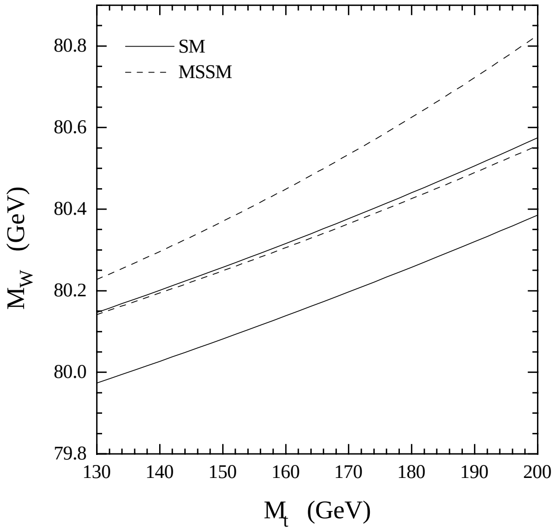

Abbildung 2.7: *Predictions for M_W as a function of M_t in the SM (solid lines) and in the MSSM (dashed lines).*

The principle uncertainty in the prediction of the W mass is provided by the top and Higgs masses. Conversely, a precise direct measurement of the W mass together with an accurate top mass will indirectly constrain the Higgs mass. The comparison of the direct measurement of the W boson with the indirect prediction is particularly important to test the standard theory of electroweak unification at the loop level. Further, a direct measurement of the W mass helps to constrain a possible extension of the Standard Model such as the Minimal Supersymmetric Standard Model (MSSM), Figure 2.7[18]. MSSM predicts new particles and these particles could contribute to the W boson mass via loop corrections, which would be visible in the comparison of the direct measurement with the indirect prediction of the W boson mass. Thus, the comparison can constrain the allowed parameter space of these kinds of models.

Kapitel 3

Description of the Experiment

An understanding of experimental tools is an important part of the study of elementary particle physics. How are elementary particles produced and how are they detected ?

Nowadays accelerators are used to produce particles in controlled collisions between subatomic particles. The advantage of accelerators is that beams of particles can be prepared according to the purpose of the study. For the analysis presented in this thesis, the Large Electron Positron Collider (LEP) at CERN, the European Laboratory for Particle Physics is used. When the beams of particles compressed into bunches of up to some 10^{11} particles collide with each other, many particles can be produced. To obtain as much information as possible about these particles, their interactions with the material of the detectors must be observed. The experiment should consist of many different sub-detectors with specific characteristics. To avoid a loss of particles, the complex detector has a 4π coverage. For this thesis, the L3 detector is used.

In the following the LEP collider and the L3 experiment are described. Emphasis is placed on the parts of the detector which are important for the direct reconstruction of the W boson in $e^+e^- \to W^+W^- \to q\bar{q}q\bar{q}$ events.

3.1 The LEP Collider

The LEP machine is an e^+e^- collider built at CERN in the vicinity of Geneva, Switzerland. This circular machine with circumference of 26.67 km is the largest particle collider in the world.

The basic components of this accelerator are the radio frequency (RF) cavities, the dipole magnets, the quadrupole and sextupole magnets and the vacuum chamber. The cavities represent the accelerating component and act like a short section of a linear accelerator. The radio frequency oscillations in the cavities are used to establish a moving electromagnetic wave in the structure, with the longitudinal component of the electric field moving in phase with the particles. So long as this phase relationship can be maintained, the particles will be continually accelerated. The dipole magnets are used to bend the particles and keep them moving in a circle. The magnetic field has to be gradually increased to keep in step with the accelerating particles. The quadrupole and sextupole magnets are used to focus the particles and to keep them tightly packed. The particles can be lost travelling inside the beam pipe, since collisions may occur with molecules of air. To prevent this, the beam pipe consists of a vacuum chamber.

LEP has 3368 magnets to bend the particle beams and keep them in orbit. In the dipole magnets an electron bends one way and a positively charged positron bends the other way. Thus LEP can circulate the beams of electrons and positrons in opposite directions using the same magnets. Each bunch contains more than 10^{11} particles, but on average only one in about 40 000[1] collisions between the bunches produces an electron-positron collision. For this reason the LEP design is based on the principle of a storage ring. The bunches of electrons and positrons are accelerated to a desired final energy and then kept at their final energy for several hours, allowing each bunch to travel round the ring more than 10 000 times a second. The acceleration scheme used at LEP2 is a 2 × 4 bunch-mode[2]. Four equally spaced bunches per beam collide every 22 μs at the

---

[1] This number is taken from the operation of LEP at the Z peak.

[2] For the operation of LEP at the Z peak, the bunch train scheme was used. Hereby, the bunches are replaced by trains of up to 4 smaller bunchlets, which have a distance of 250 ns in time. Therefore, collisions may occur more frequently than in bunch-mode leading to an increase in luminosity. At LEP2, there are usually only four bunches per beam, but with a

interaction points around the LEP ring, where the bunches are about 1500 μm long, 250 μm wide in the horizontal direction and 10 μm wide in the vertical direction in the plane transverse to the beam direction. Two reasons account for the large scale of the machine. First, a charged particle moving along a curved path radiates photons and loses energy, which is proportional to $\frac{E^4}{m^4\rho}$ per turn. Here E is the energy, m is the mass of the particle and ρ is the bending radius. For a fixed energy of the particles in the accelerator, the loss of energy can be reduced, if the bending radius is large. Secondly, if the bending radius is small, the magnetic field required for the bending must be stronger for the same desired beam energy. These reasons make things difficult, if the particles are accelerated to very high energies. For electrons the losses are very severe. At LEP, a 100 GeV electron loses on average approximately 3 GeV of energy per turn, which must be replenished by the acceleration system.

The stages through which electrons and positrons are injected into LEP are shown in Figure 3.1. The injection system consists of several steps: First the LEP Injector Linear accelerator (LIL) ramps electrons to 200 MeV and smashes them onto a tungsten target to produce positrons, or, alternatively, simply passes them through to a second LIL which alternately pushes electrons and positrons up to 600 MeV. The following Electron Positron Accumulator (EPA) collects the two particle species into geometrically small packages called bunchlets, and groups up to four bunchlets into bunches. When accumulated to a sufficiently large intensity, the particles are passed to the Proton Synchrotron (PS) operating as a 3.5 GeV e^+e^- synchrotron. Lastly the Super Proton Synchrotron (SPS) is used to bring particle bunches up to an energy of 20–22 GeV. And finally the bunches are injected into LEP and accelerated to the final energy of e.g. 189[3] GeV.

LEP has four interaction points, where the four LEP experiments L3 [24], ALEPH [25], DELPHI [26] and OPAL [27] are installed. Until the final energy is reached the electron and positron beams are separated in the interaction points using electrostatic separators. In the case of colliding beams, a system of qua-

---

much higher current

[3] The energy of 189 GeV was reached in the year 1998. At the end of LEP2, the final energy of 208 GeV could be reached.

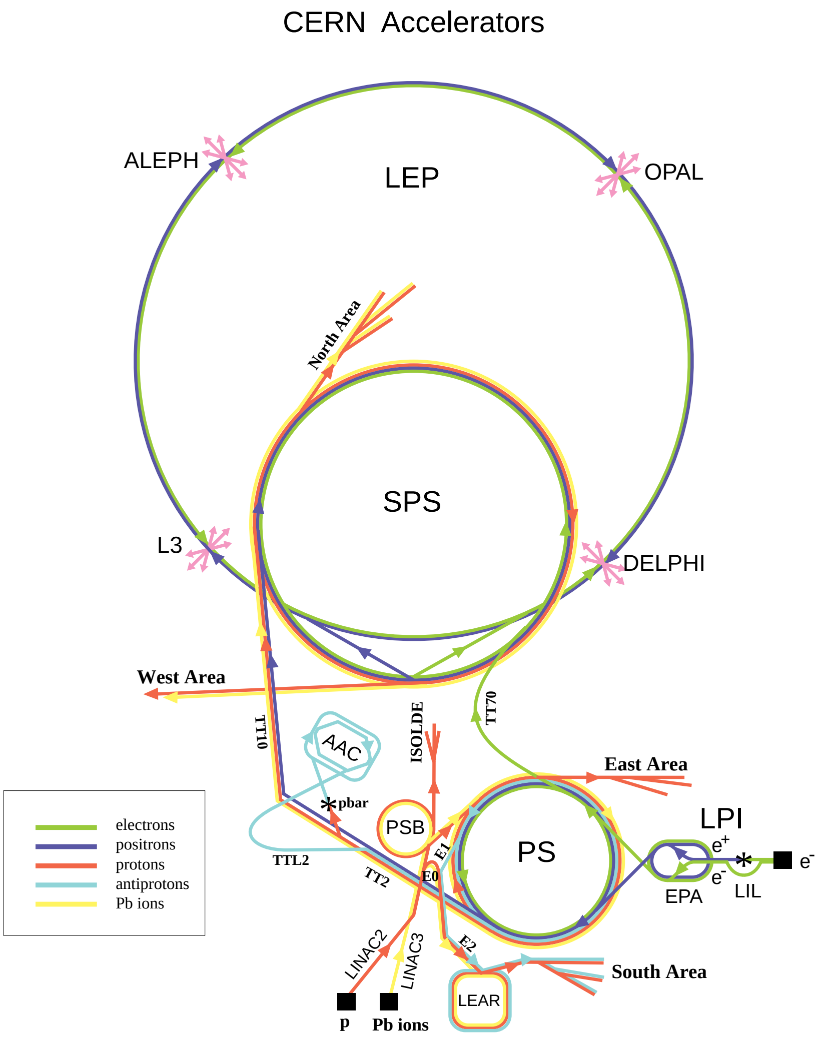

LEP: Large Electron Positron collider
SPS: Super Proton Synchrotron
AAC: Antiproton Accumulator Complex
ISOLDE: Isotope Separator OnLine DEvice
PSB: Proton Synchrotron Booster
PS: Proton Synchrotron

LPI: Lep Pre-Injector
EPA: Electron Positron Accumulator
LIL: Lep Injector Linac
LINAC: LINear ACcelerator
LEAR: Low Energy Antiproton Ring

Abbildung 3.1: *CERN accelerators including LEP storage ring with interaction points and injection system.*

drupole magnets allows focusing and transversal adjustment of the beams which is important because this controls the luminosity.

The instantaneous rate of events from colliding beams is given by

$$\frac{dN}{dt} = \sigma\mathcal{L}, \tag{3.1}$$

where σ is the cross section of the process of interest and $\mathcal{L}$ is the luminosity, which is the rate of the electron-positron interaction per unit surface. The luminosity at LEP for one interaction point can be calculated via

$$\mathcal{L} = \frac{N_{e^+}N_{e^-}n_b f}{4\pi\sigma_x\sigma_y}, \tag{3.2}$$

where $N_{e^\pm}$ is the number of electrons and positrons in the colliding bunches, n_b is the number of bunches per beam and f is the revolution frequency of a bunch. The surface is introduced in the denominator by the product of σ_x and σ_y which are the transverse dimensions of the beam at the interaction point (IP). The maximum luminosity of $10^{32}cm^{-2}s^{-1}$ [28, 29] was reached in 1998 and 1999. In the following analysis only the integrated luminosity is used which can be obtained by integrating the above equation 3.2 over the time interval of the data taking period. See section 3.2.6 for a more precise procedure.

Energy Calibration

One of the main goals at LEP2 is the precise measurement of the W mass. But the beam energy sets the absolute energy scale for this measurement, leading to an uncertainty. The experiments reconstruct the decay of the W^+W^- pair using a kinematic fit, and the kinematic fit takes the beam energy, E_{beam} as a constraint. Therefore the error on E_{beam} enters directly as an error on M_W. The expected statistical error on the W mass at the end of LEP2 is 25 MeV. To avoid a significant influence of the beam energy uncertainty on the total error, a precision of 10 - 15 MeV on E_{beam} is desired.

During the LEP1 period, a precise measurement of the beam energy was obtained using the method of resonant depolarization (RDP), which allowed a high precision of typically 1 MeV [30]. At LEP2 energies, however, this method cannot

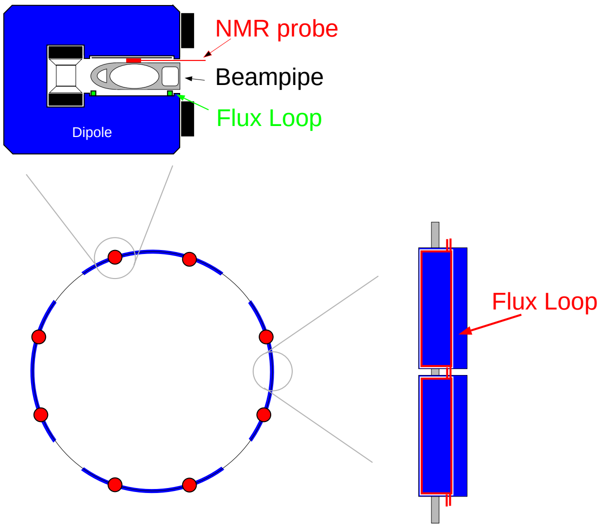

Abbildung 3.2: *The NMR probes and flux-loops used for monitoring the LEP magnetic field.*

be used, since polarisation has only been observed in LEP up to beam energies of 60 GeV. For the data analysed in this thesis, an alternative NMR (nuclear magnetic resonance) -extrapolation method is used. Here, the local magnetic fields, as measured by 16 NMR probes installed inside some selected bending dipoles around the LEP ring (see Figure 3.2), are calibrated against RDP in the energy interval 40 - 60 GeV. This calibration is applied to give the energy in the physics regime of around 100 GeV. It is assumed that the relation between NMR and the beam energy is linear and valid up to physics energies. The NMR sample corresponds to a small fraction of the field, while the flux-loops[4] also installed inside the dipoles (see Figure 3.2) provide a measurement of 97 % of the total bending field. Thus the flux-loop measurements are used to cross-check the beam energy determined by the NMR probes [31].

At LEP2, the beam energy is determined with a precision of 25 MeV [32] for the data taken during 1997 at $\sqrt{s} = 183$ GeV. The analysis of the 1998 data led to a beam energy uncertainty of 20 MeV [33] at $\sqrt{s} = 189$ GeV. For the runs at

---

[4] The Flux Loop consists of a closed electrical loop threading through the dipoles; the integrated induced voltage when altering the dipole currents is a direct measure of the magnetic field generated by the main ring dipoles.

higher center-of-mass energies, LEP plans to use the LEP spectrometer[34] for further improvement in the measurement of the beam energy. The spectrometer determines the beam energy by measuring the bend angle of the beam in a lattice dipole of known integrated field.

3.2 L3 Detector

Giant detectors observe what happens when high energy particles collide with each other. The detection of an elementary particle means the localisation, identification and measurements of its energy and momentum. For this information to be useful, it is needed with a sufficient resolution. Since no detector can be sensitive to all types of these requirements, in practice experiments use several different detectors in combination. They are designed to be sensitive to certain types of radiation in a given energy range. The detectors installed at the LEP site, L3 [24], ALEPH [25], DELPHI [26] and OPAL [27], are very large multicomponent detectors which integrate many different sub-detectors in a single device. They are giant, because the particles coming out of the interaction point are very energetic and thus need bigger detectors to stop them or to get better momentum resolution.

The L3 detector is the largest of the four LEP detectors and is designed with special emphasis on a high resolution energy measurement of photons, electrons, jets and an accurate momentum measurement of muons[24, 35, 36, 37, 38, 39]. Thus its most impressive components are the precise muon spectrometer, a high precision electromagnetic crystal calorimeter as well as a fine-grained hadron calorimeter. A perspective view of the detector is shown in Figure 3.3 and its inner components are displayed in Figure 3.4. The individual components of the whole apparatus can be grouped with respect to their angular coverage into a barrel part, endcap regions, and sub-detectors at very low angles relative to the beam axis.

Starting from the interaction point, the L3 detector consists of the following independent and modular sub-detectors: A silicon micro-strip vertex detector (SMD) is used to accurately reconstruct the decay vertex of short-lived particles. Outside of the vertex detector, a multi-wire drift chamber (TEC) is used, which

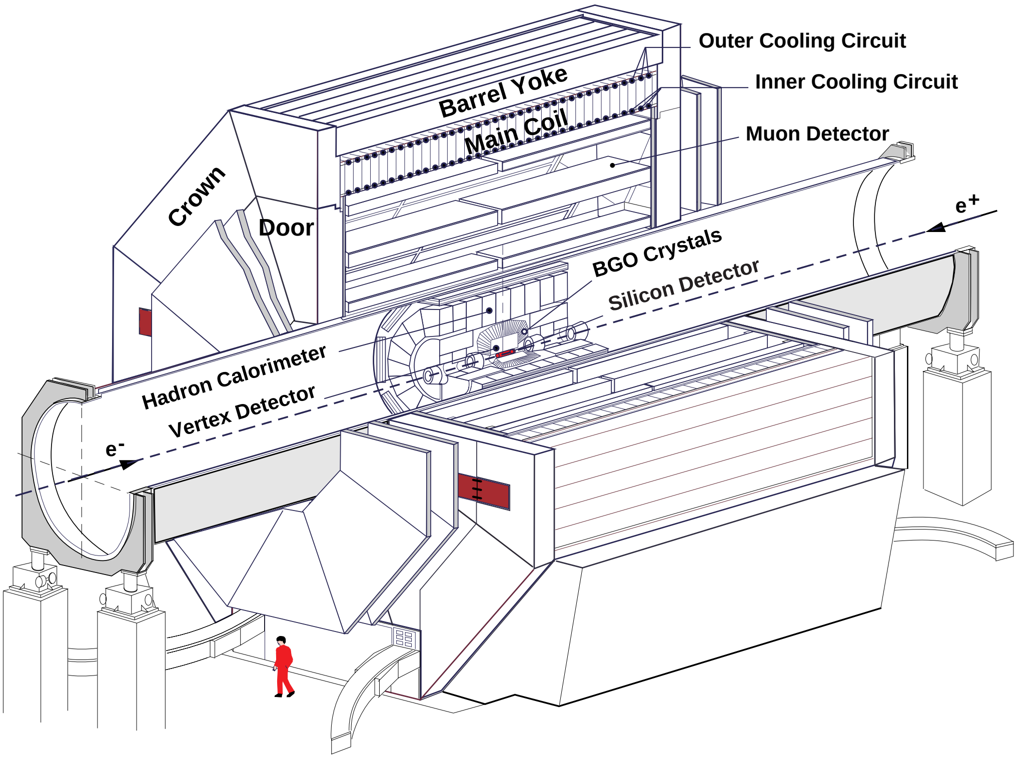

Abbildung 3.3: *Perspective view of the L3 detector.*

allows reconstruction of the trajectories of charged particles and classification of them using the ionisation left in the detectors. This inner tracking system is surrounded by an electromagnetic calorimeter (BGO) which gives a measurement of the energy deposited by charged tracks and photons. It's also capable of giving position information for photons, and assists in electron identification via its characteristic electromagnetic shower shape. Outside the electromagnetic calorimeter, an array of scintillation counters are situated for a precise timing information while a hadron calorimeter determines the energies of hadrons. The hadron detector is the most important device to detect hadronic W decay products. The inner detector parts are mounted within a steel support tube having a diameter of 4.45 meters and a length of 32 meters. Finally, outside the support tube the muon spectrometer is installed to identify and measure the momentum of muons. All detector parts[5] are embedded in a solenoidal magnet providing a

---

[5] Except for a part of the forward-backward muon spectrometer [40] (see section 3.2.5), which is mounted outside the magnet and the Very Small Angle Tagger (VSAT) [41] (see

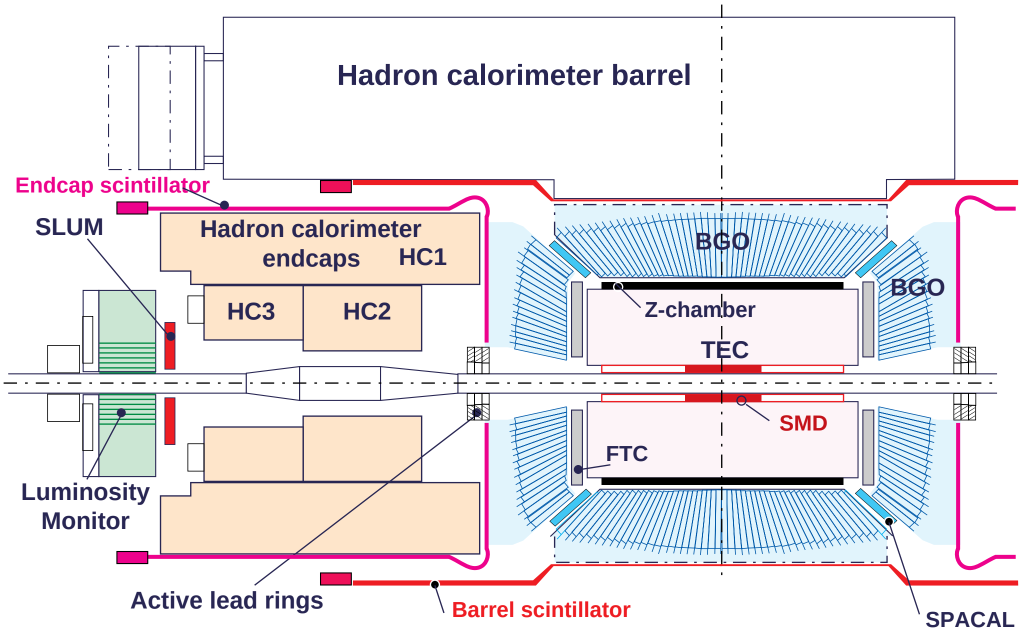

Abbildung 3.4: *Inner components of the L3 detector. Although not indicated in the figure, the L3 detector is left-right symmetric, i.e. symmetric with respect to the plane perpendicular to the beam axis and origin in the centre of the detector.*

homogeneous field of 0.5 Tesla parallel to the beam axis. In addition, the iron doors (see Figure 3.3) are wrapped with coils providing a toroidal field of 1.2 Tesla, which ensures the measurement of muon momenta in the forward-backward muon chambers. The outer diameter of the L3 experiment is about 12 meters and its length along the beam pipe is about 14 meters.

The L3 reference system is defined in the following way. From the nominal interaction point which is at the geometrical centre of the detector, the x axis points to the centre of the LEP ring, while the z axis points along the beam pipe in the flight direction of the beam electrons. The y axis is defined vertically upwards, being orthogonal to both the x - and z axis. Here, the θ coordinate measures the angle subtended at the origin with respect to the z axis, and ϕ represents the angle in the xy plane (also called rϕ plane), with $\phi = 0$ for the x

---

section 3.2.6)

axis.

3.2.1 Inner Tracking System

By the passage of a charged particle through a detector, it can interact electromagnetically with atoms. If an electric field is applied, the electrons released as part of electron-ion pairs will drift towards the anode and create an electrical signal. This idea is used in gas detectors.

Gaseous detectors, common in the form of proportional chambers, are based on the observation of secondary electrons in an electric field. If the field is strong enough, an electron will gain sufficient energy to cause secondary ionization and create further electron-ion pairs. The new electrons are again accelerated by the electric field and will cause another ionization, leading to a chain of such processes. An avalanche of electrons will develop and their collection at the anode will give a pulse. The position information of a particle can be obtained given the fact that the electrons take time to drift from their point of production to the anode. If the drift time can be measured accurately (to within a few ns) and if the drift velocity is known, then high spatial resolutions of 100-200 μm can be achieved.

Semiconductor detectors are essentially like gaseous detectors producing electron-hole pairs instead of electron-ion pairs. The electrons and holes separate in the presence of an electric field and collect at the electrodes, producing a detectable current. Since arrays of strips can be used to form detectors, the very narrow gaps of these strips of order 10 μm can give an extremely good position resolution of order 5 μm.

The momentum and direction of a charged particle are determined from the curvature of its track inside a magnetic field. A charged particle moving in a magnetic field yields a helix. The size of the radius is proportional to the transverse momentum. The charge of the particle can be determined from the sign of the curvature.

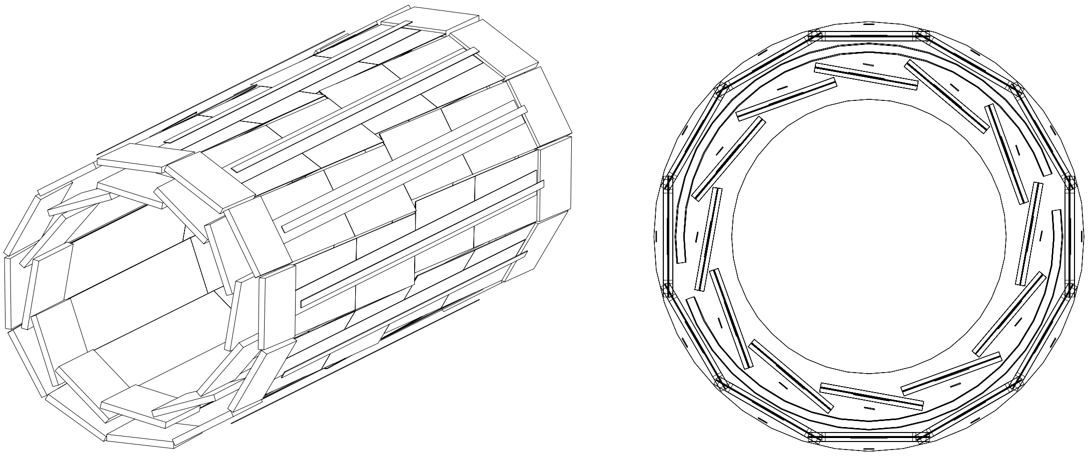

Abbildung 3.5: *SMD layout.*

Silicon Microvertex Detector (SMD)

Since the beginning of 1993 the Silicon Microvertex Detector (SMD) [42] is the innermost part of the central tracking system of L3, while the L3 detector in general had been collecting data since the beginning of LEP operation in 1989. The main purpose of this detector is to provide a more accurate position measurement near the beam pipe for tracks which are reconstructed in the drift chamber. The spatial resolution of the SMD is 7 μm in the rϕ plane and 14 μm in the rz plane. This provides a better reconstruction of vertices stemming from particles with very short lifetime, like the τ lepton or hadrons containing b or c quarks. It also results in an improved momentum resolution.

The detector is constructed of two double-sided cylindrical layers of silicon sensors approximately 6 and 8 cm from the beam axis. Each layer consists of 12 identical ladders, those on the inner layer being tilted slightly to fit into the smaller circumference (Figure 3.5). A ladder consists of four 70 mm long and 40 mm wide wafers. The SMD covers a polar angle range of $29^\circ \leq \theta \leq 151^\circ$ with both layers and $21^\circ \leq \theta \leq 159^\circ$ with the inner layer only.

Time Expansion Chamber (TEC)

The central tracking chamber surrounding the SMD is designed to give the best possible resolution in the limited volume available inside the electromagnetic calorimeter. The momentum of a charged particle is determined from the cur-

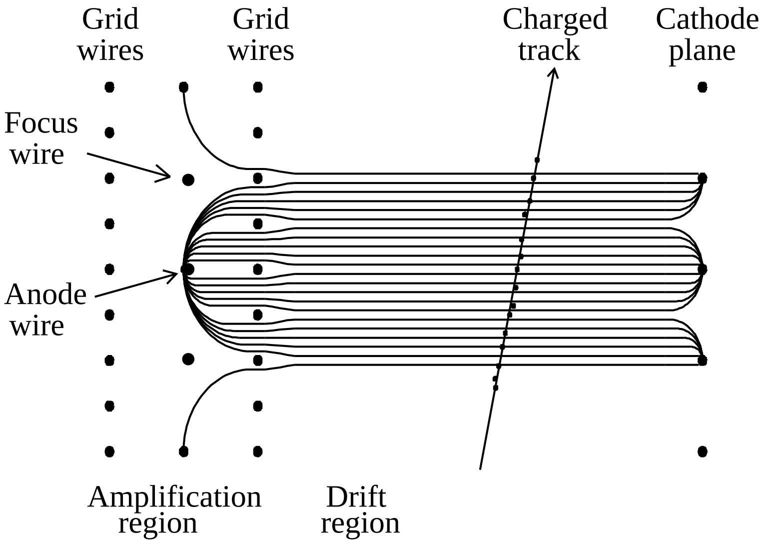

Abbildung 3.6: *Principle of a time expansion chamber.*

vature of its track in an applied magnetic field. To measure the charge of a 50 GeV particle at 95% confidence level in the 0.5 Tesla magnetic field, a single hit resolution of about 50 μm is required in 50 wires for the available lever arm of 31.7 cm radially. This is realised by L3 using a drift chamber with a detection principle of a Time Expansion Chamber (TEC). In a TEC, a large drift region with a low, uniform field is separated from the high field amplification region close to the anode by a plane of grid wires (see Figure 3.6). The high electric field causes a high multiplication and thus a large readout signal, and the plane of grid wires ensures the homogeneity of the electric field in the drift region. The TEC operates with a gas mixture of 80% CO_2 and 20% ISO-butane, which has a low longitudinal diffusion and thus permits a low drift velocity of less than 6 μm/ns – about 10 times less than what is used in a conventional drift chamber. The combination of a low drift velocity in the drift region and a high, clear signal due to the amplification near the anode guarantees the high spatial resolution. The pressure in the TEC is 1.2 bar, and the temperature is 18°C.

The TEC is surrounded by an aluminium cylinder of 46 cm radius and has a sensitive length of 98 cm. It consists of two concentric cylinders, the inner one having 12 sectors and the outer one 24. Each sector has a central anode plane and is separated from its neighbouring sectors by cathode planes (Figure 3.7).

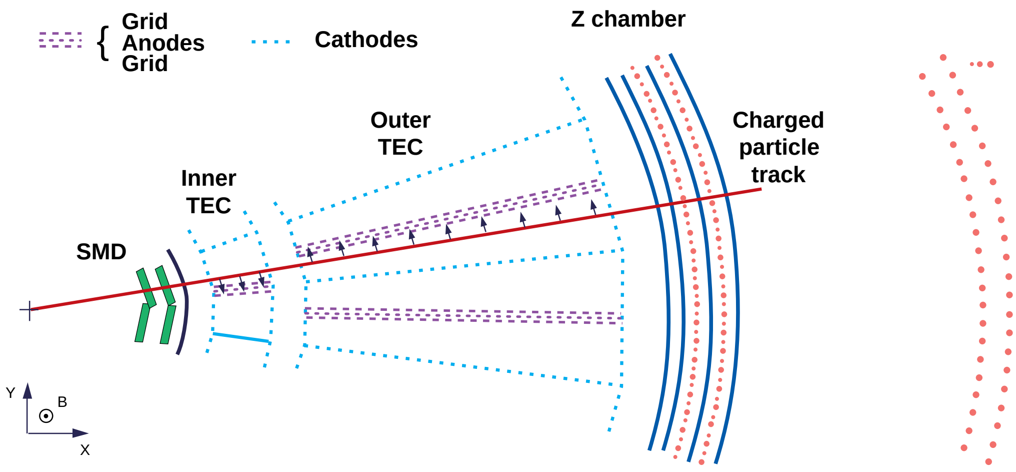

Abbildung 3.7: *The L3 tracking system consists of the SMD, the TEC and the Z chamber. The $r\phi$ view of one sector of the tracking system and a schematic drawing is shown for the case in which a particle crosses the tracking system.*

The displacement of the outer sectors with respect to the inner ones and the use of pick-up wires in the grid planes of the outer TEC helps to solve the problem of left-right-ambiguity.

The anode wires parallel to the z axis measure only the xy coordinates of an ionisation track. To measure the z coordinate, 11 out of the total 62 sense wires are read out on both sides of the wire thus additionally rendering the z coordinate through comparison of the two pulse integrals. This is the charge division method. However, this method yields a resolution of the order of centimeters, which is not good enough. To improve measurements of the z coordinate, an additional Z-chamber is used.

Z-Chamber

The outer surface of the TEC cylinder is equipped with a thin four-layer cylindrical proportional chamber called Z–chamber [43], covering the angular range of $42^\circ \leq \theta \leq 138^\circ$, see Figure 3.7. Here, four points of each track are measured

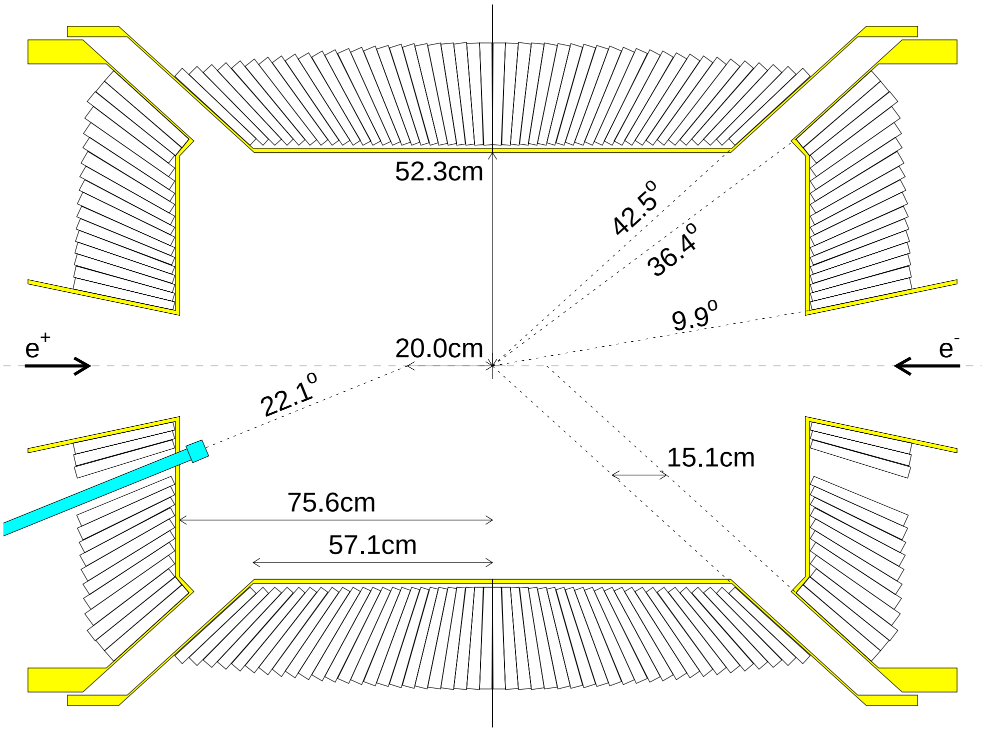

Abbildung 3.8: *Side view of the BGO electromagnetic calorimeter.*

using cathode strip readout. The strips have a pitch of 4.45 mm and incline with respect to the beam axis by angles of 69°, 90°, –69° and again 90°. The position resolution of the z-chamber is 320 μm.

FTC

At lower polar angles not covered by the Z–chamber a Forward Tracking Chamber (FTC) [44, 45] is located between the TEC end-flanges and the BGO endcap calorimeter (Figure 3.4).

3.2.2 Electromagnetic Calorimeter

A calorimeter is a block of absorber/detector, or a sandwich construction with separate layers of absorber and detector. The latter is a sampling calorimeter. Calorimeters are important detectors for measuring the energy and position of a particle, because they can detect neutral particles as well as charged particles. If a particle interacts with the material of the calorimeter, it will generate a secondary particle which will generate further particles themselves, so that a shower (cascade) develops. Normally all of the primary energy is deposited in the calorimeter, and the energy information can be read out. Since the characteristics of electromagnetic (caused by electrons and photons) and hadronic showers (caused by hadrons) are different, it is common practice to design two separate detectors for each purpose.

When a high-energy electron or positron interacts with matter, the predominant energy loss is due to bremsstrahlung, while for the photons the predominant process is e^+e^- pair production. Thus the initial electron or photon will generate a cascade until the energy of the newly generated particles are too low to generate further particles.

The electromagnetic calorimeter of the L3 experiment is designed to have excellent energy and spatial resolution for photons and electrons over a wide energy range (from 100 MeV to 100 GeV). Accordingly, an inorganic crystal made of Bismuth Germanate ($Bi_4Ge_3O_{12}$ called BGO) is chosen. BGO has a great stopping power due to its high density and high atomic number. To get high resolution of energy, the BGO calorimeter is used for both showering and detection rather than measuring only a sampled fraction of the complete shower. The whole calorimeter consists of about 11000 crystals. The arrangement of the crystals including the most important geometrical dimensions are shown in Figure 3.8.

The crystals have the shape of a truncated pyramid with a length of 24 cm (equivalent to more than 21 radiations lengths[6]), a front surface of 2×2 cm^2 and a rear surface of 3×3 cm^2 (Figure 3.9). All crystals point to the vertex, and each crystal is viewed by two photodiodes glued to its rear face to detect the BGO scintillation light. The energy resolution of BGO is about 5% at 100 MeV and below 1% above 2 GeV. The position resolution resulting from the center-of-gravity method is less than 2 mm for electromagnetic showers.

In 1996 the gaps between the barrel and endcap parts of the BGO were equipped with a "spaghetti" calorimeter (SPACAL) [46]. The SPACAL consists

---

[6] The radiation length in BGO is 1.12 cm [22]

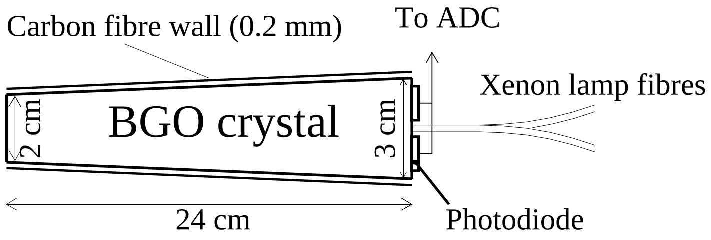

Abbildung 3.9: *BGO crystal.*

of lead bricks with several scintillating fibres inside.

3.2.3 Scintillation Counters

An array of 30 plastic scintillation counters in the barrel and 16 in the endcap region surrounds the electromagnetic calorimeter (Figure 3.4) [47]. The scintillation light is read out by photomultipliers. Providing a precise timing information with a resolution of about 0.8 ns in the barrel region and 1.9 ns for the endcaps, the scintillators can be used to identify muons originating from cosmic air showers which do not correlate with the beam crossing time.

3.2.4 Hadron Calorimeter and Muon Filter

The hadron calorimeter (HCAL) [48] of L3 is a fine sampling calorimeter made of uranium and brass absorber plates interspersed with proportional wire chambers. It is cylindrical in shape and positioned directly behind the scintillation counters viewed from the interaction point. It is divided into a barrel part covering $35^\circ \leq \theta \leq 145^\circ$ in polar angle and two endcaps extending the coverage down to 5.5°. This means that the hadronic calorimeter system covers 99.5% of 4π. The barrel calorimeter is composed of 9 rings along z, where each ring is symmetrically divided into 16 modules in the azimuthal direction. The endcap calorimeter consists of three rings on each side, one outer ring and two inner rings.

Hadronic showers are qualitatively similar to electromagnetic ones, but the scale of the hadronic shower is much larger, leading to thicker devices. E.g. in the endcaps of the L3 hadron calorimeter, the amount of material traversed by a particle originating at the interaction point varies between 6 and 7 nuclear ab-

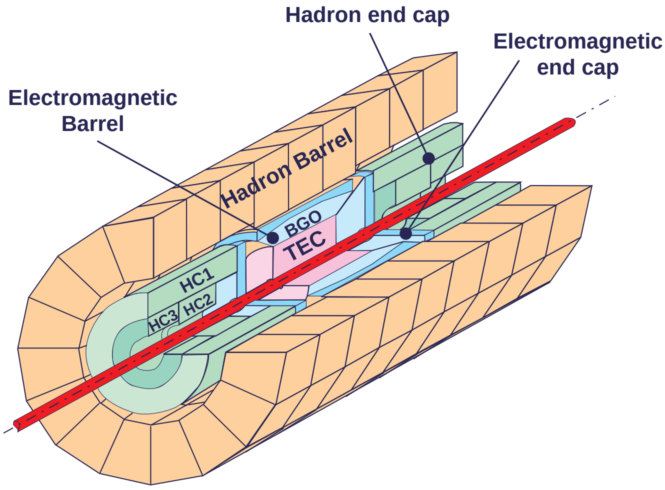

Abbildung 3.10: *Hadron calorimeter system.*

sorption lengths. A further difference is the more complex shower development. The nuclear excitation and leakage of secondary muons and neutrinos from the calorimeter will not give rise to an observable signal in the detector. To correct for this, fission compensation introducing layers of depleted uranium absorber plates into the calorimeter is used. Low-energy neutrons from nuclear breakup cause fission in the uranium and thus their energy is converted into charged particle ionization. This energy is measured and serves as the compensation.

The energy resolution of calorimeters is in general much worse for hadrons than for electrons and photons because of the greater fluctuations in the development of the hadron shower as mentioned above. The energy resolution is typically $\Delta E/E \approx 0.55/\sqrt{E}$, where E is measured in GeV. Combining the information from the BGO and hadron calorimeters, a resolution of 10% in total energy and 2° in direction of jets has been achieved for hadronic two-jet events at the Z^0 pole.

In order to reduce punch-through of hadrons into the muon chambers, an instrumented brass plate muon filter provides an extra 1.03 absorption length

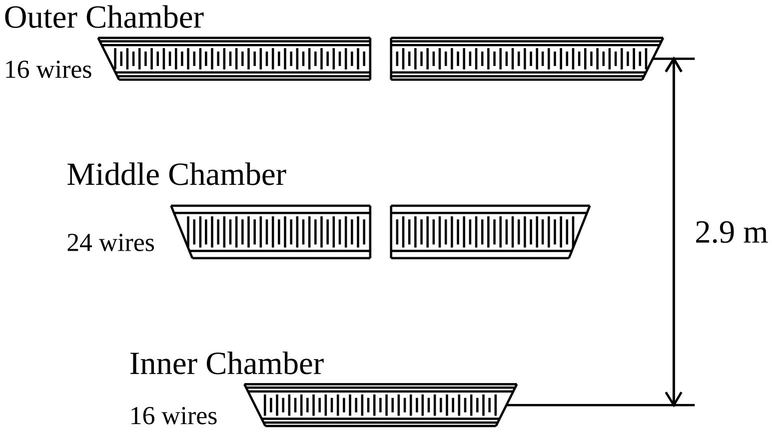

Abbildung 3.11: *rϕ view of a barrel muon chamber octant.*

of material around the barrel part of the HCAL. It consists of eight octants in the azimuthal direction. The barrel calorimeter and muon filter act as particle filters, so that only non-showering particles can reach the muon spectrometer.

3.2.5 Muon Spectrometer

The muon detector is designed for high precision measurements of the momentum of muons. Since the resolution of the transverse momentum is proportional to $1/L^2$ (L=length of the track), it is the biggest sub-detector of L3. Like calorimeters and scintillators, it is composed of a barrel part [49, 50] and endcaps [40]. The barrel consists of two “ferris wheels”, each made up of eight octants supporting three layers of precision multi-wire drift chambers. There are two chambers in the outer layer with 16 signal wires each, two chambers in the middle layer with 24 signal wires each, and one chamber in the inner layer with 16 signal wires (Figure 3.11) all measuring the track coordinates in the rϕ plane (P chambers) which represents the bending plane. The angular coverage for the three layers is $44^\circ \leq \theta \leq 136^\circ$. The transverse momentum of muons is extracted from the sagitta of the muon track (see Figure 3.12). The single wire resolution of the P chambers of 200 μm yields a momentum resolution of 2.5% at 45 GeV. Both sides of the inner and outer P chambers are equipped with additional drift chambers (Z chambers) which measure the coordinates along the beam with a resolution of about 500 μm.

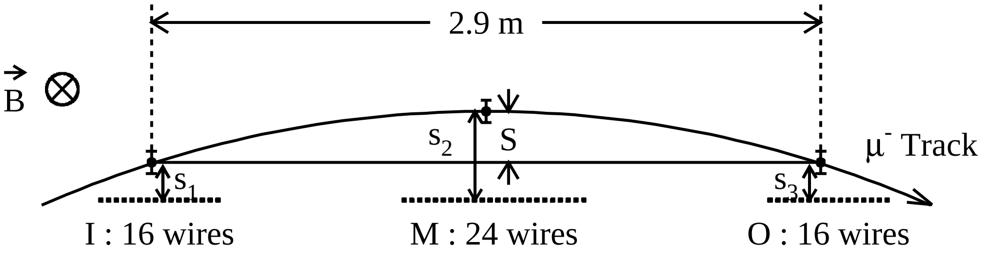

Abbildung 3.12: *Sagitta measurement in the barrel muon chambers.*

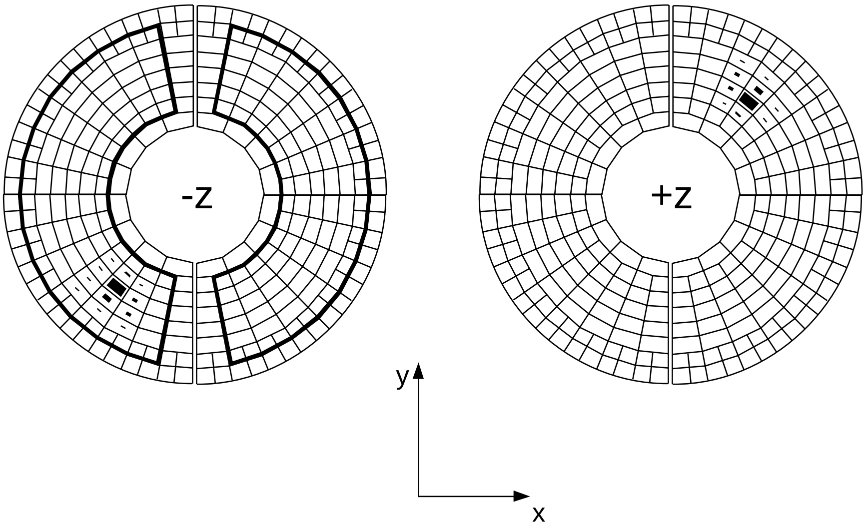

Abbildung 3.13: *Crystal arrangement in the luminosity monitors. The energy depositions of a small angle Bhabha event are also shown.*

The endcap – or forward-backward – muon chambers extend the angular coverage down to a polar angle of 24°. Both endcaps consist of three layers where one layer is mounted inside and two layers are mounted outside the iron doors, which contain a toroidal magnetic field and return the flux of the L3 solenoid magnetic field. The momentum resolution in the forward-backward chambers varies strongly with the polar angle of the muon from 4% to 30% for a 45 GeV particle and is limited through multiple scattering in the 90 cm thick doors.

3.2.6 Luminosity Monitor

For a precise measurement of the Standard Model parameters like the cross section of certain processes, a measurement of the integrated luminosity is crucial. As already mentioned, luminosity is defined through the equation 3.1. However, the parameters of the LEP machines and fills are not well known to calculate the luminosity at the individual experimental interaction points with sufficient accuracy, i.e., on a sub-percent level. Hence, a different approach is chosen by the LEP experiments. The luminosity is measured directly with a detector at the interaction region. The idea here is to determine the unknown cross section measuring it in units of a known cross section. At e^+e^- colliders, the reaction used is elastic e^+e^- scattering at small angles (Bhabha scattering) because it has a very high rate and is caused by the dominating γ exchange in the t–channel, an almost pure QED process which can be computed with very high precision:

$$\int \mathcal{L} dt = \frac{N_{Bhabha}}{\sigma_{Bhabha}}, \tag{3.3}$$

where N_{Bhabha} is the number of Bhabha events and σ_{Bhabha} represents the corresponding cross section.

The luminosity monitor [51] of L3 consists of a silicon strip tracker called SLUM followed by a highly segmented BGO array. The system covers a polar angle of $1.4^\circ \leq \theta \leq 3.9^\circ$ and is situated 2.73 m away from the interaction point in both directions (see Figure 3.4). The two half cylinders of each detector contain 304 BGO crystals which are situated parallel to the beam axis (see Figure 3.13). The energy resolution of the calorimeter is about 2% at 45 GeV. The angular resolution of the system is improved by the SLUM providing three layers of a silicon strip detector on each side. Two layers with strips in parallel to the beam axis measure the polar angle and one layer with strips perpendicular to the beam axis measures the azimuthal angle of incoming particles. The angular resolution is 0.4 mrad in θ and 0.5° in ϕ.

The measured luminosities at various centre-of-mass energies of the LEP 2 program are listed in table 3.1.

Year	$\sqrt{s}$ (GeV)	$\mathcal{L}$ (pb^{-1})
1996	161.3	10.8
1996	172.1	10.2
1997	182.7	55.5
1998	188.6	176.4
1999	192-202	233.9
2000	200-208	212.5

Tabelle 3.1: *Centre-of-mass energies [52, 53, 54, 55, 56] and measured luminosities at LEP2.*

3.2.7 Trigger

The bunch crossing rate at LEP2 is 45 kHz which is the frequency at which the L3 detector opens its gate. This means that the data acquisition system of L3 has to decide in less than 22 μs, the time between two beam crossings, if an e^+e^- annihilation took place and in the affirmative, if the events should be recorded. Since the amount of data is too large to be handled, a trigger system is used. The triggering is performed in a three-level process with increasing complexity at each level. This reduces the event rate and thus leaves more time for more elaborate decisions at each stage. In this way, a beam crossing rate of 45 kHz is reduced to a few Hz of events which are eventually recorded.

Level-1 Trigger

The level-1 trigger consists of five sub-triggers and decides whether to initiate the digitisation of the detector data or whether to drop the event. Therefore, dead time occurs only in the case of an event being accepted by level-1. In the case of a positive decision, the detector data is digitised within 500 μs. The level-1 rate of positive decisions is typically 20 Hz at LEP2, with a dead time incurred from the digitizations of less than 5%.

The energy trigger [57, 58, 59, 60] processes the information given by electromagnetic and hadron calorimeters and selects events which deposit energy in the calorimeters. The quantities used are: the total calorimeter energy; the energy in the electromagnetic calorimeter alone; and these two energies measured only in the barrel region. Typical thresholds are 25, 15 and 8 GeV respectively. For the single photon events, the trigger has a threshold of 0.9 GeV. The main source of background is electronic noise.

The TEC or charged particle trigger [61] searches for tracks pointing to the interaction vertex in the $r\phi$ projection. The event is accepted if there are at least two TEC tracks of less than 60° acoplanarity.

The scintillator trigger is based on the signal of the barrel and endcap scintillators. It is used to select high multiplicity events as well as to reject cosmic muons by requiring the timing to be in a gate around the beam crossing.

The muon trigger [62] selects events with at least one muon reaching the muon chambers. The high trigger rate of 10 Hz due to cosmic muons is significantly reduced to less than 1 Hz by requiring a hit in the scintillator in a gate around the beam crossing.

The luminosity trigger requires two back-to-back luminosity monitor segments, both with an energy above a threshold. An energy deposit greater than 30 GeV is required in the luminosity monitors by the single tag trigger. It is used to select Bhabha events in the luminosity monitors.

Level-2 Trigger

The level-1 triggers attempt to select interesting events. In contrast, the level-2 trigger [63, 64] is designed to reject non-physical background events arising from electronic noise, beam-gas and beam-wall interactions as well as synchrotron radiation. Events triggered by more than one level-1 sub-trigger are never rejected. Here, information not available in time for a level-1 decision is used, too. In particular, information on the vertex along the beam axis using the charge division measurement from the TEC, energy depositions in the BGO and hadron calorimeters correlated in a coarse $\theta - \phi$ map and longitudinal and transverse energy imbalance arising from the energy measurement are used. Averaged over all level-1 triggers, the rejection rate is between 20% to 30%. In case of a positive decision the input to level-2 plus all level-2 results are forwarded to the level-3 trigger. The total rate is typically 10 Hz.

Level-3 Trigger

The level-3 trigger [65] is applied when the event is digitized on the basis of the full detector readout. The accurate digital data with its finer granularity and higher resolution allows thresholds to be determined more precisely and electronic noise problems are further reduced. Events with multiple level-1 triggers or a luminosity trigger are passed through untouched. The event selection is based on the correlation of energy deposited in the BGO and HCAL, the reconstruction of muon tracks in the Z chambers, and the reconstruction of the vertex in the TEC. The level-3 trigger rejects about 40% to 60% of all events with an output rate of 3 to 5 Hz.

The output from the level-3 trigger is delivered into a memory buffer of the main online computer. From this buffer all events are written to tape and selected events dispatched to ten separate monitoring programs. In addition, processes on this and the other online computers control the data taking, monitor, log and adjust detector settings, and calibrate the various detector and trigger elements.

Kapitel 4

Monte Carlo Simulation

Computer simulation is an essential part of the data analysis. It helps to understand the physics, the response of the detector, and systematic errors. The need of a computer simulation (Monte Carlo simulation) is more pronounced if a systematic error should be reduced at a level which makes precision tests possible.

The Monte Carlo simulation generates events in two steps:

1 Event generation,

2 Detector simulation.

These steps are presented in this chapter.

4.1 Event Generation

Programs, which simulate events of a particular process, are called event generators. The events are usually distributed in phase space according to the SM calculation as implemented in the event generator. They are stored as sets of energy-momentum four vectors and particle types. The theoretical model applied to describe particle production is illustrated for the example of a hadronic WW decay in an e^+e^- interaction. The various simulation stages are subdivided into four phases with a characteristic length δ (Fig. 4.1):

I This stage represents the decay of the W-pair into quarks and antiquarks and is the electroweak phase ($\delta = 10^{-17}$ cm). This phase is described by the electroweak theory.

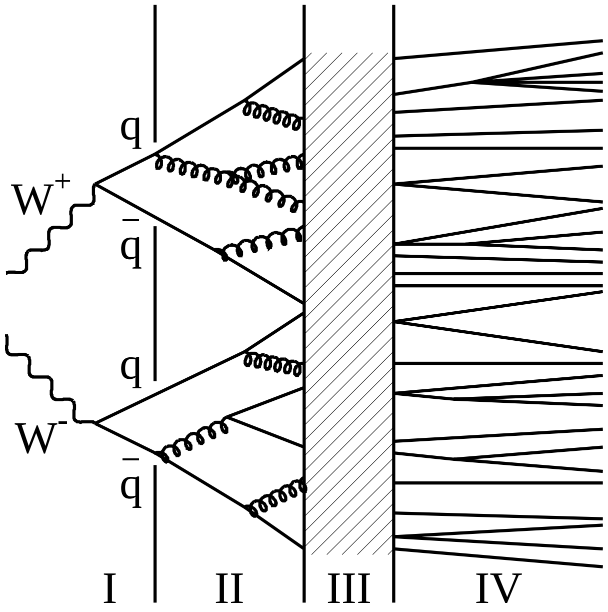

Abbildung 4.1: *Schematic view of a hadronic WW decay. The four phases of the decay process are separated by the vertical lines.*

II This is the phase ($\delta = 10^{-15}$ cm) calculable by perturbative QCD. The momentum transfer between the quarks and the radiated gluons (if any) is large.

III This is the non-perturbative QCD phase ($\delta = 10^{-13}$ cm), because the momentum transfer is small and the coupling constant becomes too large to allow calculation by perturbation theory. Thus, phenomenological models have to be used instead, like **JETSET**[66] or **HERWIG**[67, 68]. In this stage a $q\bar{q}$ pair from the W decay turns into hadrons, which can be observed. This process of the conversion of the high-energy $q\bar{q}$ pair into hadrons is called **fragmentation**. The **JETSET** model is based on the string fragmentation. A simple picture may help to understand this very complicated process. As the pair separates after production, the 'spring' joining the pair will stretch. As it stretches it stores increasing energy until it becomes energetically possible for it to break up with a new q attached to the end of the spring on one side of the break and a $\bar{q}$ of the same flavour at the other side of the break. The two segments of the spring may still be sub-

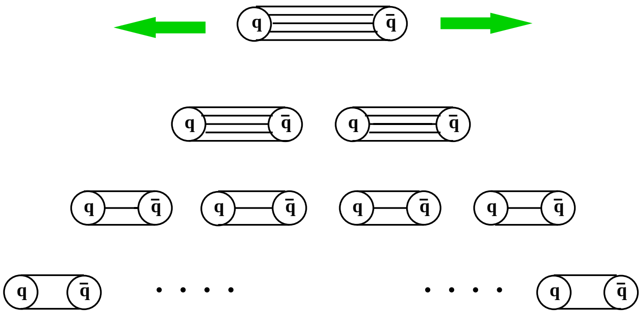

Abbildung 4.2: *A simple picture of the string fragmentation*

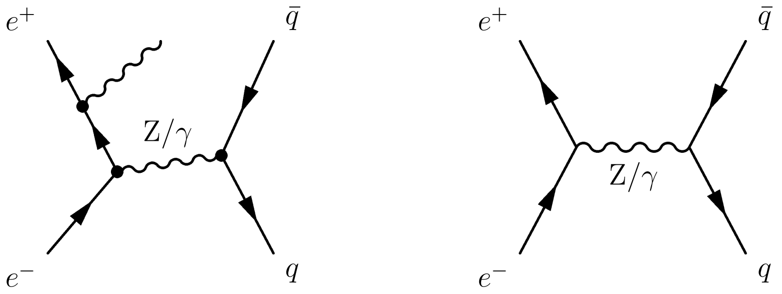

Abbildung 4.3: *Feynman diagram of the process* $\mathrm{e^+e^-} \rightarrow \mathrm{Z}/\gamma \rightarrow q\bar{q}(\gamma)$ *with and without ISR.*

ject to stretching given the possibility of the continued rapid quarks at the ends promoting further breaking. When breaking ceases we are left with several spring segments, which could for example be mesons consisting of a color-singlet system $q\bar{q}$. This characteristic is shown in Fig.4.2.

IV This phase represents the decay of unstable hadrons into more stable hadrons, which are actually observed in the detector. This stage is called the particle decay phase ($\delta > 10^{-13}$ cm). Here accurate experimental data is used to describe its behaviour.

There are various MC programs used in this analysis. One of them is **KORALW** [69], which is designed specifically to generate $\mathrm{W^+W^-}$ pairs in $\mathrm{e^+e^-}$ collisions at LEP II. This program uses **JETSET** to implement the hadronisation of quarks and decay of unstable hadrons and has the most accurate simulation of ISR. It allows multiple ISR photons with finite transverse momentum. The leptonic decays of the W and the secondary decays like in the case of the τ lepton as well as the polarisation of the τ are modelled. The production of the events is realised in lowest order by three Feynman diagrams (CC03), and this Monte Carlo sample is used to estimate the W-pair selection efficiency. The **PYTHIA** [70] generator is used for a variaty of physics processes. In this analysis, it has been used for processes like $\mathrm{e^+e^-} \rightarrow \mathrm{Z}/\gamma \rightarrow q\bar{q}(\gamma)$, $\mathrm{e^+e^-} \rightarrow \mathrm{Ze^+e^-}$, and $\mathrm{e^+e^-} \rightarrow \mathrm{ZZ}$ (see Figure 4.3,4.4).

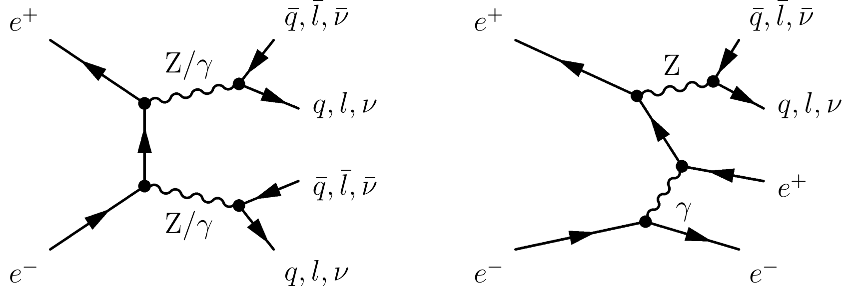

Abbildung 4.4: *Examples for ZZ and Zee production*

For the generation of two photon events (see Figure 4.5) the program **PHOJET**[71, 72] is used. There are also other MC programs which have been used for systematic checks.

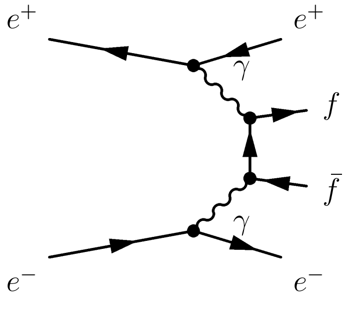

Abbildung 4.5: *Two photon interaction*

4.2 Detector Simulation

In the second step, the modelling of the response of the detector for the generated particles must be done. This includes tracking and shower simulation in the detector materials and the response of each active (chamber or calorimeter) element.

The L3 detector is modelled by the SIL3 program, which uses the **GEANT**[73] and the **GHEISHA** packages [74]. GEANT models the passage of the particles through the detector, including the interaction of the particles with matter such as ionization loss, multiple scattering, decay, photoproduction, bremsstrahlung, and other interactions. GHEISHA is a special program called by GEANT which is used for the hadronic shower simulation.

Each subdetector geometry is described to the required level of accuracy, typically 10-100 μm. For the simulation of showers the particles are tracked down to 10 KeV in the electromagnetic calorimeter and down to 1 MeV in the hadron calorimeter. Fine tuning of the parameters in the simulation is done using the results of the beam test[75]. The parameters tuned include: an optimization of the step size for particle tracking in all subdetectors; an optimization of the medium dependent energy cut-off parameters; a parametrisation of the saturation in light yield, the light collection efficiency and electronic noise in the electromagnetic calorimeter; and a simulation of uranium noise in the hadron calorimeter according to experimentally determined spectra. Hits in TEC and muon chamber are simulated using the time-to-distance relation measured in the test beam data or obtained in the calibration of Z data. Every year, the data taking period begins by a run at the Z peak to collect 2.5 pb^{-1} useful for the calibration of the different detectors.

The state of the detector during data taking is not ideal and has many time dependent imperfections like noisy crystals, disconnected sectors and wires in the muon chamber and TEC. All information on the status and calibration of the detector is stored in the L3 data base. During the reconstruction of the simulated events, each event is assigned a time and date such that the MC events are distributed over the data taking period with proper luminosity weighting. Since the simulation should be as realistic as possible, all the necessary information is retrieved from the database using the time and date recorded in each event. The reconstruction code used for the simulated events is the same as for the real data events.

Kapitel 5

Event Selection and Reconstruction

The massive W is a clear prediction from the standard electroweak theory. Therefore the properties of the events are well known and a precise prediction of the cross section from the SM exists. It can be measured with the selected W events. Thus this represents a first test of the SM concerning the W production.

How are W bosons recognized from other events arising from the collisions ?

First a picture of how the W boson events will look like will be constructed. Next, the selection of $W^+W^- \to q\bar{q}q\bar{q}$ events using the L3 detector is described.

Selections and related studies are performed for the data taken at 182.7 GeV and 188.6 GeV (see Table 3.1). The other lower center-of-mass energies were already covered by previous L3 analyses. Since the selection criteria and methods to estimate systematic uncertainties are exactly the same for both energy points, distributions are only shown and numbers are only quoted for $\sqrt{s} = 188.6$ GeV (from now on referred to as 189 GeV), unless stated otherwise. The cut positions shown in some distributions are from the final cut-based selection described in section 5.3.1.

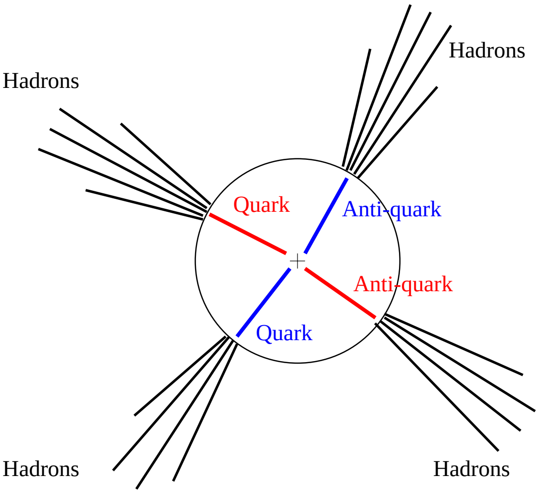

Abbildung 5.1: *Schematic illustration of the topology for* $W^+W^- \rightarrow q\bar{q}q\bar{q}$

5.1 Characteristics of the Hadronic W Events

The W boson decays due to the weak interaction. A slow process of decay may thus be expected. But the large mass of W means that there is an enormous energy release in a W decay, yielding many available energy states for the decay. Therefore the W boson decays in less than $10^{-24}s$ after its production. There is no way to detect the genuine W boson, only the decay products of the W bosons.

Approximately 46% of the W pairs produced are expected to decay in the $q\bar{q}q\bar{q}$ channel, see section 2.2.3. But in contrast to the leptons, free quarks have never been observed. What can one expect to observe in the detectors ?

In the simple picture of the string fragmentation described in section 4.1, the line of separation of the q and $\bar{q}$ is the line of stretching of the spring; when the spring breaks the force acting on the mesons occurs along this same direction and these newly produced mesons will therefore also have a tendency to move in this direction. One would therefore expect four **jets** of particles coming from the decays of two W bosons into two quark-antiquark pairs. This characteristic is shown in Figure 5.1.

The basic features of $W^+W^- \rightarrow q\bar{q}q\bar{q}$ events can be described with a computer

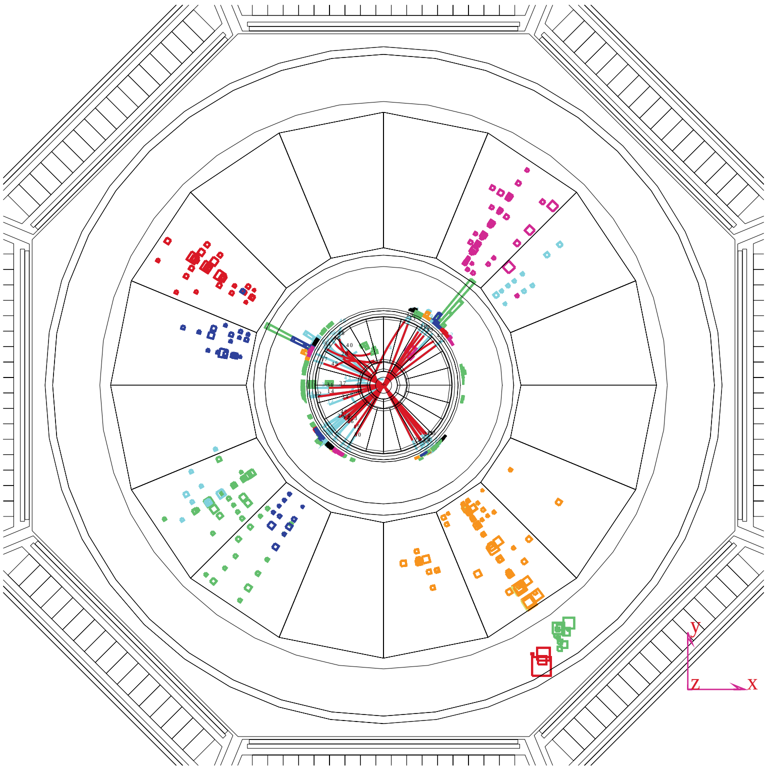

Abbildung 5.2: *A computer reconstruction of a measured* $W^+W^- \to q\bar{q}q\bar{q}$ *hadronic four-jet event observed in the L3 detector at* $\sqrt{s} = 189$ *GeV.*

reconstruction of a measured $W^+W^- \to q\bar{q}q\bar{q}$ hadronic four-jet event observed in the L3 detector at $\sqrt{s} = 189$ GeV in Figure 5.2. First, it is characterised by a four-jet like topology. The energy of the jets is very high, which translates into a high multiplicity of particles in each of the jets. In the detector, a high number of tracks and calorimeter clusters is expected. Since there is very little chance for the jets to escape the detector the desired events should have high visible energy and low missing momentum. Based on these characteristic features two methods are developed to select a hadronic WW sample with high efficiency and purity, as explained in section 5.3.1.

5.2 Standard Model Backgrounds

In the last section, the signatures for recognition of the W bosons were outlined. But in the LEP2 energy region there is a host of standard model processes. Some of these processes leave nearly the same signatures in the detector and are therefore very hard to distinguish from the W boson events. These background events are illustrated in this section.

The background to the $e^+e^- \to W^+W^- \to q\bar{q}q\bar{q}$ process is dominated by the $e^+e^- \to Z/\gamma^* \to q\bar{q}(\gamma)$ production. Most of these events are produced in association with energetic initial state photons (ISR) which boost the two-quark invariant mass back to the Z^0 mass. This is known as the radiative return to the Z". Such events can be divided into two categories. In the first category, the ISR photon escapes down the beam pipe and one observes a great deal of missing longitudinal momentum in the detector, but little or no missing momentum perpendicular to the beam pipe. In the other category, the ISR photons are detected in the BGO. These events emit a photon with a specific energy, which makes it easy to separate them from the other events. Both types of events are shown in Figure 5.3. But non-radiative $Z/\gamma^* \to q\bar{q}$ events with hard gluon radiation producing four jets are particularly difficult to distinguish from $W^+W^- \to q\bar{q}q\bar{q}$ production.

Sometimes a hard gluon is emitted by the quark or antiquark before fragmentation occurs, as a photon is radiated by an electron. But the gluon is not a 'real' particle, which can be detected in our detector. Gluons become hadrons in a similar way that quarks do. The gluon emission leading to the formation of a three-jet or a four-jet event is illustrated in Figure 5.4. The events with gluon radiation constitute only a fraction of the total $e^+e^- \to Z/\gamma \to q\bar{q}(\gamma)$ production, but with a cross section about one order of magnitude larger than that for the WW signal, see Figure 5.5.

Additional important backgrounds come from $e^+e^- \to ZZ \to q\bar{q}q\bar{q}(\gamma)$ production, since for the data analysed in this thesis, the LEP center-of-mass energy exceeds $2M_Z$. These events have a similar event topology as the signal events. But because of the small cross section, the contamination of these events in the final selected sample will be small. The singly resonant Z production $e^+e^- \to Ze^+e^-$

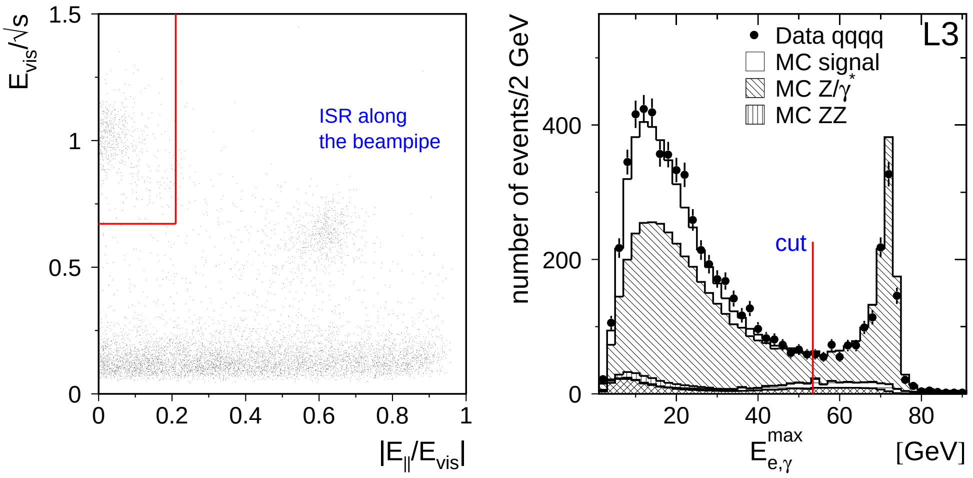

Abbildung 5.3: *In the left plot the visible energy of the data events normalised to the center-of-mass energy is shown as a function of the longitudinal momentum, which is normalised to the visible energy. The missing ISR photon events are clearly seen on the right side. The bulk of events at lower visible energies is due to two-photon collisions. The plot on the right side shows the maximum energy of the electrons or photons. A clear peak near 70 GeV comes from the ISR photons in the radiative return to the Z events. The cut position is from the final cut-based selection.*

stands for another background events. They have very small missing momentum, unless one of the final state leptons escapes down the beam pipe. Because of the leptons, they can be easily recognised. The final background process comes from the semi-leptonic decay channel $W^+W^- \to q\bar{q}l\nu$, where l stands for e, μ or τ. The characteristics of these events are a large missing momentum coming from the undetected neutrino and a high energy lepton. These events are not problematic except in the case of hadronic τ decays. But the background contamination from these events is very small with ≈ 0.6 %, see Table 5.3.

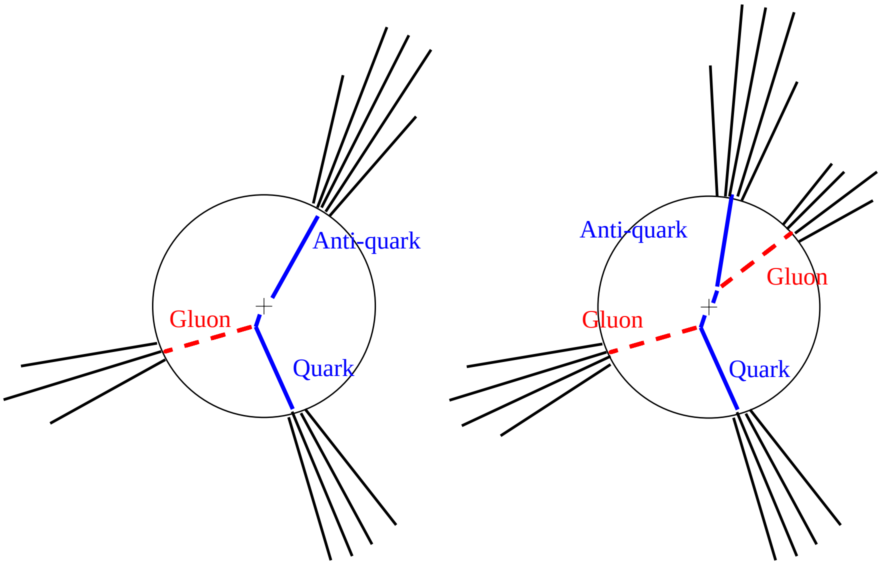

Abbildung 5.4: *Schematic illustration of the three-jet and four-jet formation in the process* $e^+e^- \to Z/\gamma^* \to q\bar{q}(\gamma)$, *where one or two gluons are radiated from the quark and the antiquark.*

5.3 Hadronic W^+W^- Event Selection

Having established the features of W decays into hadrons and outlined the characteristics that distinguish the signal events from the background events, the event selection is described in this section.

The selection of signal WW events from the collected events consists of three steps, 1. preselection, 2. preselection and final selection. The purpose of the 1. preselection is to remove non-physics, i.e., machine related background. The aim of the 2. preselection is to reject the physics background events while keeping the efficiency for the signal hadronic WW events around $\sim 98\%$. In the final selection, an optimization method is applied to extract the WW signal with high efficiency and high purity.

1. Preselection

The important step in the selection is to find variables with high discriminant power. The variables of the 1. preselection are:

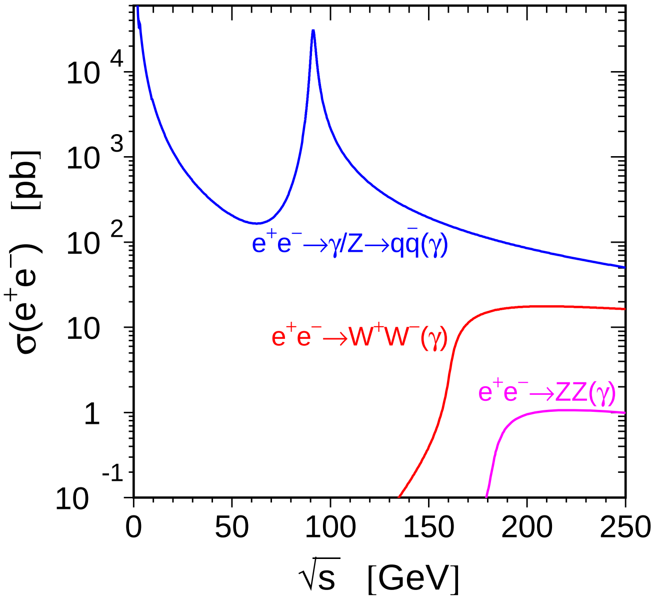

Abbildung 5.5: *Cross sections of* $q\bar{q}(\gamma), W^+W^-(\gamma)$ *and* $ZZ(\gamma)$ *production in* e^+e^- *interactions as a function of the center-of-mass energy* $\sqrt{s}$*. The* (γ) *denotes the possible presence of radiative photons.*

1. visible energy (E_{vis})
2. parallel energy imbalance $(E_{||})$ normalised to the total visible energy
3. the energy of the highest-energy electromagnetic cluster reconstructed in the BGO $(E^{max}_{e.\gamma})$
4. the number of calorimetric clusters $(N_{cluster})$
5. the perpendicular energy imbalance $(E_{\perp})$ normalised to the total visible energy

A lower cut on the total visible energy removes two-photon events and beam-gas interactions. The requirement of the total longitudinal energy $(E_{||}/E_{vis})$ to be small rejects events with a real Z and large undetected initial state radiation. The $q\bar{q}$ events with a visible ISR photon can be recognized by the energy of the highest-energy electromagnetic cluster reconstructed in the BGO $(E^{max}_{e.\gamma})$ and are rejected. The distributions of these quantities were already shown in Figure 5.3.

The quantity number of calorimetric clusters is used to reject low multiplicity events like $W^+W^- \rightarrow l\nu l\nu$, $Z/\gamma^* \rightarrow ll$. The quantity $E_\perp$ will record the presence of energetic neutrinos in the event, We are interested only in the four-jet hadronic events, so we can reject these and other neutrino events with this variable. The cuts on these quantities for the preselection of purely hadronic WW events are:

1. $E_{vis} \geq 120\ GeV$
2. $E_{||}/E_{vis} \leq 0.25$
3. $E^{max}_{\mathrm{e},\gamma} \leq 60\ GeV$
4. $N_{cluster} \geq 30$
5. $E_\perp/E_{vis} \leq 0.25$

At this level of the preselection, 5365 events out of more than 8 million are selected in the data while 5259 events are expected from the SM processes. The 1. preselection has a signal efficiency (ϵ) of 99% on CC03 events and a purity (π) of 25%, where the purity is defined as the fraction of signal events within the total expected events derived from the MC information. The fully leptonic and semileptonic WW events are considered here as background. From the background processes, more than 97% of the two photon, Zee and fully leptonic WW events are rejected. About 80% of the $Z/\gamma^* \rightarrow q\bar{q}(\gamma)$ events are removed. Table 5.1 summarizes the results of the preselection.

Jet Reconstruction

If the events have passed the pre-selection, jets can be reconstructed. In this thesis the **DURHAM**[76] jet clustering algorithm based on the calorimetric clusters (ASRCs) with energy greater than 100 MeV has been used, where the energy of the clusters were calibrated using the G-factors[1][77]. The structure of the jet reconstruction is basically the same for many existing algorithms: For

---

[1] To estimate the energy of an event from raw energy, an energy calibration is performed. For the calibration, the L3 detector is divided into 12 broad regions. The energy of a particle can be deposited in more than one such region and the total energy can be expressed as a linear sum of the weighted energy deposits ($\Sigma G_i \cdot E_i$) in the calorimeter. The weighting factors for the regions are calibrated and called G-factors.

SM process	Cross section [pb]	Generated events	1. Pre-selection	Efficiency(%)	N_{exp}
W$^+$W$^-$ $\rightarrow q\bar{q}q\bar{q}$	7.54	134041	132453	98.8	1315
W$^+$W$^-$ $\rightarrow q\bar{q}l\nu$	7.26	129123	17922	13.9	178
W$^+$W$^-$ $\rightarrow l\nu l\nu$	1.75	31336	0	0.0	0
$Z/\gamma \rightarrow q\bar{q}$	98.43	846857	163649	20.5	3557
$ZZ \rightarrow$ all	0.97	196000	103893	53.0	91
Zee	3.35	29500	947	3.2	19
e$^+$e$^-$$q\bar{q}$	15579.06	5940000	215	0.4×10^{-2}	100
Predicted events					5259
Observed events					5365

Tabelle 5.1: *Standard Model processes, cross sections, number of generated events, number of events surviving the preselection, preselection efficiencies and number of surviving events normalized to the data luminosity.*

each pair of jets i and j, where initially each ASRC is a jet, a quantity y_{ij} is calculated. The pair of jets with the smallest y_{ij} is combined into a new jet and all y_{ij} values are recalculated. Here this procedure is repeated iteratively until exactly four jets remain, corresponding to the four quarks. The quantity y_{ij} for the **DURHAM** definition is based on the relative transverse momentum :

$$y_{ij} \;=\; k^2_{\perp ij} \;=\; 2min(E_i^2, E_j^2)(1 - \cos\theta_{ij})/E^2_{vis} \tag{5.1}$$

where another popular jet definition, **JADE**[78], is essentially the invariant mass squared:

$$y_{ij} \;=\; M^2_{ij} \;=\; 2E_iE_j(1 - \cos\theta_{ij})/E^2_{vis} \tag{5.2}$$

It has been determined that the invariant mass squared definition of **JADE** is not the most relevant for the evolution of QCD jets[79]. While the **JADE** algorithm tends to cluster soft particles together even if they are not geometrically close in space, the y_{ij} of the Durham algorithm corresponds to a more geometrical scale. In addition, the **DURHAM** scheme yields a slightly superior W mass resolution[80].

2. Preselection

After the 1. preselection, there is still a lot of physics background in the selected sample ($\pi \approx 25\%$). Therefore additional quantities are used to separate the 4-jet signal events from the background processes and to increase the purity of the selected sample. To keep a high signal efficiency, the cuts on the additional quantities are loose. In the final selection, the same variables will be used again using tighter cuts. The new selection variables are based on the distinguishing characteristics mentioned above.

6. **sphericity**

   - This variable is known from the time that the first two-jet events were observable. Since the jets could not be discerned by simply looking at the pattern of outgoing tracks, one defined the jet axis. The axis was taken in the direction such that the sum of the squares of the momenta transverse to the axis was a minimum. For each event, such an axis could be found. Each event was assigned a value of sphericity defined as

     $$S = \frac{3\Sigma_i \mathbf{p}_{\perp i}^2}{2\Sigma_i \mathbf{p}_i^2} \tag{5.3}$$

     where $\mathbf{p}_{\perp i}$ is the momentum of the ith particle perpendicular to the sphericity axis. A completely two-jetlike event with outgoing particles aligned precisely with the axis would have $S = 0$. A four-jet event wouldn't be aligned and have $S > 0$. Figure 5.6 shows the distribution of the sphericity variable after applying all the other preselection criteria (N-1 preselection plot[2]).

7. **thrust**

   - The thrust is an alternative variable to sphericity that characterizes two-jet events and is defined as

     $$T = max(\frac{\Sigma_i |\mathbf{p}_i \cdot \mathbf{n}_T|}{\Sigma_i |\mathbf{p}_i|}) \tag{5.4}$$

---

[2] The preselection criteria in this context mean all the variables used in the 1. and 2. preselection.

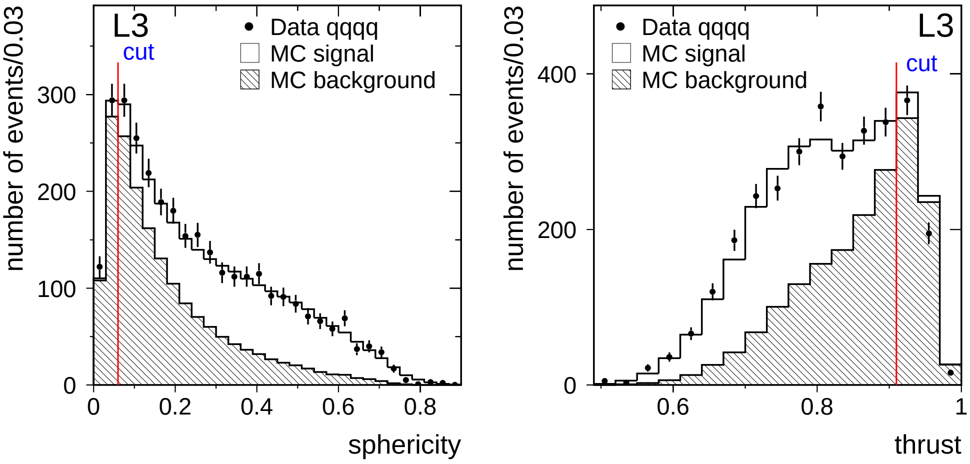

Abbildung 5.6: *Distributions of sphericity and thrust are shown after applying all the other preselection criteria. The cut positions are from the final cut-based selection.*

where $\mathbf{n}_T$ with $|\mathbf{n}_T| = 1$ is the thrust axis. Events with two, well-defined, back-to-back jets have thrust near 1. Spherical events have thrust near 0.5. Figure 5.6 shows the N-1 preselection distribution of the thrust variable.

8. **sum of the cosines between jets (SUMCOS)**

   – SUMCOS is the sum of the cosines of the 6 angles between four jets. To determine the effect of this variable, calculate the value of SUMCOS for the three different event types shown in Figure 5.7. The first type stands for a typical hadronic WW event. Assuming $\Theta_{12} = \Theta_{23} = \Theta_{34} = \Theta_{41} \approx 90^\circ$, SUMCOS has the value -2. The second type stands for a $q\bar{q}$ two-jet event with $\Theta_{23} = \Theta_{41} \approx 180^\circ$ and has SUMCOS $\approx$ -2 too. The third type stands for a three jet event, where one jet is split into two jets. It could also stand for a four jet event like $q\bar{q}gg$, where the fourth jet is coming from a soft gluon building a very small angle to the quark jet. In this case SUMCOS will be around zero. As you can see in Figure 5.8, sumcos is a powerful variable to reject three-jet-like events.

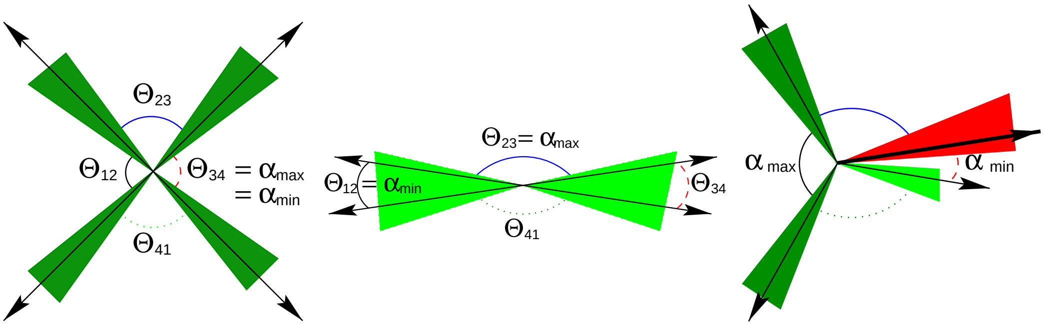

Abbildung 5.7: *possible jet reconstructions for different types of events. Some possible angles between four jets are shown.*

9. **energy angle relation of the jets (EANG)**

   – EANG is a combination of the maximal jet energy (E_{max}), minimal jet energy (E_{min}) and the minimal angle between jets (α_{min}):

   $$EANG = \frac{E_{min}}{E_{max}} \cdot \alpha_{min} \tag{5.5}$$

   Here the same exercise as in SUMCOS can be done. A typical hadronic WW event is well separated having nearly the same jet energy. A back-to-back two-jet event may have nearly the same jet energy, but the value α_{min} will be much less than in the case of a hadronic WW event. EANG will be near zero. In the case of $q\bar{q}g$ and $q\bar{q}gg$ events, beside a small value of α_{min} the difference between the maximal and minimal jet energies is large. This results in a very small value of EANG. EANG is a good variable to reject all kind of hadronic Z/γ^* decay events. Figure 5.8 shows the N-1 preselection distribution of the variable **sum of the cosines between jets** and **energy angle relation of the jets**.

The cuts on the 2. preselection variables are:

6. sphericity ≥ 0.03

7. thrust ≤ 0.95

8. sum of the cosines between jets ≤ -0.5

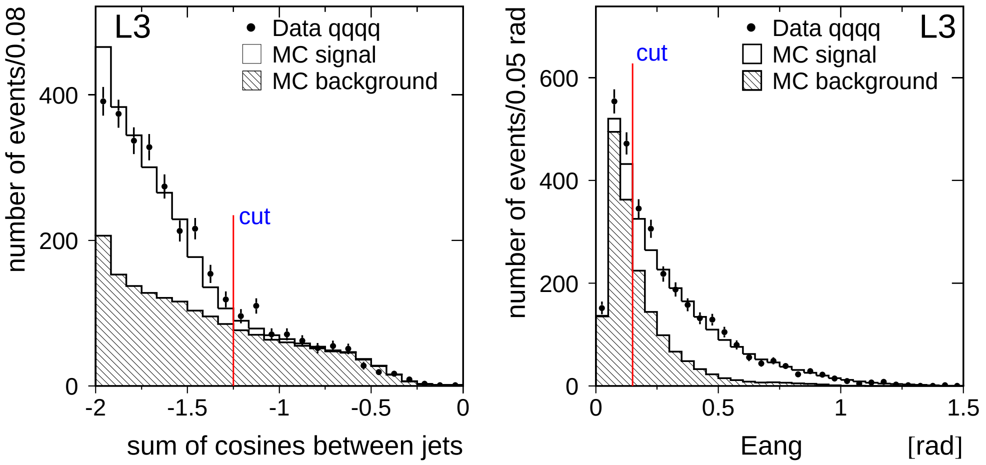

Abbildung 5.8: *The distributions of the sum of cosines of the jet-jet angles and EANG described in the text is shown after applying all the other preselection criteria. The cut positions are from the final cut-based selection.*

9. energy angle relation of the jets ≥ 0.05

After the 2. preselection, 3002 data events survive. The efficiency for the signal is 98%, and the purity after the preselection is 44%. From the background processes, the two photon, Zee and fully leptonic WW events are entirely removed. About 90% of the $Z/\gamma^* \rightarrow q\bar{q}(\gamma)$ events are removed. Table 5.2 summarizes the results of the 2. preselection.

Additional Selection Variables With High Discriminant Power

Beside the new variables mentioned in the 2. preselection, there are two additional quantities used in the final selection. The first variable is the two-jet mass.

- **two-jet mass** (m_{jj})
  - To construct the two-jet mass variable, the events are forced to be two-jet events at the reconstruction level. The quantity m_{jj} is the sum of these two masses. The distribution of this quantities is shown

SM process	Generated events	1. Preselection	2. Preselection	Efficiency(%)	N_{exp}
$W^+W^- \to q\bar{q}q\bar{q}$	134041	132453	131180	97.9	1302
$W^+W^- \to q\bar{q}l\nu$	129123	17922	13720	10.6	136
$W^+W^- \to l\nu l\nu$	31336	0	0	0.0	0
$Z/\gamma \to q\bar{q}$	846857	163649	66362	8.3	1442
$ZZ \to$ all	196000	103893	98956	50.1	87
Zee	29500	947	0	0	0
$e^+e^-q\bar{q}$	5940000	215	0	0	0
Predicted events					2967
Observed events					3002

Tabelle 5.2: *Standard Model processes, cross sections, number of generated events, number of events surviving the preselection, preselection efficiencies and number of surviving events normalized to the data luminosity.*

in Figure 5.9. Since the background events are well separated from the signal events, this variable has a high discriminant power.

Some of the variables presented above are constructed to reject the two-jet events of the process $Z/\gamma^* \to q\bar{q}$, i.e. sphericity, thrust and two-jet mass. But there are many $q\bar{q}g$ and $q\bar{q}gg$ events as well. For these events to be rejected , the variables SUMCOS and EANG are used. Another variable constructed for this purpose is the minimum cluster multiplicity of the jets.

- **minimum cluster multiplicity of the jets (N_{cl}^{min})**
  - Assume we have a $q\bar{q}g$ event. Since the event is forced into four jets, one of the three real jets must be split into two jets. So the fourth jet may consist of only half the number of the clusters of a real jet or even less, which will be visible in the number of the clusters in the jet. If a quark of a $q\bar{q}g$ event radiates a photon (FSR), this photon may result in a fourth jet. The fragmentation of a soft gluon in a $q\bar{q}gg$ event could end in a small number of hadrons. All these events can be seen looking at the minimum number of clusters in the jets (N_{cl}^{min}). In the case of a photon as a fourth jet, N_{cl}^{min} is 1. The Figure

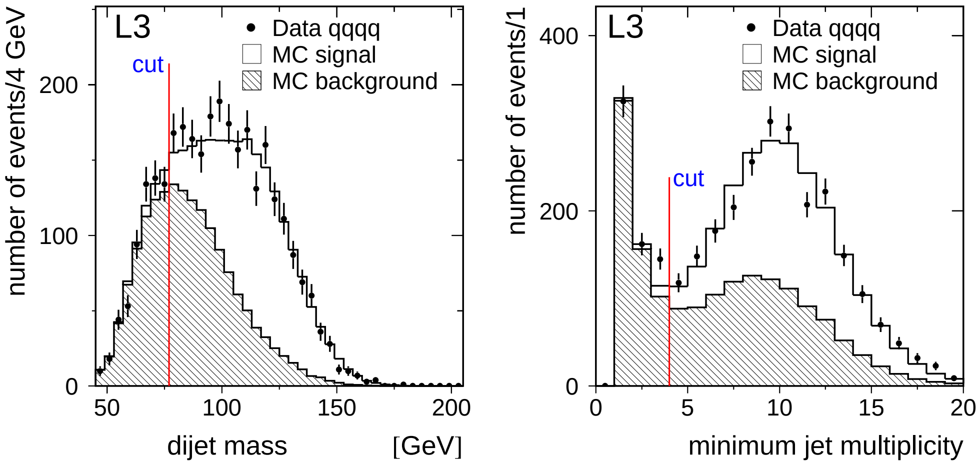

Abbildung 5.9: *Distributions of two-jet mass and the minimum cluster multiplicity of jets based on the Durham clustering is shown after the preselection level. The cut positions are from the final cut-based selection.*

5.9 shows that there are still a lot of background events after the 2. preselection, where the fourth jet is a photon.

5.3.1 Optimization of the Selection

There are two different methods used to optimize the selection.

- a cut-based analysis
- a multi-variable analysis

In a cut-based selection, cuts are applied on a set of variables, which have separating power between signal and background. This method is not an ideal one. Every time a cut is applied on a new variable, some fraction of the signal events are also rejected. Sometimes an event is rejected, because it doesn't pass a cut, even though it fulfills all the other criteria. Thus a multi-variable analysis has the advantage that it doesn't need many cuts. There are many ways of constructing a multi-variable method including the Fisher discriminant [81], a neural network [82] or a maximum-likelihood [83]. Common to all these methods is their construction of a final variable based on the information of several input variables, which could be used in the cut-based selection. The final variable should have a good separation between signal and background. The selection is done applying a cut on just this variable. This yields high performance and is normally better than using a cut-based selection. On the other hand such a multi-variable method uses highly complicated techniques and is not very transparent. A popular example is the use of a neural network.

The cut-based method is transparent as one can directly see what happens. It also gives direct access to the possible systematic sources as one can compare the data and Monte Carlo distributions step by step. The set of cuts applied is found empirically by looking at the variables using the Monte Carlo signal and background events. Thus the empirical choice of the selection cuts are not the optimal cuts. In this thesis an optimization of a cut-based selection is studied. To assure the optimization and compare the performance with a multi-variable method, a new multi-variable method is also introduced.

Cut-based Selection

The most important step in the optimization is to find the optimization criteria. The optimum performance defined in this thesis is the set of cuts that minimizes the statistical error on the cross section measurement. The expected statistical error is minimized if the product of the signal efficiency ϵ and the purity π is maximized (see Appendix A):

$$\Delta\sigma_{sig} = (\frac{\sigma_{sig}}{\epsilon \cdot \pi \cdot \mathcal{L}})^{1/2}, \tag{5.6}$$

where $\Delta\sigma_{sig}$ is the expected statistical error of the cross section and $\mathcal{L}$ stands for the data luminosity. To achieve the optimal set of cuts, the cuts on the selection variables are varied one after the other (sequential optimization). For example:

1. arbitrary choice of the selection cuts for all the variables (initial cuts)
2. Take the 1. selection variable and vary the cut position to find the maximum value of the product $\epsilon \times \pi$ while keeping the other variables at their initial cut values. If the optimal position is found, replace the initial cut value of the 1. variable with the new cut value
3. Take the next variable and do the same as for the 1. variable.

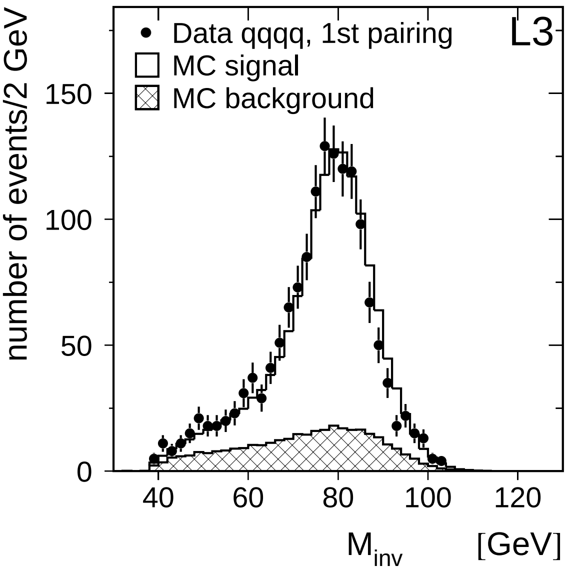

Abbildung 5.10: *Invariant mass distribution of the selected events*

4. If the optimization is done for all the variables, the 1. iteration is done. The new iteration begins with the 2. step.

After some iterations (typically 4-5 iterations), there is no further improvement and the optimal set of cuts are found. To be sure that this set of cuts does not correspond to a local minimum in $\Delta\sigma_{sig}$, the cuts can be tested using other initial cuts (1. step in the example). For the cut-based optimization, all the selection variables including the variables of the 1. preselection are used. The optimized cut values of the 1. preselection variables are:

1. $E_{vis} \geq 130\ GeV$
2. $E_{||}/E_{vis} \leq 0.25$
3. $E^{max}_{\mathrm{e},\gamma} \leq 53\ GeV$
4. $N_{cluster} \geq 30$
5. $E_{\perp}/E_{vis} \leq 0.23$

The optimized cut values for the other variables are:

6. $sphericity \geq 0.06$
7. $thrust \leq 0.91$
8. $sum\ of\ the\ cosines\ between\ jets \leq -1.25$
9. $energy\ angle\ relation\ of\ the\ jets \geq 0.12\ rad$
10. $two-jet\ mass \geq 77\ GeV$
11. $minimum\ cluster\ multiplicity\ of\ the\ jets \geq 4$

Figure 5.10 shows the distribution of the invariant mass after the optimization. One can clearly see the enhancement of the W events around 80 GeV. The efficiency obtained after the optimization is 87.4% with a purity of 78.1%. A detailed result of the selection is listed in Table 5.3. Note that the high performance of the optimization does not result only from the method but also from the right choice of selection variables.

Weighting Method

The motivation for a multi-variable selection is described above. A brief discussion of how the weighting method works follows.

Consider a variable x that has a different distribution for the signal and the background as shown in the left plot of the Figure 5.11. Instead of cutting on this distribution, we could give a weight to the events. The events on the right side, which would be accepted, are assigned a weight of one and the other events the weight of zero. If we sum the weights for all the variables and divide the sum by the number of variables, we will get a final distribution Ω as seen in Figure 5.11. This represents a very simple version of the weighting method.

A better version would be to give a weight *between* 0 and 1 instead of 0 and 1. For this we take reference histograms formed for the signal and background from the MC samples and calculate the bin weight values for each of the variables (see Figure 5.12). For each data event the weight in a given bin i of the variable x is:

$$w_i(sig) = \frac{N_i(sig)}{N_i(sig) + N_i(bg)}, \tag{5.7}$$

Sources	Accepted SM σ [pb]	Efficiency [%]	$N_{expected}$
$q\bar{q}e\nu$	0.69 x 10^{-2}	0.3	1.22
$q\bar{q}\mu\nu$	1.0 x 10^{-2}	0.4	1.81
$q\bar{q}\tau\nu$	3.46 x 10^{-2}	1.4	6.10
$Z/\gamma^* \rightarrow q\bar{q}$	1.47	1.5	259.76
$ZZ \rightarrow$ all	0.33	33.6	57.82
Zee	0.26 x 10^{-2}	0.1	0.46
e$^+$e$^-$$q\bar{q}$	0.0	0.0	0.00

Sources	Measured σ [pb]	Efficiency [%]	$N_{expected}$
$q\bar{q}q\bar{q}$	7.57 ± 0.25	87.4	1163.00

tot $N_{expected}$ = 1490.5	Efficiency = 87.4%
tot $N_{observed}$ = 1495.0	Purity = 78.1%

Tabelle 5.3: *Number of selected data events, $N_{observed}$, number of expected events from the MC study and accepted cross sections of the cut-based selection method. The selection efficiency for the signal process* e$^+$e$^-$ $\rightarrow$ W$^+$W$^-$ $\rightarrow q\bar{q}q\bar{q}(\gamma)$ *is at CC03 level.*

where $N_i(sig)$ is the number of signal events in the ith bin and $N_i(bg)$ is the number of background events in the ith bin of the variable x. This idea can be extended to more than one variable. In a multi-variable case the joint weight (Ω_{sig}) of an event is defined as:

$$\Omega_{sig} = \prod_{j}^{N} \omega^j(sig), \tag{5.8}$$

where $\omega^j(sig)$ is the weight of the event in the jth variable and N the number of variables. The separation of signal and background is much better, if the joint weight is normalised to

$$\Omega = \frac{\Omega_{sig}}{\Omega_{sig} + \Omega_{bg}}. \tag{5.9}$$

Ω_{bg} is the joint weight of an event to be background with

$$\Omega_{bg} = \prod_{j}^{N} \omega^j(bg), \tag{5.10}$$

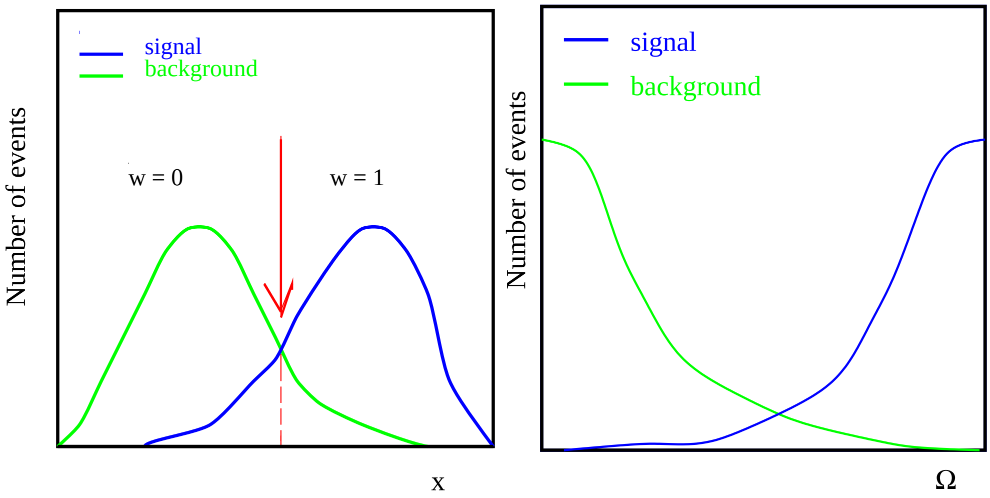

Abbildung 5.11: *The left distribution shows two separated classes of events. A weight of zero and one can be given to these events based on the cut position. On the right side, the expected final weight distribution for a simple multi-variable weighting method is illustrated.*

where $\omega^j(bg)$ is defined to be $N_{ij}(bg)/(N_{ij}(sig) + N_{ij}(bg))$, if the event lies in the ith bin for the variable j. Correspondingly, N_{ij} stands for the number of events in the ith bin for the variable j. For the selection of events, a cut is placed on the value of the joint weight as shown in Figure 5.13, which minimizes the expected statistical error.

The event weight procedure is done in three steps. First the 1. preselection and 2. preselection are applied to the events. In the second step, the same cuts as used in the cut-based selection are applied for the following variables E_{vis}, $E_{||}/E_{vis}$, $E^{max}_{\mathrm{e},\gamma}$, $N_{cluster}$, $E_{\perp}/E_{vis}$ and N^{min}_{cl}. In the last step the weights are calculated using the variables $sphericity$, $thrust$, m_{jj}, $SUMCOS$, $EANG$ and a new variable Y_{34}. Y_{34} can be considered as a parameter which measures how well the clusters of an event divide into four jets. Specifically, Y_{34} comes from the **DURHAM** jet algorithm and stands for the y_{ij} value at which the event moves from the 4- to the 3-jet category.

The use of event weights results in an improvement of efficiency on the order of 1% having the same purity as in a cut-based selection. The results are listed in Table 5.4.

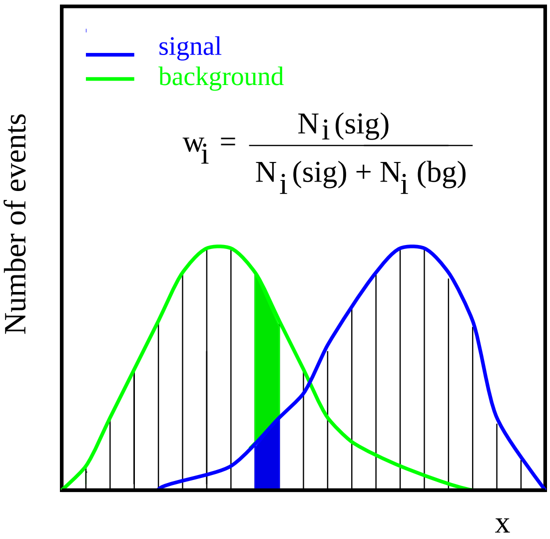

Abbildung 5.12: *This is an illustration of the binned weighting for a distribution.*

From the idea of the weighting method more improvement would have been expected than a mere 1%. But this indicates that the cut-based selection is already really optimized to the maximum possible performance. The weighting method developed here could be of more use in a search analysis or rare decay mode study, where the ratio of signal to background is much lower.

5.4 Cross Section Measurement for the Process WW $\to q\bar{q}q\bar{q}$

The observed number of selected hadronic WW events is used to measure the $W^+W^- \to q\bar{q}q\bar{q}$ production cross-section. The measured cross-section corresponds to that for $W^+W^- \to q\bar{q}q\bar{q}$ production through the three doubly resonant tree-level diagrams (**CC03**). Table 5.5 summarizes the event selections for two different center-of-mass energies. The efficiencies refer to CC03 W^+W^- events and are calculated using the **KORALW** Monte Carlo sample. The expected number of events are obtained from the signal and background MC.

The cross section measurements of $W^+W^- \to q\bar{q}q\bar{q}$ production using the selected numbers of events are listed for the two different center-of-mass energies:

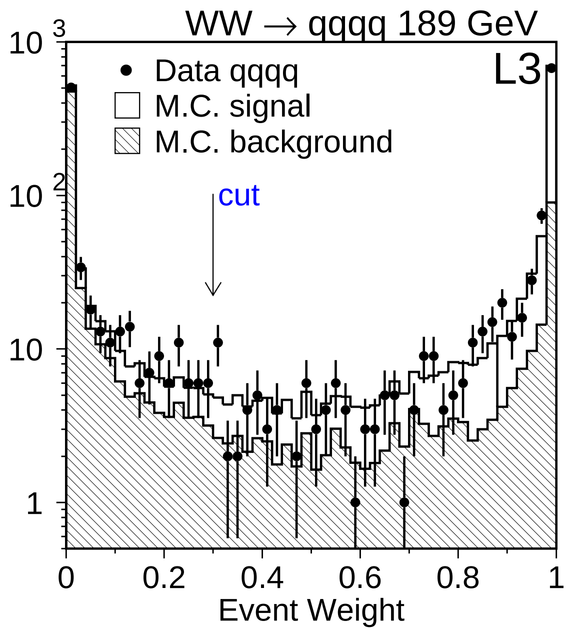

Abbildung 5.13: *Final weighting distribution for the data collected at* $\sqrt{s} = 189$ *GeV.*

$\sqrt{s}$ (GeV)	Cross Section ($W^+W^- \rightarrow q\bar{q}q\bar{q}$)
182.68	$\sigma(CC03) = 7.98 \pm 0.45 \pm 0.21$ pb
188.64	$\sigma(CC03) = 7.57 \pm 0.25 \pm 0.17$ pb

where the first error is statistical and the second systematic. As will be discussed below, the **KORALW** Monte Carlo sample is simulated with a Bose-Einstein model BE_0, which is not reliable. Thus the measured cross section values must be corrected:

$\sqrt{s}$ (GeV)	Cross Section ($W^+W^- \rightarrow q\bar{q}q\bar{q}$)
182.68	$\sigma(CC03) = 7.94 \pm 0.45 \pm 0.21$ pb
188.64	$\sigma(CC03) = 7.53 \pm 0.25 \pm 0.17$ pb

The systematic error is discussed in detail below.

Sources	Accepted SM σ [pb]	$N_{expected}$
$q\bar{q}e\nu$	0.98 x 10^{-2}	1.73
$q\bar{q}\mu\nu$	1.0 x 10^{-2}	1.77
$q\bar{q}\tau\nu$	4.16 x 10^{-2}	7.34
$Z/\gamma^{*} \rightarrow q\bar{q}$	1.29	228.02
$ZZ \rightarrow$ all	0.33	57.58
Zee	0.28 x 10^{-2}	0.50
$\mathrm{e}^{+}\mathrm{e}^{-}q\bar{q}$	0.0	0.00

Sources	Measured σ [pb]	Efficiency [%]	$N_{expected}$
$q\bar{q}q\bar{q}$	7.59 ± 0.25	86.6	1152.0

tot $N_{expected} = 1449.0$ tot $N_{observed} = 1457.0$	Efficiency = 86.6% Purity = 79.5%

Tabelle 5.4: *Number of selected data events, $N_{observed}$, number of expected events from MC study and accepted cross sections of the weighting method. The selection efficiency at CC03 level for signal process* $\mathrm{e}^{+}\mathrm{e}^{-} \rightarrow \mathrm{W}^{+}\mathrm{W}^{-} \rightarrow q\bar{q}q\bar{q}(\gamma)$ *as well as the purity are shown. The numbers are quoted for a final weight-output of greater than 0.3*

5.4.1 Systematic Errors

Any measurement is affected by a certain degree of uncertainty. The first source of uncertainty lies in the statistical error. A number of observed events always fluctuates and becomes the source of uncertainty. The other source of uncertainty comes from systematic errors.

There is no theory or model which treats systematic errors consistently. This makes the handling of systematic errors somewhat arbitrary and every physicist is aware of this. The best means of obtaining objectivity is to provide a complete list of probable factors that may contribute to the overall uncertainty and to explain exactly how the uncertainties are calculated. There are many sources of systematic error:

- Selection systematics
- MC statistics signal

$e^+e^- \rightarrow W^+W^- \rightarrow q\bar{q}q\bar{q}$					
$\sqrt{s}$ (GeV)	$\mathcal{L}(pb^{-1})$	Efficiency[%]	Purity[%]	Expected in SM	Observed
182.7	55.3	85.2	79.7	419	462
188.6	176.4	87.4	78.1	1491	1495

Tabelle 5.5: *Observed numbers of candidate events from* $W^+W^- \rightarrow q\bar{q}q\bar{q}$ *decay in each center-of-mass energy. The efficiencies refer to CC03* $W^+W^- \rightarrow q\bar{q}q\bar{q}$ *events. The W mass,* M_W*, used in MC is 80.50 GeV.*

- MC statistics background
- Background systematics
- Data/MC corrections
- ISR
- M_W and Γ_W dependence
- Hadronisation
- Colour Reconnection
- Bose-Einstein effects

Selection Systematics

Assume there is a discrepancy between the data and Monte Carlo distributions in a selection variable. If the discrepancy occurs near the cut position of the variable, the measured cross section will change with respect to variations in the actual value of a selection cut and indicate the presence of systematic errors. This systematic error can be estimated by a relative change in the cross section. The mathematical procedure to quantify this is as follows: First, a cut is varied from the standard cut position and the cross sections are measured for each of the different cut positions:

$$\sigma_i = \frac{N_i}{\epsilon_i \cdot \mathcal{L}}, \qquad (5.11)$$

where N_i is the number of selected data events after background corrections ($N_i = N_i^{obs} - N_i^{bkg}$), and ϵ_i the efficiency. The subscript $i = 1, 2, ..$ denotes a different cut setting and $i = 0$ denotes the standard settings of the cut. The relative change in cross section is given as:

$$\frac{\Delta\sigma_i}{\sigma_0} \pm \delta(\frac{\Delta\sigma_i}{\sigma_0}) \equiv \frac{\sigma_i - \sigma_0}{\sigma_0} \pm \delta(\frac{\sigma_i}{\sigma_0}), \tag{5.12}$$

which should be zero within its error δ. It can be assumed that the Monte Carlo statistical error due to ϵ_i is negligible compared to the statistical error in the number N_i of selected data events, because the number of Monte Carlo events is large compared to N_i. The absolute error in the relative change of cross section can be computed using binomial statistics:

$$\delta(\frac{\Delta\sigma_i}{\sigma_0}) = \delta(\frac{\sigma_i}{\sigma_0}) \equiv \sqrt{\frac{|N_0 - N_i|}{N_0 N_i}}. \tag{5.13}$$

If the relative change in the cross section deviates significantly from zero, a systematic difference between data and Monte Carlo is present.

The associated systematic error is derived from the deviation of the cross section when moving the cut position, assuming the deviation is bigger than the statistical error. Each cut position is varied in a reasonable range around its nominal value keeping all other cuts at their nominal position.

Given the variables chosen for the selection, two distributions are shown in Figure 5.14 which have the largest systematic errors: the minimum number of clusters in a jet and the energy angle relation of the jets. The upper plots show the distributions after applying all of the other selection criteria (called N-1 plot) while the lower plots show the change in cross section including its error when moving the cut position. The systematic error of these two selection cuts is estimated to be 0.5% and 0.8%. The systematic error for the other selection criteria is also estimated and listed in Table 5.6.

The selection criteria and their associated systematic error is shown in Table 5.6. The systematic error related to the event selection is determined to be 0.08 pb.

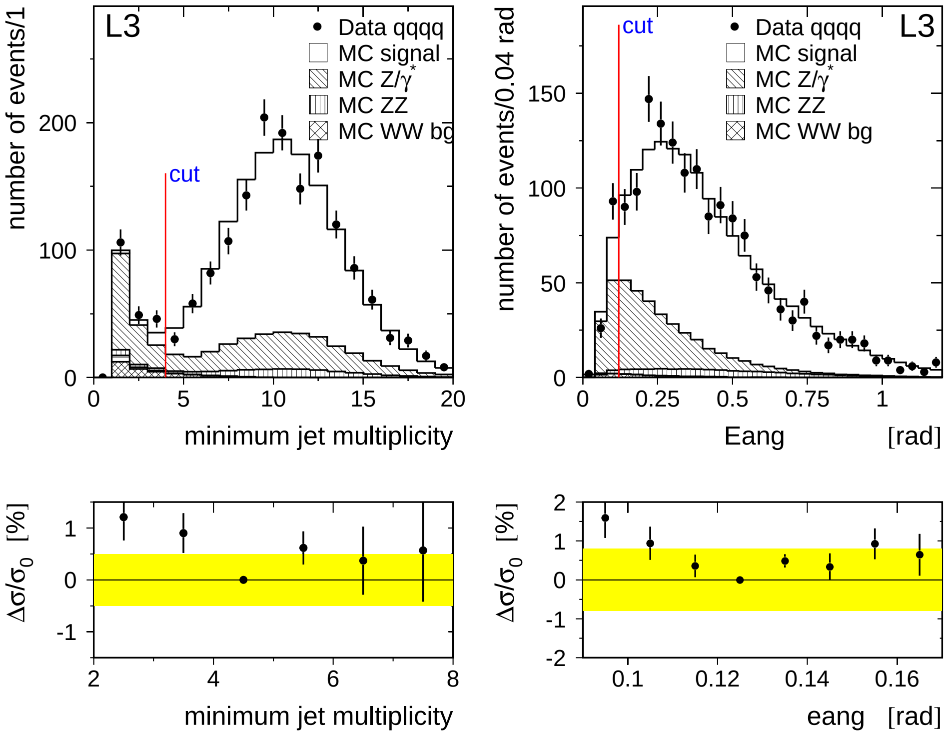

Abbildung 5.14: *The upper plots show the* **minimum cluster multiplicity of the jets** *and* **EANG** *distributions after applying all of the other selection criteria (called N-1 plot) while the lower plots show the change in cross section including its error when moving the cut position.*

Monte Carlo Statistics for the Signal

The value of the selection efficiency is one of the input parameters in the cross section measurement and the Monte Carlo events are used to calculate this value. Since there are only a limited amount of Monte Carlo events, the statistical error in the determination of this value translates directly into a systematic error. The 134041 **KORALW** MC events lead to a systematic error of 0.01 pb.

Monte Carlo Statistics for the Background

The quantity of background events is estimated using the Monte Carlo events and once again the error due to fluctuations must be taken into account. The systematic error dominated by the process $Z/\gamma^* \rightarrow q\bar{q}$ results in 0.02 pb

Selection Criterion			Variation of Cut from ... to	Error $\delta\sigma/\sigma$ [%]
E_{vis}	$\geq$	130 GeV	120 ... 140	0.1
$E_{\|\|}/E_{vis}$	$\leq$	0.25	0.15 ... 0.25	0.2
$E^{max}_{\mathrm{e},\gamma}$	$\leq$	53 GeV	37 ... 57	0.0
$N_{cluster}$	$\geq$	30	28 ... 38	0.4
E_{perp}/E_{vis}	$\leq$	0.23 GeV	0.15 ... 0.25	0.1
sphericity	$\geq$	0.06	0.0 ... 0.1	0.2
thrust	$\leq$	0.91	0.86 ... 0.95	0.0
dijetm	$\geq$	77	68 ... 86	0.3
minjmul	$\geq$	4	1 ... 8	0.5
sumcos	$\leq$	-1.25	-1.35 ... -1.15	0.2
eang	$\geq$	0.12	0.07 ... 0.17	0.8
Total			cut variation	1.1

Tabelle 5.6: *Contribution to the systematic error due to the event selection.*

Background Systematics

The statistical error from background contamination leads to the systematic error calculated above. But this error doesn't account for the effects of an incomplete simulation of the Monte Carlo events. An event generator may have implemented some decay channels with unprecise branching fractions. Since incompleteness may result in selection of the wrong cross section of the MC, the background MC distributions are varied in the normalisation corresponding to an increasing and decreasing cross section of the MCs. The main systematic source is the four-jet rate of $\mathrm{e}^+\mathrm{e}^- \to q\bar{q}(\gamma)$ events. To estimate the discrepancy between data and MC simulations, MC events must be reweighted as a function of Y_{34}. The reweighting function is derived from a comparison between data and MC simulation of hadronic Z decays collected at $\sqrt{s}$ =91 GeV. An increase of 4.8% four-jet rate w.r.t. the JETSET prediction is found [84]. Half of this increase (2.5%) is taken as the systematic error.

- 2.5% variation on $\sigma(\mathrm{Z}/\gamma^* \to q\bar{q}) \to$ 0.04 pb

The systematic error is determined to be 0.04 pb.

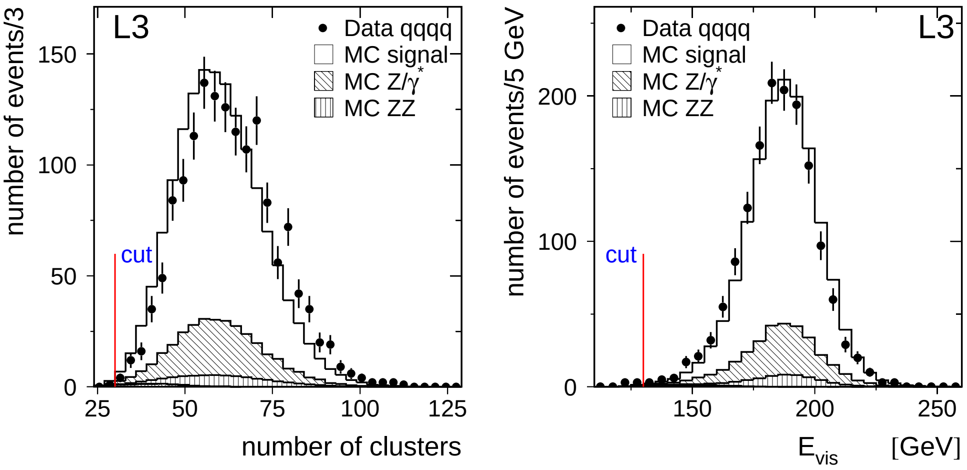

Abbildung 5.15: Variables (number of clusters and visible energy), where the data and Monte Carlo distributions do not agree very well. All selection cuts are applied.

Data/MC Corrections

The Monte Carlo simulation of the L3 detector does not perfectly reproduce the cluster multiplicity and the visible energy distribution shown in Figure 5.15. To estimate the systematic error arising from these discrepancies, a shift of 2.5 GeV energy on E_{vis} and a shift of a cluster on $N_{cluster}$ are performed on MC. Since the cuts on these two variables were loose because of the discrepancies, the resulting systematic error here is small. The total systematic error is estimated to be 0.01 pb.

Initial State Radiation

The **KORALW** event generator features QED initial state radiation up to the second order in the leading-log approximation. The effect of the missing terms on the cross section measurement is studied comparing **KORALW** and **EXCALIBUR** [21], which results in systematic error of 0.01 pb.

W mass and W width

The W pair production cross section is largely dependent on the mass of the W boson. This effect is maximal near the threshold of production. Because of

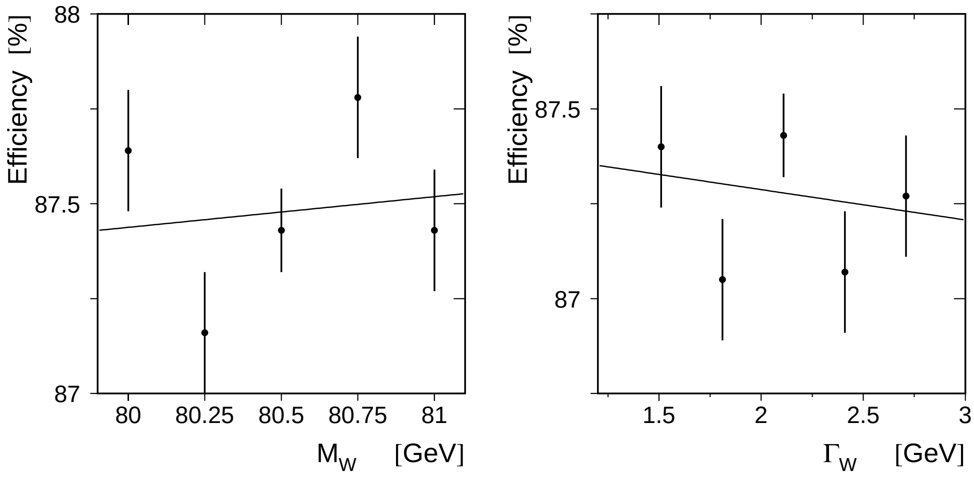

Abbildung 5.16: *The dependency of the signal efficiency on the W mass and width.*

this characteristic, the measured cross section can be directly translated into the mass of the W boson, which enables a determination of the W mass. Conversely, this means that the cross section measurement may depend on the W mass. The selection criteria are chosen in a way such that they don't use any mass or width information of the W boson. But even then there could be a slight dependency. To estimate the systematic error from these sources, MC samples with different W masses and W widths are simulated. The change in efficiency because of the use of different mass and width inputs is regarded as the systematic error. Within the variation[3] listed below, there is a very small change of efficiencies as shown in Figure 5.16. The systematic errors are negligible.

- W mass with a variation of ± 140 MeV → 0.03%

- W width with a variation of ± 60 MeV → 0.01%

---

[3] The mass and width of the W boson used for the estimation of the efficiency are 80.50 GeV and 2.11 GeV respectively. The differences between these values and the world average values [22] are taken as the variation ranges.

Jet Fragmentation and Hadronisation

As fragmentation cannot be calculated by perturbation theory, phenomenological models have to be used to generate Monte Carlo samples. **KORALW** uses the LUND string model (**JETSET**). The uncertainty associated with the LUND model is studied by comparing this model with a different fragmentation model, **HERWIG**. Two versions of **HERWIG** model are studied, one being **HERWIG**, which has implemented the tuning parameters used in ALEPH. **ALEPH-HERWIG** leads to differences of 0.06 pb. A larger difference of 0.21 pb is observed between **HERWIG** tuned in L3 and **JETSET**. Averaging these two numbers, an error of 0.14 pb is assigned as the jet fragmentation and hadronisation uncertainty.

Bose-Einstein Correlations

Bose-Einstein Correlations (BEC) are quantum mechanical effects of identical bosons. These correlations arise when the bosons are near to one another in phase space and lead to an enhancement of the number of identical bosons over that of non-identical bosons. Experimentally this effect was first observed for pions in $p\bar{p}$ collisions [85].

Since the hadronization regions of the W^+ and W^- overlap, it is natural to assume that some coherence effects are present between identical low-momentum bosons in hadronic W decays. Nonetheless, to what extent such effects would influence the cross section measurement and later the W mass measurement is difficult to determine. Theoretically this question is still not settled. However, if such correlations do exist, this could significantly bias the measurement of the W boson mass and possibly also the signal efficiency determination. Intuitively, since the BEC favours production of identical bosons close in phase-space, one would expect the softest particles from each W to be "dragged" closer to each other. This reduces the momentum of the W's and thus increases the measured W mass. The effect on the measured cross section is still not very clear. But since this effect changes the kinematics of the particles, the shape of some kinematic distributions may be distorted, resulting in a change of selection efficiency.

In principle, the evaluation of the systematic error is as follows: Generate a number of Monte Carlo events based on different models, such as

1 without BEC at all

2 BEC for pions belonging to the same W.

3 BEC for all pions in the event

Then compare the differences of the models in the selection efficiencies with the model initially used. In the case of BEC, more attention must be paid to the modelling of BEC in WW decays. Indeed, there is no theoretical solution of non-perturbative QCD and nobody knows how to implement BEC in WW decays. An algorithm used in **KORALW** to introduce BEC is LUBOEI (version BE_0) implemented in **JETSET**. This algorithm is based on the assumption that BE effects are local in phase space and lets the momenta of the bosons produced in the final-hadronisation be somewhat shifted. Additionally, the algorithm does not inherently conserve energy and momentum, and the restoring of this problem by a global rescaling of all final-state hadron momenta introduces an artificial negative shift on the measured W mass; this prescription of the momentum shift algorithm does not satisfy the quantum mechanical description of that phenomenon. It reproduces BEC only to a certain extent. As the authors of this model maintain this represents a thought-provoking worst case scenario. Therefore we should only consider it as a systematic check. There is another modification of LUBOEI code, version BE_{32}, which is used in the present thesis. The version BE_{32} agrees better with the experimental data. The versions BE_0 and BE_{32} differ in the rescaling procedures of momentum and energy after modification of the particle momenta.

The L3 experiment investigated Bose-Einstein correlations in W-pair production and the possible existence of these correlations between particles coming from different W's. No evidence for such an inter-W Bose-Einstein correlation is found [86]. The comparison of the models is shown in the Table 5.7.

The main uncertainty concerning BEC comes from the baseline Monte Carlo **KORALW**, which has a BE_0 version of BEC implemented. Since the Version BE_0 is not reliable as it results in a significant bias with respect to the W mass, the cross section value measured with the BE_0 version is corrected and a total systematic error due to BEC is quoted as 0.01 pb.

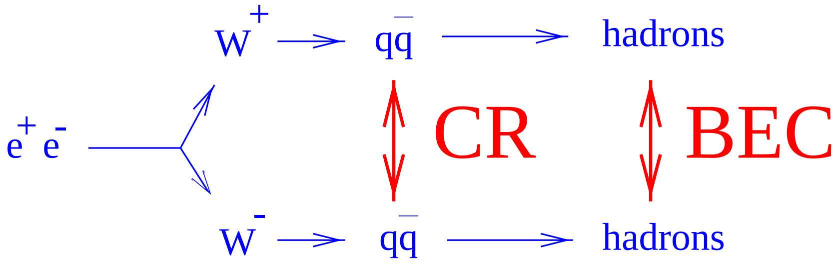

Abbildung 5.17: *Schematic view of colour recorrelations in W-pair production.*

MC generator	model comparison	systematic error [pb]
KORALW	BE_0 vs BE_{32}(same)	+0.04 ± 0.01
	BE_{32}(off) vs BE_{32}(same)	-0.01 ± 0.01
	BE_{32}(all) vs BE_0(same)	-0.01 ± 0.01
PYTHIA	BE off vs BE_{32}(same)	-0.01 ± 0.01
	BE_{32}(all) vs BE_{32}(same)	-0.01 ± 0.01

Tabelle 5.7: *The comparison of different Bose-Einstein models*

Colour Reconnection

In the reaction $e^+e^- \rightarrow W^+W^-$, two dijet systems $W^+ \rightarrow q_1\bar{q}_2$ and $W^- \rightarrow q_3\bar{q}_4$ are produced essentially on top of each other. Since these two initial colour-singlet systems evolve almost simultaneously, concern arises that the quarks and gluons from the two sources may cross-talk. This effect is called colour reconnection.

In a colour-reconnected event, the event topology is changed with respect to the original event. Therefore a change in the selection efficiency is expected. The MC programs PYTHIA and ARIADNE have been adapted to simulate the effects with various available models. The comparisons are shown in Table 5.8. The Monte Carlo models ARIADNE I and II used in this analysis are not tuned to describe Z pole data. To be realistic, half of the difference found in the models ARIADNE I and II is taken into account. Data comparisons disfavour

MC generator	model comparison	systematic error [pb]
PYTHIA	SK I	+0.02 ± 0.01
	SK II	+0.00 ± 0.01
	SK II'	+0.02 ± 0.01
ARIADNE	CR I	-0.01 ± 0.01
	CR II	+0.02 ± 0.01
	CR III	+0.06 ± 0.01

Tabelle 5.8: *Comparison of different models concerning the colour reconnection.*

the ARIADNE model CR III, leading to its exclusion. The largest error for models compatible with the data is the one from SK II'. This difference of 0.02 pb is assumed to be the systematic error due to colour reconnection.

Summary of Systematic Errors

The total systematic error is calculated as the quadratic sum of the individual contributions summarized in Table 5.9. The systematic uncertainty of the cross section measurement is mainly due to the selection and imperfect simulation of the fragmentation and hadronisation. A total systematic error of 0.17 pb on the measured cross section is obtained at the center-of-mass energy of 189 GeV.

5.4.2 Interpretation of the Results

In this thesis, the results from the cross-section for the doubly resonant production of W bosons in *hadronic decays* based on a data sample collected in 1997 and 1998 at the average center-of-mass energies of 183 GeV and 189 GeV are presented. The cross section corresponds to W pair production through the three doubly resonant tree-level diagrams involving s-channel γ and Z exchange and t-channel ν exchange (CC03 diagrams). The selection efficiency was defined only with respect to these diagrams. There are many additional diagrams which lead to the same four-fermion final states. For the hadronic final state, corrections which account for the interference between the CC03 diagrams and the additional diagrams are generally expected to be negligible at these energies.

Systematic Error of Cross Section Measurement		
Source	Systematic Error [pb]	
	$\sqrt{s} = 183\text{GeV}$	$\sqrt{s} = 189\text{GeV}$
Selection systematics	0.14	0.08
MC statistics signal	0.01	0.01
MC statistics background	0.02	0.02
Background systematics	0.08	0.04
ISR	0.01	0.01
W mass (±0.25 GeV)	0.02	0.00
W width (±0.50 GeV)	0.05	0.00
Hadronisation	0.11	0.14
Bose-Einstein effects	0.01	0.01
Colour Reconnection	0.03	0.02
Total	0.21	0.17

Tabelle 5.9: *Contributions to the systematic error in the cross section measurement. The total systematic error is the quadratic sum of the individual contributions*

Figure 5.18 shows the hadronic cross section results of the process $e^+e^- \rightarrow W^+W^- \rightarrow q\bar{q}q\bar{q}(\gamma)$ as a function of the center-of-mass energy,$\sqrt{s}$. The measurements at the average center-of-mass energies of 161 and 172 GeV are the results of published L3-analyses while the other two points at 183 and 189 GeV correspond to the results of this thesis. As one can clearly see, the results are in agreement with the predictions of the Standard Model. In other words, the measurements of the cross sections are already sensitive to large cancellations typical of the non-abelian gauge theory structure of the SM. The dotted curve in the figure shows the expectation if only t-channel neutrino exchange in W-pair production is considered, and the dashed curve is obtained by additionally including only the s-channel photon exchange diagram in the consideration as opposed to the Z exchange one. The existence of the triple gauge boson vertex of the SM is clearly presence in the data. A detailed study of the triple gauge boson couplings (TGC) is undertaken through another analysis [87] which looks at both the total W-pair- cross section and the angular production distributions, since they will be affected by an anomalous values of the gauge couplings. Ad-

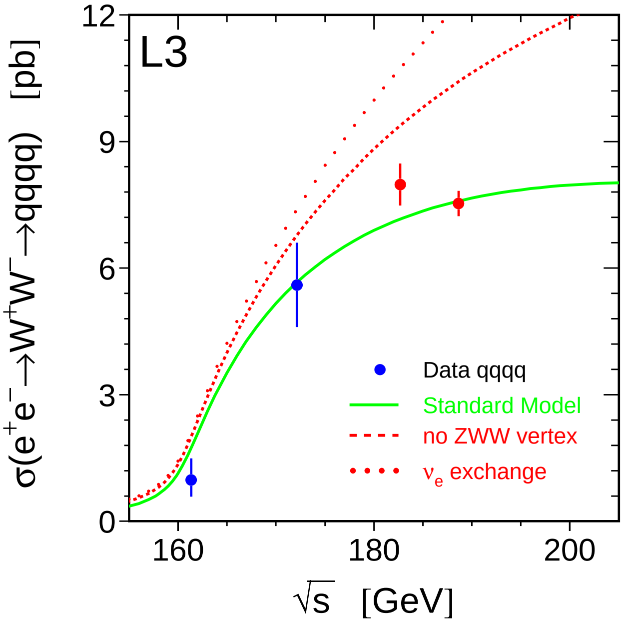

Abbildung 5.18: *The hadronic cross section of the process* $\mathrm{e^+e^-} \rightarrow \mathrm{W^+W^-} \rightarrow q\bar{q}q\bar{q}(\gamma)$ *as a function of the center-of-mass energy,*$\sqrt{s}$*. The published measurements at* $\sqrt{s}$ = 161 *GeV and* $\sqrt{s}$ = 172 *GeV, and the new measurement of this analysis at* $\sqrt{s}$ = 183 *GeV and* $\sqrt{s}$ = 189 *GeV are shown as points with error bars, combining statistical and systematic errors in quadrature. The solid curves show the SM expectation.*

ditionally, the relative contribution of each helicity state is modified, which in turn affects the angular distributions of the W decay products.

The cross section measurement at the center-of-mass energy of 183 GeV is with a value of 7.94 ± 0.50 pb about 1.5 standard deviations higher than the Standard Model expectation of 7.17 ± 0.14 pb (**GENTLE**). Several cross-checks have been performed and no systematic bias has been identified leading to the conclusion that the higher cross section is a statistical fluctuation. Other analyses[4] using a neural network [88] or my own event weighting methods yield

---

[4] There are a number of independent selections developed by different persons or teams which analyse the same data and which are essential for cross-checking

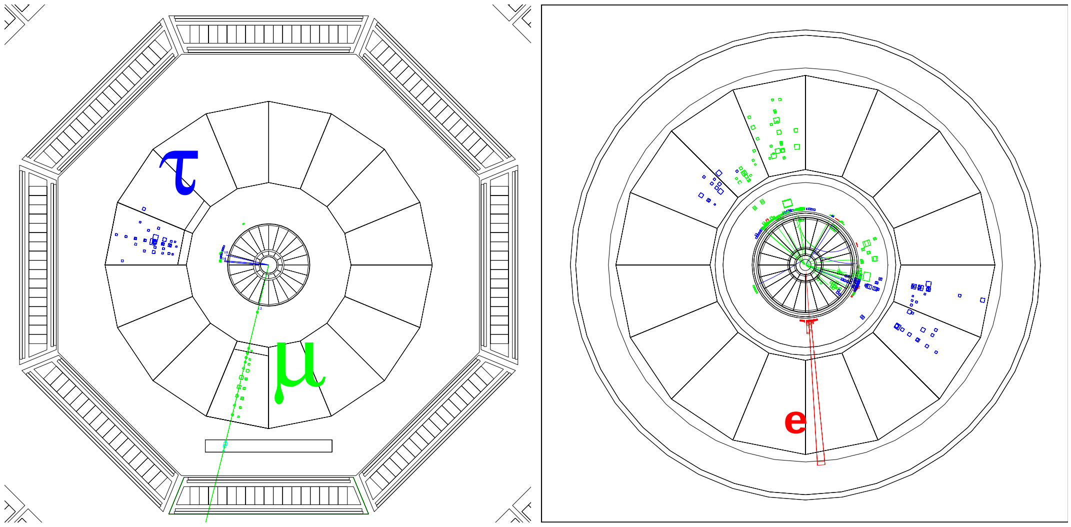

Abbildung 5.19: *Left:* $\mathrm{W}^{+}\mathrm{W}^{-} \rightarrow \tau\nu\mu\nu$ *event observed in the L3 detector. Right:* $\mathrm{W}^{+}\mathrm{W}^{-} \rightarrow q\bar{q}\mathrm{e}\nu$ *event observed in the L3 detector.*

consistent results. The results of this thesis are compared to the published L3 results [88, 84]:

$\sqrt{s}$ (GeV)	Cross Section ($\mathrm{W}^{+}\mathrm{W}^{-} \rightarrow q\bar{q}q\bar{q}$) [pb]	
	This Thesis	L3 Published
182.68	$7.94 \pm 0.45 \pm 0.21$	$8.35 \pm 0.46 \pm 0.23$
188.64	$7.53 \pm 0.25 \pm 0.17$	$7.36 \pm 0.24 \pm 0.18$

5.5 Selection of the other Final States

The events of the final states $\mathrm{e}^{+}\mathrm{e}^{-} \rightarrow \mathrm{W}^{+}\mathrm{W}^{-} \rightarrow q\bar{q}\mathrm{e}\nu$, $q\bar{q}\mu\nu$, $q\bar{q}\tau\nu$, $l\nu l\nu$ are selected by other analyses of L3 [88, 84]. These events are used for the determination of the total cross-section of the W-pair production and the W decay branching fractions. Further, these events are used for the measurement of the W mass later in this thesis. Thus, the selection is briefly outlined.

Leptonic events, $\mathrm{W}^{+}\mathrm{W}^{-} \rightarrow l\nu l\nu$ are characterized by

- two acoplanar, energetic leptons[5]

---

[5] However, one (both) of these leptons can be a τ, which typically decays to a narrow hadronic jet.

- large missing momentum due to neutrinos
- identification of e, μ and τ

They are mainly selected by requiring two acoplanar charged leptons. The main background arising from dilepton production, $e^+e^- \rightarrow l^+l^-(\gamma)$, is reject hereby. An example of selected event is shown in Figure 5.19. These final states can be produced from other neutral-current (NC) or charged-current (CC) Feynman diagrams. Thus, the signal efficiencies are determined with four-fermion (CC56+NC56) Monte Carlo samples and are quoted for the following phase-space cuts: $|\cos\theta| < 0.96$ for both charged leptons, where θ is the polar angle with respect to the beam axis, and energies greater than 15 GeV and 5 GeV for the higher and lower energy lepton, respectively. Table 5.10 and 5.11 list these efficiencies in the form of a 6-by-6 matrix. The overall efficiency in the full phase-space, based on a W-pair (CC03) Monte Carlo, is approximately 50% with a purity close to 90%.

The decay channel $W^+W^- \rightarrow q\bar{q}l\nu$ is characterised by

- two or more hadronic jets
- an isolated, energetic lepton or a narrow jet in the case of hadronic τ decays
- missing energy and momentum due to the undetected neutrino

The main background processes are $e^+e^- \rightarrow Z/\gamma$ and $e^+e^- \rightarrow Zee$. The typical efficiencies at CC03 level are 75-85% for the $q\bar{q}e\nu$ and $q\bar{q}\mu\nu$ channels, but only about 50% for the $q\bar{q}\tau\nu$ decays. The purity of the selected events is 90-95%. The signal efficiency for $q\bar{q}e\nu$ events is determined from a four-fermion (CC20) Monte Carlo sample within the following phase-space cuts: E_e, $E_\nu > 15$ GeV, where E_e and E_ν are the electron and neutrino energies; $|\cos\theta_e|$, $|\cos\theta_\nu| < 0.98$, where θ_e and θ_ν are the electron and neutrino polar angles; $M_{e\nu}$, $M_{q\bar{q}} > 45$ GeV, where $M_{e\nu}$ and $M_{q\bar{q}}$ are the electron-neutrino and quark-antiquark invariant masses. These values change due to the increasing center-of-mass energy. The selection efficiencies and the background contaminations are presented in Table 5.10 and 5.11. An example of selected event is shown in Figure 5.19.

$\sqrt{s} = 189$ GeV										
	Selection of Process $W^+W^- \rightarrow$									
	$e\nu e\nu$	$e\nu\mu\nu$	$e\nu\tau\nu$	$\mu\nu\mu\nu$	$\mu\nu\tau\nu$	$\tau\nu\tau\nu$	$q\bar{q}e\nu$	$q\bar{q}\mu\nu$	$q\bar{q}\tau\nu$	$q\bar{q}q\bar{q}$
Efficiencies [%] for										
$e\nu e\nu$	64.2	-	5.3	-	-	0.1				
$e\nu\mu\nu$	0.3	60.6	1.1	-	2.9	0.7				
$e\nu\tau\nu$	12.6	10.0	36.8	-	0.2	1.3				
$\mu\nu\mu\nu$	-	0.5	-	50.6	2.2	-				
$\mu\nu\tau\nu$	-	10.8	0.1	8.7	31.6	0.8				
$\tau\nu\tau\nu$	1.1	1.7	7.1	0.8	4.7	19.8				
$q\bar{q}e\nu$							81.5	0.2	5.3	0.3*
$q\bar{q}\mu\nu$							0.3	76.7	6.5	0.4*
$q\bar{q}\tau\nu$							1.7	3.6	50.6	1.4*
$q\bar{q}q\bar{q}$							-	-	0.3	88.0*
Observed events	49	43	38	24	26	10	363	340	329	1495
Background events	9.4	4.2	2.3	8.3	0.9	1.1	14.8	13.8	41.7	318.0
Conversion factor f	0.88	1.07	1.07	0.96	1.10	0.96	1.01	-	-	-

Tabelle 5.10: *Summary of results of the different event selections. Conversion factor f is the ratio of the CC03 cross section without cuts and the four fermion cross section within phase-space cuts calculated with* **EXCALIBUR**. *The values marked with a '*' are based on the* **KORALW** *with BE_{32} model.*

$\sqrt{s} = 183$ GeV										
	Selection of Process $W^+W^- \to$									
	eνeν	e$\nu\mu\nu$	e$\nu\tau\nu$	$\mu\nu\mu\nu$	$\mu\nu\tau\nu$	$\tau\nu\tau\nu$	$q\bar{q}$eν	$q\bar{q}\mu\nu$	$q\bar{q}\tau\nu$	$q\bar{q}q\bar{q}$
Efficiencies [%] for										
eνeν	62.1	-	8.0	-	-	0.2				
e$\nu\mu\nu$	0.1	56.5	1.4	-	4.1	0.2				
e$\nu\tau\nu$	11.0	9.0	37.6	-	0.5	3.6				
$\mu\nu\mu\nu$	-	0.1	-	45.6	2.7	-				
$\mu\nu\tau\nu$	-	9.1	0.3	6.8	33.2	1.2				
$\tau\nu\tau\nu$	1.9	1.1	9.3	0.5	7.7	22.0				
$q\bar{q}$eν							85.4	0.1	4.8	0.2*
$q\bar{q}\mu\nu$							0.2	77.0	6.0	0.2*
$q\bar{q}\tau\nu$							2.1	4.3	50.1	1.3*
$q\bar{q}q\bar{q}$							-	-	1.3	85.8*
Observed events	9	9	11	8	14	3	112	108	77	462
Background events	1.4	0.8	3.8	0.1	1.2	2.4	6.7	5.7	10.6	82.3
Conversion factor f	0.90	1.07	1.07	0.95	1.09	0.95	1.09	-	-	-

Tabelle 5.11: *Summary of results of the different event selections. Conversion factor f is the ratio of the CC03 cross section without cuts and the four fermion cross section within phase-space cuts calculated with* **EXCALIBUR**. *The values marked with a '*' are based on the* **KORALW** *with BE_{32} model.*

5.6 W Decay Branching Fractions and W-pair Cross Section

Based on the selected data of the fully hadronic channel of this thesis and all the other selected data of the final states $\mathrm{e^+e^-} \to \mathrm{W^+W^-} \to q\bar{q}\mathrm{e}\nu$, $q\bar{q}\mu\nu$, $q\bar{q}\tau\nu$, $l\nu_l l\nu_l$ as described in the previous section, the total CC03 production cross sections of W-pairs at the center-of-mass energies of 183 GeV and 189 GeV and W decay branching fractions can be determined simultaneously in one maximum likelihood fit. A joint analysis must be performed, since there are correlations between the semileptonic channels and between the purely leptonic channels (see the non-vanishing off-diagonal terms in the efficiency matrices of Table 5.10 and 5.11). The total likelihood is given by the product of Poisson probabilities $P(N_i, \mu_i)$ to observe N_i events when μ_i are expected:

$$\begin{aligned} L &= \prod_i P(N_i, \mu_i) \\ \mu_i &= (\sum_j \epsilon_{ij}\sigma_j) \cdot \mathcal{L}_i + N_i^{bg}, \end{aligned} \tag{5.14}$$

where ϵ_{ij} is the efficiency of the selection process i to select events of channel j, N_i^{bg} is the remaining background events arising from other processes, and $\mathcal{L}_i$ is the luminosity used in the analysis of process i. To get the fit parameters for the total W-pair cross sections $\sigma_{\mathrm{WW}}(183\ \mathrm{GeV})$, $\sigma_{\mathrm{WW}}(189\ \mathrm{GeV})$ and the W decay branching fractions, the channel cross sections must be replaced as follows:

$$\begin{aligned} \sigma^k_{l\nu l\nu} &= \frac{\sigma^k_{\mathrm{WW}}}{f^k_{l\nu l\nu}}\ Br(\mathrm{W} \to l\nu)]^2 \\ & \text{for identical lepton flavours with } l = \mathrm{e}, \mu, \tau \\ \sigma^k_{l\nu l'\nu'} &= \frac{\sigma^k_{\mathrm{WW}}}{f^k_{l\nu l'\nu'}}\ 2Br(\mathrm{W} \to l\nu)Br(\mathrm{W} \to l'\nu') \\ & \text{for different lepton flavours with } l = \mathrm{e}, \mu, \tau \\ \sigma^k_{\mathrm{e}\nu q\bar{q}} &= \frac{\sigma^k_{\mathrm{WW}}}{f^k_{\mathrm{e}\nu q\bar{q}}}\ 2Br(\mathrm{W} \to \mathrm{e}\nu)Br(\mathrm{W} \to q\bar{q}) \\ \sigma^k_{l\nu q\bar{q}} &= 2\sigma^k_{\mathrm{WW}}\ Br(\mathrm{W} \to l\nu)Br(\mathrm{W} \to q\bar{q}) \text{ with } l = \mu, \tau \\ \sigma^k_{q\bar{q}q\bar{q}} &= \sigma^k_{\mathrm{WW}}\ Br(\mathrm{W} \to q\bar{q})^2, \end{aligned} \tag{5.15}$$

where k stands for the center-of-mass energies, and f_i^k is a conversion factor for the channel i at the center-of-mass energy k. It is given by the ratio of the total CC03 cross section and the four-fermion cross section within phase-space cuts. For the $q\bar{q}\mathrm{e}\nu$ and the $l\nu l\nu$ final states the efficiencies are determined within phase-space cuts to reduce contributions from processes not mediated by W-pair production. The measured four-fermion cross sections are scaled by the conversion factors f_i^k, listed in Table 5.10 and 5.11, to obtain the CC03 cross sections.

Three different maximum likelihood fits have been performed. In the first case $\sigma_{\mathrm{WW}}(183\ \mathrm{GeV})$, $\sigma_{\mathrm{WW}}(189\ \mathrm{GeV})$ and leptonic branching fractions are determined without the assumption of charged-current lepton universality in W decays. Under the assumption that

$$Br(\mathrm{W}\to \mathrm{e}\nu) + Br(\mathrm{W}\to \mu\nu) + Br(\mathrm{W}\to \tau\nu) + Br(\mathrm{W}\to q\bar{q}) \;=\; 1 \qquad (5.16)$$

the fit results are

$$\begin{aligned}
Br(\mathrm{W}\to \mathrm{e}\nu) &= 10.60 \pm 0.46 \pm 0.16\ \% && (\mathrm{SM} = 10.83\%)\\
Br(\mathrm{W}\to \mu\nu) &= 9.96 \pm 0.46 \pm 0.15\ \% && (\mathrm{SM} = 10.83\%)\\
Br(\mathrm{W}\to \tau\nu) &= 11.23 \pm 0.63 \pm 0.22\ \% && (\mathrm{SM} = 10.82\%)\\
\sigma_{\mathrm{WW}}(183\ \mathrm{GeV}) &= 16.16 \pm 0.65 \pm 0.26\ \mathrm{pb} && (\mathrm{SM} = 15.72\ \mathrm{pb})\\
\sigma_{\mathrm{WW}}(189\ \mathrm{GeV}) &= 16.44 \pm 0.38 \pm 0.22\ \mathrm{pb} && (\mathrm{SM} = 16.24\ \mathrm{pb}) \qquad (5.17)
\end{aligned}$$

where the first uncertainty is statistical and the second systematic. The systematic error includes contributions from the uncertainties in the efficiency, background cross section and luminosity. The contributions to the systematic errors of the fully leptonic and semileptonic channels can be found in the other analyses of L3 [88, 84]. The correlations between the above measurements are less than 30%. The results are consistent with lepton universality and the Standard Model expectations.

In the second fit, the additional constraint of charged-current lepton universality[6],

$$Br(\mathrm{W}\to \mathrm{e}\nu) \;=\; Br(\mathrm{W}\to \mu\nu) \;=\; Br(\mathrm{W}\to \tau\nu) \;=\; (1 - Br(\mathrm{W}\to q\bar{q}))/3, \qquad (5.18)$$

---

[6] For the current level of experimental precision, the effect of $Br(\mathrm{W}\to\tau\nu)$ being $\approx 0.1\%$ lower than $Br(\mathrm{W}\to \mathrm{e}\nu)$ and $Br(\mathrm{W}\to\mu\nu)$ has been neglected.

is assumed, which is supported by our results. A fit to $Br(\mathrm{W} \rightarrow q\bar{q})$ and the two total cross sections as unknowns yields

$$
\begin{aligned}
Br(\mathrm{W} \rightarrow q\bar{q}) &= 68.36 \pm 0.69 \pm 0.33\,\% \qquad (\mathrm{SM} = 67.51\%) \\
\sigma_{\mathrm{WW}}(183\ \mathrm{GeV}) &= 16.10 \pm 0.66 \pm 0.26\ \mathrm{pb} \\
\sigma_{\mathrm{WW}}(189\ \mathrm{GeV}) &= 16.36 \pm 0.37 \pm 0.22\ \mathrm{pb} \qquad (5.19)
\end{aligned}
$$

The hadronic branching fraction obtained in this fit agrees with the published L3 value[84]:

$\sqrt{s}$ (GeV)	$Br(\mathrm{W} \rightarrow q\bar{q})$	
	This Thesis	L3 Published
183-189	$68.36 \pm 0.69 \pm 0.33$ %	
162-189		$68.20 \pm 0.68 \pm 0.33$ %

In the final fit, the W decay branching fractions of the SM are assumed and the total CC03 cross sections are measured. For comparison, the results of this fit are shown together with the published L3 values [88, 84]:

$\sqrt{s}$ (GeV)	Cross Section ($\mathrm{W}^+\mathrm{W}^- \rightarrow q\bar{q}q\bar{q}$) [pb]	
	This Thesis	L3 Published
182.68	$16.13 \pm 0.66 \pm 0.26$	$16.53 \pm 0.67 \pm 0.26$
188.64	$16.39 \pm 0.37 \pm 0.22$	$16.24 \pm 0.37 \pm 0.22$

The difference in the total cross sections is due to different selections of the hadronic channels.

Extraction of the matrix element $|V_{cs}|$

The study of hadronic decays of the W boson enables the investigation of the couplings strength of W Bosons to different flavours. The fraction of W bosons decaying into a pair of hadronic jets with different flavours is proportional to the sum of the squared magnitudes of the corresponding elements of the Cabibbo-Kobayashi-Maskawa (CKM) matrix. A measurement of the production rates of different flavours therefore gives access to the individual CKM matrix elements. In $\mathrm{e}^+\mathrm{e}^- \rightarrow \mathrm{W}^+\mathrm{W}^-$ events at LEP2, the extraction of the matrix element $|V_{cs}|$ might be possible with a direct measurement of the production fraction of charm in W decays.

Another way to extract the $|V_{cs}|$ is using the hadronic branching ratio. The idea is the following: According to the Standard Model, the hadronic branching ratio of the W boson depend on the six elements V_{ij} of the CKM quark mixing matrix. The W boson can't decay into the top quark because of the large mass, thus the V_{ij} do not involve the top quark. This can be expressed as

$$\frac{Br(\mathrm{W} \to q\bar{q})}{1 - Br(\mathrm{W} \to q\bar{q})} = (1+\frac{\alpha_s(M_\mathrm{W})}{\pi})(|V_{ud}|^2+|V_{cd}|^2+|V_{us}|^2+|V_{cs}|^2+|V_{ub}|^2+|V_{cb}|^2), \tag{5.20}$$

where $\alpha_s(M_\mathrm{W})$ is taken to be 0.1185 ± 0.0020. Higher-order corrections to this formula are below 1%. The branching fraction $Br(\mathrm{W} \to q\bar{q})$ obtained from the fit assuming lepton universality gives

$$V^2 = \sum_{i=u,c;j=d,s,b} |V_{ij}|^2 = 2.083 \pm 0.064 \pm 0.032. \tag{5.21}$$

Since V_{cs} is the least well known CKM matrix element, it is most useful to determine. The current world-average values and errors of the other matrix elements of V_{CKM}[22] give a squared sum of 1.05 ± 0.01. Using these results, the measured hadronic branching fraction is interpreted as

$$|V_{cs}| = 1.035 \pm 0.032 \pm 0.016, \tag{5.22}$$

where the statistical uncertainty includes the α_s error and the errors of the other V_{ij} elements. But the error is dominated by the statistical error of the W branching ratios. This result does not assume the unitarity of V_{CKM}, and it is consistent with the existing direct measurement from D meson decay, $|V_{cs}| = 1.04 \pm 0.16$ [22].

5.7 Preliminary Results at $\sqrt{s}$=192-202 GeV

In 1999 LEP increased its centre-of-mass energy from 192 GeV in the beginning of the data taking phase to 196 GeV, 200 GeV and 202 GeV. A total luminosity of 29.7 pb^{-1}, 83.7 pb^{-1}, 82.8 $pb^{-1}$and 37.0 pb^{-1}has been recorded at these center-of-mass energies with the L3 detector. The hadronic W-pair events are selected at these energies using the cut-based selection method used at $\sqrt{s}$= 189 GeV. The selection results are summarized in Table 5.12. Altogether 1943 hadronic WW-pair events are selected.

$\sqrt{s}$ (GeV)	$W^+W^- \rightarrow q\bar{q}q\bar{q}$			
	N_{data}	N_{bg}	ϵ [%]	purity [%]
191.60	233	54.8	87	78
195.54	676	148.4	87	79
199.54	735	144.7	85	79
201.75	299	67.5	85	79

Tabelle 5.12: *Number of selected L3 data events, N_{data}, number of expected non-W background events, N_{bg} at four different center-of-mass energies. The efficiency and the purity of the selected events are calculated using CC03 Monte Carlo events.*

The production cross section of W-pairs decaying into the $q\bar{q}q\bar{q}$-channel are:

$\sqrt{s}$ (GeV)	$\mathcal{L}$ (pb)	Cross Section ($W^+W^- \rightarrow q\bar{q}q\bar{q}$)
191.60	29.7	$\sigma(CC03) = 6.91 \pm 0.59 \pm 0.17$ pb
195.54	83.7	$\sigma(CC03) = 7.28 \pm 0.36 \pm 0.17$ pb
199.54	82.8	$\sigma(CC03) = 8.40 \pm 0.39 \pm 0.17$ pb
201.75	37.0	$\sigma(CC03) = 7.39 \pm 0.55 \pm 0.17$ pb.

The old measurements at center-of-mass energies of 162 GeV, 172 GeV, 183 GeV, 189 GeV, and the new preliminary results at $\sqrt{s} = 192 - 202$ GeV presented here are compared to the Standard Model expectation in Figure 5.20. Again, the results are in good agreement with the SM expectation and both non-Abelian s-channel diagrams with triple-gauge-boson couplings are needed to obtain agreement with our measurements.

Recently, new preliminary predictions of the SM CC03 cross sections have appeared in the form of the Monte Carlo programs YFSWW3 [89] and RacoonWW [90]; both of these programs are still in a state of development. Their preliminary predictions are respectively 2.0% and 2.4-2.8% lower than the ones from GENTLE [91] and agree better with the data than GENTLE.

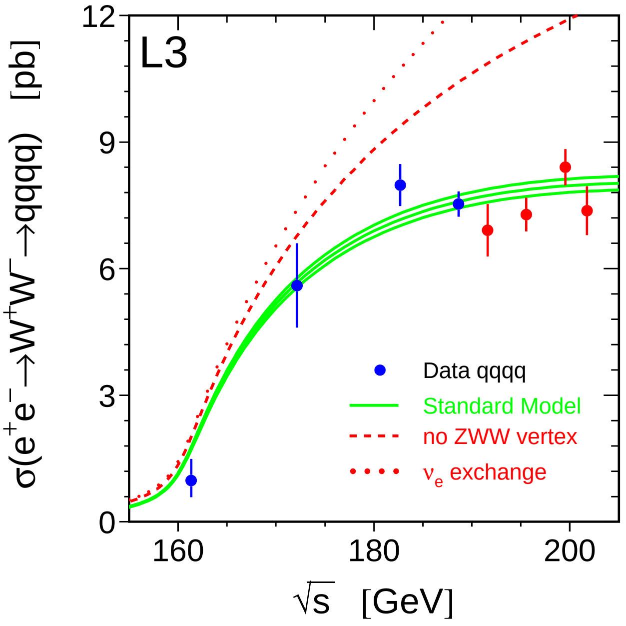

Abbildung 5.20: *The W-pair cross section as a function of the center-of-mass energy. The solid curve shows the SM expectation as calculated with GENTLE. The theoretical error on the GENTLE cross section amounts to 2% and is indicated through two additional solid curves.*

Kapitel 6

W Mass Measurement

In 1996, the first W bosons were produced in LEP at a center-of-mass energy of $\sqrt{s} \simeq$ 161 GeV. This center-of-mass energy lies just above the W pair production threshold. Much larger samples of W pairs were obtained in the following years at higher center-of-mass energies.

Before 1996, the discovery and studies of W bosons have taken place in p$\bar{\text{p}}$ collisions [92, 93, 94, 95], where a single W is produced predominantly through quark-antiquark annihilation. Figure 6.1 shows the lowest-order diagram.

W bosons are identified by their decay into $e\nu_e$ and $\mu\nu_\mu$ final states to defeat the enormous QCD background. In the W decay products, the lepton (e or μ) momentum is measured. The neutrino escapes undetected, but the transverse momentum of the neutrino can be measured, which is the missing transverse momentum of an event. But the neutrino momentum component along the beam

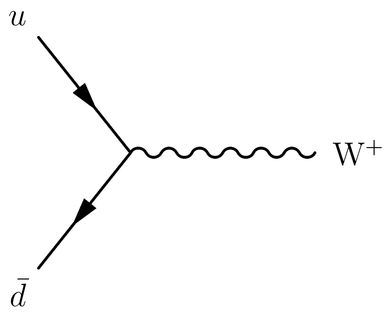

Abbildung 6.1: *Lowest-order diagram for W*

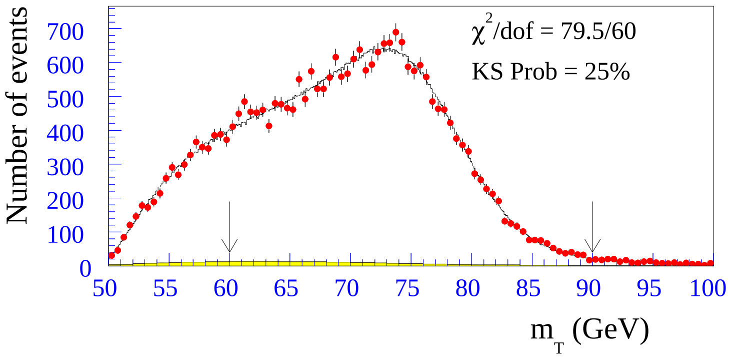

Abbildung 6.2: *Spectrum of m_T from the D0 experiment. The superimposed curve shows the maximum likelihood fit and the shaded region shows the estimated background [96].*

pipe cannot be measured. Because of the unknown longitudinal component of the neutrino, the invariant mass for W $\rightarrow$ $l\nu$ cannot be reconstructed. Therefore, to measure the W mass, the transverse mass and transverse electron or muon momentum spectra are used.

$$m_T = \sqrt{2p_T(l)p_T(\nu)[1-\cos(\phi(l)-\phi(\nu))]}, \tag{6.1}$$

where ϕ is the angle in the transverse plane. A transverse mass distribution is shown in Figure 6.2.

At LEP2, the measurement of the W mass can be performed in two ways, using the information of the W pair production cross-section or by directly reconstructing the decay products of the W.

The cross-section for the process $e^+e^- \rightarrow W^+W^-$ increases very rapidly near the kinematic threshold of $\sqrt{s} = 2M_W$. This means that for a given $\sqrt{s}$ near threshold, the value of the cross-section is very sensitive to M_W. This is illustrated in Figure 6.3. On the other hand, the strong dependency of the cross-section on the value of M_W is almost independent of the other parameters of the SM. Therefore in this threshold region, it is possible to extract the W boson mass from the data by measuring the cross-section and comparing it with theoretical

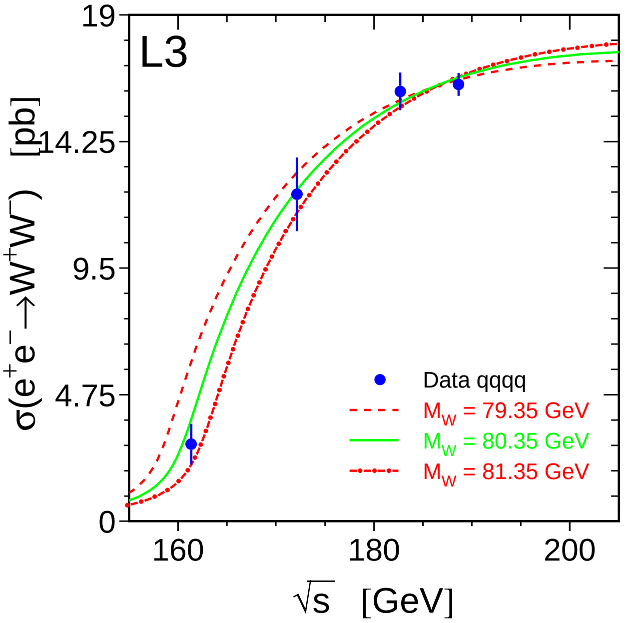

Abbildung 6.3: *The cross section* $\sigma_{\rm WW}$*, of the process* $\mathrm{e^+e^-} \rightarrow \mathrm{W^+W^-} \rightarrow f\bar{f}f\bar{f}(\gamma)$ *as a function of the center-of-mass energy,* $\sqrt{s}$*. The published measurements [97, 98] and new results of section 5.6 are shown as points with error bars, combining statistical and systematic errors in quadrature. The solid and dashed curves show the Standard Model expectations for the given W masses.*

predictions in the context of the Standard Model. Such measurements of the mass of the W boson are complementary to those at p$\bar{\rm p}$ colliders and to those of LEP2 data, where the mass is measured through a direct reconstruction of the decay products of the W. The first measurement of $M_{\rm W}$ from the LEP2 data was extracted in this way [97, 98, 99, 100, 101].

This chapter describes the measurement of $M_{\rm W}$ above the $\mathrm{W^+W^-}$ production threshold at $\sqrt{s} \backsimeq$ 183 GeV and $\sqrt{s} \backsimeq$ 189 GeV. Contrary to p$\bar{\rm p}$ collisions, at LEP2, W's can be detected through all decay modes, and the center-of-mass energy can be precisely determined. Thus, energy and momentum constraints can be applied to the event reconstruction. In semileptonic W pairs, where one W boson decays into two hadronic jets and the other into a lepton and a neutrino, these constraints are very useful. The missing momentum and energy in the event can be measured and assigned to the neutrino, which allows for the reconstruction of the invariant mass. In W pairs decaying into four jets, the reconstruction of the invariant mass can be improved, since these kinematic constraints compensate for the relatively poor jet energy resolution. From the purely leptonic decays, where two neutrinos are missing, the reconstruction of the invariant mass is not possible and those topologies are thus not used here. However, the energies of the two most energetic jets of each event, E_l^{max} and E_l^{min}, can be used for the extraction of the W mass in this channel [102].

The W boson mass is determined from fits to the reconstructed invariant mass spectrum of the selected hadronic and semileptonic $\mathrm{W}^+\mathrm{W}^-$ events. There are several methods to measure the W boson mass. As a precise measurement of M_W with sub-promille accuracy is desired, any systematic effect must be controlled to an accuracy of a few MeV. The methods used in this thesis to analyse the data in terms of M_W are the following:

1. Monte Carlo calibration

2. Reweighting of Monte Carlo events.

The Monte Carlo Calibration method is based on an analytic fit to the measured mass spectrum. The W mass obtained through the fit is calibrated with the MC events. Thus this method is called MC Calibration method and it will be explained in detail in section 6.2. An alternative method, reweighting, is also developed and used to cross-check the results from the MC Calibration method. The reweighting method produces MC mass spectra corresponding to any given mass. The W mass is determined by comparing the shape of the reconstructed invariant mass distribution from the data with that from the reweighted MC spectra.

In general, both methods make use of Monte Carlo events. Thus any method must be checked for possible systematic biases resulting from using Monte Carlo event samples.

6.1 Invariant Mass Reconstruction

The procedures to reconstruct the invariant mass of the W candidates in each event require several steps. The jet finding was already discussed in the previous chapter. Next, the kinematic fitting is discussed in detail, followed by a description of the jet pairing method in the case of a hadronic channel.

6.1.1 Kinematic Fitting

Doing experimental physics always means facing uncertainties in observable quantities due to detector resolution and the estimation of unknown parameters. In most cases, it is of a great help, if one can find a way to connect observable quantities as well as unobservable unknowns through a set of algebraic restrictions. The most effective way to do this in this analysis is a kinematic fit. With the help of a kinematic fit, a probability can be calculated, how well a set of observed quantities and unknowns like the variables for an unseen particle fit to a certain kinematic hypothesis. Here, the observables are varied according to their experimental resolution until a solution for the hypothesis is found. At the same time, the difference between the fitted and corrected quantities is minimised. For a successful minimization, the constraining equations will supply estimates for the unmeasured variables as well as improved measurements for the measured quantities.

The fit always incorporates the constraints of energy and momentum conservation. Beside these, some other constraints can be introduced. In our case, an additional constraint could test the hypothesis that the two masses reconstructed per event are the same. For energy and momentum conservation, the constraints are as following:

$$\sum_{i=1}^{N} E_i - E_0 = 0 \quad \text{and} \quad \sum_{i=1}^{N} \mathbf{p_i} - \mathbf{p_0} = \mathbf{0}, \tag{6.2}$$

where E_0 and $\mathbf{p_0}$ are energy and momentum of the initial system. N is the number of particles. In case of $\mathrm{e^+e^-}$ collisions at LEP, $\mathbf{p_0} = \mathbf{0}$ and $E_0 = \sqrt{s}$. N is 4 due to four final fermions corresponding to four jets [1]. An additional

---

[1] The charged lepton and missing neutrino are counted as jets

constraint might be

$$(E_1 + E_2)^2 - (\vec{p}_1 + \vec{p}_2)^2 - m_{\mathrm{W}}^2 = 0 \quad , (E_3 + E_4)^2 - (\vec{p}_3 + \vec{p}_4)^2 - m_{\mathrm{W}}^2 = 0 \quad , \tag{6.3}$$

where jet1 and jet2 are assumed to be the decay product of the first W boson and jet3 and jet4 of the other W boson [2]. When determining the W mass, giving an input mass as a constraint is not ideal. But reconstructing two masses m_1 and m_2 and constraining them to be equal greatly improves the W mass resolution.

Lagrange Multipliers

From a mathematical point of view, the kinematic fit is a minimization procedure. From the many possible solutions for the fit, it selects the one, which differs the least from the observed measurement. The quantity to be minimized is chi-square (χ^2), which is defined as follows: Assume we are given a set of N independent experimental values $y_1, y_2, ..., y_N$ and want to obtain the true values $\eta_1, \eta_2, ..., \eta_N$ of the observables. In this case, the observables $\mathbf{y}$ are the energies and the polar and azimuthal angles of reconstructed jets. For hadronic jets, the velocity $\beta_i = |\vec{p}_i|/E_i$ of the jet is kept at its measured value as systematic effects cancel in the ratio. If it is assumed that the individual measurements y_i are normally distributed about their true values η_i with variance σ_i^2, the most probable values of the unknown η_i's are those which make

$$\chi^2 \equiv \sum_{i=1}^{N} (\frac{y_i - \eta_i}{\sigma_i})^2 = \text{minimum}, \tag{6.4}$$

where a simple case of uncorrelated observations is assumed. If the observations are correlated, with errors and covariance terms given by the (symmetric) covariance matrix $V(\mathbf{y})$, the χ^2 is defined as

$$\chi^2 \equiv \sum_{i=1}^{N} \sum_{j=1}^{N} (y_i - \eta_i) V_{ij}^{-1} (y_j - \eta_j). \tag{6.5}$$

In the minimization, a set of K constraints of the form

$$f_k(\eta_1, \eta_2, ..., \eta_N, \xi_i, \xi_2, ..., \xi_J) = 0, \qquad k = 1, 2, ..., K \tag{6.6}$$

---

[2] The jet pairing is explained in detail in section 6.1.4

must be taken into account. A set of $\boldsymbol{\xi} = (\xi_1, \xi_2, ..., \xi_J)$ stands for the J unmeasured variables. In this case, these variables include the W mass, missing neutrino momentum variables.

A way to incorporate the constraints into the χ^2 equation is the method of Lagrange multipliers. In this method, we introduce K additional unknowns $\boldsymbol{\lambda} = (\lambda_1, ..., \lambda_K)$, called *Lagrange multipliers* and rephrase the problem by requiring

$$\chi^2(\boldsymbol{\eta}, \boldsymbol{\xi}, \boldsymbol{\lambda}) \ = \ (\mathbf{y} - \boldsymbol{\eta})^{\mathbf{T}}\mathbf{V}^{-\mathbf{1}}(\mathbf{y})(\mathbf{y} - \boldsymbol{\eta}) \ + \ \mathbf{2}\boldsymbol{\lambda}^{\mathbf{T}}\mathbf{f}(\boldsymbol{\eta}, \boldsymbol{\xi}) \ = \ \mathbf{minimum}. \quad (6.7)$$

At a minimum χ^2 value, the derivatives of χ^2 with respect to all unknowns are equal to zero, and we get the following set of equations:

$$\begin{aligned} \nabla_\eta \chi^2 &= -2V^{-1}(\mathbf{y} - \boldsymbol{\eta}) \ + \ \mathbf{2F}_\eta^{\mathbf{T}}\boldsymbol{\lambda} = \mathbf{0}, && \text{N equations} \\ \nabla_\xi \chi^2 &= 2F_\xi^T \boldsymbol{\lambda} = \mathbf{0}, && \text{J equations} \\ \nabla_\lambda \chi^2 &= 2\mathbf{f}(\boldsymbol{\eta}, \xi) = \mathbf{0}, && \text{K equations} \end{aligned} \quad (6.8)$$

where the matrices F_η (of dimension K×N) and F_ξ (dimension K×J) are defined by

$$(F_\eta)_{ki} \ \equiv \ \frac{\partial f_k}{\partial \eta_i}, \ \ (F_\xi)_{kj} \ \equiv \ \frac{\partial f_k}{\partial \xi_j}. \quad (6.9)$$

They allow the determination of the unmeasured neutrino momentum vector. For $q\bar{q}e\nu$ and $q\bar{q}\mu\nu$ events, the fit problem involves 4 constraints based on the constraints of energy-momentum conservation and 1 constraint of the equal mass of the reconstructed two masses m_1 and m_2 and 3 unmeasured unknowns due to the neutrinos. Therefore one deals here with a 2C-fit. For $q\bar{q}q\bar{q}$ events it is a 5C kinematic fit with the constraint of the equal mass and 4C kinematic fit without the constraint of the equal mass.

Goodness of fit

Doing a fit, it is desirable to have a quantitative measure of how close the overall agreement between the fitted quantities $\boldsymbol{\eta}$ and the measurements $\mathbf{y}$ are. The χ^2_{min} value obtained in a particular minimization provides this measure of the goodness-of-fit. We expect the measurements to be corrected in an order of σ, since this represents the assumed uncertainty (resolution). If one or more measurements have to be corrected more than one σ to fit the constraints, the

χ^2_{min} value will become larger. Assuming that the measurements are distributed Gaussian around the true values with the given value of σ's and knowing the degrees of freedom n of the fit, the chi-square probability can be calculated.

$$CL(\chi^2_{min}) = \int_{\chi^2_{min}}^{\infty} f(u;n)du \;=\; 1 \;-\; F(\chi^2_{min};n), \tag{6.10}$$

where $f(u;n)$ is the chi-square p.d.f. and $F(\chi^2_{min};n)$ the cumulative chi-square distribution for n degrees of freedom. The chi-square probability, called also confidence level (CL), gives the probability for obtaining a higher value for χ^2_{min} in a new minimization with similar measurements and the same hypothesis. A small value of χ^2_{min} corresponds to a larger CL(χ^2_{min}), which means that the fit was good. In contrast, a very large value χ^2_{min} implies a small CL(χ^2_{min}), or a bad fit. It must be noted that the kinematic fit does not say anything about the quality of the measurements, only indicating how well the measurements agree with a given hypothesis.

The CL distribution for many events will be uniform over the interval [0,1], if the hypothesis is good. This characteristic can be used to look for some indications. For example, if CL is strongly peaked at very low probability this may reveal a contamination of "wrong" events, which can be background events or very poorly reconstructed events. A cut on this distribution may help to distinguish between "*right*" and "*wrong*" events. Similarly, a skew distribution for CL with an excess on the high (or low) probability side may indicate that the errors in the measurements have systematically been set too high (low). A CL distribution of 5C fits in the $q\bar{q}q\bar{q}$ channel is shown in Figure 6.4.

Pulls

Beside the uniform distribution of CL(χ^2_{min}) between 0 and 1, a closer look at the pulls for the measured variables helps to verify the validity of resolutions used in the fit. The pull directly measures the deviation between the observation y_i (original measured value) and the final fitted value η_i. The i-th pull is defined as

$$pull_i \;=\; \frac{y_i - \eta_i}{\sqrt{\sigma^2(y_i) - \sigma^2(\eta_i)}}, \tag{6.11}$$

where $\sigma(y_i)$ and $\sigma(\eta_i)$ are the error estimates on the measured and fitted values. The minus sign in the denominator has its origin in the fact that the two quan-

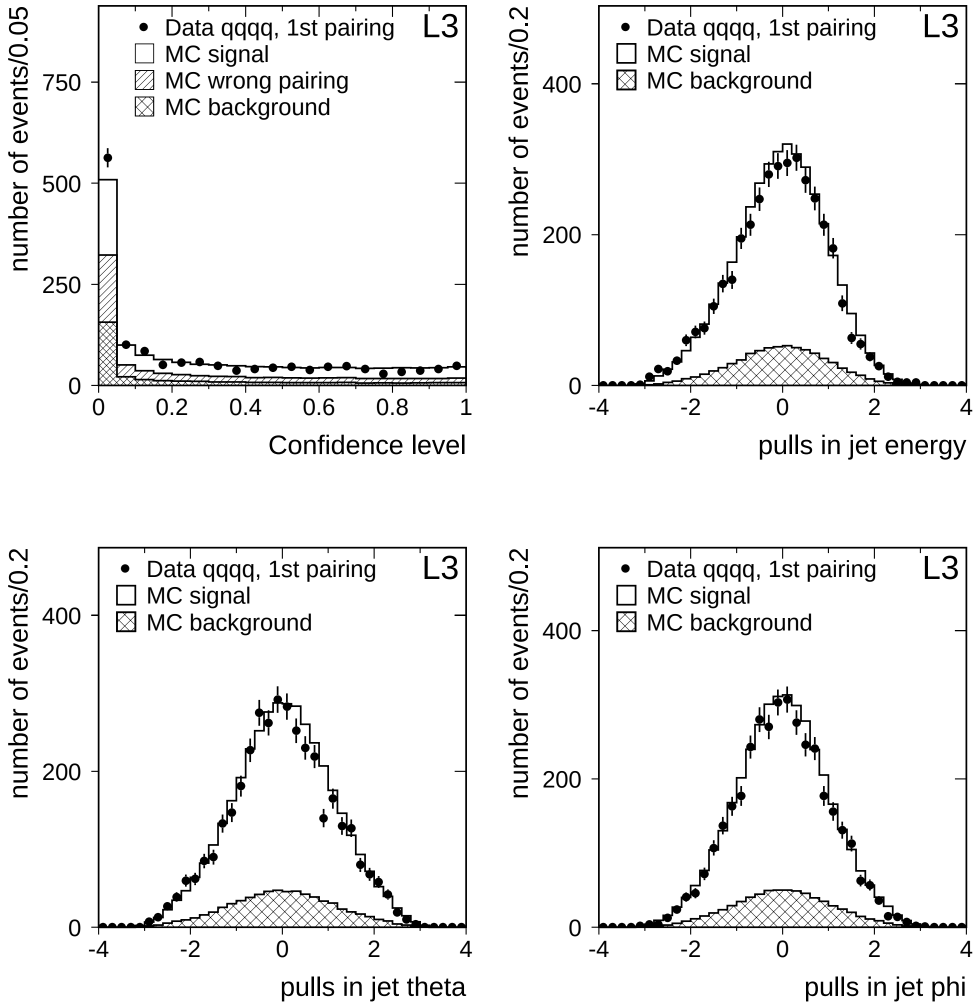

Abbildung 6.4: *CL of the 5C fit for the hadronic WW decay channel. A flat distribution of the confidence level indicates that the measured errors are correct. The first bin of the confidence level distribution is high and shows that there are many events which do not confirm with the hypothesis. The pull distributions of the constrained 5C fit are gaussian with a width of* $\sigma = 1$*, indicating correct resolution measurements. The asymmetry in the energy pull is explained in the text.*

tities in the numerator are completely (positively) correlated [103]. Ideally, the pull distribution for a variable y_i over many events should have a mean of zero and a Gaussian width of $\sigma = 1$. A deviation from this shape may indicate an incorrect assumed deviation for a given resolution, or worse, a non-Gaussian resolution. If the observed pull distribution is substantially wider (narrower) than the Gaussian distribution, the error in that observation has most likely been consistently taken too small (large). Figure 6.4 shows the pull distribution of 5C fit in the $q\bar{q}q\bar{q}$ channel with the constraint of $\mathrm{CL}(\chi^2_{min}) > 1\%$. As expected, the means of the θ and ϕ distributions are consistent with zero and the gaussian widths are consistent with unity. There is a negative asymmetry in the energy pulls. This is due to missing energy caused by ISR. This will be explained in detail in subsection 6.1.3.

6.1.2 Results of the Kinematic Fit

For all the selected events the kinematic fit converges successfully, producing a flat $\mathrm{CL}(\chi^2_{min})$ above 5% which is well described by the Monte Carlo. The results of the fit are shown in Figure 6.5 with the invariant mass distribution for the $q\bar{q}q\bar{q}$ channel before and after the fit. The mass differences before and after the fit with respect to the generated mass was also compared, which are shown for $q\bar{q}l\nu$ and $q\bar{q}q\bar{q}$ in Figure 6.6. In case of the $q\bar{q}q\bar{q}$ channel, only the events with the right jet pairing are considered. Before the fit, the mass distribution is very wide. The mass resolutions after the fit are improved by a factor of ~ 3 for $\mathrm{W^+W^-} \rightarrow q\bar{q}q\bar{q}$ and by a factor of ~ 2 for $\mathrm{W^+W^-} \rightarrow q\bar{q}l\nu$. As one can see on the CL distribution in Figure 6.4, CL can be used to eliminate possible background which does not comply with the $\mathrm{W^+W^-}$ hypothesis. However, a fraction of $\mathrm{W^+W^-}$ up to about 30% in the 4-jet channel fails to give a good fit. This is mainly due to incorrect pairing and poorly reconstructed events. The constrained fit assumes that the errors on the measured quantities are Gaussian. There are several factors leading to non-Gaussian errors. The most important is gluon radiation and ISR, though overlapping jets may also play a role. The hard gluon radiation results in the 5th jet in an event. Since events are always forced to 4-jet events, the treatment of jets as independent objects is no longer valid, as one extra jet may be split into two and added to two different jets. Even a soft gluon may make the jets broader in a specific direction resulting in a non-Gaussian error. Since these effects are

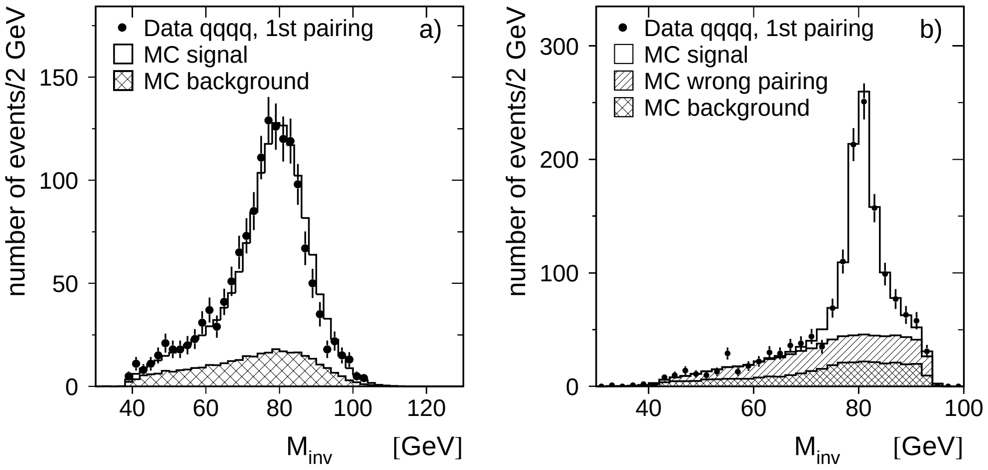

Abbildung 6.5: *Invariant mass distribution before and after the kinematic fit in the $q\bar{q}q\bar{q}$ channel are shown; a) reconstructed invariant mass distribution before the kinematic fit, b) reconstructed invariant mass distribution after the kinematic fit without any cut on the CL distribution.*

not implemented in the fit, each of these effects will lead the events to accumulate near low CL. An attempt was made to treat 5-jet events correctly, which gave a good fit for some fraction. But because of the combinatorial problem, their inclusion has little effect on the ultimate mass resolution.

Rescaling Method

For $W^+W^- \to q\bar{q}\tau\nu$, the event contains at least two unmeasured neutrinos in the final state. To improve the invariant mass resolution, the energies of the two hadronic jets are rescaled.

The first step is to include the beam energy constraint:

$$E_i + E_j = E_{beam}, \tag{6.12}$$

where no ISR is assumed. This leads to a determination of the rescaled reconstructed invariant mass

$$m_{ij}(\text{rescaled}) = \frac{E_{beam}}{E_i + E_j} m_{ij}, \tag{6.13}$$

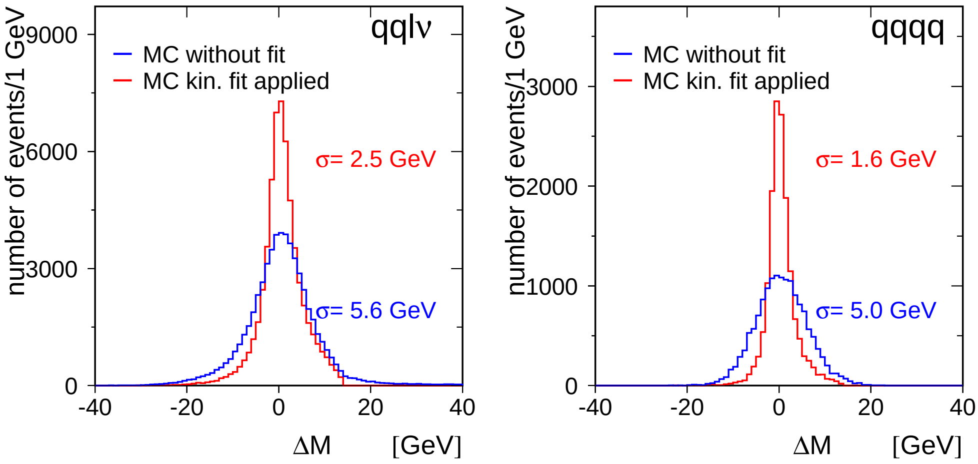

Abbildung 6.6: *The resolution distribution before and after the kinematic fit in the $q\bar{q}e\nu$ and $q\bar{q}q\bar{q}$ channels are shown.*

where $m_{ij} = \sqrt{(E_i + E_j)^2 - (\vec{p}_i + \vec{p}_j)^2}$ stands for the invariant mass of the $q\bar{q}$ system.

6.1.3 Effects of Initial State Radiation

The effects of initial state radiation depend on whether the emitted photon is detected or not. Let us assume that the photon is not detected, since this is the case for the majority of events. In the case of an excluded ISR photon, the assumption of energy conservation is not true, since ISR lowers the W^+W^- center-of-mass energy ($\sqrt{s'} = \sqrt{s} - E_{ISR}$) available for W pair production. Thus after the constrained fit, the energy of two W bosons ($E_{W_1} + E_{W_2}$) will be too high, which leads to the asymmetric shape of energy pulls. The ISR energy spectrum is shown in Figure 6.7 for the signal Monte Carlo, where the average ISR per event is about 2.2 GeV. ISR also has a sizeable systematic shift $\triangle m$ in the reconstructed jet-jet invariant masses:

$$\triangle m_{inv} \approx m_{inv} \frac{E_{ISR}}{\sqrt{s}}. \tag{6.14}$$

If the exact shift of the W mass coming from ISR is known, this effect can be calibrated. The more critical dilemma is that the shape of the invariant

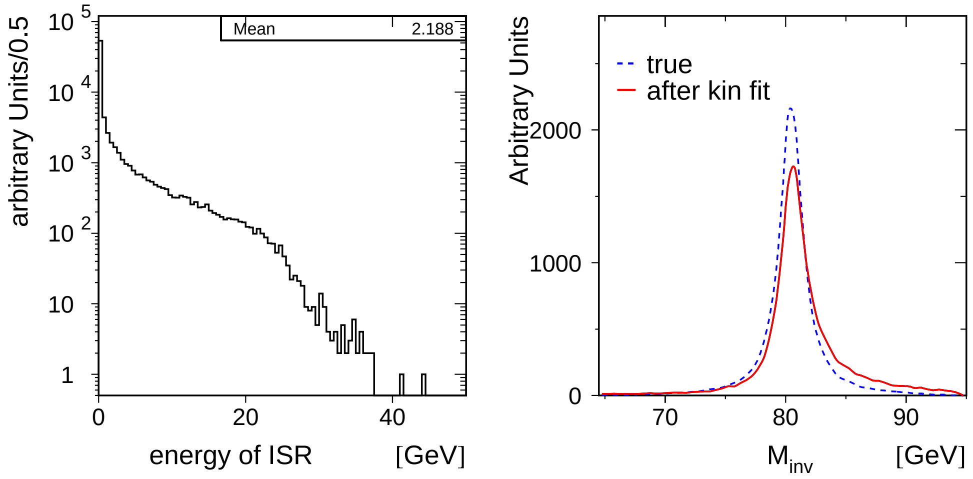

Abbildung 6.7: *The distribution on the left side shows the summed energy of the ISR's per event based on the Monte Carlo simulations. The distribution on the right side shows the effect of the ISR's on the shape of the invariant mass after the kinematic fit. The solid line shows the invariant mass distribution of the W bosons after the kinematic fit and the dashed line the generated invariant mass distribution of the W bosons with detector resolution.*

mass distribution is distorted from the expected Breit-Wigner shape according to formula 2.50. This is shown in Figure 6.7. Here, it might be useful to implement the ISR in the constrained fit. The study shows however, that a fit assuming the photon going in the z direction (in the forward direction or the opposite), gives an even worse resolution. This happens because the fit constrains the events with very low ISR photon energies or no ISR photons (γ_{ISR}) resulting in a missing photon along the z direction. The alternative is to implement the loss of ISR photon energy only for events which fail to fit the hypothesis with no γ_{ISR}. Indeed this helps a bit, but the improvement is marginal. Thus this thesis chooses not to allow for γ_{ISR} in the constrained kinematic fit and to account for it in the mass measurement.

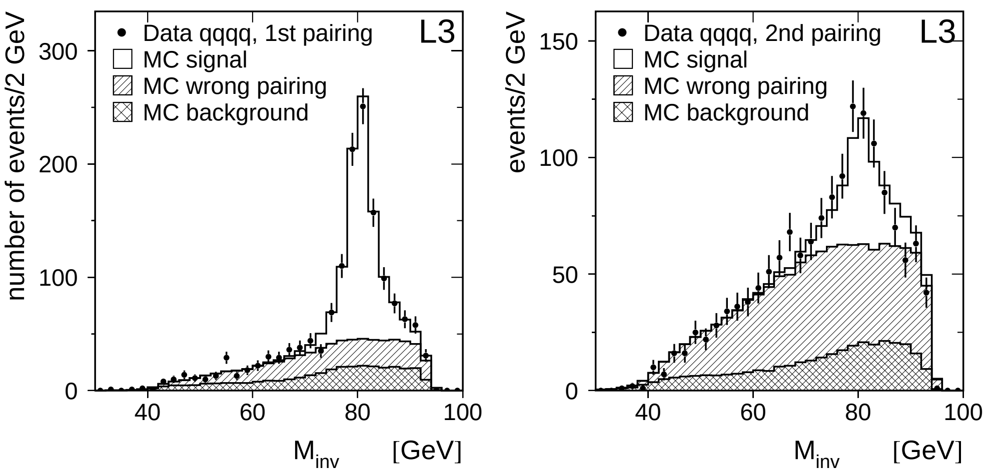

Abbildung 6.8: *Distributions of reconstructed invariant masses, M_{inv}, after applying the kinematic fit using the equal-mass constraint for $q\bar{q}q\bar{q}$ events selected in the 189 GeV data.*

6.1.4 Jet Pairing for $q\bar{q}q\bar{q}$ Channel

Looking at the result of the constrained fit in Figure 6.5, one might wonder about the tail. It is clear that the background events don't necessarily peak around 80 GeV, but what about the signal events ? In order to apply the equal mass constraints, one has to select the correct two jet-jet pairs to form the two W bosons. Events with incorrect pairs behave like the background events and don't have any information about the W boson. They are distributed over the hole range without peaking around 80 GeV. Clearly this jet pairing problem appears only in the 4-jet channel, where we have three possible ways to pair the four jets into two jet-jet pairs. In this thesis, the correct combination is determined with the help of the kinematic fit: For each of the three possibilities to combine four jets into two pairs, a kinematic fit is performed. The results with the largest and second largest fit probabilities are shown in Figure 6.8. The ambiguity in the choice of the jet pairing leads to a combinatorial background. In the first jet pairing, which corresponds to the best χ^2 fit probability, only 63% of the signal events have correct pairings. For the second best pairing, it is 30%. However, the signal-to-background ratio in the relevant signal region around $m_{inv} \approx 80$

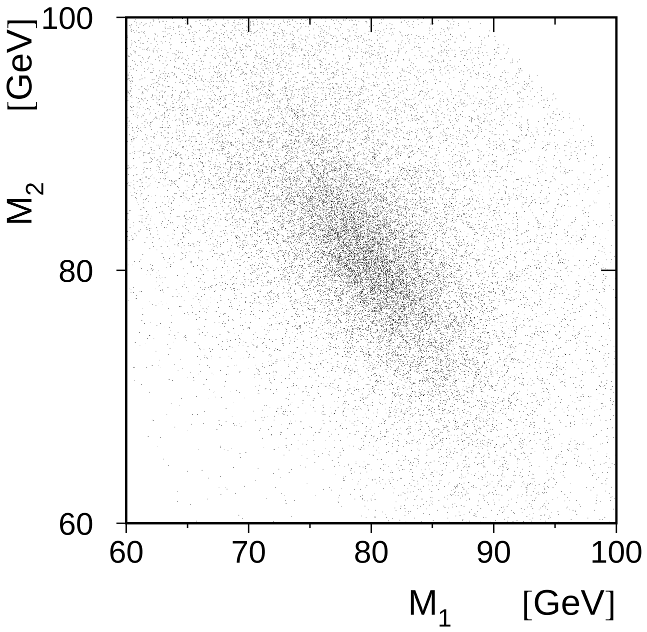

Abbildung 6.9: *Scatter plot of the two reconstructed invariant masses of selected MC data after a 4C kinematic fit.*

GeV is improved, see Figure 6.5. The pairing with the second highest likelihood is included as an additional distribution, to cover the low efficiency of the pairing algorithm.

6.1.5 Final Reconstruction

Here are some last remarks and corrections, before extracting the W mass from the invariant mass distribution.

As the kinematic fit imposes constraints of energy-momentum conservation, the kinematic quantities describing the four final-state fermions are strongly correlated after the fit. Indeed the two reconstructed invariant masses are strongly anti-correlated after energy-momentum constraints are applied. Figure 6.9 shows this relation based on the signal Monte Carlo events. Because of these correlations, the two W's are not independent. If the two W masses were treated as separate measurements, the statistical error on the W mass would be underestimated. Thus we construct the average invariant mass per event, which is then used for the determination of the W mass.

Another important correction with regard to the shapes of the reconstructed invariant masses is introduced by an additional requirement as to the quality of the reconstruction. Since a poorly reconstructed event smears out the good mass resolution from the well reconstructed events, we reject events with a CL value less than 5% in the process $W^+W^- \rightarrow q\bar{q}l\nu$. In the process $W^+W^- \rightarrow q\bar{q}q\bar{q}$, the CL cut is at 1% for the best pairing and 5% for the second best pairing. The final distributions of the largest and second largest fit probabilities in the process $W^+W^- \rightarrow q\bar{q}q\bar{q}$ are shown in Figure 6.10

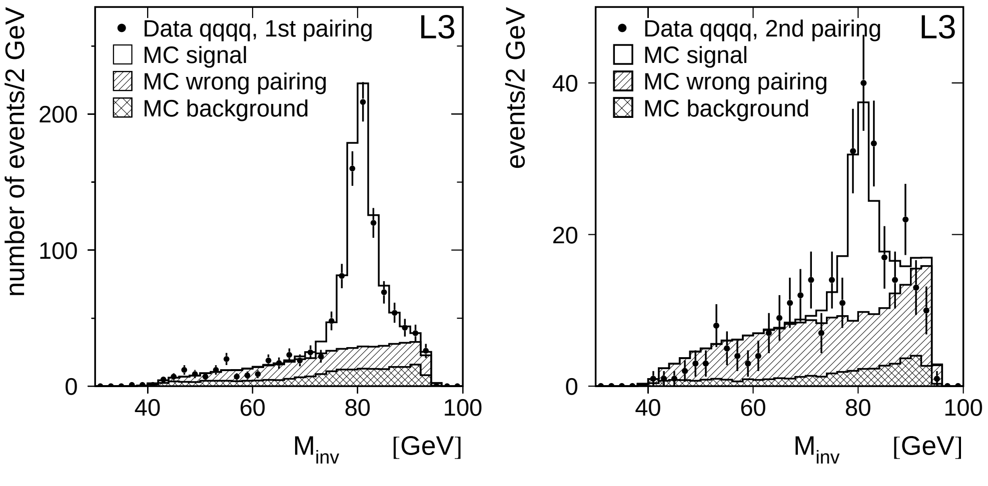

Abbildung 6.10: *Distributions of the reconstructed invariant mass, M_{inv}, for the $q\bar{q}q\bar{q}$ events after the final reconstruction as described in the text. In the left side the best pairing after a 1% cut on the CL distribution is shown and on the right side the second best pairing after a 5% cut on the CL distribution is shown.*

6.2 Monte Carlo Calibration

The MC calibration method is a shape-fit, thus the mass is determined by the shape of the invariant mass distribution. To fit the invariant mass distributions of Figure 6.10, this method uses an analytic function, e.g. a Breit-Wigner. The same fitting procedure is applied to both data and MC events. Since for the latter the input W mass is known, the MC results can be used to evaluate the bias $\triangle$ of this method and the method can be calibrated. For the calibration, assume we have five MC samples with different generated input W boson masses. After the fits are applied, we end up with 5 fit results of the MC samples and one fit result of the data. The Monte Carlo results are used to evaluate the bias δ of this method:

$$\delta \equiv M_{fit}^{MC} - M_{\mathrm{W}}^{MC}, \tag{6.15}$$

where the bias depends on the final state analysed. The mass of the W boson measured in the data is the fitted mass of the data after this correction for the bias δ:

$$M_{\mathrm{W}} = M^{data} - \delta. \tag{6.16}$$

The error of the fitted mass of the data is corrected in the same way, which will become more clear later in this section.

This procedure automatically takes all biases into account as long as they are implemented in the Monte Carlo simulation. For the Monte Carlo samples used in this thesis, the biases such as the initial-state radiation, detector resolutions and efficiencies, selection cuts etc are implemented. The quality of the Monte Carlo simulation concerning the description of the underlying physics and the detector response enters in the systematic error of this method. The main difficulty of this method is, that there is no unique function to be used in the fit. The quality of the fit in terms of the statistical error depends strongly on how well the applied function can describe the shape of the invariant mass and how good the resolution of the invariant mass itself is. For example, the fitting results of the invariant mass distributions before and after the kinematic fit will have about a factor of two difference in the statistical error.

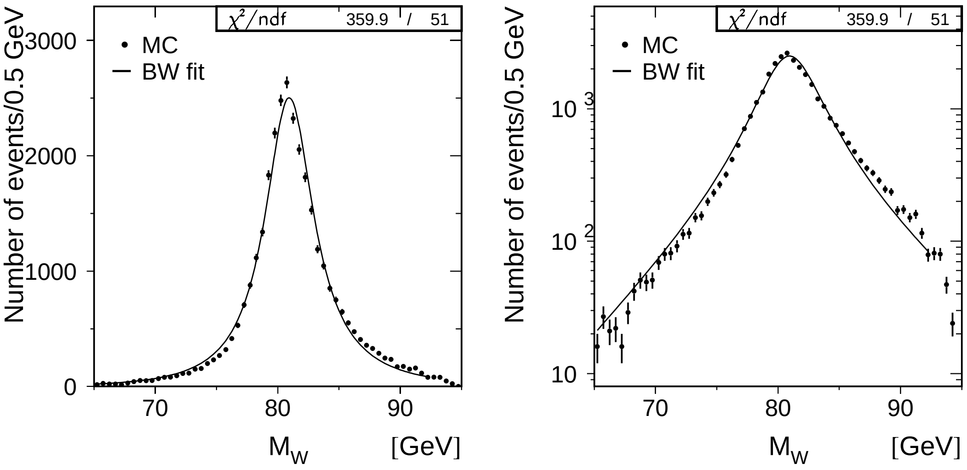

Abbildung 6.11: *The fit results for the expression 6.17 is shown in a linear and a logarithmic y axis. The solid lines show the results of the fits of* M_{W} *to the simulated Monte Carlo events.*

6.2.1 Signal Shape

First consider the $q\bar{q}l\nu$ channel as it does not have the complications of more than one jet-jet combination.

The $q\bar{q}l\nu$ channel

The first step in fitting the W line-shape is to find a suitable function. The relativistic Breit Wigner is a good choice as the probability function:

$$\mathrm{BW}(m_{rec}|M_{\mathrm{W}},\Gamma_{\mathrm{W}}) = \frac{1}{\pi}\frac{\Gamma_{\mathrm{W}}}{M_{\mathrm{W}}}\frac{m_{rec}^2}{(m_{rec}^2 - M_{\mathrm{W}}^2)^2 + m_{rec}^4\Gamma_{\mathrm{W}}^2/M_{\mathrm{W}}^2}. \tag{6.17}$$

The probability distribution is the same if m_{rec} is the average W boson mass per event. However, a fit to the invariant mass spectrum using this function isn't very successful, as shown in Figure 6.11. Due to ISR, the invariant mass spectrum is asymmetric, while the fit function used is symmetric. To overcome this problem, a variety of analytic forms were investigated. It has been found

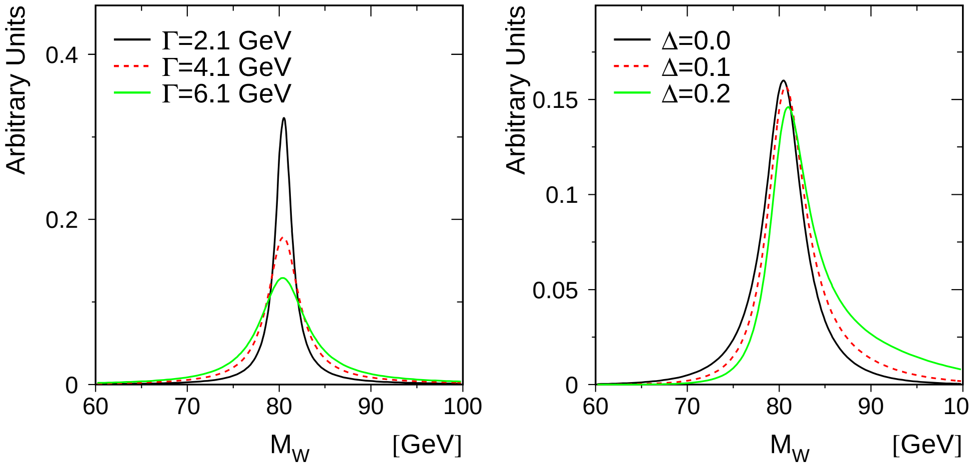

Abbildung 6.12: *On the left, Breit-Wigner function is shown in dependence on the width. On the right, Breit-Wigner is multiplied by GAUSS, and the effects for different* $\triangle$*'s are shown.*

that the effect of ISR can be approximated by multiplying the Breit-Wigner by

$$\mathrm{GAUSS}(m_{rec}|M_{\mathrm{W}}, \triangle, \sigma_{\mathrm{G}}) \;=\; \frac{1}{\sqrt{2\pi}\sigma_{\mathrm{G}}}\, exp(-\frac{(M_{\mathrm{W}}(1+\triangle)-m_{rec})^2}{2\sigma_{\mathrm{G}}^2}). \qquad (6.18)$$

The mean value of GAUSS is increased to a higher W mass by an amount of $\triangle \times M_{\mathrm{W}}$, and the shape becomes slightly asymmetric by multiplying GAUSS to the Breit-Wigner function. These characteristics are very similar to that which we have already observed in Figure 6.7. The parameters $\triangle$ and σ_{G} must be obtained from Monte Carlo studies. The σ_{G} of GAUSS has a strong correlation with the width of the Breit-Wigner, and after adjusting both parameters, a good approximation to the resolution is achieved. These two approximations are visualised in Figure 6.12.

The total width of the W boson can be extracted simultaneously with the mass. But in this thesis, the width of the W boson is constrained to the value of the Standard Model [18],

$$\Gamma_{\mathrm{W}}^{\mathrm{SM}} \;=\; \frac{3G_\mu M_{\mathrm{W}}^3}{2\pi\sqrt{2}}\,(1+\frac{2}{3}\frac{\alpha_s}{\pi}), \qquad (6.19)$$

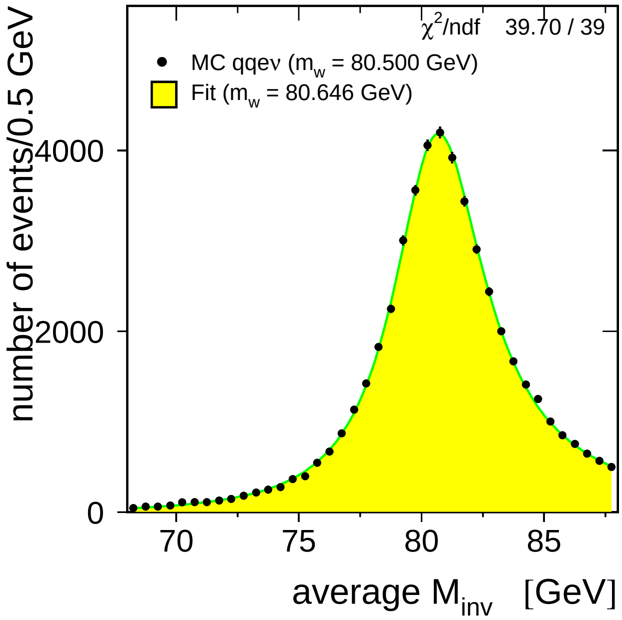

Abbildung 6.13: *Reconstructed mass distribution of the $q\bar{q}e\nu$ channel from a MC sample generated with M_W=80.50 GeV for $\sqrt{s}$=189 GeV. The solid curve displays the result of a binned maximum likelihood fit to a relativistic Breit-Wigner × GAUSS in the range 68-88 GeV.*

to increase the accuracy on M_W. Since we want to constrain the width of W boson to the SM, it is desirable to decompose Γ_W as follows

$$\Gamma_\mathrm{W} = \Gamma_\mathrm{W}^\mathrm{SM} + \sigma_\mathrm{BW}, \tag{6.20}$$

where σ_BW represents the experimental effects as the detector resolution[3]. The values for σ_BW, σ_G and $\triangle$ are determined for each channel separately using Monte Carlo events. Typical σ_BW values from the $q\bar{q}l\nu$ and $q\bar{q}q\bar{q}$ channels are 3.8 GeV and 2.4 GeV respectively.

Figure 6.13 shows the fit result of this function with respect to the reconstructed mass distribution for Monte Carlo events in the $q\bar{q}e\nu$ channel. The number

---

[3] This is true to some extent only, since σ_BW is strongly correlated with the σ_G of GAUSS and $\triangle$.

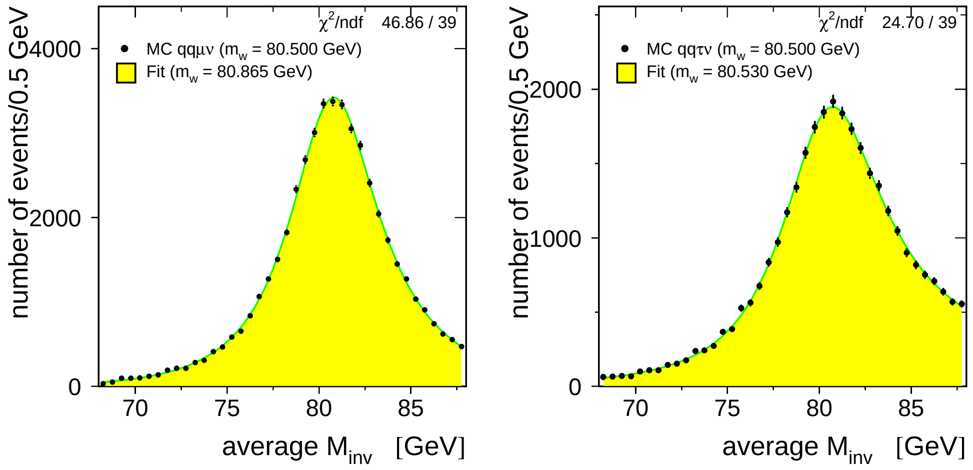

Abbildung 6.14: *Reconstructed mass distributions of the $q\bar{q}\mu\nu$ and $q\bar{q}\tau\nu$ channels from the MC samples generated with M_{W}=80.50 GeV for $\sqrt{s}$=189 GeV and the fit results*

of Monte Carlo events used in the fit corresponds to an integrated luminosity of about 28700 pb^{-1}. The same fit function is also applied to the $q\bar{q}\mu\nu$ and $q\bar{q}\tau\nu$ channels. The results are shown in Figure 6.14.

The $q\bar{q}q\bar{q}$ channel

The $q\bar{q}q\bar{q}$ channel is more complicated because there are 3 possible jet pair combinations and incorrect pairings cannot be avoided. The Breit-Wigner × GAUSS function fits well the reconstructed mass distribution for samples of Monte Carlo events with the right pairing, but it does not give a satisfactory description for both the right and wrong pair events together. We need to find an additional function to describe the shape of wrong pairing events. This is difficult because there is no physics based function like a Breit-Wigner rendering this shape. An excellent fit function for right pair events is not as powerful as it could be, if the function for wrong pair events fits badly with the shape of the reconstructed mass distribution for wrong pair events. Fortunately the fit method used here is well suited to deal with this type of problem. We take the shape of wrong pair events from Monte Carlo events and smooth it to avoid the effects of statistical

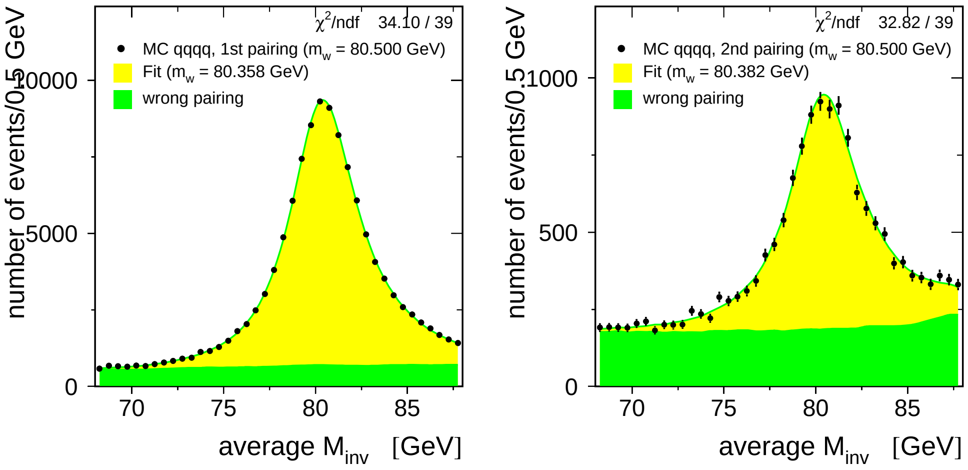

Abbildung 6.15: *Reconstructed mass distribution from a MC sample generated with M_{W}=80.50 GeV for the $\sqrt{s}$=189 GeV and the fit result*

fluctuation. The overall fraction of wrong pairings is fixed to the Monte Carlo expectation. This is allowed, since the wrong pair events are independent of M_{W}.

Figure 6.15 shows the fit result of this function in relation to the reconstructed mass distribution for Monte Carlo events in $q\bar{q}q\bar{q}$ events. The number of Monte Carlo events used in the fit corresponds to an integrated luminosity of about 28700 pb^{-1}. As one can see, the invariant mass distribution for the second best χ^2 pairing events is well described by this function, too.

Linearity

The next step is to check the linearity. We see in Figure 6.13 that the fitted W mass is not the same as the generated W mass. This is the bias which must be corrected later in the analysis. But what about if the bias depends on the W mass ? In this case, we can't take a constant value to correct for the bias. To investigate the absence of mass dependency, we use additional Monte Carlo samples (each of them has $\mathcal{L} \sim$ 6700 pb^{-1}) generated at four different W masses and apply the same fit. Figure 6.16 shows the fit results of separate samples and the fit results as a function of those generated in the case of the qq$e\nu$ channel.

In the last distribution, a linear two parameter χ^2 fit is performed to the points:

$$M_{\mathrm{W}}^{fit} = a + bM_{\mathrm{W}}^{true}, \tag{6.21}$$

where a and b are offset and slope of a straight line, and they are allowed to vary in the fit. The result of the linearity test shows that the fit to M_{W} is consistent with a linear hypothesis.

6.2.2 Background Shape

Background mainly arises in the $\mathrm{W}^+\mathrm{W}^- \rightarrow q\bar{q}q\bar{q}$ and $\mathrm{W}^+\mathrm{W}^- \rightarrow q\bar{q}\tau\nu$ channels, and can be separated into two categories: W mass dependent and W mass independent backgrounds.

W Mass Independent Backgrounds

The main background is due to the $\mathrm{Z} \rightarrow q\bar{q}(\gamma)$ process. Again no function is used to describe the background shape. Instead, the shape from the Monte Carlo events as seen in the wrong pair events in the $q\bar{q}q\bar{q}$ channel are taken. The background fraction is determined from Monte Carlo, and it is kept constant in the fit.

W Mass Dependent Backgrounds

W mass dependent backgrounds are those W events, which belong to the other channels but are selected for the a certain channel. They are difficult to describe, because this problem cannot be handled like the other background events. If we take the shape from the Monte Carlo events, it immediately leads to biases, because the Monte Carlo events are generated at a particular M_{W}. The best way to solve this problem is to treat these background events as the signal events and to fit them together with the signal events. Any possible bias is corrected in the calibration. The percentage of these types of background events in $\mathrm{W}^+\mathrm{W}^- \rightarrow q\bar{q}q\bar{q}$ channel is less than 1 %. The W mass dependent background plays a significant role in the $\mathrm{W}^+\mathrm{W}^- \rightarrow q\bar{q}\tau\nu$ channel, where this type of background event represents ≈ 15 % of all events.

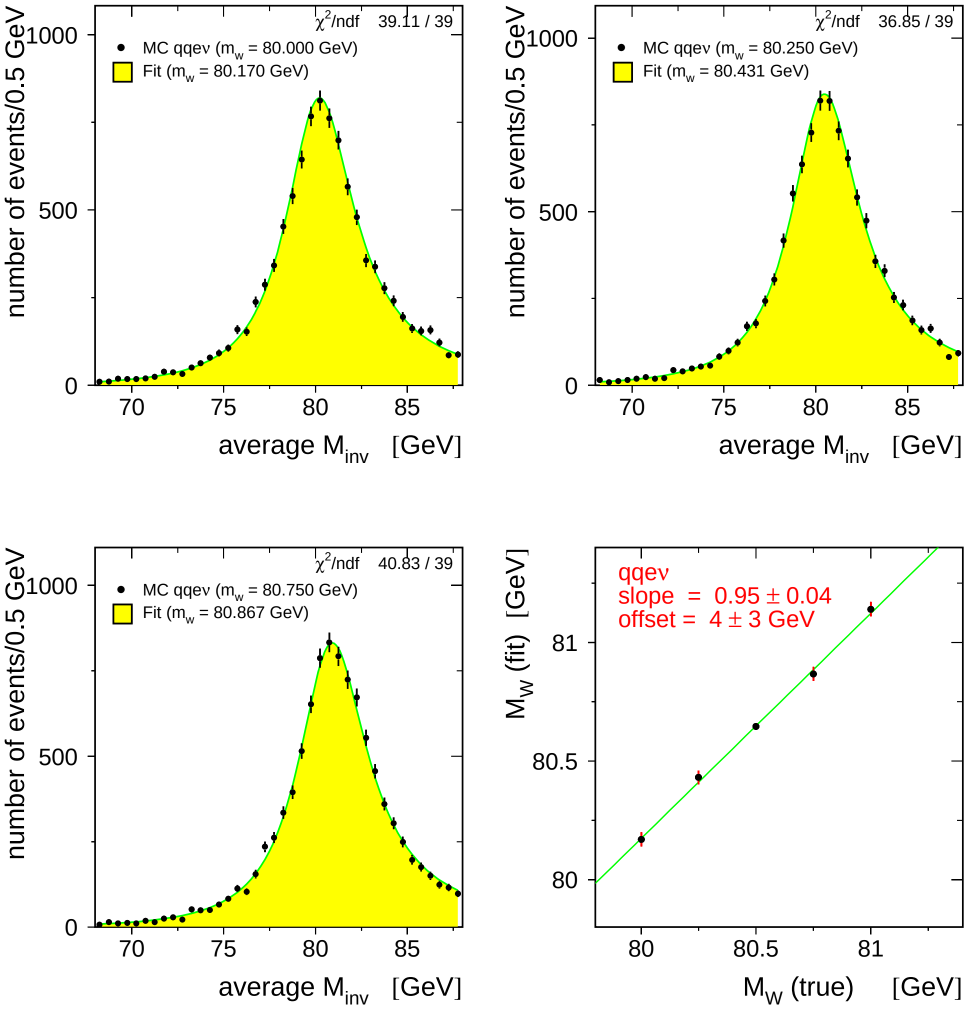

Abbildung 6.16: *Reconstructed mass distributions from the $q\bar{q}e\nu$ MC samples generated with M_W=80.00 GeV, 80.25 GeV and 80.75 GeV for $\sqrt{s}$=189 GeV and the fit results shown in solid lines. The last distribution shows the calibration curve.*

6.2.3 Results of the Fit at 189 GeV

To extract M_{W} from the reconstructed mass distribution of the data, a binned maximum likelihood fit is used. In this method, the value for the hypothesis M_{W} which is most consistent with the observed data is a value for M_{W} which maximizes the likelihood

$$\begin{aligned} L(M_{\mathrm{W}}) &= \prod_{i}^{K} \frac{\lambda_i^{N_i} e^{-\lambda_i}}{N_i!} \\ \lambda_i &= \lambda_i(M_{\mathrm{W}}) = N_i^{sig}(M_{\mathrm{W}}) + N_i^{bg}, \end{aligned} \tag{6.22}$$

where N_i is the number of data events in bin i and N_i^{bg} the expected number of W mass independent background events in bin i. K stands for the mass range. $N_i^{sig}(M_{\mathrm{W}})$ is the number of the expected signal and W mass dependent background events in bin i and can be calculated using the signal function:

$$\begin{aligned} N_i^{sig}(M_{\mathrm{W}}) &= (1 - f_{wrong}) f_{norm}\, p_i + N_i^{wrong} \\ p_i(M_{\mathrm{W}}) &= \int_{a_i}^{b_i} BW(m, M_{\mathrm{W}})\; GAUSS(m, M_{\mathrm{W}})\, dm, \end{aligned} \tag{6.23}$$

where f_{wrong} is the fraction of the wrong pair events in the signal events, f_{norm} is the normalisation factor to the total number of signal data ($N^{data} - N_{bg}^{MC}$) and N_i^{wrong} is the expected number of wrong pair events in bin i. The a_i and b_i are the bin boundaries. In the semi-leptonic channels, N_i^{sig} takes the simple form

$$N_i^{sig}(M_{\mathrm{W}}) = f_{norm}\, p_i. \tag{6.24}$$

The fit is performed separately on the four channels and limited to the range (68-88) GeV. The lower boundary is fixed to this value, because it is already in the tail of the distributions for the signal events (signal events with correct pairing in case of hadronic channel). The Monte Carlo studies show that the signal shape is well described up to $m_{rec} \sim 90$ GeV by this function. For the upper boundary, 88 GeV is taken, thus fixing a range where the fit quality is good.

The observed invariant mass distributions together with the fit results for the first and second pairing in $q\bar{q}q\bar{q}$ events are shown in Figure 6.17. The distributions for the semileptonic final states are shown in Figure 6.18. Monte Carlo studies show that the two values for M_{W} from fitting the distributions of the

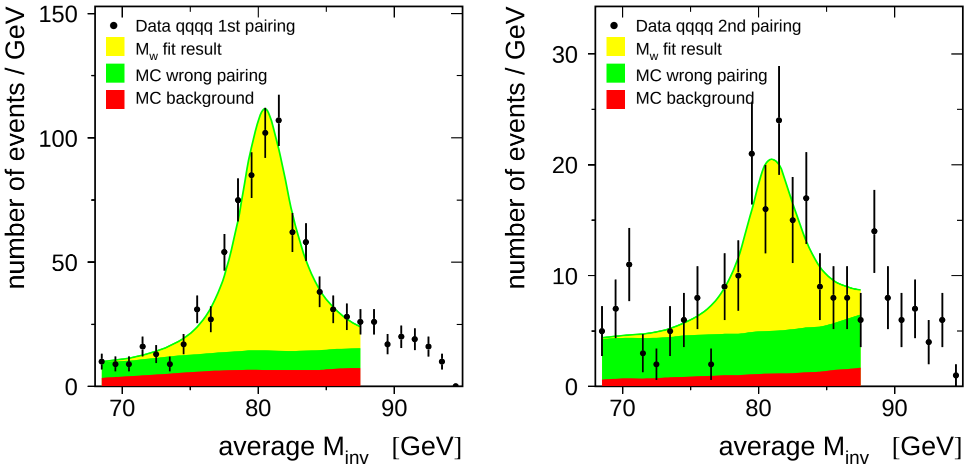

Abbildung 6.17: *Reconstructed mass distributions for $q\bar{q}q\bar{q}$ events selected in the 189 GeV data: first pairing and second pairing. The solid curves and light shading display the results of the fits of M_W to the indicated final states. The wrong pairing events are shown in the medium shaded region and the background alone by the dark shaded region.*

best and the second best combination separately have a correlation of (-0.4 ± 1.1)%, which is negligible. The third pairing is not used for the measurement of the W mass, since there is not much gain in W information.

The fitted masses must be corrected as already mentioned before. The bias correction is determined using KORALW Monte Carlo events corresponding to various input values of M_W at the same beam energy as the data.

To eliminate statistical and bin size problems and to account for the fluctuation arising from background events, many random subsamples of Monte Carlo signal and background events corresponding to the same integrated luminosity of the data are used to obtain the bias. These subsamples were processed through the same event selection and mass reconstruction, to account for all the possible biases from which the data may suffer. The subsamples correspond to 100 - 300 MC experiments for each input value of M_W, and they are fitted to the data. The mean value of the fit results from subsamples with a given mass input are used for the fitted value of those Monte Carlo events. Given Monte Carlo events

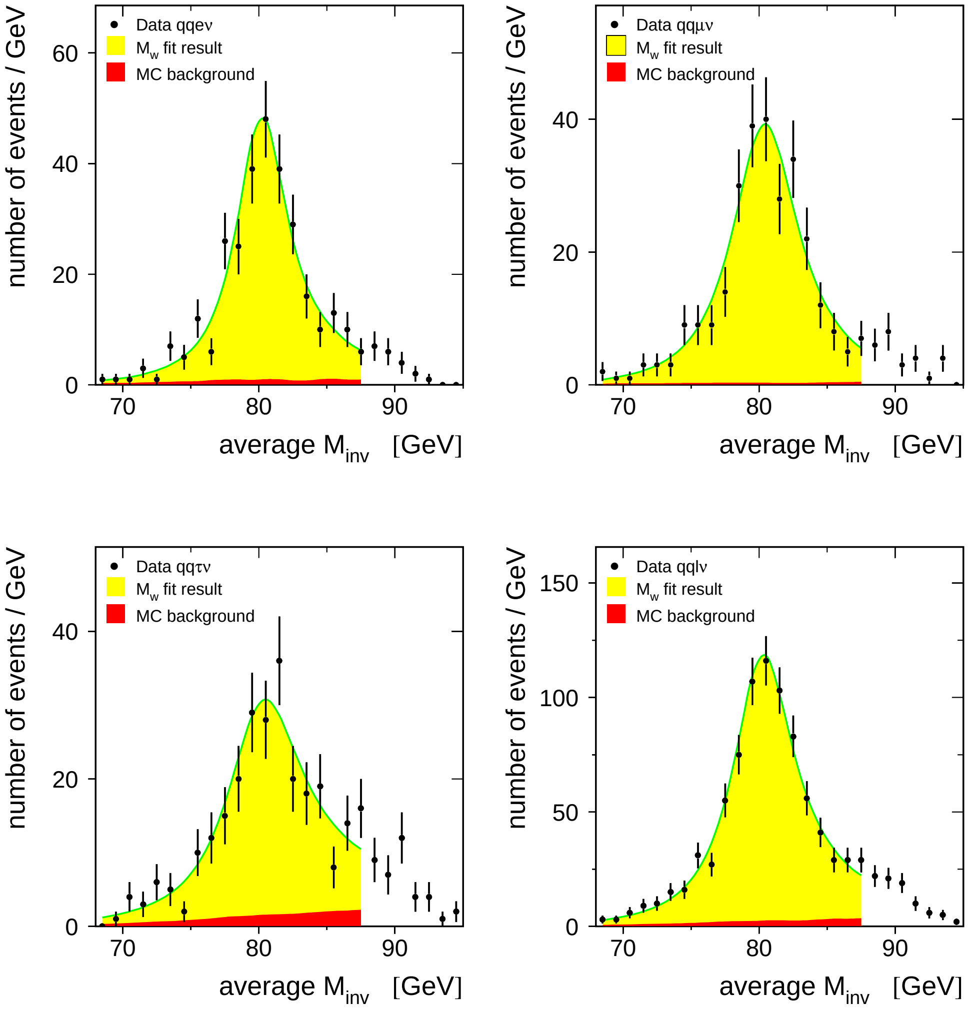

Abbildung 6.18: *Reconstructed mass distributions for the data at 189 GeV:*$q\bar{q}e\nu$*,* $q\bar{q}\mu\nu$*,* $q\bar{q}\tau\nu$ *and* $q\bar{q}l\nu$*, the combination of the three channels. The solid curves and light shaded areas display the results of the fits of* $M_{\rm W}$ *to the indicated final states. The background alone is shown by the dark shaded region.*

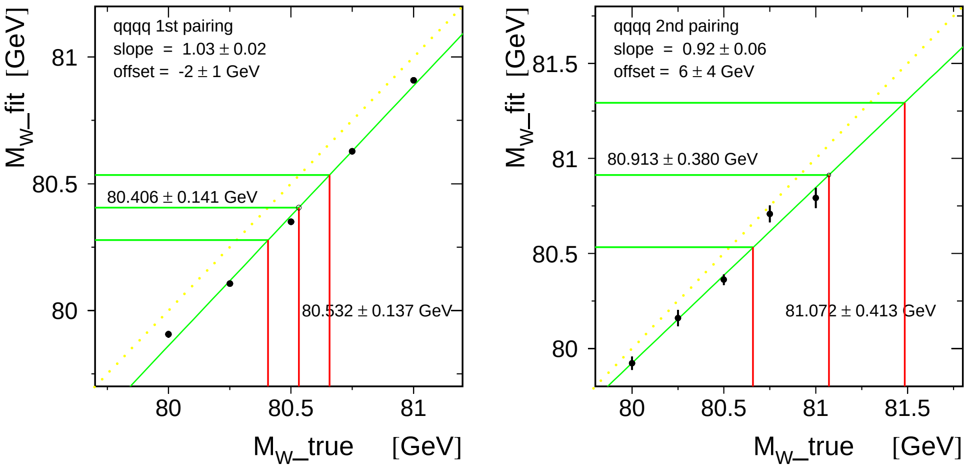

Abbildung 6.19: *Mean of the fitted masses versus generated mass for many Monte Carlo subsamples with five different input masses. The solid line through the points show the linear two parameter fits, used to obtain the bias corrections. The results of fitted and corrected masses are shown for the first best and the second best pairing in* $q\bar{q}q\bar{q}$ *events.*

with five different input values of M_{W}, five fitted values of M_{W} result. Again a linear two parameter χ^2 fit is performed with these values, and the slope and the offset of the straight line are determined. This straight line is used as the calibration curve. Figure 6.19 shows the calibration curves with the fitted and corrected masses and their errors for the $q\bar{q}q\bar{q}$ events. Those for the semileptonic final states are shown in Figure 6.20.

The linear fits of the final states indicate that the measurements are consistent with a linear hypothesis. The calibration curves from the linear two parameter χ^2 fits are taken and the fitted W masses and their errors are corrected based on these curves. The fit results are summarized in Table 6.1. The expected statistical errors have been determined using the subsamples constructed for the calibration curves. For the expected errors, the spreads of the fit results such as the mean values for the fitted mass values are taken and the correction is applied. The expected errors conform not only with the errors returned by the fits but also with those achieved in the fits to the data.

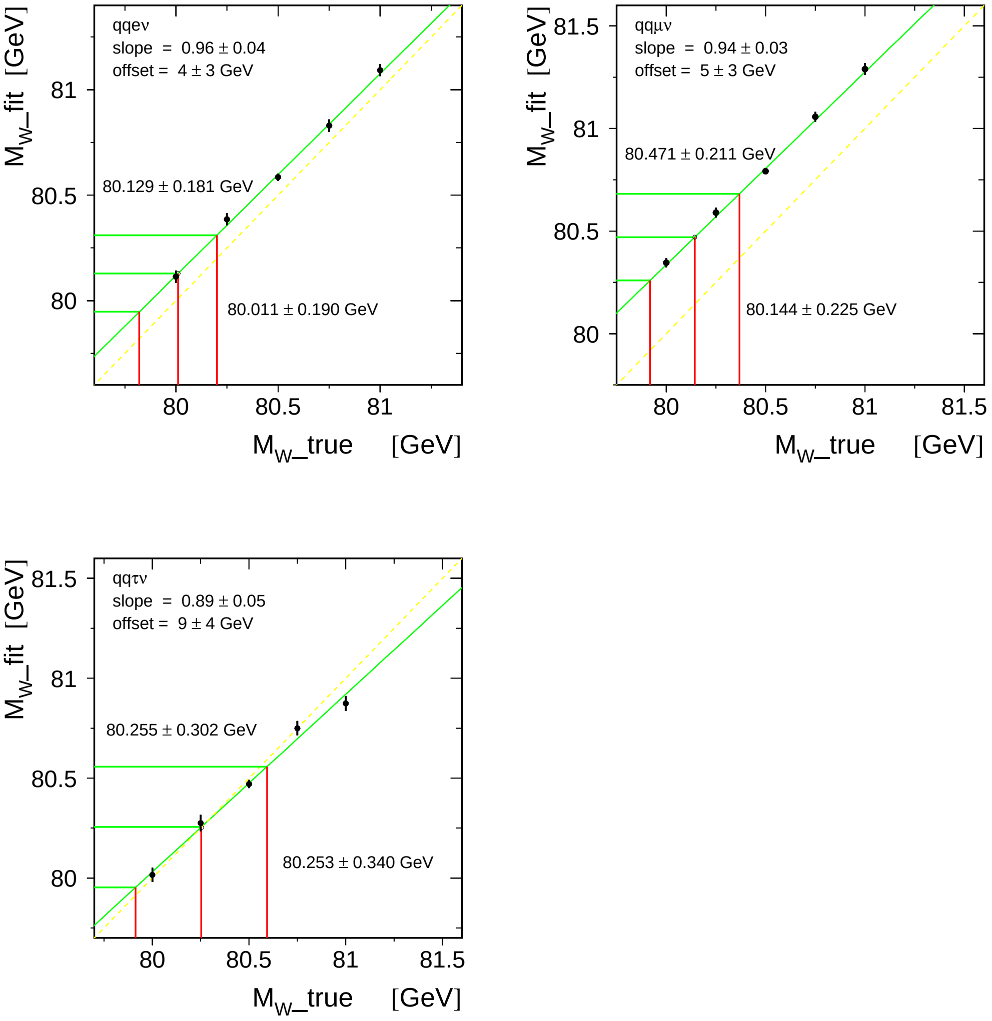

Abbildung 6.20: *Mean of the fitted masses versus generated mass for many Monte Carlo subsamples with five different input masses. The solid lines through the points show the linear two parameter fits used to obtain the bias corrections. The results of fitted and corrected masses are shown for the semileptonic final states.*

$\sqrt{s}$ = 189 GeV			
Process	Fitted mass [GeV]	Corrected mass [GeV]	Expected stat. error [GeV]
$q\bar{q}e\nu(\gamma)$	80.129 ± 0.181	80.011 ± 0.190	± 0.185
$q\bar{q}\mu\nu(\gamma)$	80.471 ± 0.211	80.144 ± 0.225	± 0.212
$q\bar{q}\tau\nu(\gamma)$	80.255 ± 0.302	80.253 ± 0.340	± 0.362
$q\bar{q}q\bar{q}(\gamma)$ 1st	80.406 ± 0.141	80.532 ± 0.137	± 0.125
$q\bar{q}q\bar{q}(\gamma)$ 2nd	80.913 ± 0.380	81.072 ± 0.413	± 0.495
$q\bar{q}l\nu(\gamma)$		80.095 ± 0.134	± 0.130
$q\bar{q}q\bar{q}(\gamma)$		80.586 ± 0.130	± 0.121
$f\bar{f}f\bar{f}(\gamma)$		80.346 ± 0.093	± 0.089

Tabelle 6.1: *Summary of fit results and Monte Carlo corrections to M_{W} for the Breit-Wigner fit method using the data collected at 189 GeV. The errors are statistical only. There is a small overlap of events between channels.*

$\sqrt{s}$ = 189 GeV		
	model comparison	correction [MeV]
$q\bar{q}q\bar{q}(\gamma)$ 1st	BE_0 vs BE_{32}(same)	-89 ± 23
$q\bar{q}q\bar{q}(\gamma)$ 2nd	BE_0 vs BE_{32}(same)	-140 ± 75
$q\bar{q}q\bar{q}(\gamma)$ 1st+2nd	BE_0 vs BE_{32}(same)	-93 ± 22

Tabelle 6.2: *mass differences between two Bose-Einstein models.*

As already mentioned in section 5.4.1, a correction of the mass from BE_0 version to BE_{32} version is necessary, to cover the incorrect implementation of Bose-Einstein effects in the BE_0 model. Table 6.2 shows the differences observed in the models for the $q\bar{q}q\bar{q}$ channel. Based on this study, the value for the M_{W} of $q\bar{q}q\bar{q}$ channel is corrected and the results are shown in Table 6.3. The mass of the W boson is

$$M_{\mathrm{W}}(189\ \mathrm{GeV}) = 80.300 \pm 0.093\ \mathrm{GeV}, \tag{6.25}$$

where the error is statistical only.

$\sqrt{s}\ =\ 189$ GeV	
Process	Fitted mass [GeV]
$q\bar{q}q\bar{q}(\gamma)$(before BE correction)	80.586 ± 0.130
$q\bar{q}q\bar{q}(\gamma)$(after BE correction)	80.493 ± 0.130
$f\bar{f}f\bar{f}(\gamma)$(after BE correction)	80.300 ± 0.093

Tabelle 6.3: *Final fit results of M_{W} using data collected at 189 GeV after the correction of Bose-Einstein models mentioned above. The errors are statistical only.*

6.2.4 Results of the Fit at 183 GeV

The measurement of M_{W} at $\sqrt{s} = 183$ GeV is done in exactly the same way as at $\sqrt{s} = 189$ GeV. The fit results are given in Table 6.4, and are compared with the data in Figure 6.22 and in Figure 6.21. The calibration curves with the fitted and corrected masses and their errors are shown in Figure 6.23 and in Figure 6.24.

As already mentioned in section 5.4.1, a correction of the mass from BE_0 version to BE_{32} version is necessary to cover the incorrect implementation of Bose-Einstein effects in the BE_0 model. The Table 6.5 shows the corrected result of the hadronic channel. The mass of the W boson is

$$M_{\mathrm{W}}(183\ \mathrm{GeV})\ =\ 80.532\ \pm\ 0.166\ \mathrm{GeV}, \tag{6.26}$$

where the error is statistical only.

6.3 Systematic Effects

The systematic errors on the fitted W mass arise from various sources and are divided into systematic errors correlated between final states and systematic errors uncorrelated to final states.

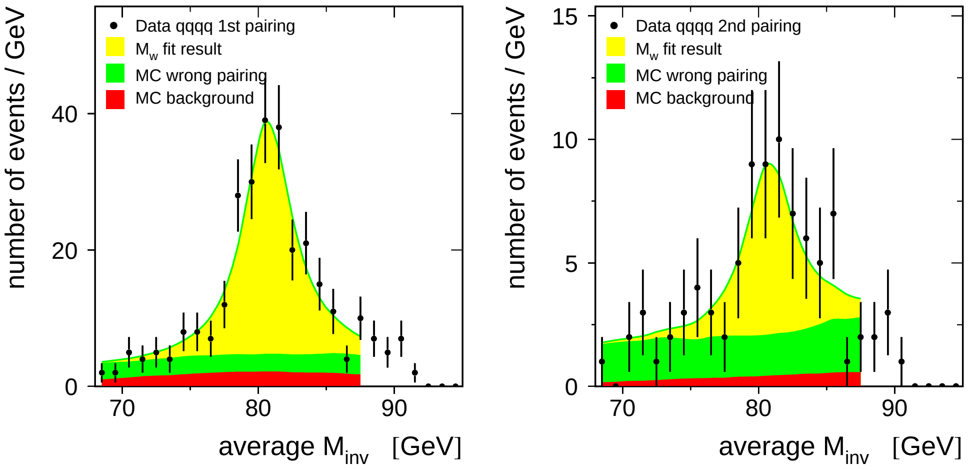

Abbildung 6.21: *Reconstructed mass distributions for $q\bar{q}q\bar{q}$ events selected in the 183 GeV data set: first pairing and second pairing. The solid curves and light shading display the results of the fits of M_W to the indicated final states. The wrong pairing events are indicated by the medium shaded region and the background by the dark shaded region.*

6.3.1 Correlated Errors

The LEP Beam Energy Uncertainty

The LEP beam energy is used as an absolute energy scale in the kinematic fit. The uncertainty of the beam energy will thus affect the reconstructed mass spectrum. Since the beam energy of LEP is known with an accuracy of ±20 MeV for the 1998 data period [104], the influence of this uncertainty on the W mass fit results can be estimated by changing the beam energy in the range of this uncertainty. This is studied with Monte Carlo events by changing the beam energy before performing the kinematic fits and comparing the mass fit results for different beam energies. An error of 17 MeV is is assigned as systematic error.

Initial State Radiation

The effects of the initial state radiation are not included in the kinematic fits. Since the energy conservation constraint of the kinematic fit increases systemati-

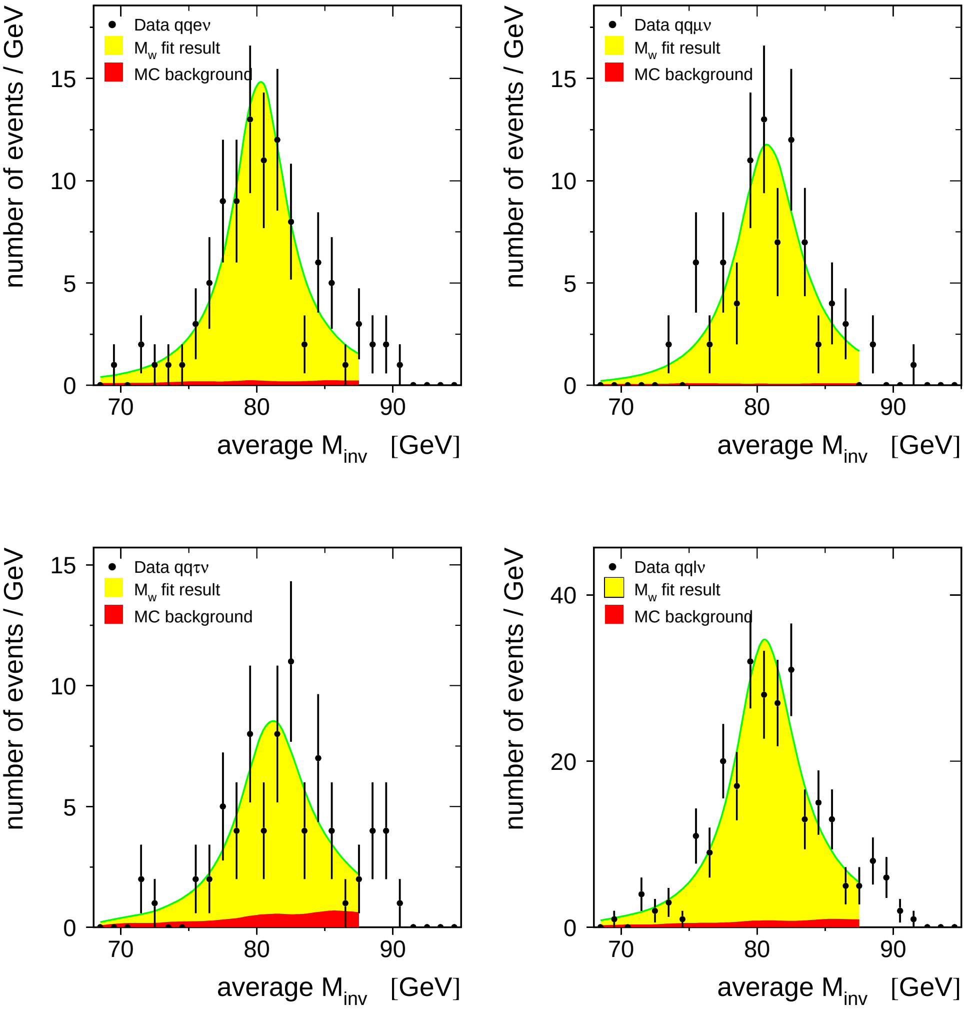

Abbildung 6.22: *Reconstructed mass distributions for the data at 183 GeV:*$q\bar{q}e\nu$*,* $q\bar{q}\mu\nu$*,* $q\bar{q}\tau\nu$ *and* $q\bar{q}l\nu$*, the combination of the three channels. The solid curves and light shading display the results of the fits of* M_W *to the indicated final states. The background itself is indicated by the dark shaded region.*

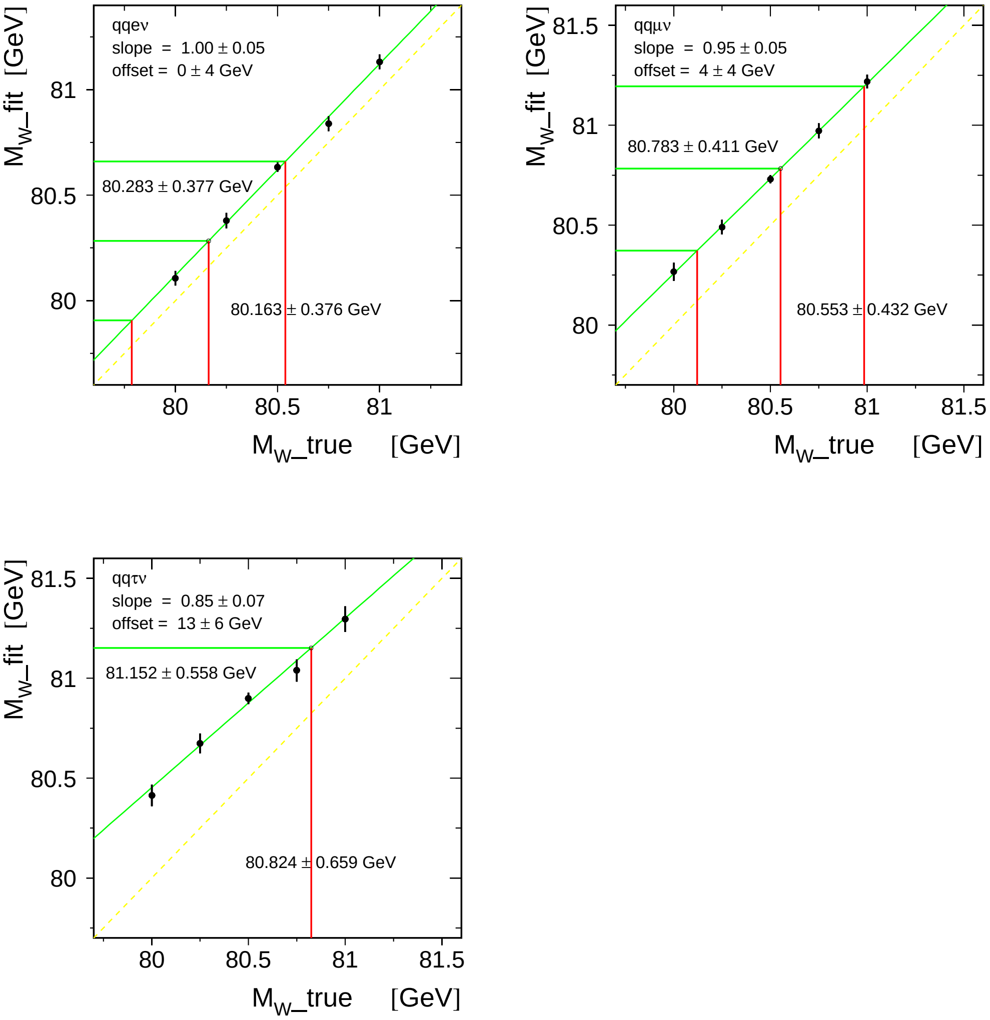

Abbildung 6.23: *Mean of the fitted masses versus generated mass for Monte Carlo subsamples with five different input masses. The solid line through the points show the linear two parameter fits used to obtain the bias corrections. The results of fitted and corrected masses are shown for the semileptonic final states.*

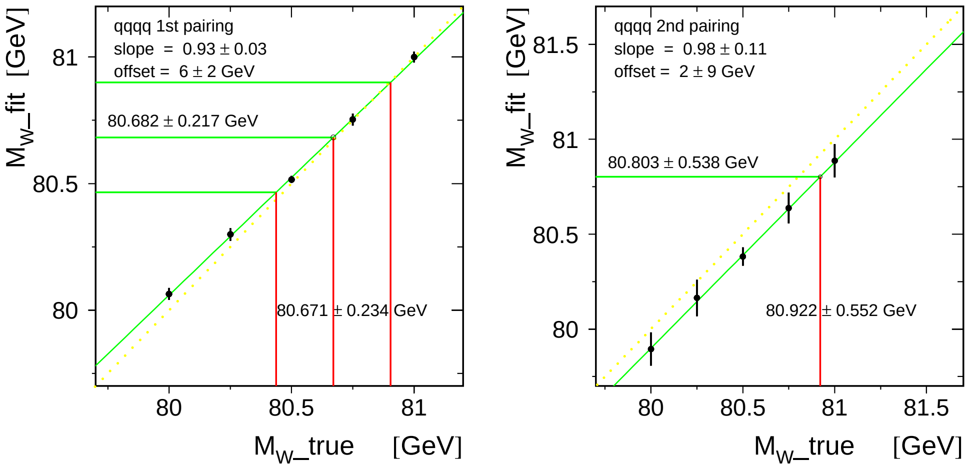

Abbildung 6.24: *Mean of the fitted masses versus generated mass for Monte Carlo subsamples with five different input masses. The solid line through the points show the linear two parameter fits used to obtain the bias corrections. The results of fitted and corrected masses are shown for the semileptonic final states.*

cally the reconstructed invariant mass, the fitted masses are higher. This bias is taken into account in both the reweighting and MC calibration fit method. But the correlated bias is only as accurate as the simulations in the Monte Carlo. There is still some systematic uncertainty due to incomplete modelling of ISR. To estimate this effect, a comparison is made between the Monte Carlo generators KORALW and EXCALIBUR, implementing different radiation schemes. The differences are $\approx$ 10 MeV, and they are shown in Table 6.12.

Jet Measurement

The MC calibration and reweighting procedures rely on the Monte Carlo assuming an accurate jet measurement. The uncertainty in the simulation of the energies and angles of jets and of their resolutions can influence the fit results of the W mass and is therefore a source of systematic error. The uncertainties in the simulation of jet properties as energies and angles are carried out studying hadronic $q\bar{q}(\gamma)$ events collected at the Z pole and at 189 GeV [105]. It is found

$\sqrt{s}$ = 183 GeV			
Process	Fitted mass [GeV]	Corrected mass [GeV]	Expected stat. error [GeV]
$q\bar{q}e\nu(\gamma)$	80.283 ± 0.377	80.163 ± 0.376	± 0.361
$q\bar{q}\mu\nu(\gamma)$	80.783 ± 0.411	80.553 ± 0.432	± 0.376
$q\bar{q}\tau\nu(\gamma)$	81.152 ± 0.558	80.824 ± 0.659	± 0.586
$q\bar{q}q\bar{q}(\gamma)$ 1st	80.682 ± 0.217	80.671 ± 0.234	± 0.253
$q\bar{q}q\bar{q}(\gamma)$ 2nd	80.803 ± 0.538	80.922 ± 0.552	± 0.838
$q\bar{q}l\nu(\gamma)$		80.408 ± 0.261	± 0.238
$q\bar{q}q\bar{q}(\gamma)$		80.709 ± 0.215	± 0.242
$f\bar{f}f\bar{f}(\gamma)$		80.587 ± 0.166	± 0.170

Tabelle 6.4: *Summary of fit results and Monte Carlo corrections to M_{W} for the BW fit method using the data collected at 183 GeV. The errors are purely statistical. There is a small overlap of events between channels.*

that they are consistent with a jet energy scaling by 0.1 GeV, a smearing of the jet energies by 1% and a smearing of the jet positions by 0.5°. To estimate the systematic error of the measured W mass, the jet properties are changed before the kinematic fits and the variation of the fitted mass values are determined. The change of the fitted mass values are regarded as systematic errors, and the total error is obtained adding the errors from all these checks in quadrature, see Table 6.6. This is the dominant experimental systematic error.

$\sqrt{s}$ = 183 GeV	
Process	Fitted mass [GeV]
$q\bar{q}q\bar{q}(\gamma)$(before BE correction)	80.709 ± 0.215
$q\bar{q}q\bar{q}(\gamma)$(after BE correction)	80.616 ± 0.215
$f\bar{f}f\bar{f}(\gamma)$(after BE correction)	80.532 ± 0.166

Tabelle 6.5: *Final fit results of M_{W} using data collected at 183 GeV after the correction of Bose-Einstein models mentioned above. The errors are statistical only.*

$\sqrt{s}$ = 189 GeV				
	Observed M_{W} shift in MeV			
	$q\bar{q}e\nu$	$q\bar{q}\mu\nu$	$q\bar{q}\tau\nu$	$q\bar{q}q\bar{q}$
E_{jet} smearing by 5 %	-3	-10	1	+6
E_{jet} + 0.2 GeV	+10	+48	+28	0
E_{jet} + 1.0 GeV	+45	+201	+129	-2
E_{jet} - 0.2 GeV	-10	-30	-23	0
E_{jet} - 1.0 GeV	-45	-182	-133	-6
Jet angle smearing by 0.5°	-2	+1	+5	+1
Jet angle smearing by 2°	+5	+7	-16	+3
	Rescaled errors			
E_{jet} smearing by 1 %	1	2	1	1
E_{jet} scale ± 0.1 GeV	5	20	15	1
Jet angle smearing by 0.5°	1	2	5	1
total systematic	5	20	15	1

Tabelle 6.6: *Systematic errors in jet measurements*

Fragmentation and Decay

Fragmentation and particle decays are simulated using string fragmentation as implemented in the PYTHIA Monte Carlo program. The influence of the choice of the hadronisation model on the results of the fitted mass is studied by comparing the string fragmentation and the cluster fragmentation as implemented in the HERWIG Monte Carlo program [67, 68]. The difference in the fitted masses is taken as an estimate for the systematic error, and this error is determined for each channel separately. The errors range from 20 to 70 MeV depending on the channels.

Fitting Method

The fitting method itself may have some bias. Since the the events are binned, the bin size is varied and half of the maximal effect with respect to the calibrated mass is taken as systematic error, see Table 6.7. The uncertainty on the wrong pairing fraction doesn't substantially affect the measured W mass, since the distributions of the wrong pairing events are flat.

$\sqrt{s}$ = 189 GeV				
Bin size [GeV]	Observed M_{W} shift in MeV			
	$q\bar{q}e\nu$	$q\bar{q}\mu\nu$	$q\bar{q}\tau\nu$	$q\bar{q}q\bar{q}$
0.25	+32	+18	+62	+16
0.50	0	0	0	0
1.00	+42	+10	+26	+4
total systematic	20	10	30	10

Tabelle 6.7: *Systematic errors in the fitting method*

6.3.2 Uncorrelated Errors

MC Statistics

Finite MC statistics means that the calibration constants will have a statistical error. But these errors are included automatically in the calibration procedure. In the correction procedure of the mass from BE_0 version to BE_{32} version, the uncertainty due to the limited amount of available MC events is 22 MeV. This statistical error is included in the estimation of the Bose-Einstein effect. Thus to avoid a double counting, no systematic error is quoted for MC statistics separately.

Selection

The effect of selection cuts on the measured W mass is automatically taken into account. Nevertheless the cut on the probability of the kinematic fit is varied to estimate the selection uncertainty. The interval of reconstructed invariant masses being fitted can be seen as an additional selection cut. To study the effect on the measured W mass of varying the mass window, the mass window of the nominal $68 < M_{inv} < 88$ GeV is varied over a range of ±2 GeV. The errors range from 10 to 25 MeV depending on the channels, see Table 6.12

Background

Background miss-modelling may change both the total accepted background cross section as well as the shape of the invariant mass spectrum arising from the background. To study the effect of background normalisation, the total ac-

$\sqrt{s}\ =\ 189$ GeV		
	Observed M_W shift in MeV	
	$q\bar{q}e\nu$	$q\bar{q}\mu\nu$
E_l shift by +10 % of σ_E	+39	+70
E_l shift by -10 % of σ_E	-33	-45
E_l smearing by 25 % of σ_E	-4	+13
Lepton angle smearing by 25 % of σ_θ	-1	+8
total systematic (rescaled)	10	20

Tabelle 6.8: *Systematic errors in lepton measurements*

cepted background cross section is varied within its error as evaluated for the cross section measurement, see section 5.4.1. Actually, the normalisation doesn't substantially affect the measured W mass. The effect of the background shape is estimated by measuring W masses shifting only the background shape over a range of ±2 GeV. The systematic errors are below 20 MeV.

Lepton Measurement

For $q\bar{q}e\nu$ and $q\bar{q}\mu\nu$ events, the reconstruction of the lepton energy and angles affects the invariant mass reconstruction, because the missing momentum calculation for the neutrino derives from these measurements. In analogy to hadronic jets, control samples of $l^+l^-(\gamma)$ events selected at the Z pole are used to cross check the reconstruction of leptons. Energy scales and resolutions are varied within their errors (energy shift by ±2.5% and energy and angle smearing by 10% of the resolutions) and the resulting effect on the W mass is quoted as a systematic error. Table 6.9 shows the results.

Bose-Einstein Effects

Both Bose-Einstein and colour reconnection effects affect only the W mass measurement in the $\mathrm{W}^+\mathrm{W}^- \rightarrow q\bar{q}q\bar{q}$ channel. As discussed in section 5.4.1, a significant bias in the measured W mass could arise from these effects. The systematic error concerning the Bose-Einstein effect is estimated by comparing MC simulations at 189 GeV center-of-mass energy including and excluding the modelling of these effects. Correlations between particles only inside each hadro-

$\sqrt{s}$ = 189 GeV		
	Observed shift in MeV	
	$q\bar{q}e\nu$	$q\bar{q}\mu\nu$
E_l shift by +10 % of σ_E	+39	+70
E_l shift by -10 % of σ_E	-33	-45
E_l smearing by 25 % of σ_E	-4	+13
Lepton angle smearing by 25 % of σ_θ	-1	+8
total systematic	10	20

Tabelle 6.9: *Systematic errors in lepton measurements*

$\sqrt{s}$ = 189 GeV		
MC generator	model comparison	systematic error [MeV]
KORALW	BE off vs BE_{32}(same)	-11 ± 28
	BE_{32}(all) vs BE_{32}(same)	-56 ± 28
PYTHIA	BE off vs BE_{32}(same)	+13 ± 23
	BE_{32}(all) vs BE_{32}(same)	-21 ± 21

Tabelle 6.10: *mass differences between several Bose-Einstein models.*

nically decaying W boson are studied as well as correlations of particles coming from different W bosons. In Table 6.10, the comparison of the models are listed for $\sqrt{s}$ = 189 GeV. The L3 experiment investigated Bose-Einstein correlations in the W^+W^- overlap region and the possible existence of these correlations between particles coming from different W's. No evidence for such an inter-W Bose-Einstein correlation is found [86]. Thus the model BE_{32}(all) isn't taken into consideration for the systematic error estimation. We end up with two numbers, (-11 ± 28) MeV and (+13 ± 23) MeV. In this analysis, the largest error of 28 MeV is regarded as systematic error arising from the Bose-Einstein effect.

Colour Reconnection

There has been much work done on the effects of colour re-arrangement at the hadronization level. However hadronization is poorly understood and progress can only be made through constructing models. Since we are interested in determining the effects of colour reconnection on the measured W mass, our first

$\sqrt{s}$ = 189 GeV	
MC generator	systematic error [MeV]
ARIADNE CR I	+2 ± 22
ARIADNE CR II	+56 ± 22
SK I	+19 ± 20
SK II	-32 ± 20
SK II'	-40 ± 20

Tabelle 6.11: *mass differences between several Colour Reconnection models.*

aim is to find physical observables, which may depend on these effects. Several observables have been studied such as the mean charged multiplicity[4]. With the sensitivity afforded by present statistics, no indication of such reconnection effects is observed [109]. Thus for the estimation of the systematic error arising due to colour reconnection, several scenarios are studied: the models SK I, II and II' as implemented in PYTHIA 5.7, the ARIADNE model type I and II. For the models ARIADNE I and II, half of the mass difference found is taken into account as in section 5.4.1. Table 6.11 lists the results of this study. The L3 data are compatible with any of these models, but a recent measurements of gluon jets in Z° decays [110] strongly disfavours the ARIADNE colour reconnection model. Accordingly, an error of 40 MeV based on the SK II' model is assigned as colour reconnection systematic error.

6.3.3 Systematics Summary

The different sources of systematic errors investigated in this analysis are summarized in Table 6.12. Concerning the final state interactions at $\sqrt{s} = 183$ GeV, the systematic errors are assumed to be the same as at $\sqrt{s} = 189$ GeV.

---

[4] The charged multiplicity has been of a great interest, because Ellis-Geiger model [106, 107] suggested that the mean hadronic charged multiplicity in $W^+W^- \to q\bar{q}q\bar{q}$ events, $< n_{ch}^{4q} >$, may be as much as 10% smaller than twice the hadronic charged multiplicity in $W^+W^- \to q\bar{q}l\nu$ events, $< n_{ch}^{q\bar{q}l\nu} >$ [108]. The predictions of the Ellis-Geiger model are different from data and other models [109]. Thus this model is not regarded.

	Final State							
Systematic Errors on M_{W} [MeV]	$\sqrt{s}$ = 183 GeV				$\sqrt{s}$ = 189 GeV			
	$q\bar{q}e\nu$	$q\bar{q}\mu\nu$	$q\bar{q}\tau\nu$	$q\bar{q}q\bar{q}$	$q\bar{q}e\nu$	$q\bar{q}\mu\nu$	$q\bar{q}\tau\nu$	$q\bar{q}q\bar{q}$
LEP Energy	25	25	25	25	17	17	17	17
ISR	15	15	15	10	15	10	10	5
FSR	10	10	10	5	10	10	10	5
Jet Measurement	10	25	25	10	5	20	15	1
Fragmentation	20	30	60	60	20	30	70	60
Fitting Method	15	15	15	10	20	10	30	10
Total Correlated	41	52	73	68	38	44	80	63
Selection	10	10	10	20	15	10	10	25
Background	5	0	20	10	5	0	15	5
Lepton Measurement	15	15	-	-	10	20	-	-
Bose-Einstein Effects	-	-	-	30	-	-	-	30
Colour Reconnection	-	-	-	40	-	-	-	40
Total Uncorrelated	19	16	22	55	19	22	18	56
Total Systematic	45	54	76	87	42	49	82	84

Tabelle 6.12: *Systematic errors in the determination of M_{W} for the different final states. The contributions listed in the upper part of the table are treated as correlated when combining different final states. The contributions listed in the lower part are treated as uncorrelated between channels. Total errors are obtained by adding the individual contributions in quadrature.*

6.4 Reweighting Method

In section 6.2, we have produced 5 MC samples with W masses between 80 GeV and 81 GeV, and the fit result of the data has been corrected for possible biases based on these samples. Since Monte Carlo simulations are used, one could try to produce MC samples in 10 MeV steps or even in 1 MeV steps and scan the invariant mass distributions. The input W mass of a generated MC sample which best fits the data distribution will be taken as the mass of the W boson. In this way one need not calibrate or care about resolution effects since this method is bias free by definition. Technically, this method is possible, but it would require a lot of CPU time and disk space for storage. Therefore, a reweighting procedure is used instead.

In the reweighting method, we produce a large Monte Carlo sample at one reference W mass, M_{W}^{ref}. To produce the detector level invariant mass distribution at a different value of M_{W}^{new}, a reweighting factor is calculated such that the sum of the accepted background and reweighted accepted signal events coincide with the observed number of events. Thus, the mass is entirely determined by the shape of the invariant mass distribution. This value represents the ratio of the probability that the event would be produced assuming the new value of M_{W}^{new} to the probability that this same event would be produced for the input value M_{W}^{ref}. The reweighting factor for the ith event is given by

$$w_i(M_{\mathrm{W}}^{new}) = \frac{BW(M_{\mathrm{W}}^{new}, m_1^i) \cdot BW(M_{\mathrm{W}}^{new}, m_2^i)}{BW(M_{\mathrm{W}}^{ref}, m_1^i) \cdot BW(M_{\mathrm{W}}^{ref}, m_2^i)}, \tag{6.27}$$

where m_1, m_2 are the invariant masses of the W Bosons at the generator level. The running-width relativistic Breit-Wigner function of 6.17 is taken for this purpose, since the production probabilities for the W events in CC03 diagrams are given by

$$P(M_{\mathrm{W}}, \Gamma_{\mathrm{W}}, m_1, m_2) \propto \sigma_0(m_1, m_2, s) \times BW(M_{\mathrm{W}}, \Gamma_{\mathrm{W}}, m_1) \times BW(M_{\mathrm{W}}, \Gamma_{\mathrm{W}}, m_2), \tag{6.28}$$

where σ_0 is the Born level cross section for producing a pair of the two W bosons with masses m_1, m_2 at a center-of-mass energy $\sqrt{s}$. Only the invariant mass distributions of both reconstructed W's per event are considered and reweighted in this thesis, even though other distributions containing information of the W mass (e.g. W production angles) could also be used and reweighted.

The background invariant mass distributions are derived from Monte Carlo and are assumed to be independent of M_{W}. They are normalised to the expected number of background events.

The compatibility of the reweighted Monte Carlo and data invariant mass distributions is calculated through a binned likelihood method. The best estimator

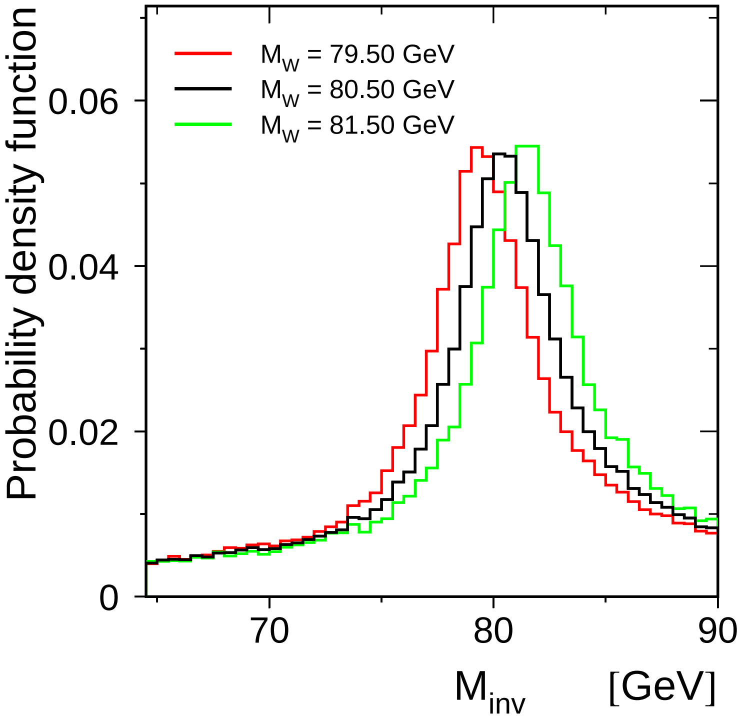

Abbildung 6.25: *Invariant mass distributions for a reference W mass of 80.50 GeV and two reweighted masses of 79.50 and 81.50 GeV. All distributions are normalized to the same number of events.*

of the W mass is the one that maximizes the likelihood function :

$$
\begin{aligned}
L(M_{\mathrm{W}}) &= \prod_{i=1}^{K} \frac{\lambda_i^{N_i} e^{-\lambda_i}}{N_i!} \\
\lambda_i &= \lambda_i(M_{\mathrm{W}}) = N_i^{bg} + N_i^{sig}(M_{\mathrm{W}}), \qquad (6.29)
\end{aligned}
$$

where N_i stands for the amount of data in bin i and N_i^{bg} and N_i^{sig} for the expected number of background and signal events from Monte Carlo. K is the number of bins. A decomposition of the signal events into the right and wrong pair events is not necessary, since the reweighting method doesn't distinguish between them.

Figure 6.25 shows how the reweighting method changes the invariant mass distribution from a reference W mass ($M_{\mathrm{W}}^{ref} = 80.50$ GeV) to two different M_{W}

values of 79.50 and 81.50 GeV. All distributions are normalized to the same number of events.

6.4.1 Statistical Power of Weighted Events

So far, the reweighting method seems to be well suited for the W mass estimation. There still remains one important unknown. The weighted events have limited statistical power. For a set of n events, the effective number of generated events (n_{eff}) is given through

$$n_{eff} = \frac{(\sum_{i=1}^{n} w_i)^2}{\sum_{i=1}^{n} w_i^2} \leq n. \tag{6.30}$$

If n_{eff} is small compared to the number of generated events, the Monte Carlo simulation through the reweighting method is inefficient.

Figure 6.26 shows the distributions of weights when the reference sample $M_{\mathrm{W}}^{ref} = 80.50$ GeV is reweighted to other masses. Those distributions reweighted to very different W masses have a large RMS. This shows that the more different M_{W} is from M_{W}^{ref}, the more the weights differ from unity, thus lowering the effective number of events. The loss of n_{eff} is approximately 50% for a new W mass value that is 1 GeV away from the reference W mass, M_{W}^{ref}. Therefore, the reference Monte Carlo sample must be quite large in order to avoid statistical fluctuations from the reweighting process and the resulting bias from the limited statistics. In this analysis, all available Monte Carlo samples are used in the reweighting procedure to minimise this effect. To fit the data, approximately 300.000 selected MC events are used for the $q\bar{q}q\bar{q}$ channel.

6.4.2 Linearity

A critical test of the methodology is the absence of any bias. For this check, five samples of simulated events with known W mass values of 80.00, 80.25, 80.50, 80.75 and 81.00 GeV are used. Figure 6.27 shows the fitted masses as a function of the generated ones for all the channels. The results of a linear two parameter (slope and offset) least squares fit to the final state demonstrate that the response of the likelihood fit to M_{W} is compatible with the ideal case of a linear relation with a slope of one and an offset of zero. The test for the second pair events of

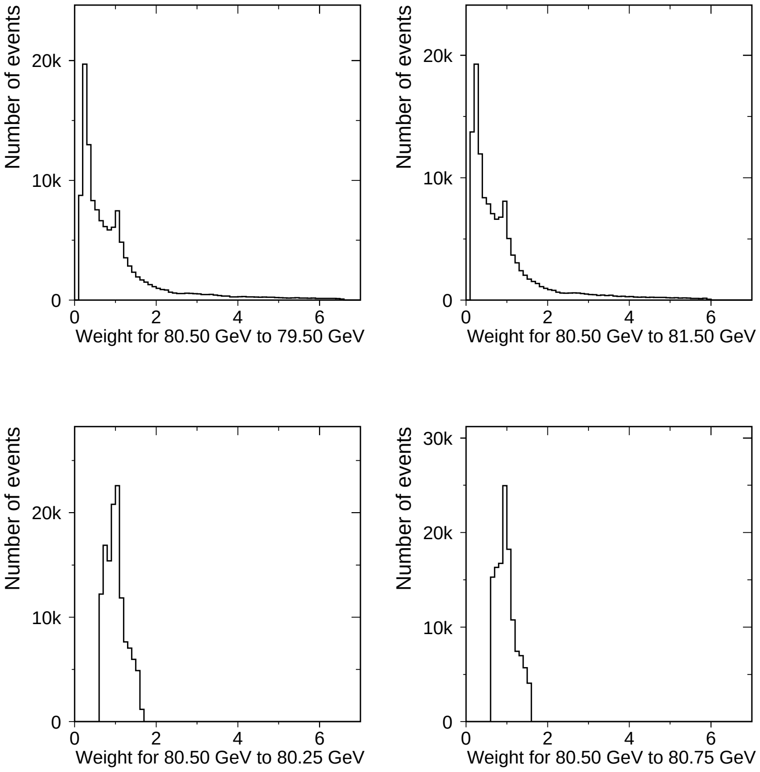

Abbildung 6.26: *Event weight distributions when the Monte Carlo reference sample at* $M_{\mathrm{W}}^{ref} = 80.50$ *GeV is reweighted to different* M_{W}*'s.*

the $q\bar{q}q\bar{q}$ channel is not shown here, but the results are also compatible with no bias.

6.4.3 Fit Results at 189 GeV

The reconstructed invariant mass distributions for the selected events in the $\sqrt{s} = 189$ GeV data sample are shown in Figures 6.28 and 6.29. The open histograms are the reweighted Monte Carlo spectra corresponding to the fitted masses. Below 60 GeV, there are only wrong pair events in the case of the $q\bar{q}q\bar{q}$ channel and nearly no $q\bar{q}l\nu$ events in the reconstructed mass distribution. Thus the mass fit is limited to the mass range 60 GeV $< M_{inv} < E_{beam}$.

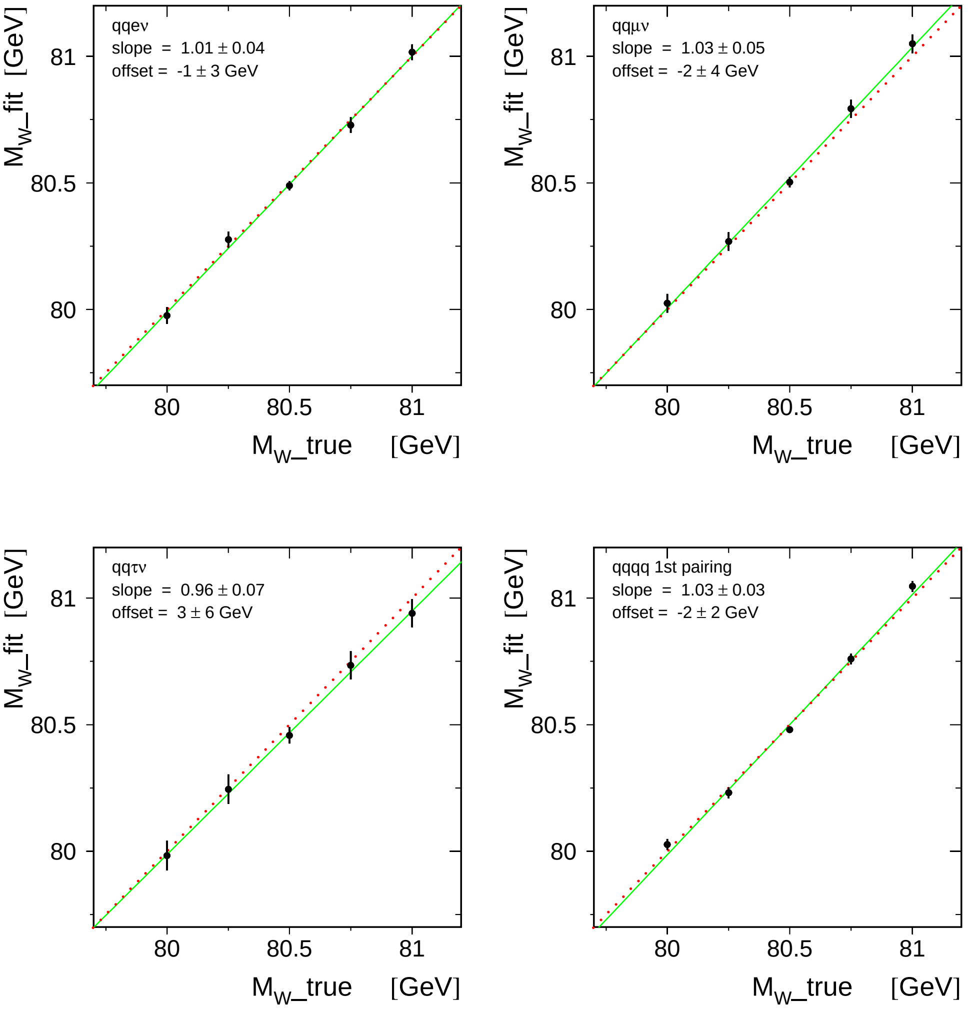

Abbildung 6.27: *Likelihood response curves from Monte Carlo samples. The solid lines through the points show the results of the linear two parameter fits. The dotted lines show the ideal case of a linear relation with a gradient of one and an offset of zero.*

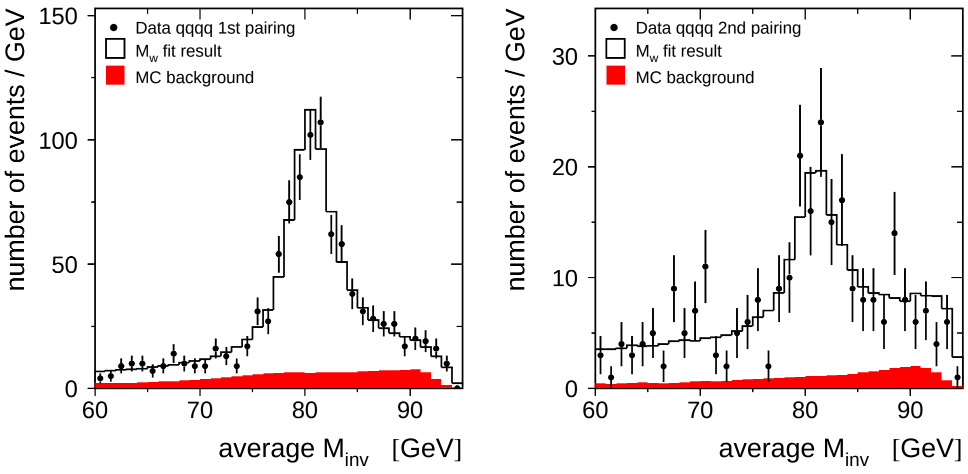

Abbildung 6.28: *Distributions of the reconstructed invariant mass after applying the kinematic fit using the equal-mass constraint for $q\bar{q}q\bar{q}$ events selected in the 189 GeV data. The points correspond to the L3 data and the open histogram to the reweighted Monte Carlo spectrum corresponding to the fitted mass. The background contribution is indicated by the dark shaded region.*

The events from different channels are fitted separately and combined afterwards. The results of the fits are given in Table 6.13.

As already mentioned in section 5.4.1, a correction of the mass from BE_0 version to BE_{32} version is necessary to cover the incorrect implementation of Bose-Einstein effects in the BE_0 model. Table 6.14 shows the differences observed in the models for the $q\bar{q}q\bar{q}$ channel, which are consistent to those found in the MC calibration method. Based on this study, M_{W} of the $q\bar{q}q\bar{q}$ channel is corrected and the results are shown in Table 6.15. The final result for the W mass is

$$M_{\mathrm{W}}(189\ \mathrm{GeV}) \; = \; 80.297 \pm 0.095\ \mathrm{GeV}, \tag{6.31}$$

where the error is only statistical. This result is in agreement with the results obtained with the Monte Carlo calibration method, providing us with an excellent cross-check of the MC calibration method.

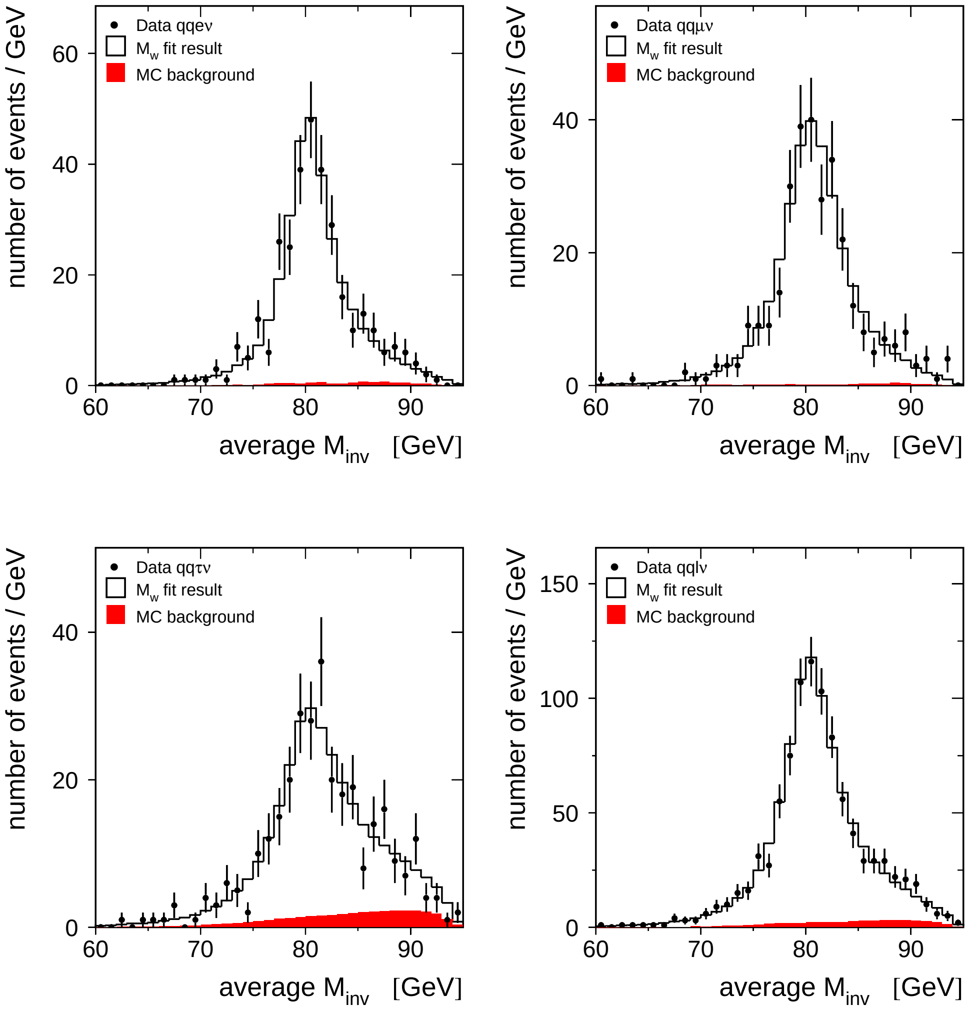

Abbildung 6.29: *The reconstructed invariant mass distribution for the selected events of type $q\bar{q}e\nu, q\bar{q}\mu\nu, q\bar{q}\tau\nu$ and $q\bar{q}l\nu$, the combination of these three channels. The points correspond to the L3 data and the open histogram to the reweighted Monte Carlo spectrum corresponding to the fitted mass. The background contribution is indicated by the dark shaded region.*

$\sqrt{s}\ =\ 189$ GeV		
Process	Fitted mass [GeV]	
	RW	BW
$q\bar{q}e\nu(\gamma)$	79.990 ± 0.200	80.011 ± 0.190
$q\bar{q}\mu\nu(\gamma)$	80.230 ± 0.219	80.144 ± 0.225
$q\bar{q}\tau\nu(\gamma)$	80.116 ± 0.350	80.253 ± 0.340
$q\bar{q}q\bar{q}(\gamma)$ 1st	80.509 ± 0.142	80.532 ± 0.137
$q\bar{q}q\bar{q}(\gamma)$ 2nd	81.030 ± 0.354	81.072 ± 0.413
$q\bar{q}l\nu(\gamma)$	80.102 ± 0.136	80.095 ± 0.134
$q\bar{q}q\bar{q}(\gamma)$	80.581 ± 0.132	80.586 ± 0.130
$f\bar{f}f\bar{f}(\gamma)$	80.349 ± 0.095	80.346 ± 0.093

Tabelle 6.13: *Summary of fit results for the reweighting fit (RW) method using the data collected at 189 GeV. The errors are statistical only. There is a small overlap of events between channels. The results of the Breit-Wigner MC calibration method (BW) are added to the table for the comparison.*

$\sqrt{s}\ =\ 189$ GeV		
	model comparison	correction [MeV]
$q\bar{q}q\bar{q}(\gamma)$ 1st	BE_0 vs BE_{32}(same)	-99 ± 24
$q\bar{q}q\bar{q}(\gamma)$ 2nd	BE_0 vs BE_{32}(same)	-123 ± 89
$q\bar{q}q\bar{q}(\gamma)$ 1st+2nd	BE_0 vs BE_{32}(same)	-101 ± 23

Tabelle 6.14: *mass differences between several Bose-Einstein models.*

6.4.4 Reproducibility Checks

It is essential to determine whether the chosen fitting method gives results that are reproducible and stable. In the linearity test, the fitted masses of Monte Carlo events are consistent with the W masses generated in the MC samples. Thus there is no bias concerning the fitted masses. But what about the errors ? Are the errors resulting from it trustworthy ? Many Monte Carlo experiments are done to test this. 100 to 150 samples corresponding to the data luminosity are randomly drawn from a large Monte Carlo event reservoir. The samples are chosen in a way that the same Monte Carlo event is not used twice. A mass

$\sqrt{s}$ = 189 GeV	
Process	Fitted mass [GeV]
$q\bar{q}q\bar{q}(\gamma)$(before BE correction)	80.581 ± 0.132
$q\bar{q}q\bar{q}(\gamma)$(after BE correction)	80.480 ± 0.132
$f\bar{f}f\bar{f}(\gamma)$(after BE correction)	80.297 ± 0.095

Tabelle 6.15: *Final fit results of M_{W} using data collected at 189 GeV after the correction of Bose-Einstein models mentioned above*

value and its error is extracted for each of the samples and plotted. Since all mass and error distributions appear to be Gaussian, a Gaussian fit is applied to the distributions. Here, two fit values are important, the spread of the mass distributions and the mean value of the fit error distributions. Figure 6.30 shows the distributions after the reweighting fit for each channel. As one can observe, the spreads of the mass distributions and the average fit errors correspond. The error of the mass fit is thus reliable. The spreads of the mass distributions are also taken as the expected statistical errors, which comply with the observed statistical errors. The results are summarized in the Table 6.16.

$\sqrt{s}$ = 189 GeV		
Process	spread of mass distribution [MeV]	average fit error [MeV]
$q\bar{q}\mathrm{e}\nu(\gamma)$	189	188
$q\bar{q}\mu\nu(\gamma)$	203	215
$q\bar{q}\tau\nu(\gamma)$	357	350
$q\bar{q}q\bar{q}(\gamma)$ 1st	128	129
$q\bar{q}q\bar{q}(\gamma)$ 2nd	377	374
$q\bar{q}l\nu(\gamma)$	129	131
$q\bar{q}q\bar{q}(\gamma)$	121	122
$f\bar{f}f\bar{f}(\gamma)$	88	89

Tabelle 6.16: *Gaussian fit to the reweighting fit results of the MC samples*

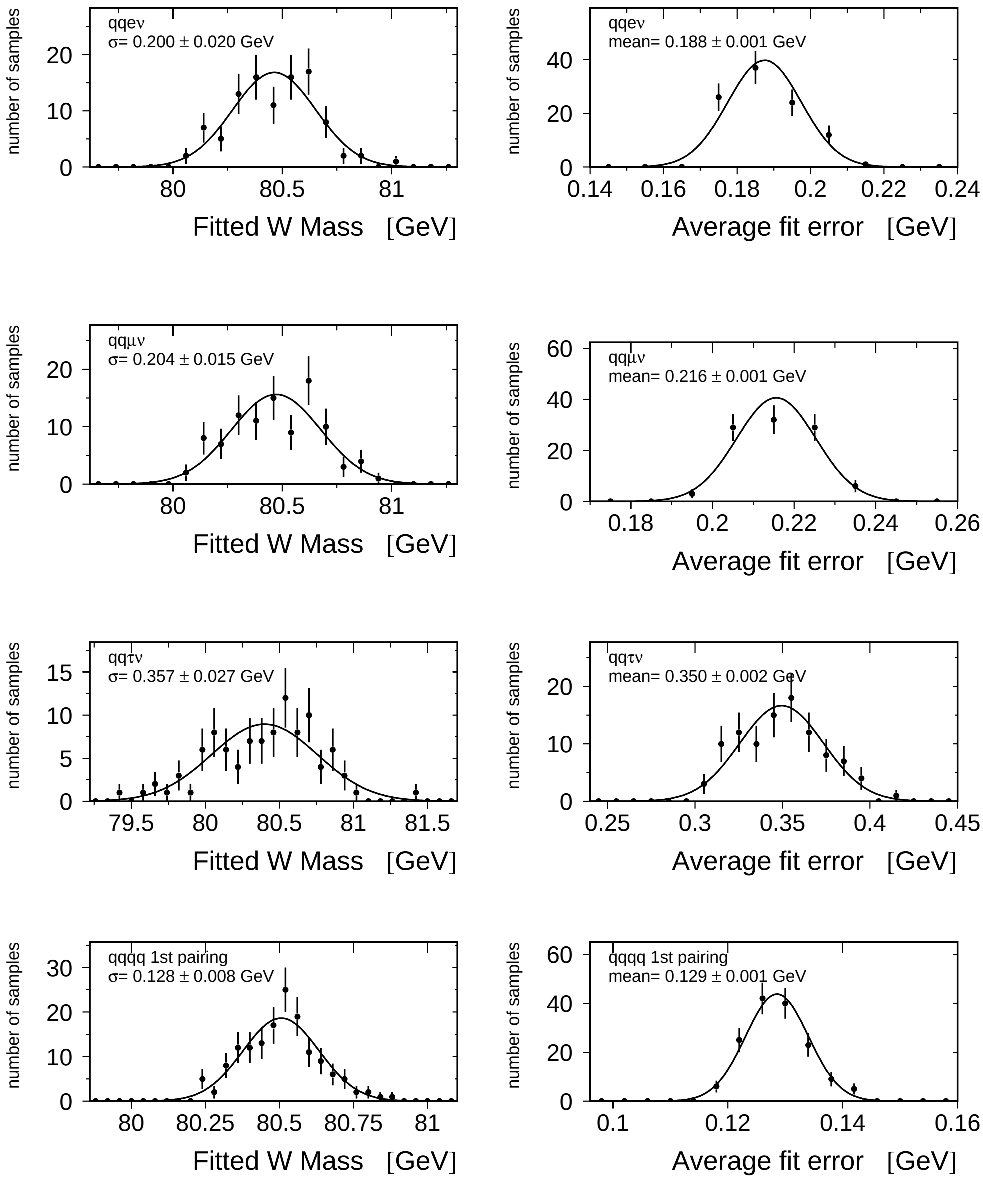

Abbildung 6.30: *Distributions of the fitted masses and parabolic fit errors for about 100 - 150 independent subsamples for each channel. For the simulation of the events,* $M_{\mathrm{W}}^{gen}= 80.50$ *GeV is used.*

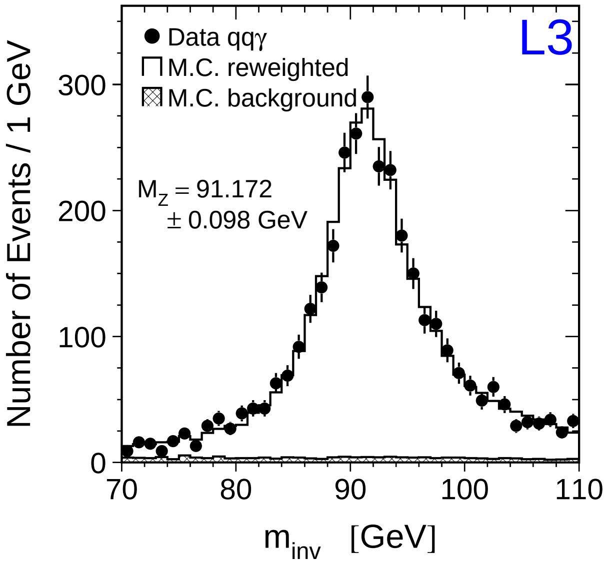

Abbildung 6.31: *Distribution of the reconstructed invariant mass, m_{inv}, after applying the kinematic fit for $q\bar{q}\gamma$ events with hard initial-state radiation selected at 183 GeV. Shown is the region corresponding to the radiative return to the Z. The solid line shows the result of the fit of M_Z. The quoted error is statistical.*

6.4.5 Z Mass Reconstruction as Consistency Check

So far two different methods have been examined to cross-check the results of the W mass measurement from each method. The results of W mass measurements obtained with the Monte Carlo calibration method are in agreement with the results of the MC reweighting method. Nonetheless, it could still be argued that these two methods both rely on the Monte Carlo. How can one be sure that the measured masses are really correct ? To test this hypothesis, the reweighting method was checked using $e^+e^- \rightarrow q\bar{q}\gamma$ events as published [111]. The events were selected at $\sqrt{s} = 183$ GeV. For such events, the hard initial-state radiative photon reduces the center-of-mass energy of the e^+e^- interaction and the invariant mass distribution of the jet-jet system shows a clear Z mass spectrum near 91 GeV. From this invariant mass spectrum, the Z mass was extracted using the same reweighting method as it is applied for the W mass measurement. If the Z mass extracted by this method is consistent with the Z mass measurement derived from cross section measurements at center-of-mass energies close to the Z pole, one can be sure, that the W mass determined through this method is correct and reliable.

The reconstructed mass spectrum is shown in Figure 6.31. The fitted Z mass is $M_\mathrm{Z} = 91.172 \pm 0.098$ GeV, where the error is statistical. The Z mass from the cross section measurements is $M_\mathrm{Z} = 91.190 \pm 0.003$ GeV [112] and thus in agreement.

6.5 Test of CPT Invariance

Through the entire analysis, the masses of W bosons have been assumed independent of their charge. But how is this known ?

The properties of $\mathrm{e}^+\mathrm{e}^-$ collisions at LEP2 allow the production of W's in a clean environment and create a unique opportunity to measure the masses of charged W bosons in direct reconstruction. For this purpose the data sample used for the W mass measurement can be used. This test is important, because it tests a basic prediction of CPT invariance, that the masses of W^+ and W^- are equal.

For a stable massive particle the CPT invariance is easy to understand. Such a particle state $|\mathbf{a}>$ is an eigenstate of the Hamiltonian $\mathbf{H}$ of the theory, and in the rest system of $\mathbf{a}$ the eigenvalue $\mathbf{m}$ is the mass of $\mathbf{a}$:

$$\mathbf{H}|\mathbf{a}\rangle = \mathbf{m}|\mathbf{a}\rangle \tag{6.32}$$

Now apply a CPT transformation to this equation. $\mathbf{H}$ transforms by assumption into itself, and $|\mathbf{a}>$ into the antiparticle state $|\bar{\mathbf{a}}>$. Hence the masses of $\mathbf{a}$ and $\bar{\mathbf{a}}$ are equal.

For unstable particles, i.e. resonances, one requires quantum field theory. Resonances appear as complex poles in the corresponding S matrix elements, at $z = (m - i\Gamma/2)^2$. Stable particles appear as real poles. Γ is the total decay rate and, by definition, m is the mass of the resonance. Now study the FULL propagator (includes all self interactions) of an (unstable) particle, for instance the W^+, and the corresponding propagator for the antiparticle, i.e. W^-. CPT invariance implies that both propagator functions are equal, hence also their poles [113].

In the following, the determination of the masses of the charged W bosons are described.

6.5.1 Masses of the Charged W Bosons for $\mathrm{W}^+\mathrm{W}^- \to q\bar{q}l\nu$

The selection of $\mathrm{W}^+\mathrm{W}^- \to q\bar{q}l\nu$ events with $l = \mathrm{e}, \mu$ requires an identified high energy electron or muon, two hadronic jets and missing momentum due to one neutrino. The electric charge of the jet-jet system can be extracted from the determination of the charge of the lepton. The neutrino four-momentum vector is constructed by using the missing three-momentum vector, taken to be massless.

In order to determine the masses of positively and negatively charged W bosons, the invariant mass distributions without kinematic fit are used. The kinematic fit improves the mass resolution, but the two masses of the W bosons in each event are strongly anti-correlated after it. The extraction of the masses is done with the reweighting method as described in section 6.4. The events fitted are limited to the mass range 40 GeV $< M_{inv} <$ 130 GeV. The reconstructed invariant mass distributions at $\sqrt{s} = 183 - 189$ GeV are shown in Figure 6.32. The mass differences between W^+ and W^- are:

$$\begin{array}{ll} q\bar{q}\mathrm{e}\nu & M_{\mathrm{W}^+} - M_{\mathrm{W}^-} = +0.59 \pm 0.76 \text{ GeV} \\ q\bar{q}\mu\nu & M_{\mathrm{W}^+} - M_{\mathrm{W}^-} = +0.68 \pm 0.67 \text{ GeV} \end{array}$$

The errors are only statistical, since the systematic errors cancel out in the difference. The combined result of $q\bar{q}\mathrm{e}\nu$ and $q\bar{q}\mu\nu$ final states is

$$q\bar{q}l\nu \qquad M_{\mathrm{W}^+} - M_{\mathrm{W}^-} = +0.64 \pm 0.50 \text{ GeV}$$

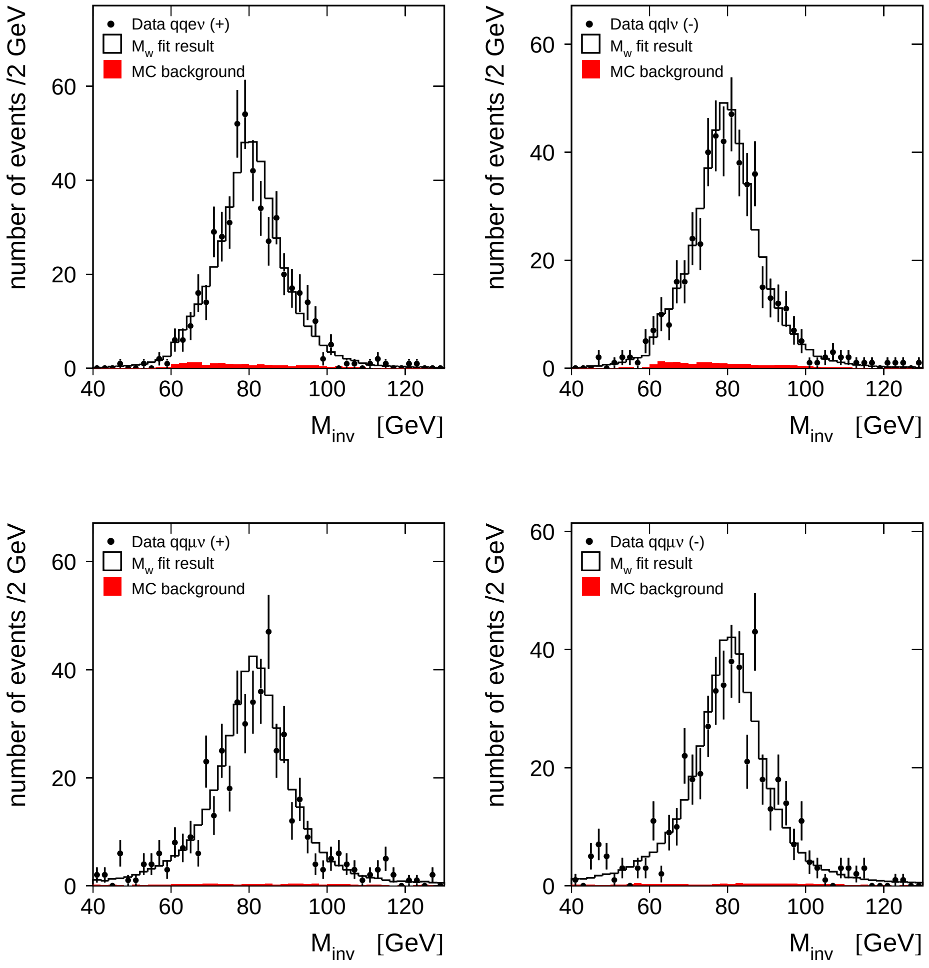

Abbildung 6.32: *Distributions of reconstructed invariant masses. The plots on the left side show the positively charged W bosons and the plots on the right side the negatively charged W bosons of the data (points with error bars) at* $\sqrt{s} = 183 - 189$ *GeV. The solid line histograms are the fit results. The background contributions are indicated by the dark shaded region.*

6.5.2 Masses of the Charged W Bosons for $W^+W^- \rightarrow q\bar{q}q\bar{q}$

Reconstruction of W Charge

Clustering algorithms take the large number of particles produced in high-energy collisions and cluster them into a small number of jets. Such a simplification of the events reflects the partonic picture. If so, there might be a way to estimate the charges of the initial quarks. Actually this was proposed by Field and Feynman [114] in 1978 in order to separate u and d quarks in jets. Since we assume that the initial quark ends up in the high momentum hadrons, the most common jet charge parameterisation is

$$Q_{jet} \;=\; \frac{\sum q_i(\vec{p_i}\cdot\vec{P}_{jet})^\kappa}{\sum(\vec{p_i}\cdot\vec{P}_{jet})^\kappa}, \tag{6.33}$$

where q_i is the charge of the ith charged particle, $\vec{p_i}$ is the ith particle's momentum and $\vec{P}_{jet}$ is the momentum of the jet. The parameter κ is a weighting factor. The idea behind this is that the particles closest to the jet axis with the highest energy carry most information of the initiating parton's charge.

This method is applied to $e^+e^- \rightarrow W^+W^- \rightarrow$ four jets [115]. The W charge determination uses the fact that the two Ws have well defined charges, assuming the jets have been correctly paired. For each event, the charge difference is determined as follows

$$\triangle Q \;=\; Q_{W1} \;-\; Q_{W2} \;=\; q_{j1}+q_{j2}-(q_{j3}+q_{j4}), \tag{6.34}$$

where Q_{Wi} stands for the charge of W bosons and q_{ji} for the jet charge. If the value of $\triangle Q$ is positive, W1 is assumed to be the W^+. If it's the other way around, W2 is assumed to be the W^+. This method allows for a correct charge assignment in 69% of the case of right jet pairing. The W charge difference is shown in Figure 6.33 [115]. Two pairs of jets are formed, corresponding to the two W bosons. The chosen criterion maximizes the sum of the two jet-jet invariant masses and the smaller mass of the two masses, excluding the combination with the mass difference of two masses bigger than 25 GeV. On Monte Carlo events, the resulting pairing is found to be correct for 62% of all selected $q\bar{q}q\bar{q}$ events at $\sqrt{s} = 183 - 189$ GeV. Be careful that the pairing algorithm is not the same as in section 6.1.4.

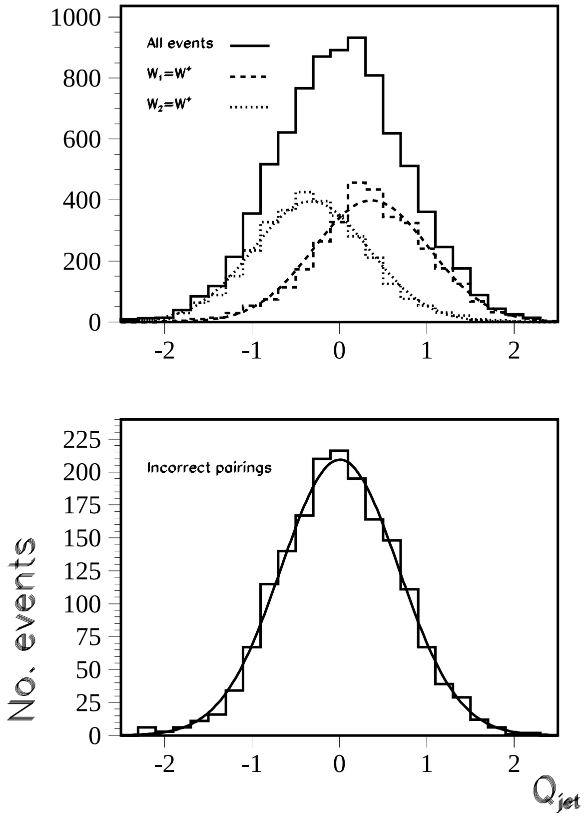

Abbildung 6.33: *W charge difference. The upper plot shows all WW events (solid line), events in which* $\mathrm{W}_1 = \mathrm{W}^+$ *(dashed line) and events in which* $\mathrm{W}_2 = \mathrm{W}^+$*. The lower plot shows all WW events in which the jets were incorrectly paired.*

The events with incorrect pairing do not bias the fit results, since they have no mass information. But the events with incorrect charge will bias the fit results. To reduce the charge confusion in $q\bar{q}q\bar{q}$ events, the polar angle of the W^-, $\cos\Theta_\mathrm{W}$, is used. The distribution is shown in Figure 6.34. The events with wrong assignment of the W charge are moved from $\cos\Theta_\mathrm{W}$ to $-\cos\Theta_\mathrm{W}$. They are indicated by the light shaded region, assuming the jets have been correctly paired. Events with $\cos\,\Theta_\mathrm{W} > 0$ are retained. Monte Carlo studies indicate a correct charge assignment in 89% of the case of right jet pairing. The pairing in the surviving signal events is improved. It is correct for 67% of all selected

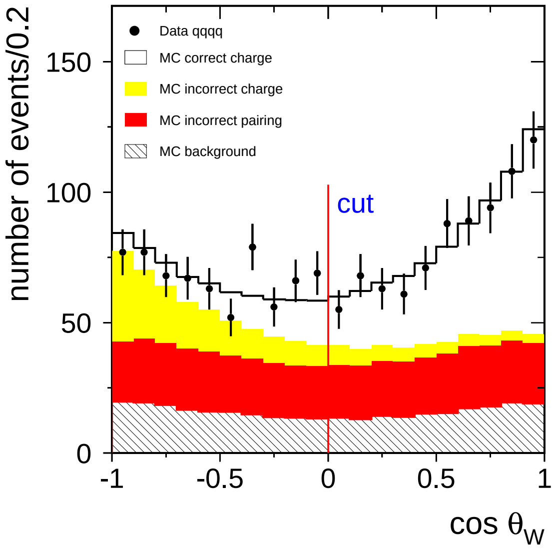

Abbildung 6.34: *The polar angle of* W$^-$ *boson. The plot shows all WW events (solid line), events with incorrect charge assignment (light shaded region), events in which the jets were incorrectly paired (dark shaded region) and background events (hatched region).*

$q\bar{q}q\bar{q}$ events.

Masses of the Charged W Bosons

In order to determine the masses of positively and negatively charged W bosons, the invariant mass distributions without kinematic fit are used as mentioned in section 6.5.1. The extraction of the masses is done with the reweighting method as described in section 6.4. The events fitted are limited to the mass range 30 GeV $< M_{inv} <$ 130 GeV. The reconstructed invariant mass distributions at $\sqrt{s} = 183 - 189$ GeV are shown in Figure 6.35. Since 11% of each data sample has incorrect charge, the fitted masses have to be calibrated. For the calibration, the following relations are used:

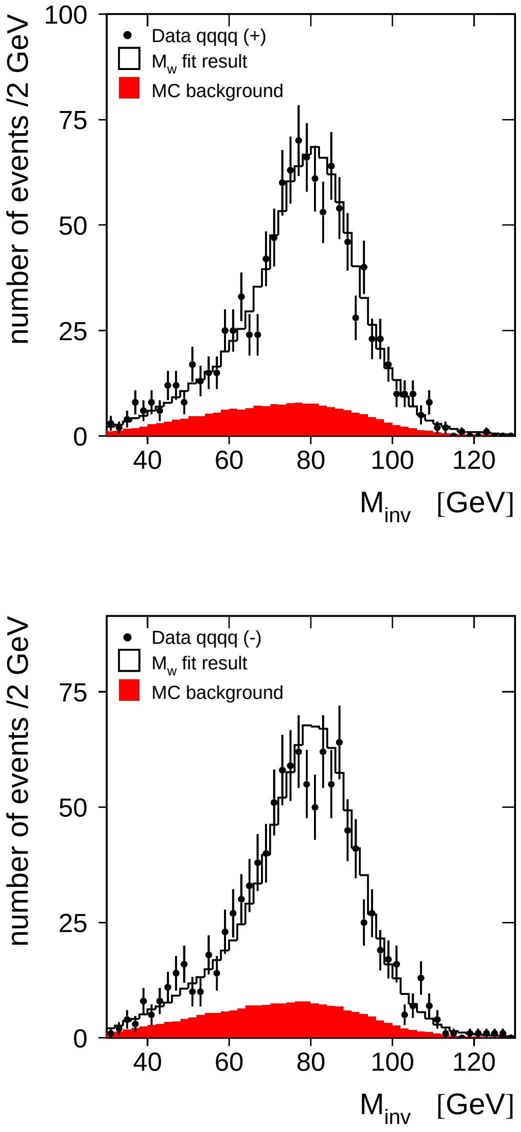

Abbildung 6.35: *Distributions of reconstructed invariant masses. The left plot shows the positively charged W bosons and the plot on the right side the negatively charged W bosons of the data (points with error bars) at* $\sqrt{s} = 183 - 189$ *GeV. The solid line histograms are the fit results. The background contributions are indicated by the dark shaded region.*

$\sqrt{s}$ [GeV]	$M_{W^+} - M_{W^-}$ [GeV]	
	Fitted Value	Corrected Value
183	-0.02 ± 1.31	-0.03 ± 1.52
189	-0.63 ± 0.80	-0.81 ± 0.92
183-189		-0.60 ± 0.79

Tabelle 6.17: *The results on the mass differences of the charged W bosons, $M_{W^+} - M_{W^-}$, for the L3 data collected at 183 - 189 GeV. The error is statistical only.*

$$M_{W^+}^{fit} = \alpha M_{W^+} + (1-\alpha) M_{W^-} \tag{6.35}$$

$$M_{W^-}^{fit} = \alpha M_{W^-} + (1-\alpha) M_{W^+} \ , \tag{6.36}$$

where $\alpha = 88.56 \pm 0.15\%$ stands for the correct charge assignment. The Table 6.17 summarises the results. The mass difference between W^+ and W^- is

$$M_{W^+} - M_{W^-} = -0.60 \pm 0.79 \text{ GeV}, \tag{6.37}$$

where the error is only statistical, since the systematic errors cancel out in the difference.

6.5.3 Results

The $\sqrt{s} = 189$ GeV results obtained from direct reconstruction of the W bosons are:

$$q\bar{q}l\nu \qquad M_{W^+} - M_{W^-} = +0.64 \pm 0.50 \text{ GeV}$$

$$q\bar{q}q\bar{q} \qquad M_{W^+} - M_{W^-} = -0.60 \pm 0.79 \text{ GeV}.$$

The results determined in the $q\bar{q}l\nu$ and $q\bar{q}q\bar{q}$ final states are in agreement with each other. They are combined and the result is

$$M_{W^+} - M_{W^-} = +0.28 \pm 0.42 \text{ GeV}.$$

This is the *first* direct measurement at LEP and the result is consistent with CPT invariance. Thus, the procedure of using the average invariant mass in the determination of the mass of W bosons is justified. It also agrees with the measurement performed at TEVATRON with a value of $M_{W^+} - M_{W^-} = -0.19 \pm 0.58$ GeV [116].

6.6 Summary

In order to determine the mass of the W boson, two methods are used in this analysis : a MC calibration method using a fit of an analytic Breit-Wigner × Gauss signal function to the data and a MC reweighting method, a comparison between data and Monte Carlo samples reweighted to correspond to different W mass values. These two methods give very consistent results and comparable errors. Since the MC calibration method is simple, robust and transparent, the results of this method are taken as the final results.

6.6.1 Results at $\sqrt{s} = 183$ GeV

The $\sqrt{s} = 183$ GeV results obtained from direct reconstruction of the W bosons are:

$$\begin{array}{rl} q\bar{q}e\nu(\gamma) & M_{\mathrm{W}} = 80.163 \pm\ 0.376\ \ (\mathrm{stat.}) \pm\ 0.045\ \ (\mathrm{syst.})\ \mathrm{GeV} \\ q\bar{q}\mu\nu(\gamma) & M_{\mathrm{W}} = 80.553 \pm\ 0.432\ \ (\mathrm{stat.}) \pm\ 0.054\ \ (\mathrm{syst.})\ \mathrm{GeV} \\ q\bar{q}\tau\nu(\gamma) & M_{\mathrm{W}} = 80.824 \pm\ 0.659\ \ (\mathrm{stat.}) \pm\ 0.076\ \ (\mathrm{syst.})\ \mathrm{GeV} \\ q\bar{q}q\bar{q}(\gamma) & M_{\mathrm{W}} = 80.616 \pm\ 0.215\ \ (\mathrm{stat.}) \pm\ 0.087\ \ (\mathrm{syst.})\ \mathrm{GeV}. \end{array}$$

The results on M_{W} determined in the $q\bar{q}e\nu$, $q\bar{q}\mu\nu$ and $q\bar{q}\tau\nu$ final states are in agreement with each other. They are averaged taking statistical and systematic errors including correlations into account:

$$M_{\mathrm{W}}^{q\bar{q}l\nu} = 80.406 \pm\ 0.261\ \ (\mathrm{stat.}) \pm\ 0.051\ \ (\mathrm{syst.})\ \mathrm{GeV}$$

and the combined result at $\sqrt{s} = 183$ GeV is

$$M_{\mathrm{W}}^{f\bar{f}f\bar{f}} = 80.524 \pm 0.166\ (stat.) \pm 0.068\ (syst.)\ \mathrm{GeV}. \qquad (6.38)$$

The published L3 results at 183 GeV [88] are for the data collected at 172-183 GeV. For the comparison, the results of this thesis at 183 GeV is combined with the published L3 results at 172 GeV [117]. The combined results for the data collected at 172-183 GeV are summarised in Table 6.18.

Process	Mass of the W Boson [GeV]	
	This Thesis	L3 Published
$q\bar{q}e\nu(\gamma)$	80.18 ± 0.33 ± 0.05	80.21 ± 0.30 ± 0.06
$q\bar{q}\mu\nu(\gamma)$	80.59 ± 0.41 ± 0.06	80.49 ± 0.36 ± 0.06
$q\bar{q}\tau\nu(\gamma)$	80.72 ± 0.56 ± 0.07	80.89 ± 0.56 ± 0.08
$q\bar{q}l\nu(\gamma)$	80.41 ± 0.23 ± 0.06	80.41 ± 0.21 ± 0.06
$q\bar{q}q\bar{q}(\gamma)$	80.66 ± 0.19 ± 0.08	80.70 ± 0.18 ± 0.07
$f\bar{f}f\bar{f}(\gamma)$	80.55 ± 0.15 ± 0.07	80.57 ± 0.14 ± 0.06

Tabelle 6.18: *The results on the mass of the W boson, M_{W}, for the L3 data collected at 172 - 183 GeV. The first error is statistical and the second systematic.*

6.6.2 Results at $\sqrt{s} = 189$ GeV

The $\sqrt{s} = 189$ GeV results from this analysis together with the preliminary L3 results submitted to the most recent conference [118] are summarised in Table 6.19.

Process	Mass of the W Boson [GeV]	
	This Thesis	L3 Preliminary
$q\bar{q}e\nu(\gamma)$	80.01 ± 0.19 ± 0.04	79.99 ± 0.20 ± 0.06
$q\bar{q}\mu\nu(\gamma)$	80.14 ± 0.23 ± 0.05	80.31 ± 0.24 ± 0.07
$q\bar{q}\tau\nu(\gamma)$	80.15 ± 0.34 ± 0.06	80.19 ± 0.33 ± 0.10
$q\bar{q}l\nu(\gamma)$	80.09 ± 0.13 ± 0.05	80.13 ± 0.14 ± 0.06
$q\bar{q}q\bar{q}(\gamma)$	80.49 ± 0.13 ± 0.08	80.56 ± 0.13 ± 0.08
$f\bar{f}f\bar{f}(\gamma)$	80.27 ± 0.09 ± 0.06	80.35 ± 0.09 ± 0.06

Tabelle 6.19: *The results on the mass of the W boson, M_{W}, for the L3 data collected at 189 GeV. The first error is statistical and the second systematic.*

The mass difference of the positively and negatively charged W bosons is determined. The result is

$$M_{\mathrm{W}^+} - M_{\mathrm{W}^-} = +0.28 \pm 0.42 \text{ GeV}.$$

6.6.3 Combination of $\sqrt{s} = 183$ GeV and $\sqrt{s} = 189$ GeV

The $\sqrt{s} = 183$ GeV and $\sqrt{s} = 189$ GeV combined results are

$$\begin{aligned} M_{\mathrm{W}}^{q\bar{q}l\nu} &= 80.155 \pm 0.119\,(stat.) \pm 0.047\,(syst.)\ \mathrm{GeV} \\ M_{\mathrm{W}}^{q\bar{q}q\bar{q}} &= 80.528 \pm 0.111\,(stat.) \pm 0.078\,(syst.)\ \mathrm{GeV}. \end{aligned} \tag{6.39}$$

The difference between M_{W} as determined in $q\bar{q}l\nu$ and $q\bar{q}q\bar{q}$ events is

$$\triangle M_{\mathrm{W}} = M_{\mathrm{W}}(q\bar{q}q\bar{q}) - M_{\mathrm{W}}(q\bar{q}l\nu) = 0.373 \pm 0.163\,(stat.) \pm 0.058\,(syst.)\ \mathrm{GeV}, \tag{6.40}$$

neglecting the theory error from Bose-Einstein and colour reconnection. It is larger than the error due to strong final state interactions (FSI), which amounts to 50 MeV. Within the statistical accuracy of the measurements, it is difficult to interpret this result. It remains to be seen whether the difference will turn out to be significant (see section 6.7 and 7.2). Averaging the results on M_{W} obtained from the $q\bar{q}l\nu$ and $q\bar{q}q\bar{q}$ event samples, including also FSI errors, the combined result yields

$$M_{\mathrm{W}} = 80.325 \pm 0.081\,(stat.) \pm 0.060\,(syst.)\ \mathrm{GeV}. \tag{6.41}$$

The results on M_{W} presented here agree well with the L3 combined measurement derived from the cross-section [97] and with the one determined at a center-of-mass energy of 162 GeV and 172 GeV [117], which is $M_{\mathrm{W}} = 80.75^{+0.26}_{-0.27}\,(exp.) \pm 0.03\,(\mathrm{LEP})$ GeV.

6.7 Preliminary Results at $\sqrt{s}$=192-202 GeV

The W mass measurements for the selected events at $\sqrt{s}$=192-202 GeV are performed with the reweighting method and preliminary results are obtained as shown in Table 6.20. The Monte Carlo Calibration method couldn't be used due to a lack of reference Monte Carlo samples with different W masses needed for the calibration. The fitting procedure is exactly the same as described for the data at $\sqrt{s}$=189 GeV in section 6.4. The invariant mass distributions with the fit results are shown in Figure 6.36. The combination of the results at the center-of-mass energies 192-202 GeV is

$$M_{\mathrm{W}}(f\bar{f}f\bar{f}) = 80.32 \pm 0.09(stat.) \pm 0.06(sys)\quad \mathrm{GeV}. \tag{6.42}$$

Process	Mass of the W Boson [GeV]	
	This Thesis	L3 Preliminary
$q\bar{q}e\nu(\gamma)$	80.37 ± 0.22 ± 0.04	80.28 ± 0.19 ± 0.05
$q\bar{q}\mu\nu(\gamma)$	80.23 ± 0.29 ± 0.05	80.23 ± 0.25 ± 0.05
$q\bar{q}\tau\nu(\gamma)$	80.62 ± 0.33 ± 0.08	80.76 ± 0.32 ± 0.07
$q\bar{q}l\nu(\gamma)$	80.38 ± 0.15 ± 0.05	80.35 ± 0.14 ± 0.05
$q\bar{q}q\bar{q}(\gamma)$	80.28 ± 0.11 ± 0.08	80.28 ± 0.12 ± 0.07
$f\bar{f}f\bar{f}(\gamma)$	80.32 ± 0.09 ± 0.06	80.31 ± 0.09 ± 0.06

Tabelle 6.20: *The results on the mass of the W boson, M_W, for the L3 data collected at 192 - 202 GeV. The first error is statistical and the second systematic.*

It is expected that many of the systematic uncertainties concerning the mass measurement of the W boson don't depend on the center-of-mass energies. Thus the systematic error is taken from the analysis of the data collected at 189 GeV. The values presented here are already corrected concerning BE correlations ($BE_0 \rightarrow BE_{32}$). The preliminary L3 result submitted to the most recent conference [118] is $M_\mathrm{W}(f\bar{f}f\bar{f}) = 80.31 \pm 0.09 \pm 0.06$ GeV.

The combination of this result with the previous results at center-of-mass energies of 183 GeV and 189 GeV is done and the difference between the mass reconstructed in the hadronic and semileptonic channels is studied:

$$M_\mathrm{W}(q\bar{q}q\bar{q}) = 80.402 \pm 0.078(stat.) \pm 0.072(sys) \quad \mathrm{GeV} \tag{6.43}$$

$$M_\mathrm{W}(q\bar{q}l\nu) = 80.235 \pm 0.094(stat.) \pm 0.047(sys) \quad \mathrm{GeV}, \tag{6.44}$$

The preliminary result on the difference between M_W in $q\bar{q}l\nu$ and $q\bar{q}q\bar{q}$ events is determined to be:

$$\triangle M_\mathrm{W} = M_\mathrm{W}(q\bar{q}q\bar{q}) - M_\mathrm{W}(q\bar{q}l\nu) = 0.17 \pm 0.12(stat.) \pm 0.05(sys) \quad \mathrm{GeV}. \tag{6.45}$$

Again the systematic errors due to FSI are not included in this calculation.

Averaging the results on M_W obtained from the $q\bar{q}l\nu$ and $q\bar{q}q\bar{q}$ event samples, including also FSI errors, yields:

$$M_\mathrm{W} = 80.312 \pm 0.060(stat.) \pm 0.058(sys) \quad \mathrm{GeV}. \tag{6.46}$$

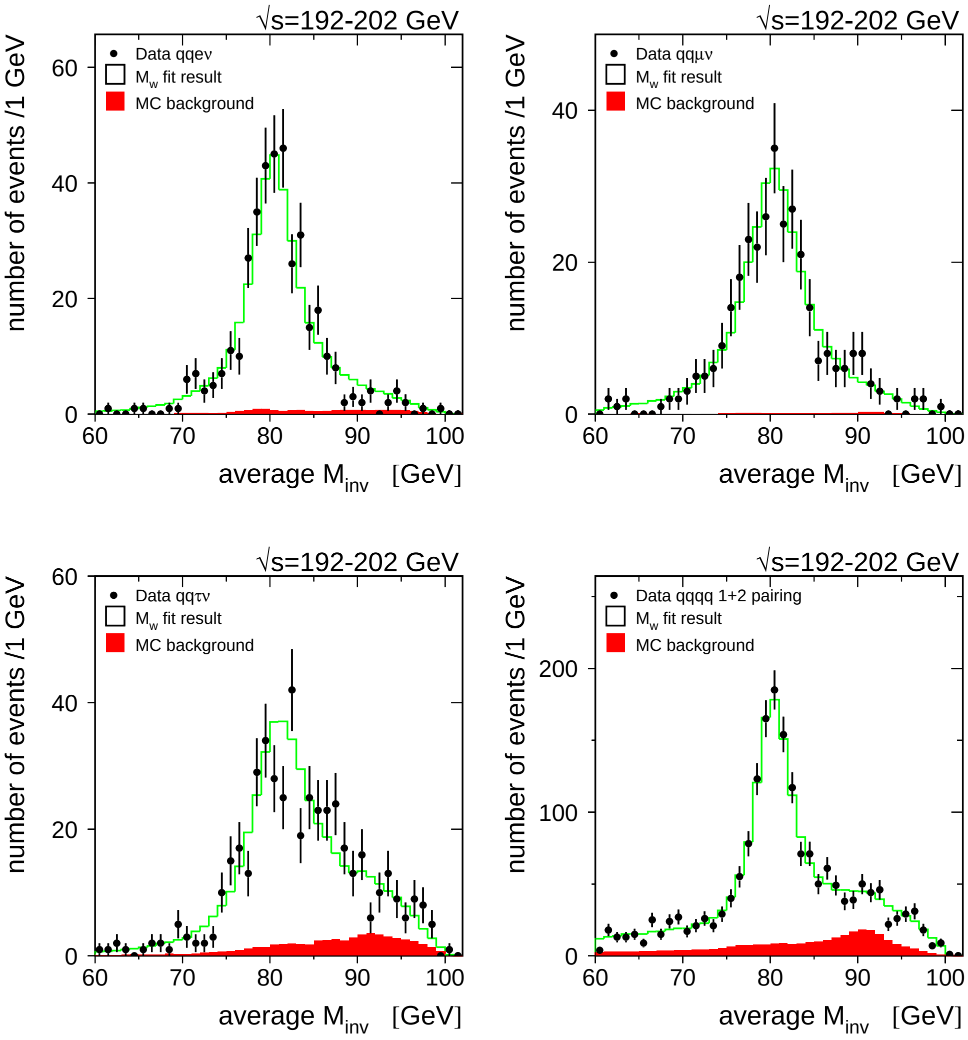

Abbildung 6.36: *Distributions of reconstructed invariant mass, M_{inv}, after applying the kinematic fit using the equal-mass constraint for events selected in the 192-202 GeV L3 data. The solid lines show the result of the fits of M_{W}. The background contribution is indicated by the dark shaded region.*

The published L3 result at the center-of-mass energies of 161-172 GeV[117] is $M_{\mathrm{W}} = 80.72 \pm 0.32 \pm 0.09$ GeV, and the result derived from the measurements of the total W-pair production cross section is $M_{\mathrm{W}} = 80.78 \pm 0.43$ $(exp.) \pm$ 0.03 (LEP) GeV. Combining these results with the result of this thesis yields:

$$M_{\mathrm{W}} = 80.340 \pm 0.058(stat.) \pm 0.057(sys) \quad \mathrm{GeV}. \tag{6.47}$$

This result is in good agreement with the preliminary L3 combined result (161-202 GeV) submitted to the most recent conference [118], which is $M_{\mathrm{W}} = 80.375 \pm 0.058 \pm 0.051$ GeV.

Kapitel 7

Discussion of the Results and Outlook

At LEP2, a total of $\sim 700\ pb^{-1}$ has been recorded by each of the four LEP collaborations at the center-of-mass energies up to a maximum of 208 GeV. This means that LEP2 is providing a substantial sample of W bosons, which has been analysed. In this chapter, the results obtained in each LEP experiments and the results of TEVATRON are combined to increase the precision of the measurements. The final results will then be interpreted. This chapter ends with an outlook concerning the W mass.

7.1 WW Cross Section at LEP2

Figure 7.1 shows the LEP-combined results of the W-pair cross section (CC03), assuming Standard Model decay branching ratios for the W decays. The data points are the LEP averages. All LEP experiments have final measurements at 183-189 GeV [119, 120, 88, 121, 122, 123, 84, 124] and preliminary results at 192-208 GeV [125, 126, 127, 128, 129]. Also shown are the Standard Model predictions using the GENTLE and RacoonWW/YFSWW3 (shaded area) with a possible theoretical uncertainty, and for comparison the cross section if the ZWW coupling did not exist (dashed line), or if only the t-channel ν exchange existed (dotted line). We see that ν exchange alone does not fit the data. The theoretical uncertainty of RacoonWW/ YFSWW3 is about 0.5% instead of 2%

in GENTLE[130]. The gauge nature of both the γW^+W^- and ZW^+W^- couplings present in the Standard Model are needed.

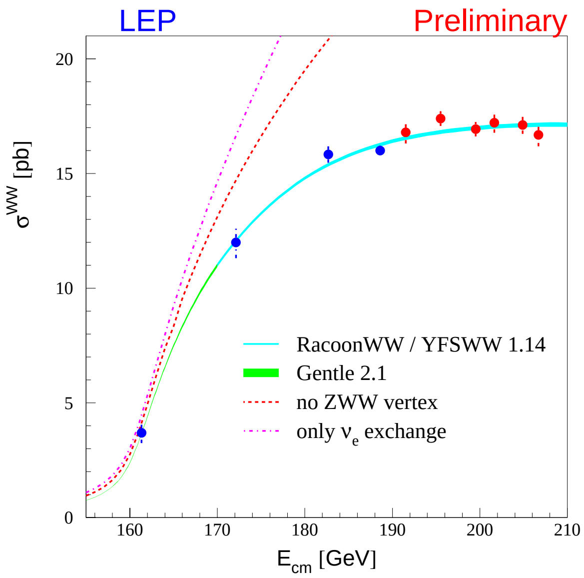

Abbildung 7.1: *The W-pair cross section as a function of the center-of-mass energy.*

From the measurement close to the threshold, the first LEP2 measurement of M_W was obtained [131]

$$M_W \;=\; 80.40 \pm 0.220 \pm 0.025(\text{LEP})\ \text{GeV}. \tag{7.1}$$

From the cross sections, the branching ratio for W decays via the electron, muon, tau and hadronic modes have been determined. The LEP average branching fractions[129] are shown in Figure 7.2 and summarised in Table 7.1. The results of DELPHI and L3 are up to center-of-mass energies up to 202 GeV only. The results for the individual leptonic channels are consistent with lepton universality, and the average leptonic branching fraction is also consistent with the SM expectation.

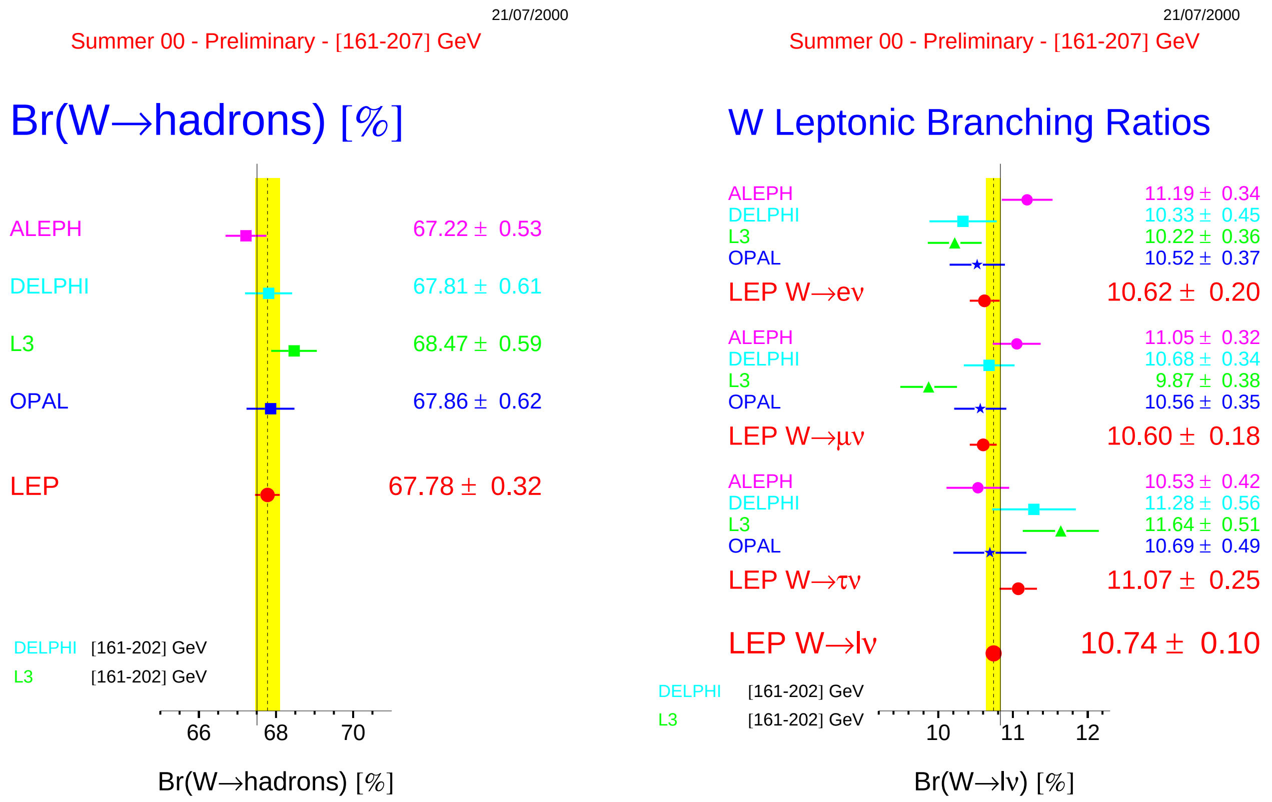

Abbildung 7.2: *Combined LEP hadronic and leptonic branching fractions including preliminary measurements at 192-207 GeV.*

Decay mode	Branching Fractions (%)
$Br(\mathrm{W} \rightarrow \mathrm{e}\nu)$	10.62 ± 0.20
$Br(\mathrm{W} \rightarrow \mu\nu)$	10.60 ± 0.18
$Br(\mathrm{W} \rightarrow \tau\nu)$	11.07 ± 0.25
$Br(\mathrm{W} \rightarrow l\nu)$	10.74 ± 0.10
$Br(\mathrm{W} \rightarrow q\bar{q})$	67.78 ± 0.32

Tabelle 7.1: *LEP average W decay branching fraction measurements. Results are preliminary.*

The hadronic W branching fraction can be reinterpreted in terms of the CKM matrix elements V_{cs} without need for a CKM unitarity constraint:

$$|V_{cs}| = 0.989 \pm 0.016. \tag{7.2}$$

This value is much more precise than the existing direct measurement from D meson decay, $|V_{cs}| = 1.04 \pm 0.16$ [22].

TEVATRON measurements of $Br(\mathrm{W} \rightarrow \mathrm{e}\nu)$ from D0 and CDF are $10.50 \pm 0.30\%$ and $10.39 \pm 0.35\%$ respectively. These give an average of $10.43 \pm 0.25\%$ [129], which agrees well with the LEP results.

7.2 W Mass Measurement

The W boson mass results presented in this section are obtained from data recorded over a range of center-of-mass energies, $\sqrt{s} = 161$ - 202 GeV during the 1996-1999 operation of the LEP collider. These data correspond to an integrated luminosity of $\approx 480\ pb^{-1}$ per experiment.

At center-of-mass energies above the W pair threshold, the W mass is obtained through the direct reconstruction of the decay products of W bosons. Each experiment of LEP uses several different techniques for measuring the W mass. Other than the methods used in this thesis, the convolution method used in DELPHI is worth mentioning. In this method, an event-by-event maximum likelihood fit to a relativistic Breit-Wigner convoluted with a Gaussian resolution function plus a background shape is applied to the selected W events [132].

Common to all the methods are the reliance on simulated events.

A combined W mass measurement has been obtained from the results of the four LEP experiments in the $q\bar{q}q\bar{q}$ and $q\bar{q}l\nu$ channels. All LEP experiments have final W mass results based on the combined 172 GeV and 183 GeV data [133, 134, 111, 135]. The W mass results based on data collected at 189-202[1] GeV are preliminary for all LEP experiments [137, 138, 118, 139]. Figure 7.3 shows the results for hadronic and semileptonic channels separately. The combined W mass measurements [129] are :

$$\begin{aligned} M_{\mathrm{W}}^{non-4q} &= 80.427 \pm 0.051 \text{ GeV}, &(7.3)\\ M_{\mathrm{W}}^{4q} &= 80.432 \pm 0.073 \text{ GeV}. &(7.4)\end{aligned}$$

The difference between hadronic and leptonic masses is

$$M_{\mathrm{W}}^{4q} - M_{\mathrm{W}}^{non-4q} = +5 \pm 51 \text{ MeV}, \qquad (7.5)$$

neglecting the theory error from Bose-Einstein and colour reconnection. Since this difference is small, the bias of the value M_{W} from the FSI effects can be assumed to be small.

The overall LEP average W mass measurement combined with the W mass determination from the WW cross section yields

$$M_{\mathrm{W}}^{\mathrm{LEP}} = 80.427 \pm 0.046 \text{ GeV}. \qquad (7.6)$$

The world average of direct measurement including the result from $p\bar{p}$ colliders, 80.452 ± 0.062 GeV [23], are shown in Figure 7.4 with its value of

$$M_{\mathrm{W}} = 80.436 \pm 0.037 \text{ GeV} \quad \text{(World Average)}. \qquad (7.7)$$

The LEP2 measurement is consistent with those from the $p\bar{p}$ colliders and is slightly more precise. The world average of direct measurements has a reduced error that begins to challenge that of the very precise indirect W mass prediction from a global fit to all other high precision electroweak data and the prediction from νN scattering at NuTeV and CCFR. This precise measurement of the W

---

[1] ALEPH and OPAL have published their results at 189 GeV [102, 136].

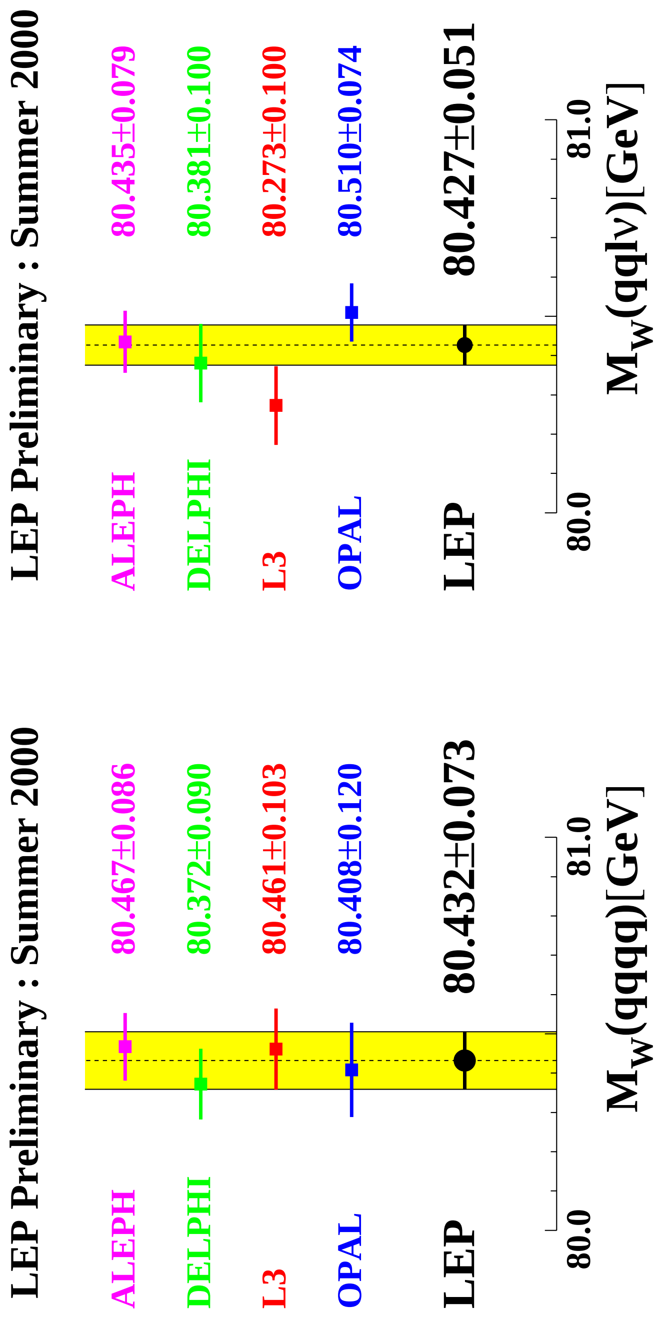

Abbildung 7.3: *Combined LEP W mass measurements from direct reconstruction of semileptonic and fully leptonic WW decays at the center-of-mass energies up to 202 GeV. The results are preliminary.*

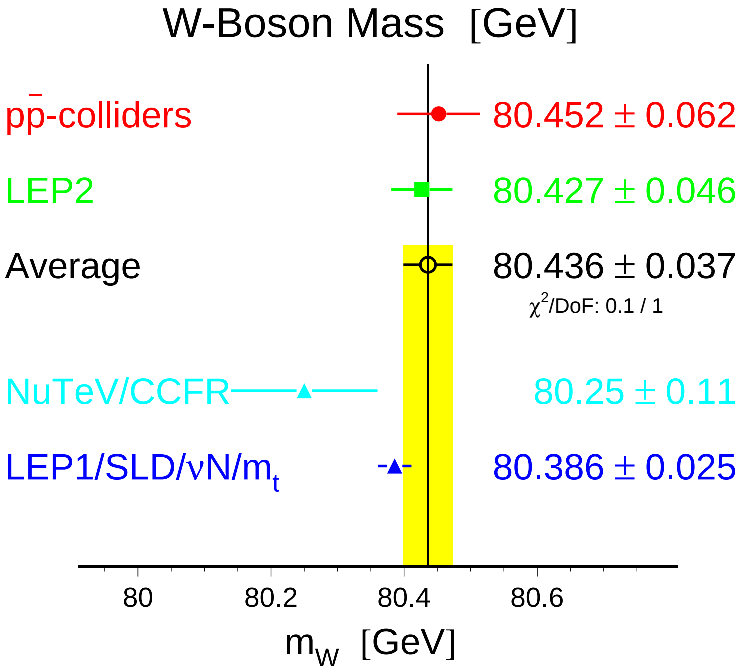

Abbildung 7.4: *Combination of the result from LEP2 and $p\bar{p}$ colliders*

mass provides us an interesting further feature. With the direct and indirect measurements of the top quark, it can test the consistency of the Standard Model. This is shown in Figure 7.5[23], where the mass of the t-quark from direct observation of top events is $M_t = 174.3 \pm 5.1$ GeV. It illustrates also the impact of these measurement for constraining $M_{\rm H}$. It is evident, that the data from the direct and indirect measurements independently favour a light Standard Model Higgs boson.

A global fit to all the precision electroweak data predicts a mass of Higgs boson [140]

$$M_{\rm H} \;=\; 60\;^{+52}_{-29}\;\text{GeV}. \tag{7.8}$$

In this fit the validity of the SM is assumed. The Higgs mass is extracted from the measurements of radiative corrections. Figure 7.6[140] shows the $\triangle\chi^2$ distribution of the fit results. The solid line is the result of the fit. The shaded band represents an estimate of the theoretical error (uncalculated higher-order corrections). The vertical band is the 95% CL exclusion limit from the direct

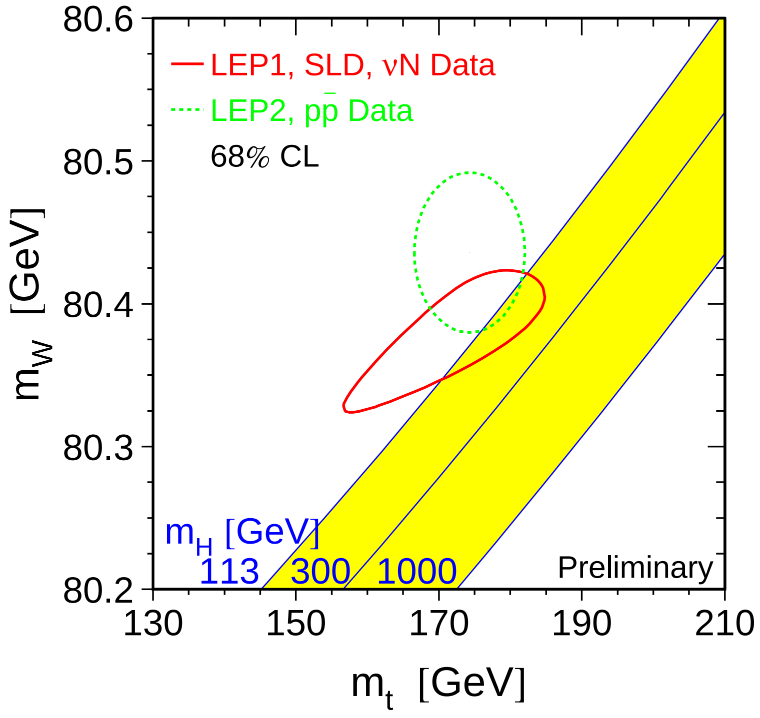

Abbildung 7.5: *Contours of M_{W} and M_t from direct measurements (dotted ellipse) compared with the predictions based on the precision electroweak data analysed within the Standard Model (solid curve). Also shown is the Standard Model relationship for masses as a function of the Higgs mass.*

search, $M_{\mathrm{H}} > 113 GeV$ [141]. The dashed curve is the results obtained when using the evaluation of $\triangle\alpha^{(5)}_{\mathrm{had}}(m^2_{\mathrm{Z}})$, the contribution of light quarks to the photon vacuum polarisation, from Reference [140]. The Higgs boson is so close, that it might be possible to discover this boson at the TEVATRON or even at LEP. A LEP error of $\triangle M_{\mathrm{W}}$ in the region of 30 MeV from the direct measurement would help to constraint the Higgs mass very significantly, which will be possible at the end of LEP2 data analysis. So we look forward for a better W mass measurement.

The Minimal Supersymmetric Standard Model (MSSM) is the most promising new-physics candidate. It is therefore especially important to consider the MSSM

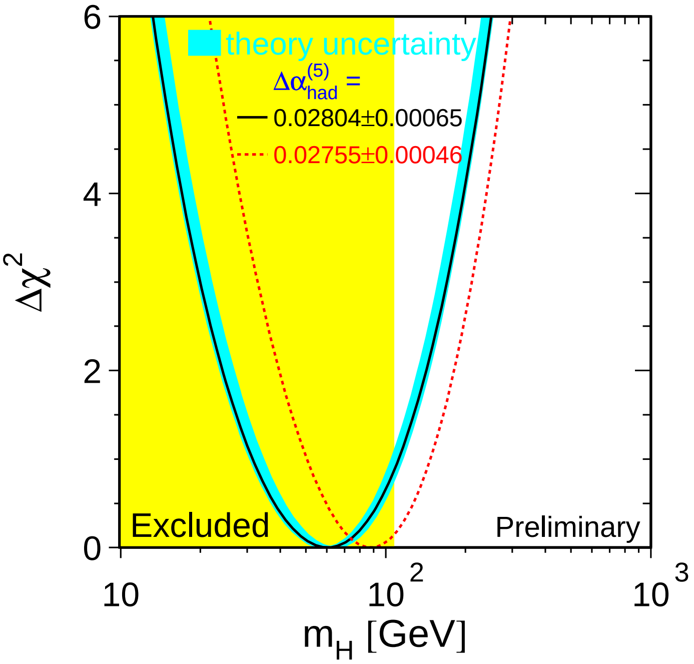

Abbildung 7.6: *The line is the result of the fit using all electroweak data. The band represents an estimate of the theoretical error and the vertical band the 95% CL exclusion limit from the direct search. The dashed curve is the results obtained using the evaluation of* $\triangle\alpha^{(5)}_{\mathrm{had}}(m^2_{\mathrm{Z}})$*, the contribution of light quarks to the photon vacuum polarisation, from Reference [140]*

prediction for M_{W}. Figure 7.7 shows the range of predictions for the W boson mass in the Standard Model and the MSSM, where it is assumed that no direct discovery of supersymmetric particles is made at LEP2. Precise determinations of the W boson mass and the top quark mass could be very helpful to distinguish between the models.

7.3 Experimental Prospects for the Future

The W mass measurements presented in this thesis are not final. The results obtained from data recorded over a range of center-of-mass energies 189-202 GeV

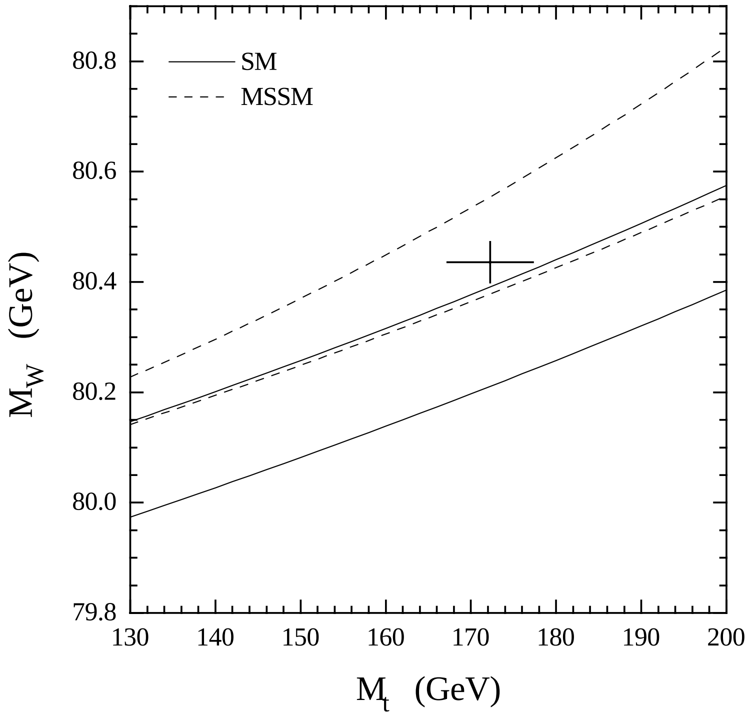

Abbildung 7.7: *The predicted W mass as a function of the top quark mass in the Standard Model (area between solid lines) and in the MSSM (area between the dashed lines). The point is the world average for the masses of the W boson and top quark from the direct measurements.*

are still preliminary. The data collected 2000, which correspond to an integrated luminosity of $\approx 215\ pb^{-1}$ per experiment, has to be analysed. This will provide significant further improvements in precision and further important tests of the Standard Model. But it also requires more work and care to the systematic difficulties like FSI in the $q\bar{q}q\bar{q}$ channel.

Interesting questions like the origin of mass may be answered in LEP data. At the time of writing, excitement has been generated by the 'signal' for a Higgs boson with $m_H = 115.0^{+1.3}_{-0.7}$ GeV, reported by the LEP collaborations and the LEP Working Group on Higgs boson searches [141]. If the Higgs doesn't weigh 115 GeV, the constraint to the allowed Higgs mass will be tighter due to the improvements in the W mass measurements. But it may be found at the Fermilab TEVATRON collider during its next run. We can also hope for an improvement of the W mass measurement from TEVATRON, which will constrain the allowed Higgs mass further.

After completion of the LEP2 program, W boson physics will be continued at the TEVATRON, where the run-II is expected to deliver 2 fb^{-1} to the D0 and CDF experiments by 2003. However, a plan for reaching 15 fb^{-1} by 2007 has been proposed. The next machine, which can contribute to W physics, is the Large Hadron Collider (LHC). The LHC is currently built at CERN and will start in 2005. The W physics program will be similar to those in the TEVATRON, but LHC will deliver higher luminosities. Another proposed machine is a high-energy e^+e^- linear collider with center-of-mass energy of about 500 GeV. A linear collider (LC) is a natural successor of LEP and will provide us the most suitable device to study the properties of the W boson, since the process $e^+e^- \to W^+W^-$ should be a major component of the e^+e^- annihilation cross-section for center-of-mass energies above a few hundred GeV. A future LC is planned at particle physics laboratories in Japan (KEK), in the USA (SLAC) and in Germany (DESY). A muon collider could be another possibility, but it is not clear whether it will be technically possible to build such a machine. Nevertheless, the proposed machines will open a new era of precision weak interaction experiments and we hope that they can become a tool to probe for the next scale of fundamental physics.

Anhang A

Optimization of the Selection

In this appendix, it is shown how the expected statistical error on the cross section measurement is minimized if the product of the signal efficiency and the purity is maximized. The cross section is defined as:

$$\sigma_{sig} = \frac{N_{observed} - N_{bg}}{\epsilon\mathcal{L}}, \tag{A.1}$$

where ϵ is the signal efficiency. The error of the cross section is

$$\begin{aligned} (\delta\sigma_{sig})^2 &= (\tfrac{\partial\sigma_{sig}}{\partial N_{observed}} \cdot \triangle N_{observed})^2 + \text{ the other terms} \\ &\approx (\tfrac{\triangle N_{observed}}{\epsilon\mathcal{L}})^2 \\ &= \tfrac{N_{sig}+N_{bg}}{\epsilon^2\mathcal{L}^2}, \end{aligned}$$

where the other terms (proportinal to $\triangle\epsilon$ and $\triangle\mathcal{L}$) are small compared to the first term and are neglected for the further calculation. In the third step $N_{observed} = N_{sig} + N_{bg}$ is assumed, which is the case for a best possible agreement between MC prediction and the observed data. In this case $\sigma_{sig} = N_{sig}/(\epsilon\mathcal{L})$ and the error of the cross section takes the form

$$\begin{aligned} (\delta\sigma_{sig})^2 &= \tfrac{\sigma_{sig}}{\epsilon\mathcal{L}} \tfrac{N_{sig}+N_{bg}}{N_{sig}} \\ &= \tfrac{\sigma_{sig}}{\epsilon\pi\mathcal{L}}, \end{aligned}$$

where $\pi = N_{sig}/(N_{sig} + N_{bg})$ stands for the purity.

Literaturverzeichnis

[1] S. L. Glashow, Nucl. Phys. **22** (1961) 579.

[2] S. Weinberg, Phys. Rev. Lett. **19** (1967) 1264.

[3] D. V. Volkov and V. P. Akulov, Phys. Lett. **B46** (1973) 109–110.

[4] J. Wess and B. Zumino, Nucl. Phys. **B70** (1974) 39–50.

[5] Abdus Salam and J. Strathdee, Fortschr. Phys. **26** (1978) 57.

[6] Pierre Fayet, Nucl. Phys. **B90** (1975) 104–124.

[7] Halzen, F., Quarks & Leptons, (John Wiley & Sons Inc., 1984).

[8] Renton, P., Electroweak interactions, (Cambridge University Press, 1990).

[9] Kane, G., Modern elementary particle physics, (Addison-Wesley Publishing Company, 1993).

[10] Hollik, W., hep-ph/9602380 (1995).

[11] Ellis, J., Presented at Les Houches Summmer School on Cosmology and Large Scale Structure, Les Houches, France (1993).

[12] M. Goldhaber and L. Grodzins and A. W. Sunyar, Phys. Rev. **109** (1958) 1015–1017.

[13] Super-Kamiokande *Collab.*, Y. Fukuda *et al.*, PRL **81** (1998) 1562.

[14] LSND *Collab.*, C. Athanassopoulos *et al.*, PRL **81** (1998) 1774.

[15] Physics at LEP 2, vol. 2: Software, (CERN yellow report 96-01, 1996).

[16] T. Muta and R. Najima and S. Wakaizumi, Mod. Phys. Lett. **A1** (1986) 203.

[17] W. Beenakker, K. Kolodziej and T. Sack, Phys. Lett. **B258** (1991) 469.

[18] Physics at LEP 2, vol. 1, (CERN yellow report 96-01, 1996).

[19] ed. G. Altarelli and G. Martinelli, (Yellow Report CERN 86-02, 1986).

[20] D. Bardin and A. Olshevsky and M. Bilenkii and T. Riemann, Phys. Lett. **B308** (1993) 403–410.

[21] F.A. Berends, R. Pittau and R. Kleiss, Nucl. Phys. **B424** (1994) 308.

[22] D. E. Groom and others, Eur. Phys. J. **C15** (2000) 1.

[23] LEPEWWG, Combination of Results Presented at ICHEP2000, Internal report, http://lepewwg.web.cern.ch/LEPEWWG/plots/, 2000.

[24] L3 *Collab.*, B. Adeva *et al.*, Nucl. Inst. Meth. **A 289** (1990) 35.

[25] ALEPH *Collab.*, D. Decamp *et al.*, Nucl. Inst. Meth. **A 294** (1990) 127.

[26] DELPHI *Collab.*, P. Aarnio *et al.*, Nucl. Inst. Meth. **A 303** (1991) 233.

[27] OPAL *Collab.*, K. Ahmet *et al.*, Nucl. Inst. Meth. **A 305** (1991) 275.

[28] M. Lamont, *LEP: Review of 1998*, SPS & LEP Performance Workshop, 9th Chamonix (1999).

[29] R.W. Assmann, *LEP performance in 1999*, SPS & LEP Performance Workshop, 10th Chamonix (2000).

[30] R.Assmann *et al.*, Eur.Phys.J. **C 6** (1999) 187–223.

[31] G. Wilkinson, *Energy calibration: status and prospects*, LEP Energy Working Group Internal Note (2000).

[32] The LEP Working Group, *LEP energy calibration above the W pair production threshold*, Contribution to the 29th ICHEP (1998).

[33] LEPWG, *Evaluation of the LEP center-of-mass energy for data taken in 1998*, LEP Energy Working Group Internal Note (1999).

[34] Bernd Dehning, *The LEP spectrometer*, SPS & LEP Performance Workshop, 9th Chamonix (1999).

[35] L3 *Collab.*, M. Chemarin *et al.*, Nucl. Inst. Meth. **A 349** (1994) 345.

[36] L3 *Collab.*, M. Acciarri *et al.*, Nucl. Inst. Meth. **A 351** (1994) 300.

[37] L3 *Collab.*, G. Basti *et al.*, Nucl. Inst. Meth. **A 374** (1996) 293.

[38] L3 *Collab.*, I.C. Brock *et al.*, Nucl. Inst. Meth. **A 381** (1996) 236.

[39] L3 *Collab.*, A. Adam *et al.*, Nucl. Inst. Meth. **A 383** (1996) 342.

[40] A. Adam *et al.*, Nucl. Inst. Meth. **A 383** (1996) 342.

[41] T. Van Rhee, F. Filthaut and F. Linde, L3 Internal Note 2117 (1997).

[42] M. Acciarri *et al.*, Nucl. Inst. Meth. **A 351** (1994) 300.

[43] K. Deiters *et al.*, Nucl. Inst. Meth. **A 323** (1992) 162.

[44] G. Alkhazov *et al.*, L3 Internal Note 1862 (1995).

[45] D. Prokofiev *et al.*, L3 Internal Note 1895 (1995).

[46] G. Basti *et al.*, Nucl. Inst. Meth. **A 374** (1996) 293.

[47] U. Uwer, L3 Internal Note 2003 (1996).

[48] O. Adriani *et al.*, Nucl. Inst. Meth. **A 302** (1991) 53.

[49] G. Chiefari *et al.*, Nucl. Inst. Meth. **A 277** (1989) 187.

[50] S. Lanzano *et al.*, Nucl. Inst. Meth. **A 289** (1990) 335.

[51] I.C. Brock *et al.*, Nucl. Inst. Meth. **A 381** (1996) 236.

[52] The LEP Energy Working Group Collaboration, LEP ECAL/97-04 (1997).

[53] The LEP Energy Working Group Collaboration, A. Blondel *et al.*, CERN-EP/98-191, CERN-SL/98-073 (1998).

[54] The LEP Energy Working Group Collaboration, LEP ECAL/98-01 (1998).

[55] The LEP Energy Working Group Collaboration, LEP ECAL/99-01 (1999).

[56] The LEP Energy Working Group Collaboration, LEP ECAL/00-01 (2000).

[57] R. Bizzarri *et al.*, Nucl. Inst. Meth. **A 283** (1989) 799.

[58] R. Bizzarri, F. Cesaroni, S. Gentile, G. Lunadei, M. Fukushima and T. Hebbeker, Nucl. Inst. Meth. **A 317** (1992) 463.

[59] R. Bagnaia, R. Bizzarri, F. Cesaroni, S. Gentile and G. Lunadei, Nucl. Inst. Meth. **A 323** (1992) 528.

[60] R. Bagnaia, R. Bizzarri, F. Cesaroni, S. Gentile and T. Hebbeker, Nucl. Inst. Meth. **A 324** (1993) 101.

[61] P. Bene *et al.*, Nucl. Inst. Meth. **A 306** (1991) 150.

[62] T. Dai and M. Fukushima, L3 Internal Note 668 (1989).

[63] Y. Bertsch *et al.*, Nucl. Inst. Meth. **A 340** (1994) 309.

[64] S.P. Beingessner *et al.*, Nucl. Inst. Meth. **A 340** (1994) 322.

[65] C. Dionisi *et al.*, Nucl. Inst. Meth. **A 336** (1993) 78.

[66] T. Sjöstrand, Comp. Phys. Comm. **39** (1986) 347.

[67] G. Marchesini and B.R. Webber, Nucl. Phys. **B 310** (1988) 461.

[68] G. Marchesini *et al.*, Comp. Phys. Comm. **67** (1992) 465.

[69] M. Skrzypek, S. Jadach, W. Placzek and Z. Wąs, CERN-TH/95-205 (1995).

[70] T. Sjöstrand, Comp. Phys. Comm. **82** (1994) 74.

[71] R. Engel, Z. Phys. **C 66** (1995) 203.

[72] R. Engel and J. Ranft, Phys. Rev. **D 54** (1996) 4244.

[73] R. Brun *et al.*, GEANT 3, CERN DD/EE/84-1 (Revised) (1987).

[74] H. Fesefeldt, RWTH Aachen, PITHA 85/02 (1985).

[75] L3 Collab., B. Adeva *et al.*, Nucl. Instr. and Meth. **A 289** (1990) 35.

[76] S. Bethke, Z. Kunszt, D.E. Soper and W.J. Stirling, Nucl. Phys. **B 370** (1992) 310.

[77] S. Banerjee, J.Casaus, S.Sarker, L3 Internal Note 2394 (1998).

[78] JADE Collab., W. Bartel *et al.*, Z. Phys. **C 20** (1983) 187.

[79] S. Catani, Y.L. Dokshitzer, M. Olsson, G. Turnock and B.R. Webber, Phys. Lett. **B 269** (1991) 432.

[80] T.Aziz *et al.*, L3 Internal Note 1993 (1993).

[81] R. Duda and P. Hart, *Pattern Classification and Scene Analysis*, (John Wiley & Sons Inc., 1973).

[82] C. Peterson *et al.*, Comp. Phys. Comm. **81** (1994) 185.

[83] R. Barlow, J. Computat. Phys. **72** (1987) 202.

[84] L3 *Collab.*, M. Acciarri *et al.*, submitted to Phys.Lett.B, hep-ex/0008026 (2000).

[85] G. Goldhaber et al, Phys. Rev. Lett. **3** (1959) 181.

[86] L3 *Collab.*, M. Acciarri *et al.*, Phys. Lett. **B 493** (2000) 233–248.

[87] L3 *Collab.*, M. Acciarri *et al.*, Phys. Lett. **B467** (1999) 171.

[88] L3 *Collab.*,M. Acciarri *et al.*, Phys. Lett. **B436** (1998) 437.

[89] S. Jadach and W. Placzek and M. Skrzypek and B. F. L. Ward and Z. Was, Phys. Rev. **D61** (2000) 113010.

[90] A. Denner and S. Dittmaier and M. Roth and D. Wackeroth, Phys. Lett. **B475** (2000) 127.

[91] D. Bardin *et al.*, Comput. Phys. Commun. **104** (1997) 161.

[92] UA1 *Collab.*, G. Arnison *et al.*, Phys. Lett. **122B** (1983) 103.

[93] UA2 *Collab.*, M. Banner *et al.*, Phys. Lett. **122B** (1983) 476.

[94] CDF *Collab.*, F. Abe *et al.*, Phys. Rev. Lett. **75** (1995) 11.

[95] D0 *Collab.*, S. Abachi *et al.*, Phys. Rev. Lett. **77** (1996) 3309.

[96] D0 *Collab.*, B. Abbott *et al.*, Phys. Rev. **D58** (1998) 092003.

[97] L3 *Collab.*, M. Acciarri *et al.*, Phys. Lett. **B398** (1997) 223–238.

[98] L3 *Collab.*, M. Acciarri *et al.*, Phys. Lett. **B407** (1997) 419–431.

[99] ALEPH *Collab.*, R. Barate *et al.*, Phys. Lett. **B401** (1997) 347–362.

[100] DELPHI *Collab.*, P. Abreu *et al.*, Phys. Lett. **B397** (1997) 158–170.

[101] OPAL *Collab.*, K. Ackerstaff *et al.*, Phys. Lett. **B389** (1996) 416–428.

[102] ALEPH *Collab.*, R. Barate *et al.*, Eur. Phys. J. **C17** (2000) 241–261.

[103] A.G. Frodesen *et al.*, *Probability and Statistics in Particle Physics*, Universitetsforlaget (1979).

[104] G. Wilkinson, in Proceedings of the Workshop on LEP-SPS Performance - Chamonix X -, Chamonix, January, 2000, , 2000).

[105] A. Straessner, private communication.

[106] J. Ellis and K. Geiger, Phys. Rev. **D54** (1996) 1967.

[107] K. Geiger, Comput. Phys. Commun. **104** (1997) 70.

[108] J. Ellis and K. Geiger, Phys. Lett. **B404** (1997) 230.

[109] OPAL *Collab.*, G. Abbiendi *et al.*, Phys. Lett. **B453** (1999) 153–168.

[110] OPAL *Collab.*, G. Abbiendi *et al.*, Eur. Phys. J. **C11** (1999) 217–238.

[111] L3 *Collab.*, M. Acciarri *et al.*, Phys. Lett. **B454** (1999) 386.

[112] L3 *Collab.*, M. Acciarri *et al.*, Eur. Phys. J. **C16** (2000) 1–40.

[113] W. Bernreuther, private communication.

[114] R. Field and R.P. Feynman, Phys. Rev. **D 18** (1978) 3320.

[115] P. Fisher, L3 Internal Note 1998 (1998).

[116] CDF *Collab.*, F. Abe *et al.*, PRL **65** (1990) 2243.

[117] L3 *Collab.*, M. Acciarri *et al.*, Phys. Lett. **B413** (1997) 176.

[118] L3 *Collab.*, L3 Internal Note 2575, contributed paper to ICHEP2000, Osaka, **516**.

[119] ALEPH *Collab.*, R. Barate *et al.*, Phys. Lett. **B453** (1999) 107–120.

[120] DELPHI *Collab.*, P. Abreu *et al.*, Phys. Lett. **B456** (1999) 310–321.

[121] OPAL *Collab.*, G. Abbiendi *et al.*, Eur. Phys. J. **C8** (1999) 191.

[122] ALEPH *Collab.*, R. Barate *et al.*, Phys. Lett. **B484** (2000) 205–217.

[123] DELPHI *Collab.*, P. Abreu *et al.*, Phys. Lett. **B479** (2000) 89–100.

[124] OPAL *Collab.*, G. Abbiendi *et al.*, Phys. Lett. **B493** (2000) 249–265.

[125] ALEPH Collaboration, contributed paper to ICHEP2000, Osaka, (abstract 288) (2000).

[126] DELPHI Collaboration, contributed paper to ICHEP2000, Osaka, (abstract 458) (2000).

[127] L3 Collaboration, L3 note 2514, contributed paper to ICHEP2000, Osaka (2000).

[128] OPAL Collaboration, contributed paper to ICHEP2000, Osaka, (abstract 512) (2000).

[129] A.Gurtu, *Precision Tests of the Electroweak Gauge Theory*, talk presented at ICHEP2000, Osaka, 2000.

[130] M.W.Gruenewald *et al.*, hep-ph/0005309.

[131] The LEP Collaborations ALEPH, DELPHI, L3, OPAL, the LEP Electroweak Working Group and the SLD Heavy Flavour and Electroweak Groups, CERN-PPE/97-154 (2000).

[132] DELPHI *Collab.*, P. Abreu *et al.*, Eur. Phys. J. **C2** (1998) 581.

[133] ALEPH *Collab.*, R. Barate *et al.*, Phys. Lett. **B453** (1999) 121–137.

[134] DELPHI *Collab.*, P. Abreu *et al.*, Phys. Lett. **B462** (1999) 410–424.

[135] OPAL *Collab.*, G. Abbiendi *et al.*, Phys. Lett. **B453** (1999) 138–152.

[136] OPAL *Collab.*, G. Abbiendi *et al.*, hep-ex/0009018 (2000).

[137] ALEPH Collaboration, *Measurement of the W Mass and Width in* e^+e^- *Collisions at* $\sqrt{s}$ *=192-202 GeV*, contributed paper to ICHEP2000, Osaka, **301**.

[138] DELPHI Collaboration, *Measurement of the W mass and width at cms energies from 189-202 GeV*, contributed paper to ICHEP2000, Osaka, **658**.

[139] OPAL Collaboration, *Measurement of the Mass and Width of the W boson*, PN422, contributed paper to ICHEP2000, Osaka, **658**.

[140] B.Pietrzyk, *The Global Fit of Electroweak data*, proceeding submitted to ICHEP2000, Osaka, 27 July - 2 August, 2000.

[141] P.Igo-Kemenes, *Status of Higgs Boson Searches*, talk presented at LEP seminar, Nov. 3, 2000.

Acknowledgements

I thank my thesis advisor Prof. Thomas Hebbeker for giving me the opportunity to do this research. His constant support and guidance throughout the time of this thesis helped me to complete this work. The weekly meetings gave excellent opportunity to gain insight into various aspects of high energy physics.

It was a pleasure to work with Martin Grünewald. I thank him for many enlightening discussions and helpful suggestions.

I would like to thank all members of the L3 collaboration and especially members of the W group and Muon Chamber group. In particular I would like to mention Prof. S.C.C. Ting. Under his impressive leadership, a challenging work environment is provided within the L3 collaboration.

I thank the European Organisation of Nuclear Research (CERN) for their hospitality and giving me the opportunity to work there and use their facilities, especially the CERN car, for doing this work.

I have been privileged to make an acquaintance with the colleagues of the Humboldt University Berlin and DESY Zeuthen. I enjoyed our “social events” a lot.

I thank my parents for their love and support.

Erklärung

Hiermit erkläre ich, die Dissertation selbständig und ohne unerlaubte Hilfe angefertigt zu haben.

Ho Jong Lee

Lebenslauf

Name: **Ho Jong Lee**

Geburtsdatum: 05.Mai 1968
Geburtsort: Ahn-Dong, S.Korea.
Staatsangehörigkeit: Koreanisch.

1974-1979	Grundschule in Donghae und Ahn-Dong, S.Korea.
1980-1982	Sang-Un- und Jin-Kwang-Gymnasiums, S. Korea.
1982-1989	Besuch des Gottfried-Keller-Gymnasium (Einstufung in die 7. Klasse) mit abschließendem Abitur in Berlin.
Nov. 1989	Studium der Physik an der Ludwig-Maximilians-Universität München.
Nov. 1991	Vordiplom in Physik.
1995-1996	Diplomarbeit bei der *Crystal-Barrel*-Gruppe in Uni. München mit einem Aufenthalt am CERN.
Sept. 1996	Diplom in Physik
1996-1999	Wissenschaftlicher Mitarbeiter der Humboldt-Univeristät zu Berlin; Aufenthalt am europäischen Forschungslabor CERN in Genf zur Teilnahme am L3 Experiment
1999-2000	Graduiertenkolleg “Strukturuntersuchungen, Präzisionstests und Erweiterungen des Standardmodells der Elementarteilchenphysik”